

Exploring Extensions of the Scalar Sector of the Standard Model

Ph.D. Thesis

by

Najimuddin Khan



Discipline of Physics, Indian Institute of Technology Indore,
Khandwa Road, Simrol, Indore - 453552, India

Exploring Extensions of the Scalar Sector of the Standard Model

A THESIS

*Submitted in partial fulfillment of the
requirements for the award of the degree*

of

DOCTOR OF PHILOSOPHY

by

Najimuddin Khan



**Discipline of Physics, Indian Institute of Technology Indore,
Khandwa Road, Simrol, Indore - 453552, India**

Dedicated
to
My Family

Acknowledgements

First and foremost, I gratefully acknowledge the continual guidance and support of my adviser, Dr. Subhendu Rakshit. His dedication to research and pursuit of physics has been an invaluable source of inspiration and encouragement to me. I would also like to thank my PSPC committee members, Dr. Manavendra N Mahato, Dr. Antony Vijesh for serving as my committee members even at hardship.

I would like to thank Prof. Amitava Raychaudhuri, Prof. Amitava Datta, Prof. Biswarup Mukhopadhyaya, Dr. Avirup Shaw, Avinanda Chaudhuri, Nabanita Ganguly for their wonderful collaboration. You supported me greatly and were always willing to help me.

A special thanks to my family. Words cannot express how grateful I am to my **MAA-ABBA** for all of the sacrifices that you've made on my behalf. Your prayer for me was what sustained me thus far. I would also like to thank all of my relatives who supported, and incited me to strive towards my goal.

“There are some people in life that make you laugh a little louder, smile a little bigger and live just a little bit better”FRIENDS. My jolly friends Minarul Islam, Lalsha Khan, Imran Ali. Thanks dude for helping to live. I would like to thank my JAJABOR friend at IIT Indore Mr. Sudeep Ghosh. You are the best person at IIT Indore who always fight with me and gave a lot of love to me. It is also unforgettable moments with VAI-BON: Sidharta Karmakar and Sujata.

Abstract

The Standard Model is one of the most successful theories which describes strong, weak and electromagnetic forces and interactions between the elementary particles. The scalar boson has been found at the Large Hadron Collider (LHC) on 4th July 2012 that has confirmed the Higgs mechanism. Although, the properties of this scalar are consistent with the Higgs as predicted by the standard model (SM), the experimental data still allow an extension of the scalar sector. The standard model fails to explain few physical phenomena in Nature, for example, the presence of dark matter, existence of massive neutrino, the observed matter-antimatter asymmetry, inflation of the Universe, etc. These phenomena indicate the presence of new physics beyond the standard model. In this thesis, various extensions of the scalar sector have been considered comprising of different $SU(2)_L$ multiplets. The main purpose for writing this thesis is to explore properties of these new scalars using the weak vector boson scattering processes and from the (meta)stability of the scalar potential.

If the extended scalar sector participates in the electroweak symmetry breaking then these extra scalars need to couple with the known standard model particles. In this work, it has been shown that the vector boson scattering involving scalar boson exchanges provide a complimentary way to direct search methods to probe into the scalar sector. As different extended scalar sectors have similar types of scalar fields, e.g., an extra CP -even Higgs, charged Higgs etc., these new physics models can give rise to the similar types of experimental signatures. In this work, it has been shown that it is possible to distinguish between such models at various vector boson scattering processes by looking at the resonances. Also, the shapes of the resonances can provide further insight to the relevant parameter space of these models.

As in the SM, the electroweak vacuum is metastable, it is important to explore if

an extended scalar has an answer in its reserve. As the scalar weakly interacting massive scalar particles protected by Z_2 symmetry can serve as viable dark matter candidates, it is interesting to explore if they help prolong the lifetime of the Universe. The effective Higgs potential gets modified in the presence of these new extra scalars, improving the stability of electroweak vacuum. Such an exercise has been undertaken in various kinds of extended scalar sectors. In order to show the explicit dependence of the electroweak stability on different parameters of these extended sectors, various kinds of phase diagrams have been presented. Graphical demonstrations have been provided to illustrate how the confidence level, at which stability of electroweak vacuum is excluded, depends on such new physics parameters. This study will help to estimate the lifetime of the electroweak vacuum, especially if it still remains in the metastable state in the extended scalar sectors.

List of Publications

A. Published:

1. **Najimuddin Khan** and Subhendu Rakshit, “Study of electroweak vacuum metastability with a singlet scalar dark matter”, Phys. Rev. D**90**, 113008 (2014), [arXiv:1407.6015 [hep-ph]].
2. **Najimuddin Khan** and Subhendu Rakshit, “Constraints on inert dark matter from the metastability of the electroweak vacuum”, Phys. Rev. D**92**, 055006 (2015), [arXiv:1503.03085 [hep-ph]].
3. Avinanda Chaudhuri, **Najimuddin Khan**, Biswarup Mukhopadhyaya and Subhendu Rakshit, “Dark matter candidate in an extended type III seesaw scenario”, Phys. Rev. D**91**, 055024 (2015), [arXiv:1501.05885 [hep-ph]].
4. Amitava Datta, Nabanita Ganguly, **Najimuddin Khan** and Subhendu Rakshit, “ Exploring collider signatures of the inert Higgs doublet model”, [arXiv:1610.00648 [hep-ph]] (Accepted in Phys. Rev. D).

B. Under review:

1. **Najimuddin Khan**, Subhendu Rakshit and Amitava Raychaudhuri, “Obstacles to extending R-parity violation to Supersymmetric SU(5)”, [arXiv:1509.01516 [hep-ph]].
2. **Najimuddin Khan**, Biswarup Mukhopadhyaya, Subhendu Rakshit and Avirup Shaw, “ Exploring the extended scalar sector with resonances in vector boson scattering”, [arXiv:1608.05673 [hep-ph]].

3. **Najimuddin Khan**, “ Exploring Hyperchargeless Higgs Triplet Model up to the Planck Scale”, [arXiv:1610.03178 [hep-ph]].

N.B: Entries A1, A2, B2 and B3 are parts of my thesis.

Table of Contents

Title	i
Acknowledgements	vii
Abstract	ix
List of Publications	xi
Table of Contents	xv
List of Figures	xxi
List of Tables	xxix
List of abbreviations	xxxi
1 Introduction	1
1.1 The Standard Model	2
1.2 Shortcomings of the SM	10
1.2.1 The Higgs mass hierarchy problem	10
1.2.2 Flavor Problems	11
1.2.3 Stability of the electroweak vacuum	12
1.2.4 Gravity	12
1.2.5 Gauge Unification	13
1.2.6 Dark matter	13
1.2.7 Baryon-antibaryon asymmetry	14
1.2.8 Recent LHC data and scope for an extended scalar sector . . .	14
1.3 Extended scalar sector	15
1.3.1 Constraints on the extended scalar sectors	17
1.3.1.1 The electroweak precision constraints	17
1.3.1.2 Stability of the electroweak vacuum	19

1.3.1.3	Unitarity of the scattering matrix	20
1.4	Organization of the Thesis	21
2	Dark matter: Relic Density, Direct and Indirect detections	25
2.1	Introduction	25
2.2	Evidence of Dark Matter	26
2.2.1	Galactic Rotation Curves	26
2.2.2	Gravitational Lensing and Bullet Cluster	27
2.2.3	The Cosmic Microwave Background	29
2.3	Components of Dark Matter	30
2.4	Relic Density of Dark Matter	33
2.5	Direct Detections of Dark Matter	35
2.6	Indirect Detections of Dark Matter	37
2.6.1	Gamma-ray Excess from Galactic Center	38
2.6.2	Positron Excess in the Cosmic Ray	39
2.7	Summary	40
3	Electroweak Symmetry Breaking in Extended Higgs sector	43
3.1	Introduction	43
3.2	The Standard Model with a real singlet scalar	44
3.2.1	Constraints on the SM+ S model	45
3.2.1.1	Constraints from stability of the scalar potential . . .	45
3.2.1.2	Perturbativity constraints	46
3.2.1.3	Constraints from unitarity of the scattering matrix .	46
3.2.1.4	Constraints from the LHC	47
3.2.2	Dark matter in SM+ S	47
3.3	Two Higgs doublet model	47
3.3.1	Scalar Masses and Mixing for 2HDM	49
3.3.2	Constraints on 2HDM	50
3.3.2.1	Constraints from stability of the scalar potential . . .	50
3.3.2.2	Perturbativity constraints	51

3.3.2.3	Constraints from unitarity of the scattering matrix . . .	51
3.3.2.4	Constraints from electroweak precision experiments . . .	51
3.3.2.5	Constraints from the LHC	53
3.3.3	Dark Matter in 2HDM	53
3.4	Higgs triplet model with hypercharge $Y = 0$	54
3.4.1	Scalar Masses and Mixing for HTM ($Y = 0$)	55
3.4.2	Constraints on the HTM ($Y = 0$)	56
3.4.2.1	Constraints from stability of the scalar potential . . .	56
3.4.2.2	Perturbativity bounds	57
3.4.2.3	Constraints from unitarity of the scattering matrix . .	57
3.4.2.4	Constraints from electroweak precision experiments . .	59
3.4.2.5	Constraints from the LHC	60
3.4.3	Dark Matter in HTM ($Y = 0$)	60
3.5	Higgs triplet model with hypercharge $Y = 2$	60
3.5.1	Scalar Masses and Mixing for HTM ($Y = 2$)	62
3.5.2	Constraints on the HTM ($Y = 2$)	63
3.5.2.1	Constraints from stability of scalar potential	63
3.5.2.2	Perturbativity constraints	63
3.5.2.3	Constraints from unitarity of the scattering matrix . .	64
3.5.2.4	Constraints from the neutrino mass and the elec- troweak precision experiments	64
3.5.2.5	Constraints from the LHC	65
3.5.3	Dark matter in HTM ($Y = 2$)	66
3.6	Summary	66
4	Vector boson scattering in extended Higgs sector	69
4.1	Introduction	69
4.2	Polarization of Vector Bosons	71
4.3	Connection with Electroweak Symmetry Breaking	73
4.4	Scattering cross-section: Partial Wave Analysis	74
4.5	Benchmark points in different models for $V_L V_L$ scattering	80

4.6	$V_L V_L$ scattering with extended scalar sectors	81
4.7	Summary	87
5	Metastability in Standard Model	89
5.1	Introduction	89
5.2	Effective Higgs potential in the Standard Model	90
5.2.1	Matching conditions and RG evaluation of the SM couplings	91
5.2.2	Metastability and Tunneling Probability	95
5.2.3	Bounds on the Higgs mass from metastability and perturbativity	100
5.2.4	Asymptotic safety in SM	102
5.2.5	Veltman's conditions in SM	103
5.3	Summary	103
6	Metastability in Extended Scalar Sectors of the Standard Model	105
6.1	Introduction	105
6.2	Singlet scalar extension of SM	106
6.2.1	Effective potential and RGE running	106
6.2.2	Singlet Scalar as a dark matter candidate	108
6.2.3	RGE running from $\mu = M_t$ to M_{Pl} in SM+ S	111
6.2.4	Tunneling probability and Metastability in SM+ S	114
6.2.5	Phase diagrams in SM+ S	116
6.2.6	Confidence level of vacuum stability in SM+ S	120
6.2.7	Asymptotic safety in SM+ S	121
6.3	Doublet scalar extension of SM	122
6.3.1	Inert Doublet Model	122
6.3.2	Constraints on ID model	125
6.3.2.1	Bounds from electroweak precision experiments	126
6.3.2.2	Direct search limits from LEP and LHC	128
6.3.2.3	Bounds from LHC diphoton signal strength	128
6.3.2.4	Constraints from dark matter relic density and direct search limits	130

6.3.3	Tunneling Probability and Metastability in IDM	135
6.3.4	Phase diagrams in IDM	138
6.3.5	Veltman's conditions in IDM	145
6.4	Triplet ($Y = 0$) scalar extension of the SM	146
6.4.1	Constraints on ITM	149
6.4.1.1	Bounds from LHC diphoton signal strength	149
6.4.1.2	Constraints from dark matter relic density	149
6.4.2	Tunneling Probability and Metastability in ITM	150
6.4.3	Phase diagrams in ITM	152
6.5	Summary	155
7	Summary and Conclusions	157
	Appendices	161
A	Analytical expressions for vector boson scattering	1
A.1	Amplitudes for different modes of $V_L V_L$ scattering	1
A.1.1	$W_L^+(p_1) + W_L^-(p_2) \rightarrow W_L^+(k_1) + W_L^-(k_2)$	1
A.1.2	$W_L^+(p_1) + W_L^+(p_2) \rightarrow W_L^+(k_1) + W_L^+(k_2)$	3
A.1.3	$W_L^+(p_1) + W_L^-(p_2) \rightarrow Z_L(k_1) + Z_L(k_2)$	4
A.1.4	$W_L^+(p_1) + Z_L(p_2) \rightarrow W_L^+(k_1) + Z_L(k_2)$	6
A.1.5	$Z_L(p_1) + Z_L(p_2) \rightarrow Z_L(k_1) + Z_L(k_2)$	9
A.2	Required Feynman rules for VV scattering	10
A.3	Restoration of unitarity in extended scalar sectors	12
B	Effective Higgs quartic coupling and RG-equations for SM	1
B.1	Effective Higgs quartic coupling for SM	1
B.2	Standard Model β -functions	4
B.3	β -functions for singlet scalar extended SM	6
B.4	β -functions for inert doublet extended SM	6
B.5	β -functions for inert triplet ($Y = 0$) extended SM	7

List of Figures

1.1	<i>The particle spectrum of the SM of elementary particles [3].</i>	3
1.2	<i>Schematic diagram of the Higgs potential. The potential is symmetric about the vertical axis but at the minimum the symmetry is broken. The circular line indicates the remaining $U(1)$ symmetry.</i>	7
2.1	<i>Galactic rotation curve for NGC 6503 dwarf spiral galaxy. Image credit: Katherine Freese [38].</i>	27
2.2	<i>(a) the left panel is a X-ray satellite Chandra image of the cluster of the visible matter and (b) The right panel shows a direct image of the cluster obtained with the 6.5-m Magellan telescope in the Las Campanas Observatory. The contour lines are drawn for the images produces due to the gravitational lensing by the dark matter in the galaxies. Image credit: D. Clowe et al. [39].</i>	28
2.3	<i>The figure shows temperature-temperature (TT) angular power spectrum of CMBR from the nine years WMAP data. Image credit: C. L. Bennett et al. [WMAP Collaboration] [20].</i>	29
2.4	<i>Limit on WIMP cross-sections (normalized to a single nucleon) for spin-independent coupling versus mass from different experiments. Most stringent limit comes from the LUX-2013 experiments. Image credit: Aprile E. et al. [50]</i>	36
2.5	<i>The Fermi bubble around the galactic center. Image credit: NASA/Fermi LAT.</i>	38
2.6	<i>The variations of fraction of positron flux with energy. Image credit: AMS-02. [47]</i>	39
4.1	<i>Argand diagram of the function a_l in $Re(a_l) - Im(a_l)$ plane is a unitary circle with radius 0.5.</i>	78
4.2	<i>Plots for VV scattering in 2HDM.</i>	84

4.3	<i>Plots for VV scattering in $Y=0$, HTM.</i>	85
4.4	<i>Plots for VV scattering in $Y=2$, HTM.</i>	86
5.1	<i>(a) RG evolution of the gauge couplings g_1, g_2, g_3, top Yukawa coupling y_t, Higgs self-quartic coupling λ in $\overline{\text{MS}}$ scheme and (b) RG evolution of λ in the SM and in the 3σ bands for M_t, M_h and $\alpha_s(M_Z)$ are displayed.</i>	93
5.2	<i>Higgs quartic coupling λ and effective λ_{eff}-function as a function of running RGE scale.</i>	95
5.3	<i>Higgs quartic coupling λ and corresponding β-function as a function of the running RGE scale.</i>	96
5.4	<i>Tunneling probability \mathcal{P}_0 dependence on M_t in SM. Light-green band stands for M_t at $\pm 1\sigma$. The solid blue line corresponds to the central values of M_h and $\alpha_s(M_Z)$, whereas the light-red band corresponds to the 1σ deviation in Higgs mass and light-gray band for $\alpha_s(M_Z)$.</i>	99
5.5	<i>(a) In SM, regions of absolute stability (green), metastability (yellow), instability (red) of the EW vacuum in the $M_h - M_t$ plane phase diagram. (b) Zoomed in the region of the preferred experimental range of M_h and M_t. The boundary lines (red) correspond to 1σ variation in $\alpha_s(M_Z)$. The gray areas denote the experimentally favored zones for M_h and M_t at 1, 2 and 3σ.</i>	100
5.6	<i>Phase diagram in $M_t - \alpha_s(M_Z)$ plane in SM. Regions of absolute stability (green), metastability (yellow), instability (red) of the EW vacuum are marked. The dotted lines correspond to $\pm 3\sigma$ variation in M_h and the gray areas denote the experimental allowed region for M_t and $\alpha_s(M_Z)$ at 1, 2 and 3σ.</i>	101
5.7	<i>Contour plot for $\lambda(M_{\text{Pl}}) = 0$ (red line) and $\beta_\lambda(M_{\text{Pl}}) = 0$ (blue line). Dotted lines correspond to $\pm 3\sigma$ variation in $\alpha_s(M_Z)$. The gray areas denote the experimental allowed region for M_h and M_t at 1, 2 and 3σ.</i>	101
6.1	<i>Dark matter relic density Ωh^2 as a function of the dark matter mass $M_{\text{DM}}(\equiv M_S)$ for different values of the portal coupling: $\kappa(M_Z) = 0.05$ (black), $\kappa(M_Z) = 0.10$ (brown), and $\kappa(M_Z) = 0.15$ (red). The thin blue band corresponds to the relic density of the dark matter, $\Omega h^2 = 0.1198 \pm 0.0026$ (3σ) of the present the Universe.</i>	110

6.2	SM+S allowed parameter space in the $\kappa(M_Z) - M_{DM}$ plane in agreement with the relic density constraints, direct and indirect detection. Where the upper dotted, solid in the middle and the lower dotted blue line correspond to the relic density $\Omega h^2 = 0.112, 0.1198$ and 0.1276 respectively.	111
6.3	SM+S RG evolution of the gauge couplings g_1, g_2, g_3 , top Yukawa coupling y_t , Higgs self-quartic coupling λ , Higgs portal coupling κ and scalar self-quartic coupling λ_S in \overline{MS} scheme.	112
6.4	RG evolution of λ in the SM+S for our benchmark point. 3σ bands for M_t, M_h and $\alpha_s(M_Z)$ are displayed.	113
6.5	(a) RG evolution of λ (red band), λ_{eff} (blue band) and β_λ (dot-dashed black) in SM+S for our benchmark point. (b) Evolution of λ for different $\kappa(M_Z)$. Each $\kappa(M_Z)$ corresponds to a specific M_S to satisfy DM relic density $\Omega h^2 \approx 0.1198$	114
6.6	(a) Tunneling probability \mathcal{P}_0 as a function of M_t . The left band corresponds to SM and the right one to SM+S for our benchmark point. Light-green band stands for M_t at $\pm 1\sigma$. (b) \mathcal{P}_0 as a function of $\kappa(M_Z)$ for various $\lambda_S(M_Z)$	115
6.7	(a) In SM+S, regions of absolute stability (green), metastability (yellow), instability (red) of the EW vacuum in the $M_h - M_t$ plane phase diagram is presented for the benchmark point $M_S = 620$ GeV, $\kappa(M_Z) = 0.185$ and $\lambda_S(M_Z) = 1$. (b) Similar plot for $M_S = 360$ GeV, $\kappa(M_Z) = 0.105$ and $\lambda_S(M_Z) = 1.6$. The orange region corresponds to nonperturbative zone for λ_S . The three boundary lines (dotted, solid and dotted red) correspond to $\alpha_s(M_Z) = 0.1184 \pm 0.0007$. The gray areas denote the experimentally favored zones for M_h and M_t at 1, 2 and 3σ	117
6.8	Phase diagram in $M_t - \alpha_s(M_Z)$ plane in SM+S model for our benchmark point. Regions of absolute stability (green), metastability (yellow), instability (red) of the EW vacuum are marked. The dotted lines correspond to $\pm 3\sigma$ variation in M_h and the gray areas denote the experimental allowed region for M_t and $\alpha_s(M_Z)$ at 1, 2 and 3σ	118
6.9	Phase diagram in $\kappa(M_Z) - M_S$ plane in SM+S. Regions of absolute stability (green), metastability (yellow) of the EW vacuum for $\lambda_S(M_Z) = 1$ are shown. The red solid line corresponds to $\Omega h^2 \approx 0.1198$. The red dashed lines correspond to 3σ error on Ωh^2	118

- 6.10 Phase diagram in $\kappa(M_Z) - M_h$ plane in SM+S. Regions of absolute stability (green), metastability (yellow) and instability (red) of the EW vacuum for $\lambda_S(M_Z) = 1$ are displayed. λ and/or λ_S are/is non-perturbative in the orange region. The blue dashed line corresponds to $M_h = 125.7$ GeV. 119
- 6.11 Dependence of confidence level (one-sided) at which EW vacuum stability is excluded/allowed on $\kappa(M_Z)$ in SM+S. Regions of absolute stability (green) and metastability (yellow) of EW vacuum are shown. 120
- 6.12 In SM+S model, (a) Contour plot for $\lambda(M_{\text{Pl}}) = 0$ (red line) and $\beta_\lambda(M_{\text{Pl}}) = 0$ (blue line) for our benchmark point. (b) Similar plot for $\lambda(\Lambda) = 0$ and $\beta_\lambda(\Lambda) = 0$, where $\Lambda = 3.8 \times 10^{14}$ GeV. Dotted lines correspond to $\pm 3\sigma$ variation in $\alpha_s(M_Z)$. The gray areas denote the experimental allowed region for M_h and M_t at 1, 2 and 3σ 121
- 6.13 IDM RG evolution of the couplings λ_i ($i = 1, \dots, 5$), λ_L, λ_S for the set of parameters in Table 6.3. 126
- 6.14 Allowed parameter space in $\Delta M_{H^\pm} - \Delta M_H$ plane for $M_A = 70$ GeV and $\lambda_S = 0.007$ in IDM. Constraints from S and T parameters are shown by solid black, green and red lines. The blue band corresponds the 3σ variation in $\Omega h^2 = 0.1198 \pm 0.0026$ [21]. On the brown region the unitarity bound is violated on or before M_{Pl} . The cross-hatched region is excluded from LEP II data. 127
- 6.15 In IDM, (a) Dark matter relic density Ωh^2 as a function of the dark matter mass $M_{\text{DM}} (\equiv M_A)$ for different values of the Higgs portal coupling: $\lambda_S(M_Z) = 0.002$ (black), $\lambda_S(M_Z) = 0.005$ (brown), and $\lambda_S(M_Z) = 0.008$ (red), with $\Delta M_{H^\pm} = \Delta M_H = 50$ GeV. (b) For Higgs portal coupling: $\lambda_S(M_Z) = 0.05$ (black), $\lambda_S(M_Z) = 0.10$ (brown), and $\lambda_S(M_Z) = 0.15$ (red), with $\Delta M_{H^\pm} = 1$ GeV and $\Delta M_H = 2$ GeV. The thin blue band corresponds to the relic density of the dark matter, $\Omega h^2 = 0.1198 \pm 0.0026$ (3σ) of the present the Universe. Light red band is disallowed from the Higgs invisible decay width. 132
- 6.16 (a) Tunneling probability \mathcal{P}_0 dependence on M_t . The left band (between dashed lines) corresponds to SM. The right one (between dotted lines) is for ID model for DM mass $M_A = 573$ GeV. Constraints from WMAP and Planck measured relic density, as well as XENON100 and LUX DM direct detection null results are respected for these specific choice of parameters. Light-green band stands for M_t at $\pm 1\sigma$. (b) \mathcal{P}_0 is plotted against Higgs dark matter coupling $\lambda_S(M_Z)$ for different values of $\lambda_2(M_Z)$ 136

- 6.17 *Constraints in $M_H - M_A$ plane in IDM. The cross-hatched region is excluded from LEP [150]. Choosing $M_{H^\pm} = 120$ GeV and $\lambda_S(M_Z) = 0.001$, relic density constraint is satisfied at 3σ on the blue band. The green (yellow) region corresponds to EW vacuum stability (metastability). The solid brown line correspond to $M_H = M_A$. The gray area on the left to it is of no interest to us as $M_H > M_A$ has been chosen. The dashed brown line shows the LEPI limit. On the brown region, unitarity constraints are violated before M_{Pl} 138*
- 6.18 *Phase diagram in $\Delta M_H - \Delta M_{H^\pm}$ plane for $M_A = 70$ GeV in IDM. The green and yellow regions correspond to EW vacuum stability and metastability respectively. The cross-hatched band is excluded from LEP. The brown region suffers from unitarity violation before M_{Pl} . The blue band reflects relic density constraint at 3σ 139*
- 6.19 *Phase diagram in $\lambda_S(M_Z) - M_A$ plane for $\lambda_2(M_Z) = 0.1$ in IDM. Panel (a) stands for ‘low’ DM mass. The blue band corresponds the 3σ variation in Ωh^2 when $\Delta M_{H^\pm} = 40$ GeV and $\Delta M_H = 40$ GeV. LEP direct search constraints are represented by the cross-hatched band at the bottom. Entire green region imply EW vacuum stability. Panel (b) stands for ‘high’ DM masses. The relic density band (blue) now correspond to $\Delta M_{H^\pm} = 1$ GeV and $\Delta M_H = 2$ GeV. The corresponding stable and metastable phases for EW vacuum are represented by green and yellow patches respectively. The relic density band (red) corresponds to $\Delta M_{H^\pm} = 5$ GeV and $\Delta M_H = 2$ GeV. For this, the boundary separating the EW phases is denoted by the red dashed line. 141*
- 6.20 *Phase diagrams in $M_h - M_t$ plane in IDM. Panels (a) and (b) stand for ‘low’ and ‘high’ DM masses respectively. Regions of absolute stability (green), metastability (yellow), instability (red) of the EW vacuum are also marked. The gray zones represent error ellipses at 1, 2 and 3σ . The three boundary lines (dotted, solid and dotted red) correspond to $\alpha_s(M_Z) = 0.1184 \pm 0.0007$. Details of benchmark points are available in the text. 142*
- 6.21 *Phase diagrams in $M_t - \alpha_s(M_Z)$ plane in IDM for the same sets of benchmark points as in Fig. 6.20. Notations used are also the same as in Fig. 6.20. 143*

6.22	<i>Dependence of confidence level at which EW vacuum stability is excluded (one-sided) or allowed on $\lambda_S(M_Z)$ and $\lambda_2(M_Z)$ in IDM. Regions of absolute stability (green) and metastability (yellow) of EW vacuum are shown for $\lambda_2(M_Z) = 0.1$. The positive slope of the line corresponds to the stable EW vacuum and negative slope corresponds to the metastability.</i>	144
6.23	<i>ITM RG evolution of the couplings $\lambda_1, \lambda_2, \lambda_3$ for the set of parameters in Table 6.5.</i>	148
6.24	<i>Dark matter relic density Ωh^2 as a function of the dark matter mass $M_{DM}(\equiv M_H)$ for the portal coupling: $\lambda_3(M_Z) = 0.10$ (red) in ITM. The thin blue band corresponds the relic density, $\Omega h^2 = 0.1198 \pm 0.0026$ (3σ).</i>	150
6.25	<i>(a) Tunneling probability \mathcal{P}_0 dependence on M_t. The left band (between dashed lines) corresponds to SM. The right one (between dotted lines) is for IT model for DM mass $M_H = 1897$ GeV. Dark matter constraints are respected for these specific choices of parameters. Light-green band stands for M_t at $\pm 1\sigma$. (b) \mathcal{P}_0 is plotted against Higgs dark matter coupling $\lambda_S(M_Z)$ for different values of $\lambda_2(M_Z)$.</i>	151
6.26	<i>Phase diagrams in (a) $M_h - M_t$ plane and (b) $M_t - \alpha_s(M_Z)$ plane ITM. Regions of absolute stability (green), metastability (yellow), instability (red) of the EW vacuum are also marked. The gray zones represent error ellipses at 1, 2 and 3σ. The three boundary lines (dotted, solid and dotted red) correspond to $\alpha_s(M_Z) = 0.1184 \pm 0.0007$.</i>	152
6.27	<i>Dependence of confidence level at which EW vacuum stability is excluded (one-sided) or allowed on $\lambda_3(M_Z)$ and $\lambda_2(M_Z)$ in ITM. Regions of absolute stability (green) and metastability (yellow) of EW vacuum are shown for $\lambda_2(M_Z) = 0.1$.</i>	153
6.28	<i>Phase diagram in $\lambda_3(M_Z) - M_H$ plane in ITM. Right side of the black-dotted line is allowed from the signal strength ratio of $\mu_{\gamma\gamma}$ within 68% confidence level. and the left side is excluded at 1σ. In the metastable region, the Higgs portal coupling $\lambda_3(M_Z)$ is negative, however, beyond the scale Λ_B it is greater than zero.</i>	154
A.1	<i>Generic Feynman diagrams for $W_L^+(p_1) + W_L^-(p_2) \rightarrow W_L^+(k_1) + W_L^-(k_2)$ scattering</i>	2
A.2	<i>Generic Feynman diagrams for $W_L^+(p_1) + W_L^+(p_2) \rightarrow W_L^+(k_1) + W_L^+(k_2)$ scattering.</i>	3

A.3	<i>Generic Feynman diagrams for $W_L^+(p_1) + W_L^-(p_2) \rightarrow Z_L(k_1) + Z_L(k_2)$ scattering.</i>	5
A.4	<i>Generic Feynman diagrams for $W_L^+(p_1) + Z_L(p_2) \rightarrow W_L^+(k_1) + Z_L(k_2)$ scattering.</i>	7
A.5	<i>Generic Feynman diagrams for $Z_L(p_1) + Z_L(p_2) \rightarrow Z_L(k_1) + Z_L(k_2)$ scattering.</i>	9

List of Tables

1.1	<i>Charges of the SM fermions and scalars. C is the color charge under $SU(3)_C$ group, T^3 is the third component of weak isospin of $SU(2)_L$ group, Y is the hypercharge quantum number of $U(1)_Y$ group and Q is the electric charge quantum number.</i>	5
1.2	<i>The observed signal strengths and uncertainties for different Higgs boson decay channels [24] for mass, $M_h \sim 125$ GeV. The data have been taken for proton-proton collision of center-of-mass energies, $\sqrt{s} = 7, 8$ TeV with luminosity, 20 fb^{-1}. W^*, Z^* decay to fermions. $\Gamma_{exp}(h \rightarrow \chi\chi)$ is the decay width as observed in the experiments and $\Gamma_{SM}(h \rightarrow \chi\chi)$ is the same predicted by the SM.</i>	15
4.1	<i>Different scattering processes and corresponding mediator particles for resonance in various extended scalar sectors. “✓” indicates presence of a resonance where as “✗” corresponds to no resonance peak. . . .</i>	87
5.1	<i>SM observables which can be taken as input to fix the SM fundamental parameters g_1, g_2, g_3, y_t and λ.</i>	92
6.1	<i>Benchmark points with dark matter mass $M_{DM} < M_h/2$, which is allowed from the relic density constraint on the DM of WMAP and Planck, $\Omega h^2 = 0.1198 \pm 0.0026$ within 3σ confidence level, direct detection LUX (2013) and Higgs invisible decay width from the LHC. . .</i>	109
6.2	<i>Values of all SM+S coupling constants at $M_{Pl} = 1.2 \times 10^{19}$ GeV with $M_t = 173.1$ GeV, $M_h = 125.7$ GeV and $\alpha_S(M_Z) = 0.1184$.</i>	111
6.3	<i>A set of values of all ID model coupling constants at M_t and M_{Pl} for $M_A = 573$ GeV, $\Delta M_{H^\pm} = 1$ GeV, $\Delta M_H = 2$ GeV, and $\lambda_S(M_Z) = 0.001$.</i>	125

6.4	<i>Benchmark points with dark matter mass $M_{DM} < M_h/2$, with $M_{H^\pm} = 200$ GeV and $M_{H^\pm} = 180$ GeV, which is allowed from the relic density constraint of WMAP and Planck, $\Omega h^2 = 0.1198 \pm 0.0026$ within 3σ confidence level, direct detection LUX (2013) and Higgs invisible decay width from the LHC.</i>	131
6.5	<i>A set of values of all ITM coupling constants at M_t and M_{Pl} for $M_{DM} = 1897$ GeV.</i>	148
A.1	<i>$A_{2,g}$ and $A_{2,S}$ for $W_L^+ W_L^- \rightarrow W_L^+ W_L^-$ process. C and \hat{C} can be found in Appendix A.2.</i>	13
A.2	<i>$A_{2,g}$ and $A_{2,S}$ for $W_L^+ W_L^+ \rightarrow W_L^+ W_L^+$ process. C and \hat{C} can be found in Appendix A.2.</i>	14
A.3	<i>$A_{2,g}$ and $A_{2,S}$ for $W_L^+ W_L^- \rightarrow Z_L Z_L$ process. C, C' and \tilde{C} can be found in Appendix A.2.</i>	14
A.4	<i>$A_{2,g}$ and $A_{2,S}$ for $W_L^+ Z_L \rightarrow W_L^+ Z_L$ process. C, C' and \tilde{C} can be found in Appendix A.2.</i>	15

List of abbreviations

SM	Standard Model
BSM	Beyond Standard Model
VEV	Vacuum expectation value
EW	Electroweak
EWSB	Electroweak symmetry breaking
EWPT	Electroweak precision test
LHC	Large Hadron Collider
ATLAS	A Toroidal LHC Apparatus
CMS	Compact Muon Solenoid
LEP	Large Electron Positron Collider
CMBR	Cosmic Microwave Background Radiation
WIMP	Weakly interacting massive particles
DM	Dark Matter
S -matrix	Scattering-matrix
WMAP	Wilkinson Microwave Anisotropy Probe
SM+ S	Standard Model with a real singlet scalar
2HDM	Two Higgs doublet model
HTM	Higgs triplet model
IDM	Inert doublet model
ID	Inert doublet
ITM	Inert triplet model

IT	Inert triplet
VBS	Vector boson scattering
RG	Renormalization group
RGE	Renormalization group equation
NNLO	next-to-next-to leading order
VC	Veltman's condition

Chapter 1

Introduction

The unification of electric and magnetic fields in classical electromagnetism was realized by James Clerk Maxwell in 1864. Similarly, the Standard Model (SM) electroweak theory unifies the electromagnetic and weak forces. This was first proposed by Sheldon Glashow in 1961. Abdus Salam and Steven Weinberg revised the Glashow's electroweak theory by having the masses for W^\pm and Z bosons. The SM describes what matter is made of and how it holds together. The basic ideas are: all matter is made of elementary particles, and these particles interact with each other by exchanging other particles associated with the fundamental forces. The SM Lagrangian is designed to respect certain mathematical symmetries. The equations of motion derived from this Lagrangian have enabled physicists to make predictions about various observables which have been successfully tested in particle physics laboratories. Nearly every quantity that has been measured in particle physics laboratories over the past five decades up to energy of TeV falls right on the predicted value, within experimental error margins. This has made the SM of particle physics one of the best tested and established fundamental theory of the Nature. In the SM, the Higgs mechanism is believed to give rise to the masses of

all the elementary particles through spontaneous symmetry breaking of the gauge symmetry. Discovery of a Higgs-like scalar boson at the Large Hadron Collider (LHC) on 4th July 2012 [1, 2], confirms that the Higgs mechanism is responsible for electroweak symmetry breaking.

Although the SM is one of the most successful theories, it is unable to explain various experimental observations, e.g., it fails to explain non-zero neutrino masses, baryon-antibaryon asymmetry in Nature, mysterious nature of dark matter and dark energy. Moreover the SM does not incorporate the theory of gravitation. Also it is plagued with its own theoretical problems such as the hierarchy problem related to the mass of the Higgs, mass hierarchy and mixing patterns in leptonic and quark sectors etc. The mechanism by which the SM particles get their respective masses, and the deficiencies of the SM from the theoretical as well as experimental points of view, will be discussed in the following section.

1.1 The Standard Model

The standard model is the theory used to describe the fundamental forces (except gravity) and the interactions between fundamental particles. It can explain the three fundamental forces namely the strong, weak and electromagnetic interactions in terms of local gauge symmetries $SU(3)_C$, $SU(2)_L$, and $U(1)_Y$ respectively. The strong interaction between quarks and gluons is governed by $SU(3)_C$. The group $SU(2)_L \otimes U(1)_Y$ is responsible for electroweak interactions. The weak force is mediated by the massive W^\pm and Z bosons, whereas a massless vector gauge boson, the photon, mediate the electromagnetic force between electrically charged particles. In the SM, there are three different gauge coupling constants g_1 , g_2 , and g_3 , corresponding to these groups which are instrumental in determining the strength of the forces. The gauge coupling constant g_3 of group $SU(3)_C$ is large, e.g., $g_3 = 1.17$ at an energy scale $M_t = 173$ GeV. The electromagnetic force is small compared to

the strong force due to smallness of g_1 and g_2 , e.g., $g_1 = 0.36$ and $g_2 = 0.67$ at energy scale M_t . The weak force is even smaller than the electromagnetic force as it is suppressed by a massive gauge boson propagator.

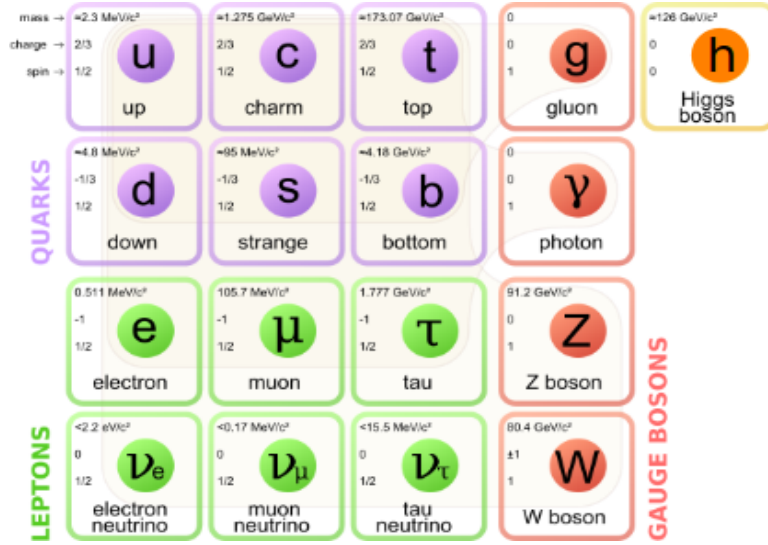


Figure 1.1: The particle spectrum of the SM of elementary particles [3].

In the SM, there are six quarks and six leptons and their antiparticles. Each quark comes with three colors namely red, green, and blue. The SM also includes gauge bosons such as photon, W^\pm , Z , and gluons and one neutral Higgs field (see Fig. 1.1). Higgs is the only particle in the SM which is responsible for the masses of all particles.

In the chiral representation, the four-component Dirac fermions (ψ) can be split into two separate pieces for the left-handed and right-handed fermions:

$$\psi_L = \frac{1 - \gamma_5}{2} \psi \quad \text{and} \quad \psi_R = \frac{1 + \gamma_5}{2} \psi.$$

A left-handed *up-type* quark and a left-handed *down-type* quark together form a quark doublet under $SU(2)_L$. Similarly, a left-handed charged lepton and the corresponding left-handed neutrino forms a doublet. Right-handed fermions are singlets under the same group.

The left-handed quark doublet Q_L and lepton doublet χ_L are denoted as,

$$Q_L \equiv \begin{pmatrix} u_L \\ d_L \end{pmatrix} \quad \text{and} \quad \chi_L \equiv \begin{pmatrix} \nu_{lL} \\ l_L \end{pmatrix}, \quad (1.1)$$

Right-handed quark singlet q_R and lepton singlet l_R are given by,

$$q_R = u_R, d_R; \quad \text{and} \quad l_R, \quad (1.2)$$

where u represents the *up-type* quarks of the three generations u, c, t ; and d stands for the *down-type* quarks d, s, b . The charged leptons are denoted by $l = e, \mu, \tau$ with the corresponding left-handed neutrinos $\nu_l = \nu_e, \nu_\mu, \nu_\tau$. Right-handed neutrinos are not included in the SM.

Also, the SM complex scalar transform as a doublet under $SU(2)_L$ and is given by,

$$\phi = \begin{pmatrix} \phi^+ \\ \phi^0 \end{pmatrix},$$

where $\phi^+ = \frac{\phi_1 + i\phi_2}{\sqrt{2}}$ is the complex charged scalar field and $\phi^0 = \frac{\phi_3 + i\phi_4}{\sqrt{2}}$ is the neutral complex scalar field.

In the following, the electroweak part of the SM Lagrangian symmetric under $SU(2)_L \otimes U(1)_Y$ will be presented, which determines electroweak interactions and masses of the particles. It is given by,

$$\mathcal{L}_{SM} = \mathcal{L}_{fermions} + \mathcal{L}_{gauge} + \mathcal{L}_{Higgs} + \mathcal{L}_{Yukawa}.$$

The kinetic terms of the fermions and their interactions with gauge bosons can be written as,

$$\mathcal{L}_{fermions} = i\bar{Q}_L \gamma^\mu D_\mu^L Q_L + i\bar{\chi}_L \gamma^\mu D_\mu^L \chi_L + i\bar{q}_R \gamma^\mu D_\mu^R q_R + i\bar{l}_R \gamma^\mu D_\mu^R l_R, \quad (1.3)$$

where the covariant derivative of fermion doublet with left chirality is defined as,

$$D_\mu^L = \left(\partial_\mu + ig_2 T^a W_\mu^a + ig_1 \frac{Y}{2} B_\mu \right), \quad (1.4)$$

and the covariant derivative of singlet fermion with right chirality is given by,

$$D_\mu^R = \left(\partial_\mu + ig_1 \frac{Y}{2} B_\mu \right). \quad (1.5)$$

Field	$SU(3)_C$	$SU(2)_L$	T^3	$U(1)_Y$	$Q = T^3 + \frac{Y}{2}$
$Q_L = \begin{pmatrix} u_L \\ d_L \end{pmatrix}$	3	2	$\begin{pmatrix} \frac{1}{2} \\ -\frac{1}{2} \end{pmatrix}$	$\frac{1}{3}$	$\begin{pmatrix} \frac{2}{3} \\ -\frac{1}{3} \end{pmatrix}$
u_R	3	1	0	$\frac{4}{3}$	$\frac{2}{3}$
d_R	3	1	0	$-\frac{2}{3}$	$-\frac{1}{3}$
$L_L = \begin{pmatrix} \nu_L \\ l_L \end{pmatrix}$	1	2	$\begin{pmatrix} \frac{1}{2} \\ -\frac{1}{2} \end{pmatrix}$	-1	$\begin{pmatrix} 0 \\ -1 \end{pmatrix}$
l_R	1	1	0	-2	-1
$\phi = \begin{pmatrix} \phi^+ \\ \phi^0 \end{pmatrix}$	1	2	$\begin{pmatrix} \frac{1}{2} \\ -\frac{1}{2} \end{pmatrix}$	1	$\begin{pmatrix} 1 \\ 0 \end{pmatrix}$

Table 1.1: *Charges of the SM fermions and scalars. C is the color charge under $SU(3)_C$ group, T^3 is the third component of weak isospin of $SU(2)_L$ group, Y is the hypercharge quantum number of $U(1)_Y$ group and Q is the electric charge quantum number.*

The second and third terms of the equation 1.4 are related to $SU(2)_L$ and $U(1)_Y$ gauge transformations respectively. W_μ^a ($a=1,2,3$) are the $SU(2)_L$ gauge bosons, corresponding to three generators of $SU(2)_L$ group and B_μ is the $U(1)_Y$ gauge boson. In the SM, the generators of $SU(2)_L$ are 2×2 matrices $T^a = \frac{1}{2}\tau^a$, where the τ^a , are the Pauli spin matrices,

$$\tau^1 = \begin{pmatrix} 0 & 1 \\ 1 & 0 \end{pmatrix}, \quad \tau^2 = \begin{pmatrix} 0 & -i \\ i & 0 \end{pmatrix}, \quad \tau^3 = \begin{pmatrix} 1 & 0 \\ 0 & -1 \end{pmatrix}.$$

Y is the weak hypercharge operator, generator of $U(1)_Y$ group. The hypercharge operator, defined as a linear combination of the electromagnetic charge operator Q and the third generator $T^3 = \frac{\tau^3}{2}$ of $SU(2)_L$, is given by,

$$Y = 2(Q - T^3).$$

The third component of weak isospin, T_3 , hypercharge quantum numbers Y and the electric charge Q of left-handed and right-handed fermions and scalar fields are summarized in Table 1.1.

The gauge part of the Lagrangian contains the kinetic term and interaction term of

the gauge bosons and can be written as,

$$\mathcal{L}_{gauge} = -\frac{1}{4}W_{\mu\nu}^a W^{a,\mu\nu} - \frac{1}{4}B_{\mu\nu}B^{\mu\nu}.$$

The field strength tensors are defined as,

$$\begin{aligned} B_{\mu\nu} &= \partial_\mu B_\nu - \partial_\nu B_\mu, \\ W_{\mu\nu}^a &= \partial_\mu W_\nu^a - \partial_\nu W_\mu^a - g_2 \epsilon^{abc} W_\mu^b W_\nu^c, \end{aligned}$$

where ϵ^{abc} is structure constant of $SU(2)_L$ group such that $[T^a, T^b] = i\epsilon^{abc}T^c$.

In the SM, the gauge symmetry prevents us from adding explicit mass terms for gauge bosons. As a result, in the limit of exact symmetry, all gauge bosons are massless. To incorporate the massive W^\pm and Z bosons into the SM, the Higgs mechanism has been developed to circumvent this constraint on the mass. In this mechanism, the masses of all particles (except neutrinos) are obtained through the spontaneous breaking of the $SU(2)_L \otimes U(1)_Y$ gauge symmetry at the electroweak scale.

The part of the Lagrangian, which gives rise to the masses of the gauge bosons and the Higgs and also to the interaction between the Higgs and the gauge bosons, is given by,

$$\mathcal{L}_{Higgs} = (D^{L,\mu}\phi)^\dagger (D_\mu^L \phi) - V(\phi), \quad (1.6)$$

where $V(\phi)$ is the SM Higgs potential, and is given by,

$$V(\phi) = m^2 \phi^\dagger \phi + \lambda (\phi^\dagger \phi)^2, \quad (1.7)$$

$$\text{with, } \phi \equiv \begin{pmatrix} \phi^+ \\ \phi^0 \end{pmatrix} = \begin{pmatrix} \frac{\phi_1 + i\phi_2}{\sqrt{2}} \\ \frac{\phi_3 + i\phi_4}{\sqrt{2}} \end{pmatrix}, \quad (1.8)$$

The electroweak symmetry breaking and how the particles get masses will be discussed in the following.

In the SM the electroweak symmetry breaking (EWSB) is realized by the so-called Higgs mechanism proposed by Robert Brout, François Englert and Peter Higgs [4–

7]. In this mechanism, the real component ϕ_3 of the neutral complex scalar of the electroweak doublet acquires a non-vanishing vacuum expectation value (VEV) leading to EWSB. As a result, the gauge group $SU(2)_L \otimes U(1)_Y$ is broken down to $U(1)_{EM}$, the symmetry group that corresponds to electromagnetism.

In the SM, the Higgs potential $V(\phi)$, which is responsible for spontaneous symmetry breaking, is given in eqn. 1.7,

$$V(\phi) = m^2 \phi^\dagger \phi + \lambda (\phi^\dagger \phi)^2.$$

For $\lambda < 0$, the potential goes to $-\infty$, i.e., it gets unbounded from below at very high field values. So λ is taken to be positive. If $m^2 > 0$, the minimum of the potential is found at $|\phi| = \sqrt{\langle 0 | \phi^\dagger \phi | 0 \rangle} = 0$, where $|0\rangle$ represents the ground state. However, the minimum occurs at $|\phi| = \sqrt{\langle 0 | \phi^\dagger \phi | 0 \rangle} = \sqrt{-\frac{m^2}{2\lambda}} = \frac{v}{\sqrt{2}}$ for $m^2 < 0$ and $\lambda > 0$. In the former case, the symmetry is unbroken while in the latter case symmetry is apparently broken.

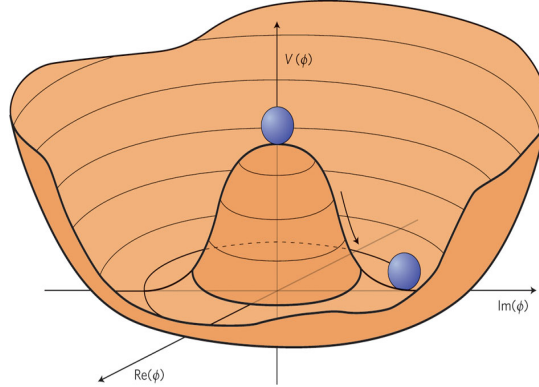


Figure 1.2: *Schematic diagram of the Higgs potential. The potential is symmetric about the vertical axis but at the minimum the symmetry is broken. The circular line indicates the remaining $U(1)$ symmetry.*

The fields ϕ_1 , ϕ_2 and ϕ_4 in eqn. 1.8 are not physical fields and do not receive any VEV. They can be removed by a particular gauge choice, known as unitary gauge choice. These unphysical fields, known as the Goldstone bosons, are ‘eaten’ by the massless W^\pm and the Z bosons, so that they get massive. In this gauge, the scalar

field can be written as,

$$\phi = \begin{pmatrix} 0 \\ \frac{h+v}{\sqrt{2}} \end{pmatrix}, \quad (1.9)$$

where $\phi_3 = h + v$, h is the physical Higgs boson. Using the eqns. 1.7, and 1.9, the eqn. 1.6 can be written explicitly as,

$$\begin{aligned} \mathcal{L}_{Higgs} &= \frac{1}{2} \partial_\mu h \partial^\mu h + (h+v)^2 \left(\frac{g_2^2}{4} W_\mu^+ W^{\mu-} + \frac{g_1^2 + g_2^2}{8} Z_\mu Z^\mu \right) \\ &\quad - \frac{1}{4} \lambda (h+v)^2 ((h+v)^2 - 2v^2) + \dots \end{aligned} \quad (1.10)$$

The charged W^\pm bosons are defined as $W_\mu^\pm = \frac{W_\mu^1 \mp i W_\mu^2}{\sqrt{2}}$. The Z boson and photon are orthogonal combinations of W_μ^3 and B_μ : $Z_\mu = c_W W_\mu^3 - s_W B_\mu$ and $A_\mu = s_W W_\mu^3 + c_W B_\mu$. $c_W \equiv \cos \theta_W$ and $s_W \equiv \sin \theta_W$, where θ_W is the Weinberg angle. It can be expressed in terms of the gauge coupling constants as,

$$\theta_W = \cos^{-1} \left(\frac{g_2}{\sqrt{g_1^2 + g_2^2}} \right). \quad (1.11)$$

One can express the electric charge in terms of the gauge coupling constants g_1 and g_2 as, $e = \frac{g_1 g_2}{\sqrt{g_1^2 + g_2^2}}$, which determines the strength of the electromagnetic interaction.

The mass terms for W^\pm and Z bosons as well as for the Higgs boson h from eqn. 1.10 can be identified as,

$$\begin{aligned} M_W^2 &= \frac{1}{4} g_2^2 v^2, \\ M_Z^2 &= \frac{1}{4} (g_1^2 + g_2^2) v^2, \\ M_h^2 &= 2\lambda v^2, \end{aligned}$$

where the photon A_μ remains massless after symmetry breaking, i.e., the vacuum breaks the original symmetry $SU(2)_L \times U(1)_Y$ in such a way that only the $U(1)_{EM}$ survives as the residual symmetry with a conserved charge $Q = T_3 + \frac{Y}{2}$.

Like the gauge bosons, explicitly adding the quark or lepton mass terms ($-m\bar{\psi}\psi$) in eqn. 1.3 violates the $SU(2)_L$ gauge symmetry. To retain the gauge invariance, the fermion mass needs to be introduced into the SM after EWSB through the Yukawa

interaction between the Higgs field and the fermions fields. The Yukawa part of the SM Lagrangian is given by,

$$\mathcal{L}_{Yukawa} = - \sum_{i,j=1}^3 (y_d^{ij} \bar{Q}_{iL} \phi d_{jR} + y_u^{ij} \bar{Q}_{iL} \tilde{\phi} u_{jR} + y_l^{ij} \bar{\chi}_{iL} \phi l_{jR}) + h.c., \quad (1.12)$$

where ϕ is the SM complex scalar doublet and $\tilde{\phi} = i\tau_2 \phi^*$, $y_{d=d,s,b}$ are the Yukawa couplings for *down-type* quarks, $y_{u=u,c,t}$ for *up-type* quarks and $y_{l=e,\mu,\tau}$ for charged leptons. Q_L and χ_L represent the left-handed quark and lepton doublet, u_R, d_R are right-handed singlet quarks and l_R are the right-handed singlet charged leptons. Here i, j are the generation indices.

Using eqns. 1.1, 1.2 and 1.9 and substituting them into the eqn. 1.12, the Yukawa Lagrangian can be written as,

$$\mathcal{L}_{Yukawa} = \frac{1}{\sqrt{2}} (h + v) (y_d^{ij} \bar{d}_{iL} d_{jR} + y_u^{ij} \bar{u}_{iL} u_{jR} + y_l^{ij} \bar{l}_{iL} l_{jR}) + h.c.$$

The mass matrix of the fermions in flavor basis are then given by,

$$m_f^{ij} = \frac{1}{\sqrt{2}} y_f^{ij} v, \quad \text{with, } f = d, u \text{ and } l,$$

which can be diagonalized via biunitary transformations with 3×3 unitary matrices V_L^f and V_R^f as,

$$m_f^{diag} = \frac{1}{\sqrt{2}} (V_L^f)_{ki} y_f^{ij} (V_R^f)_{jk}^\dagger v = \frac{1}{\sqrt{2}} y_f^{diag} v,$$

and the mass eigenstates of quarks and leptons are defined as,

$$d'_{iL} = (V_L^d)_{ij} d_{jL}, \quad d'_{iR} = (V_R^d)_{ij} d_{jR}, \quad (1.13)$$

$$u'_{iL} = (V_L^u)_{ij} u_{jL}, \quad u'_{iR} = (V_R^u)_{ij} u_{jR}, \quad (1.14)$$

$$l'_{iL} = (V_L^l)_{ij} l_{jL}, \quad l'_{iR} = (V_R^l)_{ij} l_{jR}. \quad (1.15)$$

In the absence of right-handed neutrinos in the leptonic sector, the flavor and mass bases are the same for the leptons in the SM. But for the quark sector, both bases are different. One can get from eqns. 1.13 and 1.14, that the quarks of different flavors mix to form the mass eigenstates which take part in flavor changing charged current interactions. Using eqn. 1.3, these interactions can be written as the following

Lagrangian,

$$- \frac{g_2}{\sqrt{2}} (\bar{u}'_L \bar{c}'_L \bar{t}'_L) \gamma^\mu W_\mu^+ V_{CKM} (d'_L s'_L b'_L)^T + h.c.,$$

where $V_{CKM} = V_L^u V_L^{d\dagger}$, stands for the Cabibbo-Kobayashi-Maskawa matrix (CKM) [8, 9]. It is parameterized by three mixing angles and a phase and is given by [10],

$$V_{CKM} = \begin{pmatrix} |V_{ud}| = 0.97425 \pm 0.00022 & |V_{us}| = 0.2253 \pm 0.0008 & |V_{ub}| = 0.00413 \pm 0.00049 \\ |V_{cd}| = 0.225 \pm 0.008 & |V_{cs}| = 0.986 \pm 0.016 & |V_{cb}| = 0.0411 \pm 0.0013 \\ |V_{td}| = 0.0084 \pm 0.0006 & |V_{ts}| = 0.0400 \pm 0.0027 & |V_{tb}| = 1.021 \pm 0.032 \end{pmatrix}. \quad (1.16)$$

However, the SM does not predict any flavor changing neutral current (FCNC) at the tree level.

1.2 Shortcomings of the SM

Although the SM has been successfully tested at the permill level at LEP, there exist various kinds of theoretical inconsistencies as well as intriguing experimental observations that call for the introduction of new physics beyond the SM. A few of these shortcomings will be briefly discussed in the following subsections.

1.2.1 The Higgs mass hierarchy problem

The mass of the Higgs boson is 125.7 ± 0.3 GeV, as measured at the LHC. The SM cannot predict the Higgs mass, but relates it as $m_h^2 = 2\lambda v^2$. If the radiative corrections are included for the Higgs mass, then the following problem occurs. The one-loop radiative correction to the Higgs boson mass arising from its self-interaction and couplings with gauge boson and fermions is given by,

$$\delta m_h^2 = \frac{\Lambda_{cut}^2}{16\pi^2 v^2} (3m_h^2 + 3m_Z^2 + 6m_W^2 - 12m_t^2) + \text{logarithmic divergences} \\ + \text{finite terms.}$$

If the cut-off scale is set as $\Lambda_{cut} = M_{Pl}$ then the Higgs mass scale is naturally pushed to the Planck scale. This is known as hierarchy problem for the Higgs mass. In order to bring down m_h to the observed scale m_{EW} , a severe fine-tuning between the quadratic radiative corrections and the bare mass (at least one part in

10^{34}) is required. This level of fine-tuning is deemed unnatural. The new physics beyond the SM, for example, supersymmetry, is needed to solve this problem. In supersymmetric theories, the radiative correction to the Higgs mass arising from SM gauge bosons and fermions are canceled with the correction terms generated by their supersymmetric degrees of freedom. However, so far no experiment could confirm the presence of these superpartners of the known particles.

1.2.2 Flavor Problems

Several unresolved issues are associated with the fermionic sector, termed as flavor problems. There is no explanation of why the SM includes only three generations of fermions. In the SM, by construction, the neutrinos are massless as it does not include right-handed neutrinos. But from the neutrino oscillation experiments we got convinced that at least two neutrinos have non-zero mass. These experiments give information about the mass squared differences between neutrino eigenstates, although the individual values of the masses are not known. From cosmological measurements, it has been shown that the sum of the three neutrino masses is less than 0.1 eV [10]. As neutrino masses are tiny compared to other fermion masses, it is believed that the mechanism behind neutrino mass generation is different from the other fermions which obtain mass from the Higgs mechanism. The most popular natural explanation of small neutrino masses is via the see-saw mechanism. There are broadly three classes of such models namely type-I, type-II, and type-III see-saw models requiring involvements of right-handed neutrinos, a $SU(2)_L$ triplet scalar with hypercharge $Y = 2$ or $SU(2)_L$ hyperchargeless triplet fermions respectively [11]. Neutrinos can also get mass from non-seesaw mechanisms namely the Zee mechanism [12], supersymmetry with R -parity violation etc.

Fermions have masses in a range of eleven orders of magnitude, from the neutrino mass $\lesssim 0.1$ eV, up to the top quark mass ~ 173 GeV. A new dynamical mechanism,

e.g., a theory with horizontal symmetries is needed to explain the fermion mass hierarchy. The SM does not have an answer to the origin of the structure of the Yukawa matrices and therefore to that of the CKM matrix of eqn. 1.16. Also, as in the SM the neutrinos are massless, the neutrino flavor mixing remains unexplained. The mixing angles of the quarks are small ($\theta_{12} \sim 13^\circ$, $\theta_{23} \sim 2.4^\circ$ and $\theta_{13} \sim 0.2^\circ$) [10], whereas the mixing angles in the neutrino sector are $\sim 32^\circ$, $\sim 45^\circ$ and $\sim 9^\circ$ respectively [10]. There is no underlying mechanism in the SM to reproduce the observed fermion masses and mixing pattern.

1.2.3 Stability of the electroweak vacuum

With the revelation of the Higgs on 2012 at LHC, the existence of all SM particles have been confirmed and the values of all the parameters in the Lagrangian are known at the electroweak scale. These data indicate that if the validity of the SM is extended to M_{Pl} , a second, deeper minimum is located near the Planck scale such that, the electroweak vacuum is metastable, i.e., the transition lifetime of the electroweak vacuum to the deeper minimum is finite $\tau \sim 10^{300}$ years [13–15].

As it was shown in Refs. [16–19] that if the electroweak vacuum is metastable then Higgs cannot play the role of inflaton. Extra new degrees of freedom are needed with the SM to explain the inflation of the Universe. However, in this thesis, the issues related to inflation will not be addressed. New physics beyond the SM can alter the Higgs potential so that it enhances its stability.

1.2.4 Gravity

Massive particles experience gravitational interactions. Gravity is expected to dominate over all other fundamental forces at energy scale $\gtrsim M_{\text{Pl}}$. However, construction of models based on quantum gravity theories is outside the scope of the SM.

1.2.5 Gauge Unification

In the electromagnetism, E and B are unified, as with a single electric charge one can explain any electromagnetic phenomenon. Hence from a theoretical standpoint, a theory which can illustrate unification of all the fundamental forces at higher energies would be an appealing one. The gauge coupling constants g_1 , g_2 and g_3 corresponding to the three gauge groups in the SM, namely $U(1)_Y$, $SU(2)_L$ and $SU(3)_C$, assume different values at the electroweak scale. Assuming SM to be valid all the way to the Planck scale, one can evolve these coupling constants using RG equations. Given the accuracy involved in measured values of the SM parameters at the electroweak scale, g_1 , g_2 and g_3 do not merge to a single coupling constant at any energy before M_{Pl} , which is desirable to attain gauge unification. One can take refuge to grand unified theories based on a single gauge group like $SU(5)$ or $SO(10)$ to realize this dream.

1.2.6 Dark matter

Various kinds of astrophysical observations, e.g., anomalies in the galactic rotation curves, gravitational lensing effects in Bullet cluster etc., have indicated the existence of dark matter in the Universe. Dark matter interacts gravitationally. It has no electric charge, so we cannot observe it through its interactions with photons. The satellite based experiments such as Wilkinson Microwave Anisotropy Probe (WMAP) [20] and Planck [21] have measured the Cosmic Microwave Background Radiation (CMBR) of the Universe with unprecedented accuracy and suggest that the Universe consists of about 4% ordinary matter, 27% dark matter and the rest 69% is a mysterious unknown energy called dark energy which is thought to be the cause of accelerated expansion of the Universe. The SM fails to provide a viable dark matter candidate. To explain the observed presence of the dark matter, the presence of new physics beyond the SM is required. A popular scheme in this re-

gard is to introduce ‘weakly interacting massive particles’ (WIMP) protected by a discrete symmetry that ensures stability of these particles. The issues related to the dark matter in various extended scalar sectors will be discussed in Chapter 6.

1.2.7 Baryon-antibaryon asymmetry

Astrophysical evidences have indicated that our galaxy and its neighborhood are predominantly made of matter. The asymmetry is defined as the ratio of the difference of the baryon and anti-baryon number densities to the photon number densities in the Universe. According to recent data from WMAP[20] the asymmetry is given by,

$$\eta = (6.19 \pm 0.14) \times 10^{-10}.$$

To produce this baryon asymmetry, three ingredients are necessary as outlined by Sakharov conditions [23], such as baryon number violation, C and CP violation, and departure from thermal equilibrium.

Although the SM has the required ingredients, it cannot produce large enough baryon-to-photon ratio (η) as observed by the experiments. The new physics beyond the SM is required as one needs additional sources of CP violation. Several mechanisms have been proposed to explain the baryon asymmetry, e.g., electroweak baryogenesis, leptogenesis and GUT baryogenesis etc.

1.2.8 Recent LHC data and scope for an extended scalar sector

LHC-I, with 20 fb^{-1} data in its $\sqrt{s} = 8 \text{ TeV}$ run, has confirmed discovery of the Higgs boson of mass $M_h \sim 125 \text{ GeV}$. The Higgs signal strengths are shown in the Table 1.2 as measured from ATLAS and CMS collaborations at the LHC. The measured properties of this Higgs boson are consistent with the minimal choice of the scalar sector as in the SM. But the data still comfortably allow an extended scalar sector, which, in turn, can accommodate a more elaborate mechanism for

Signal strength, $\mu_{\chi\chi} = \frac{\Gamma_{exp}(h \rightarrow \chi\chi)}{\Gamma_{SM}(h \rightarrow \chi\chi)}$	ATLAS	CMS
$\mu_{\bar{\tau}\tau}$	1.41 ± 0.40	0.89 ± 0.3
μ_{WW^*}	1.23 ± 0.22	0.91 ± 0.23
μ_{ZZ^*}	1.5 ± 0.35	1.05 ± 0.31
$\mu_{\gamma\gamma}$	1.15 ± 0.27	1.12 ± 0.23

Table 1.2: *The observed signal strengths and uncertainties for different Higgs boson decay channels [24] for mass, $M_h \sim 125$ GeV. The data have been taken for proton-proton collision of center-of-mass energies, $\sqrt{s} = 7, 8$ TeV with luminosity, 20 fb^{-1} . W^* , Z^* decay to fermions. $\Gamma_{exp}(h \rightarrow \chi\chi)$ is the decay width as observed in the experiments and $\Gamma_{SM}(h \rightarrow \chi\chi)$ is the same predicted by the SM.*

EWSB. It is also noted that an extended scalar sector may not always participate in the electroweak symmetry breaking, e.g., as in the case of an extended inert scalar sector protected by a discrete symmetry.

Recently the ATLAS and CMS collaborations have analyzed the $\sqrt{s} = 13$ TeV data and announced the possible presence of a scalar resonance around 750 GeV [25]. The significances of the signals are 3.9σ and 3.4σ in the respective experiments. This indication has fuelled speculations about an extended scalar sector.

In the following section, the particle content of the extended scalar sectors and the constraints on these new models will be discussed.

1.3 Extended scalar sector

In this thesis, various kinds of extended scalar sectors containing an additional $SU(2)_L$ singlet, doublet or triplet with hypercharges $Y = 0, 2$, have been considered along with the SM doublet. The main purpose for writing this thesis is to explore characteristics of these new scalars using the weak vector boson scattering processes and from the (meta)stability of the scalar potential.

Each extended scalar sector can consist of different $SU(2)_L$ multiplets with different isospin, hypercharge, etc. So the structure of the scalar potential is changes in

different extended scalar sectors. The SM doublet ϕ , given in eqn. 1.8, with isospin $I = 1/2$ and hypercharge $Y = 1$, consists of two singly-charged, a neutral CP -even and a neutral CP -odd scalar fields respectively. Depending on the isospin I_i and hypercharge Y_i , other scalar multiplets contain different numbers of scalar fields with different charges. For example, a real triplet scalar with hypercharge $Y = 0$ consists of a pair of singly-charged fields and a CP -even neutral scalar field, whereas a complex triplet scalar with hypercharge $Y = 2$, has an extra doubly-charged fields, and a CP -odd neutral scalar field. After the electroweak symmetry breaking, the fields of the SM scalar doublet mix with the new fields of extra scalar sector. In the extended scalar sector, one of the linear combinations of the CP -even states is identified as the observed Higgs, whereas the other combinations become new physical CP -even scalars. Similarly, one of the combinations of singly-charged states forms a charged Goldstone boson. This is eaten by the electroweak charged gauge boson W which becomes massive. The other combinations become new singly-charged physical scalars. Also, a combination of CP -odd scalar states becomes the component of the Z boson and the other combinations of these become physical pseudoscalars. But the fields with electric charge quantum number more than one, remain as physical scalar fields. These scalar fields can have direct couplings with the SM particles, or these may get generated after the electroweak symmetry breaking. If the extra scalar fields are *odd* under a discrete Z_2 symmetry, then the SM particles cannot couple with *odd* number of the new scalar fields. This symmetry prevents the extra scalars to acquire VEVs, and hence these extra scalars do not mix with the fields of the SM scalar doublet. In this case, the electroweak symmetry breaking is fully driven by the SM Higgs doublet. The charged and CP -odd components of the SM doublet remain as Goldstone bosons and CP -even neutral component is identified with the observed Higgs.

1.3.1 Constraints on the extended scalar sectors

From experimental and theoretical considerations such as the electroweak precision experiments, absolute vacuum stability of the scalar potential and unitarity of the scattering matrix, one can put constraints on parameter space of the extended scalar sectors. In the following sections, some of these constraints are discussed.

1.3.1.1 The electroweak precision constraints

The electroweak precision constraints on the physics parameter spaces come from the precise measurement of the neutral current and charged interaction at the Large Electron–Positron Collider [26] and the Stanford Linear Collider [27], etc. The relative strength of the neutral and charge currents denoted by ρ can be expressed as,

$$\rho = \frac{M_W^2}{M_Z^2 \cos^2 \theta_W}.$$

In the SM, at tree-level, the value of the ρ parameter is equal to 1. If an extra scalar multiplet is added along with the SM scalar doublet, then the ρ parameter may be modified at the tree-level. These modifications are different for different types of multiplets. If the extra scalar is odd under any discrete symmetry under which the SM particles are even, then ρ parameter remains the same as in the SM. Note that, it will differ when radiative corrections are included into the vector boson self-energies. Let us now concentrate at tree-level only.

It was shown in the Ref. [28], that the ρ parameter can be easily calculable for any number of scalar multiplets present in the model. Let the vacuum expectation values of scalars are v_i , where i is the number of multiplets, with the $SU(2)_L$ isospin I_i and hypercharge Y_i . Masses of the gauge bosons corresponding to the neutral and charge current processes are expressed as,

$$M_Z^2 = \frac{1}{4}(g_1^2 + g_2^2) \sum_i |Y_i|^2 v_i^2,$$

$$M_{W^\pm}^2 = \frac{1}{8}g_2^2 \sum_i \{4I_i(I_i + 1) - |Y_i|^2\}v_i^2.$$

In terms of v_i , I_i and Y_i , the ρ parameter can be written as,

$$\rho = \frac{\sum_i \{4I_i(I_i + 1) - |Y_i|^2\}v_i^2}{2 \sum_i |Y_i|^2 v_i^2}.$$

In the singlet scalar extension of the SM, both isospin (I) and hypercharge (Y) of the extra scalar are zero. So there is no modification of the masses of gauge bosons (W^\pm , Z) and the same is true for ρ at the tree-level. Although, in the doublet extension, with hypercharge 1, the masses of the vector bosons get modified as $M_Z^2 = \frac{1}{4}(g_1^2 + g_2^2)(v_1^2 + v_2^2)$ and $M_W^2 = \frac{1}{4}g_2^2(v_1^2 + v_2^2)$. Then the ρ parameter for this model does not deviate from the SM at the tree-level. However, for the triplet extension of the SM, the ρ parameter can be written as,

$$\begin{aligned} \rho(Y=0) &= \frac{v_1^2 + 2v_2^2}{v_1^2}, \\ \rho(Y=2) &= \frac{v_1^2 + 2v_2^2}{v_1^2 + 4v_2^2}. \end{aligned}$$

The recent experimental fit of ρ parameter is 1.0004 ± 0.00024 [10]. This constraints the vacuum expectation value v_2 of the extra triplet scalar to be less than 4 GeV [29].

Although in an extended scalar sector, the ρ parameter may or may not get additional contribution in comparison to the SM, at loop level it is not immune to get corrected. The new physics effects can alter the vacuum polarization of the gauge bosons. These effects are encoded in the so-called Peskin–Takeuchi [30] parameters and are denoted by S , T , and U . Alternatively these can also be expressed in terms of Altarelli-Barbieri [31] parameters ϵ_1 , ϵ_2 and ϵ_3 . The correction to the ρ parameter is related with T as, $\alpha T = \Delta\rho$, where α is the fine structure constant. The generic expressions of these observables for the extended scalar sectors are given in Ref. [32]. These electroweak precision observables [33] are used in this thesis to put constraints on parameter space of new physics models.

1.3.1.2 Stability of the electroweak vacuum

The extended scalar sectors may have more than one scalar field in the potential. Due to the complicated structures of such scalar potentials, it is difficult to adjudge the stability of the minimum. A scalar potential is said to be bounded from below, if and only if the potential does not become negative infinity along any direction of the field space.

To find the boundedness of the potential one has to use the copositiviy criteria of a symmetric matrix. A symmetric matrix \mathcal{M} is copositive if the quadratic form $\chi^T \mathcal{M} \chi > 0$ for all vector $\chi > 0$, The notation $\chi > 0$ means that all the components of the vector χ are greater than zero. These criteria guarantee that the potential never becomes negative infinity and the vacuum is absolutely stable.

Let us consider a scalar potential,

$$V(\phi_i) = \sum_{i,j}^N m_{ij}^2 \phi_i \phi_j + \sum_{i,j,k,l}^N \lambda_{ijkl} \phi_i \phi_j \phi_k \phi_l.$$

For high field values, the first term can be neglected. The coefficient of the terms of the potential which contains *odd* number of fields, are taken to be zero. So, one can write the potential in biquadratic in fields and can apply the copositivity criteria to find the conditions for the boundedness of the scalar potential. The scalar potential is given by,

$$V(\phi_i) = \sum_{i,j}^N \lambda_{ij} |\phi_i|^2 |\phi_j|^2.$$

This potential can be written as in the form of a symmetric matrix $\chi^T \mathcal{M} \chi$, where χ consists of $|\phi_i|^2$ and \mathcal{M} contains λ_{ij} , here λ_{ij} is symmetric under exchange of the indices. The scalar potential is bounded from below if [34],

$$\lambda_{ii} > 0, \quad \lambda_{ij} + \sqrt{\lambda_{ii} \lambda_{jj}} > 0 \quad \text{for } i, j = 1, 2.$$

However, the copositivity criteria are no longer valid when the scalar potential become negative and has extra new minima along any direction of the field space. In

this case a minimum located at low field values is said to be metastable if the transition time from this minimum to any other minima of the potential is greater than the lifetime of the Universe, otherwise, it is unstable. The modification of copositivity criteria with metastable electroweak vacuum for the extended scalar sector will be discussed in Chapter 6.

1.3.1.3 Unitarity of the scattering matrix

Unitarity bound on the extended scalar sectors can be calculated from the scattering-matrix of different processes. The technique was developed by Benjamin W. Lee, C. Quigg, and H. B. Thacker for the SM and it can also be applied to various kinds of extended scalar sectors. The scattering-matrix for the extended scalar sector consists of different scalar-scalar, gauge boson-gauge boson, gauge boson-scalar scattering amplitudes. Using the Born approximation for partial waves, the scattering cross-section for any process can be written as,

$$\sigma = \frac{16\pi}{s} \sum_l^{\infty} (2l+1) |a_l(s)|^2,$$

where $s = 4E_{CM}^2$ is the Mandelstam variable, where E_{CM} is the center of mass energy of the incoming particles. a_l is the partial wave coefficients corresponding to specific angular momentum values l . This leads to the following unitarity constraint, $Re(a_l) < \frac{1}{2}$. At high energy the dominant contribution to the a_l , i.e., to the amplitude of the two-body scattering processes $a, b \rightarrow c, d$ comes from the diagram involving the quartic couplings. Far away from the resonance, the other contributions to the amplitude from the scalar mediated s -, t -, and u -channel processes are negligibly small. Also in the high energy limit, the amplitude of scattering process involving longitudinal gauge bosons can be approximated by the scalar amplitude in which gauge bosons are replaced by their corresponding Goldstone bosons. This is known as equivalence theorem [35]. So to test unitarity of the models with extended scalar sectors, one can construct the scattering-matrix which consists of only the

quartic couplings at very high energies. Unitary constraints demand that the eigenvalues of the scattering-matrix should be less than 8π . The detailed calculations will be shown for Higgs triplet model with a hyperchargeless scalar triplet in Chapter 3.

From the above discussions in Sections 1.3.1.2 and 1.3.1.3, it is clear that the requirement of stability of the scalar potential gives a lower bound on the quartic coupling, whereas unitarity of scattering-matrix gives the upper bound on the quartic coupling of the extended scalar sector.

These are some of the generic constraints on the extended scalar sector beyond the SM. Additional bounds on such new physics models can be put from other phenomenological studies of dark matter, neutrino mass etc. The parameter spaces of these new models are constrained from non-observation of these scalar signals at the direct search experiments at high-energetic colliders like LEP, LHC, etc. The direct search bound on the 2HDM, $\text{HTM}(Y = 0)$, and $\text{HTM}(Y = 2)$ will be discussed in the Chapter 3.

1.4 Organization of the Thesis

The organization of the thesis is as follows:

This chapter starts with a brief introduction to the standard model of particle physics. After that, the deficiencies of the SM have been discussed from the theoretical as well as experimental points of view. Generic bounds on the extended scalar sectors from the stability of the electroweak vacuum, unitarity of the scattering matrix and the electroweak precision experiments have been reviewed. Compositions of the physical and unphysical scalar fields in the extended scalar sectors have also been discussed.

An extra scalar sector protected by a discrete symmetry Z_2 can solve the puzzle of nature of dark matter in the Universe. In the second Chapter, a brief summary of

the indications of presence of the dark matter from the astrophysical observations have been discussed. The calculation of relic density of the dark matter has been reviewed. The direct and indirect detection of the dark matter in experiments has also been mentioned in brief.

In the third Chapter, various kinds of extended scalar sector such as singlet extension of the SM, type-II two Higgs doublet model and Higgs triplet model with two different hypercharges $Y = 0$ and 2 , have been reviewed. After electroweak symmetry breaking, the masses of all physical particles have been calculated in these new models. In the presence of a new extended scalar sector, the modified couplings of the Higgs-like scalar to other SM particles have been shown in terms of the mixing angles of the new extended scalar fields to the fields of SM doublet. The previously measured generic bounds on the extended scalar sectors have been applied on these models.

The extended scalar sector can be probed through longitudinal vector gauge boson scattering and it has been discussed in the fourth Chapter. The generic expressions of the longitudinal vector gauge boson scattering amplitude of the processes like (a) $W_L^\pm W_L^\mp \rightarrow W_L^\pm W_L^\mp$, (b) $W_L^\pm W_L^\pm \rightarrow W_L^\pm W_L^\pm$, (c) $W_L^\pm W_L^\mp \rightarrow Z_L Z_L$, (d) $W_L^\pm Z_L \rightarrow W_L^\pm Z_L$, and (e) $Z_L Z_L \rightarrow Z_L Z_L$ have been presented in the context of extended scalar sectors such as type-II two Higgs doublet model, and Higgs triplet models with $Y = 0$ and $Y = 2$ scalar triplets [29]. These scattering processes can be useful to distinguish these extended scalar sectors from the SM as well as between one another.

In the fifth Chapter, the stability of the electroweak vacuum of the Higgs scalar potential in the SM has been reviewed. It has been shown how the Higgs scalar potential evolves with the running energy from the electroweak scale to the Planck scale M_{Pl} . In this study, the Higgs scalar potential [13] up to two-loop quantum corrections is used and it has been improved by three-loop renormalization group

running of the coupling parameters. As a part of this thesis work a computer code has been developed to analyze a scalar potential at higher energies. In the SM, the formation of the second, deeper minimum near the Planck scale has been discussed. The detailed calculation of tunneling probability of the electroweak minimum to the deeper minimum around the Planck scale is also provided. It has been shown that the present measured values of the SM parameters imply that the stability of electroweak minimum is excluded at $\sim 3\sigma$.

As the SM is extended by additional scalar multiplets, the stability of the electroweak minimum of the Higgs potential gets improved. The extended scalar sectors with a discrete symmetry Z_2 can also provide a viable dark matter candidate. In the sixth Chapter, the effective Higgs potential has been calculated to explore the stability of the electroweak vacuum in these extended scalar sectors. The contributions to the effective Higgs potential from these new physics models have been taken at one-loop level only. In this scenario, the stability of the electroweak minimum of the new effective Higgs potential in the different extensions of the scalar sector of the SM, namely with a real singlet [15], inert doublet [36] or an inert triplet with hypercharge $Y = 0$ [37], has been explored. In these extended sectors, parameter spaces have been identified that correspond to the stable and metastable electroweak vacuum and also satisfy the relic density constraints on dark matter from Planck experiment. The modified stability conditions have also been shown when electroweak vacuum is metastable.

The last Chapter provides the summary and the conclusions of this thesis work.

Chapter 2

Dark matter: Relic Density, Direct and Indirect detections

2.1 Introduction

The last few years have seen a revolution in cosmology and astrophysics. It is confirmed that the Universe is filled with not only dark matter (DM) but also the even more enigmatic dark energy.

The analysis of observational data of the satellite-based experiments, Wilkinson Microwave Anisotropy Probe (WMAP) [20] and Planck [21] that look for such very tiny anisotropies in Cosmic Microwave Background Radiation (CMBR) suggest that the total mass-energy of the Universe contains 69% dark energy, 27% dark matter and 4% ordinary matter. The nature of these two dominant components of the Universe is currently one of the biggest mysteries in the modern particle and astrophysics. Dark matter is a hypothetical type of matter, first proposed by Fritz Zwicky in 1933. Dark matter is mysterious and invisible in nature as it can neither be seen by our eyes nor observed by any telescope. Dark matter is electrically neutral – it neither emits nor absorbs any electromagnetic radiation. If the dark matter would have electromagnetic and strong interactions with normal matter, it would have formed isotopes [22] of estimated abundance $n > 10^{-10} n_H$, which contradicts the present

upper limit of hydrogen isotopes abundance n_H . The dark matter has mass so it can interact with the ordinary matter through the gravitational interaction.

There are many convincing evidences about the existence of the dark matter in the Universe. A few of these will be discussed in the next section.

2.2 Evidence of Dark Matter

There are several observations to support the argument that the Universe contains a large amount of matter. In the year 1933, Fritz Zwicky was the first astronomer to propose the existence of dark matter. He was studying a very large cluster of galaxies nearest to the Earth: the Coma cluster. He used the Virial theorem, an equation which relates the average kinetic energy of a system to its total potential energy, to determine the gravitational mass of the cluster. He measured the total mass of the luminous object (stars and gas) in the galaxies to find that the mass of the luminous matter was not enough to keep the cluster bound, and was several times smaller than the inferred gravitational mass. Zwicky concluded that there must be non-luminous matter present in the galaxies.

2.2.1 Galactic Rotation Curves

Similar discrepancy was observed in galactic rotation curves, which is the strongest evidence of the presence of the dark matter in the galaxies. In the 1970s, Kent Ford and Vera Rubin discovered that rotation curves of galaxies are flat (see Fig. 2.1). For the analysis of a spiral galaxy, one measures the rotational velocity $v(r)$ of stars, gas etc. in the galaxy as a function of their distance r from the galactic center. The spiral galaxy has a dense central region and the density of the visible mass is reduced as one goes away from the central region. From standard Newtonian dynamics, one would expect a Keplerian decline of the rotation curve as one goes away from the dense central region of the galaxy. The observations show that instead of Keplerian decline the velocities are rather constant after a certain distance r from

the galactic center as in Fig. 2.1. The flat rotation curves have now been observed for almost all galaxies, including our galaxy, the Milky Way. If the galaxy contains far more unknown mass than the luminous object, then this flat rotation curve can be explained. It was found that more than 95% of the mass of galaxies consists of unknown dark matter.

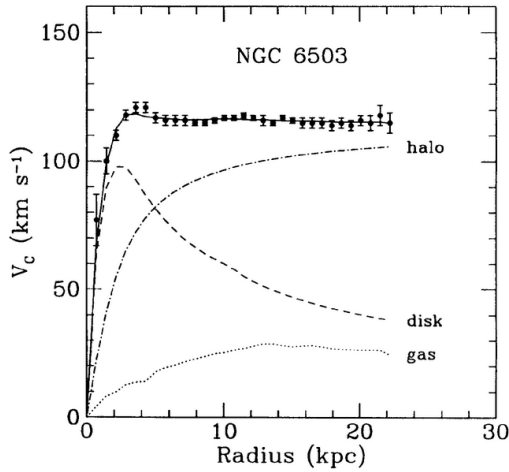


Figure 2.1: *Galactic rotation curve for NGC 6503 dwarf spiral galaxy. Image credit: Katherine Freese [38].*

2.2.2 Gravitational Lensing and Bullet Cluster

The bending of light while it passes through the vicinity of a gravitating mass gives rise to the lensing effect. This phenomenon is known as gravitational lensing. If a luminous object is present in the background of the gravitating mass at a suitable distance, then the lensing effect will create a distorted or multiple images. The observance of such lensing effects in the galaxies by unseen matter indicates the presence of dark matter. The huge amount of unseen dark matter present in the galaxies will produce ring images (Einstein's rings) through strong gravitational lensing effect. Weak lensing by smaller astronomical objects such as planets, stars, will produce distorted images. From the lensing effect, the unseen dark matter mass present in the galaxies can be estimated using the lens equation of Einstein's general

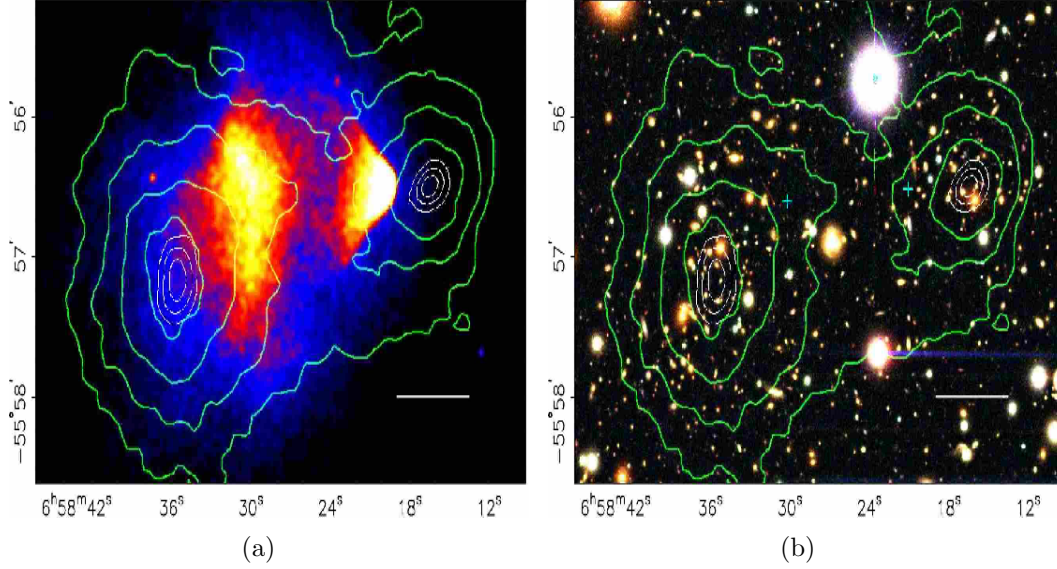


Figure 2.2: (a) the left panel is a X-ray satellite Chandra image of the cluster of the visible matter and (b) The right panel shows a direct image of the cluster obtained with the 6.5-m Magellan telescope in the Las Campanas Observatory. The contour lines are drawn for the images produces due to the gravitational lensing by the dark matter in the galaxies. Image credit: D. Clowe et al. [39].

theory of relativity. Weak and strong gravitational lensing phenomena have been used for discovering one of the most prolific evidence of dark matter in the “Bullet Cluster” in the cluster 1E0657-558. The bullet cluster was created due the collisions of two giant galaxies in the Universe. When the smaller galaxy passed through the core of the larger galaxy, the baryonic mass distribution of the smaller one suffered distortion in shape due to the enormity of the collision and it took the shape of a bullet. The X-ray analyses reveal the baryonic mass distribution in the two colliding clusters. The X-ray image of baryonic distributions are shown in Fig. 2.2(a). The colors indicate the X-ray temperature of the plasma: blue is coolest and white is hottest. Direct image of the cluster obtained with the 6.5-m Magellan telescope at the Las Campanas Observatory is shown in Fig. 2.2(b). The green contour line in Fig. 2.2(a) and (b) form due to the gravitational lensing of unknown matter (dark

matter) presence in the galaxies. One can see from these figures that the dominant population of the baryonic mass is in X-ray gas which is well separated from the respective dark matter halo of the cluster. This analysis indicates the dark matter halos in the galaxies, when passed through each other, remain unperturbed and undistorted. The phenomenon of the “Bullet Cluster” provides an observational evidence of the existence of dark matter in the galaxies and indicates that the dark matter is almost collisionless.

2.2.3 The Cosmic Microwave Background

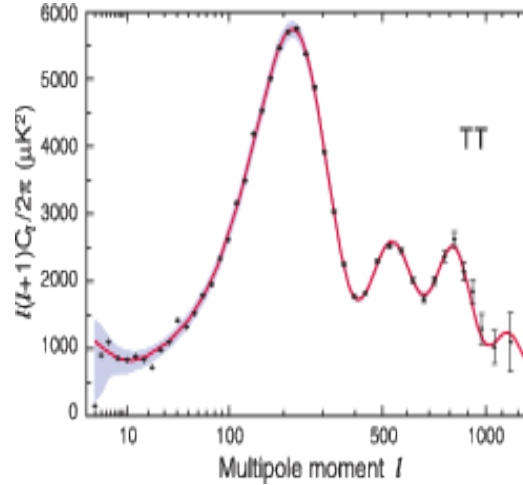


Figure 2.3: The figure shows temperature-temperature (TT) angular power spectrum of CMBR from the nine years WMAP data. Image credit: C. L. Bennett et al. [WMAP Collaboration] [20].

The Cosmic Microwave Background Radiation (CMBR) provides a snapshot of the oldest light after the ‘last scattering’ in our Universe. The last scattering took place when the Universe was just 380,000 years old. Hence, the CMBR is the earliest photograph of our Universe. The fluctuations in CMBR provide the information of the structure formations of the Universe. The anisotropies in the CMBR are capable of telling us the geometry (or curvature), the baryon content, the dark matter and dark energy content of the Universe, the value of the Hubble constant, whether

inflation occurred in the early Universe, etc. In Fig. 2.3, the correlation function C_l of temperature anisotropy of CMBR, plotted with respect to multipoles (l) shows multiple peak at different l , where $\theta = \frac{2\pi}{l}$ is the angle between two directions. This temperature anisotropy is useful to extract the physical properties of our Universe. The angular scale corresponding to the first peak in Fig. 2.3 provides the precise measurement of the curvature of the Universe. The third peak contains the information about the dark matter density in the Universe. From the ratio of the odd peaks to the even peaks, one can get information about the baryon density in the Universe.

2.3 Components of Dark Matter

So far, astrophysical and cosmological data can only tell us how much dark matter is there in the Universe, i.e., the total mass density of the dark matter and the fact that it does not interact electromagnetically and strongly. Although we are convinced that dark matter really exists, there is still no consensus on what it is composed of. The possibilities include the dense baryonic matter and the non-baryonic matter.

There are baryonic components of dark matter like Massive Compact Halo Objects (MACHOs): condensed objects such as black holes, white dwarfs, very faint stars, or non-luminous objects like planets. Using the microlensing of the light, the MACHO [40] and the EROS [41] collaborations, concluded that the MACHOs could add a few percent to the known mass discrepancy in the Galaxy halo, observed in galactic rotation curves. So if there is a baryonic component to dark matter, then it has to be quite small.

The non-baryonic dark matter particles can be grouped into three categories on the basis of their velocities, namely hot dark matter (HDM), warm dark matter (WDM), and cold dark matter (CDM). The hot dark matter mass is very small and moves almost with the speed of the light. The neutrinos can be considered

as the best candidate for the hot dark matter. There are several reasons that the neutrino cannot be considered as a viable dark matter candidate which alone fulfill the relic abundance of the Universe. There is an upper limit on neutrino mass from tritium beta decay experiments $m_\nu < 2$ eV [42]. Combined with the data from the neutrino oscillation experiments, one can find the contributions of neutrino to the matter density is $\Omega_\nu h^2 < 0.064$ [43] in the Universe. This is not enough to satisfy the total relic abundance of the Universe. For the neutrinos to dominate the halo of dwarf galaxies, one need to pack them so much that it would violate Pauli exclusion principle. The neutrino mass should be $m_\nu > 500$ eV [44], to avoid this problem. The neutrinos are so light that they are moving at the speed of light, so it is very difficult to form gravitationally bound structures from fast moving objects. The velocity of the objects will always be far above the local escape velocities. If all dark matter were neutrinos, then it would take an enormous time to form gravitationally bound structures. So neutrino cannot be a prominent dark matter candidate. The speed of warm dark matter, e.g., sterile neutrino is rather small compared with the speed of the light. The current data require a mass range of warm dark matter to be in between 0.3 keV and 3 keV. The warm dark matter is also a dark matter candidate, however, alone it is unable to explain the formation of large-scale structure. The cold dark matter moves very slowly. Currently, all viable models of structure formation indicate that the Universe is dominated by cold dark matter. It is very difficult to determine the constituents of CDM. The candidates fall roughly into two categories. (a) Axions were proposed in the late 1970s to solve the strong- CP problem in quantum chromodynamics (QCD). The Axions are favored as dark matter candidates as they interact very weakly. The best example of a nonthermal dark matter candidate is the Axion. If it was produced thermally, then it cannot fulfill the relic abundance of the Universe. Although the Axions are of very light mass $\sim \mathcal{O}(10^{-5})$ eV, however, they behave like a cold dark matter. This

was shown by authors of Ref. [45] using the proper time averaging of the perturbed oscillating scalar (Axion) field. (b) Weakly Interacting Massive Particle (WIMP) is another viable dark matter candidate. It is considered that these particles were created thermally in the early Universe.

It was observed that the Universe on large scales is not filled uniformly with matter, instead, we have large empty spaces (voids) separated by narrow filaments (gravitational interactions) and clumps of matter. This clumpy structure requires that the particles were moving slowly at the time the structure formed. This hints towards a fairly massive dark matter particle. The WIMP is the best viable candidate for the dark matter. If the WIMPs exist, mathematical modeling shows there must be about five times more of these than normal matter, which coincides with the abundance of dark matter that we observe in the Universe. The annihilation cross-section of the WIMP dark matter provides the information that they interact with one another or the other standard particles via a force similar in strength to the weak nuclear force. This is known as the “WIMP miracle”. Also it can explain the gamma-ray excess observed at Fermi LAT [46], positron excess observed at AMS-02 [47] and PAMELA [48]. These are the motivations to adopt the WIMP as the leading candidate for the cosmological dark matter.

There is also another kind of cold dark matter candidate which may fulfill the relic abundance of the Universe, for example, the strongly interacting massive particle (SIMP). These particles interact more strongly with each other. The model only works if SIMPs interact very weakly with ordinary matter.

Only WIMP dark matter has been considered in this thesis. Hence, in the following sections, the relic density calculation of the WIMPs will be addressed and the direct and indirect detection of dark matter will be briefly reviewed.

2.4 Relic Density of Dark Matter

In the early Universe, WIMPs were created and they were in thermal equilibrium with photons and other particles at a very high temperature. As the expansion continued, the temperature of the Universe kept falling down, so that the lighter particles did not have sufficient kinetic energy to produce the heavier particles. At some point, the massive particle density would drop low enough, such that, the probability of one WIMP finding another became small. These kinds of situation of particles are called “freeze-out”. The density of a specific particle at the time of freeze-out is known as the “relic-density” of this particle since its abundance remains same till today. One can calculate the exact freeze-out temperature of the particles by equating the reaction rate $\Gamma = n\sigma v$ and the rate of expansion of the Universe, i.e., the Hubble rate.

The reaction rate of particles per unit volume is given by,

$$\Gamma = n \langle \sigma v \rangle. \quad (2.1)$$

This is one of the most important quantities which is used to calculate the relic abundance of dark matter, where $\langle \sigma v \rangle$ is the thermally averaged annihilation cross-section and n is the number density of the dark matter. In radiation dominated Universe, the expansion rate is given by,

$$H = \frac{\dot{a}}{a} = g_*^{1/2} \frac{T^2}{M_{\text{Pl}}} \left(\frac{\pi^2}{90} \right)^{1/2}, \quad (2.2)$$

where g_* is the effective degrees of freedom. At the “freeze-out” temperature T_f the annihilation stopped, i.e., the expansion rate become exactly equal to the annihilation rate. Comparing the eqns. 2.1 and 2.2, we get,

$$n(T_f) \simeq g_*^{1/2} \frac{T_f^2}{\langle \sigma v \rangle M_{\text{Pl}}}.$$

Using the Boltzmann equation, one can calculate the number density n and freeze-out temperature of WIMP dark matter in the present Universe. In this case, one has to take into account (1) the rate of expansion of the Universe, (2) annihilation

and co-annihilation of the dark matter particles, and (3) decay of the dark matter particles.

$$\frac{dn}{dt} = -3Hn + \langle \sigma v \rangle (n^2 - (n^{eq})^2). \quad (2.3)$$

One can find the equilibrium number density of the dark matter using the classical Maxwell-Boltzmann distributions. For non-relativistic case, i.e, when temperature of the Universe is less than the mass of the dark matter, the equilibrium number density can be written as,

$$\begin{aligned} n^{eq} &= \int \frac{d^3p}{(2\pi)^3} e^{-E/T}, \quad \text{with} \quad E = M_{DM} + \frac{\mathbf{P}_{DM}^2}{2M_{DM}}. \\ &= e^{-x} \frac{M_{DM}^3}{(2\pi x)^{3/2}} \end{aligned}$$

where $x = \frac{M_{DM}}{T}$ and \mathbf{P}_{DM} is the momentum of dark matter.

In the radiation dominated case, $H = \frac{1}{2t}$, so using eqn. 2.2 we can get dt as,

$$dt = \frac{x dx}{H}.$$

One can write the eqn. 2.3 as,

$$\frac{dY}{dx} = -\frac{(1.32g_*^{1/2} M_{Pl} M_{DM})}{x^2} \langle \sigma v \rangle (Y^2 - Y_{eq}^2), \quad (2.4)$$

where Y is the yield of WIMPs and it is defined as the ratio of number density with the entropy density at the temperature T : $Y = \frac{n}{s}$. For dark matter mass M_{DM} , the entropy density can be written as $s = g_* (\frac{M_{DM}}{x})^3 \left(\frac{2\pi^2}{45}\right)^{1/2}$, and the yield at time of thermal equilibrium is $Y_{eq} = \frac{n^{eq}}{s} = 0.145 e^{-x} x^{3/2}$.

One can further simplify the eqn. 2.4 as,

$$\frac{dz}{dx} = -\frac{1}{x^2} (z^2 - z_{eq}^2), \quad (2.5)$$

where $z = (1.32g_*^{1/2} M_{Pl} M_{DM}) \langle \sigma v \rangle Y$ and $z_{eq} = 1.914 g_*^{1/2} M_{Pl} M_{DM} \langle \sigma v \rangle e^{-x} x^{3/2}$. $Y_0 \equiv Y(T = T_0)$ or $z_0 \equiv z(T = T_0)$ can be found by integrating the above equation from $x = 0$ (i.e., $T = \infty$) to $x = x_0 \left(\equiv \frac{M_{DM}}{T_0}\right)$, where $T = T_0$ is temperature of the Universe today.

The relic abundance of dark matter in the present Universe can be written as,

$$\Omega h^2 = \frac{M_{DM} Y_0}{\rho_c / s_0},$$

where $s_0 \sim 2890 \text{ cm}^{-3}$ is the current entropy density and $\rho_c \sim 1.05 \times 10^{-5} h^2 \text{ GeV cm}^{-3}$ is critical density of the Universe and $h = 0.72$ is the Hubble parameter.

One can calculate the freeze-out temperature of the WIMP dark matter from the Boltzmann eqn. 2.5 by analytic approximations. Approximate solutions can be found under the assumption that below the freeze-out T_f temperature $z \gg z_{eq}$ and $z \simeq z_{eq}$ above it.

For $x > x_f$, limit, the eqn. 2.5 can be written as,

$$\int_{x_f}^x \frac{dz}{z^2} = - \int_{x_f}^x \frac{dx}{x^2}.$$

In the limit $x \rightarrow \infty$, $z(x_f) \gg z(x)$, one can get $z(\infty) = x_f$.

Similarly in the other limit $x < x_f$ one can get, $z_{eq}(x_f) \simeq x_f$, which implies,

$$x_f \simeq 1.914 g_*^{1/2} M_{\text{Pl}} M_{DM} \langle \sigma v \rangle e^{-x_f} x_f^{3/2}.$$

Solving the above equation one can approximately calculate [43] x_f as,

$$x_f \approx 24 + \log \left(\frac{M_{DM}}{100 \text{ GeV}} \right) + \log \left(\frac{\langle \sigma v \rangle}{10^{-9} \text{ GeV}^{-2}} \right) - \frac{1}{2} \log \left(\frac{g_*}{100} \right)$$

From this one can get the freeze-out temperature $T_f = \frac{M_{DM}}{x_f}$ of the dark matter.

2.5 Direct Detections of Dark Matter

One can also detect dark matter directly or indirectly from experiments. With the fact that the WIMP dark matter interacts with the matter weakly, there are many experiments [49–53] which are trying to detect the dark matter directly. If WIMPs scatter from atomic nucleus then it deposits energy in the detector given by,

$$E_{\text{deposit}} = \frac{1}{2} M_{DM} v^2.$$

The energy deposition can also be written as,

$$E_{\text{deposit}} = \frac{\mu^2 v^2}{m_N} (1 - \cos \theta).$$

In the Earth frame, the mean velocity v of the WIMPs relative to the target nucleus is about 220 km/s, μ is the reduced mass of the WIMP of mass M_{DM} and the nucleus of mass m_N , and θ is the scattering angle. As the dark matter is weakly interacting, it may rarely bump into the nucleus of a detector atom and deposit energy which may create a signature at the detector. The amount of energy of a WIMP with mass $M_{DM} = 100$ GeV would deposit in the detector is $E_{deposit} \simeq 27$ keV. It is very difficult to pick out the DM signature against the background from natural radioactivity. Natural radioactivity generally emits energies around MeV range. We need a radioactively clean and cosmic radiation free environment for the detection of the dark matter in experiments. The experimental set up must be placed in the deep underground to get shielded from the cosmic-ray or any other backgrounds.

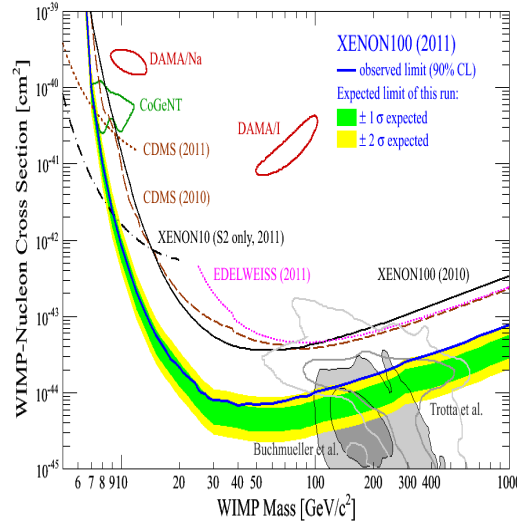


Figure 2.4: *Limit on WIMP cross-sections (normalized to a single nucleon) for spin-independent coupling versus mass from different experiments. Most stringent limit comes from the LUX-2013 experiments. Image credit: Aprile E. et al. [50]*

Dark matter detections are of two types: spin-dependent and spin-independent. In the spin-independent case, the scattering cross-section is proportional to the square of the atomic mass A , whereas the cross-sections for spin-dependent scattering are

proportional to $J(J+1)$, where J is the spin of the target nucleus. The experimental sensitivity of spin-dependent cross-section is far below than that of spin-independent cross-sections as far as the dark matter is concerned [54]. As in this thesis in various models with extended scalar sectors, a lightest neutral scalar particle is considered as a viable WIMP dark matter, only the spin-independent cross-sections are considered.

The spin-independent elastic scattering cross-section of a WIMP with the nucleus is given by,

$$\sigma = \frac{4M_{DM}^2 m_N^2}{\pi(M_{DM} + m_N)^2} [Zf_p + (A - Z)f_n]^2,$$

where A and Z are the atomic mass and atomic number of the target nucleus. f_p , $f_n \approx 0.3$ are the form factors of the proton and the neutron.

Presently non-observation of dark matter in direct detections from experiments XENON [50, 51], LUX [53] set a limit on WIMP-nucleon scattering cross-section for a given dark matter mass (see Fig. 2.4). Currently, most stringent bound is set by the LUX experiment. These experiments also ruled out the previous claim of finding signature of dark matter around 10 GeV by experiments DAMA/LIBRA [55], CoGeNT [56], CDMS [57] etc.

Various kinds of theoretical models consider dark matter particles $\sim \mathcal{O}(100)$ GeV which can easily be produced at the LHC. If the dark matter were created at the LHC, they would escape through the detectors without creating any signature. However, the dark matter would carry away energy and momentum, so one could infer their existence from the amount of energy and momentum “missing” after a collision.

2.6 Indirect Detections of Dark Matter

Indirect detection techniques are quite different for detection of the dark matter. If the dark matter and its antiparticle are the same, then dark matter can annihilate to form known standard model particles such as photons (gamma-rays), electrons e^- , positrons e^+ etc. The dark matter can then be detected indirectly through products

of such annihilations. Various kinds of the detector placed in the orbits around the Earth, for example, Fermi Gamma-ray Space Telescope (FGST), Alpha Magnetic Spectrometer (AMS), PAMELA etc., observed the excess of gamma-ray and positron excess. These observations cannot be explained from the known sources. The dark matter with different mass ranges can be an answer to this puzzle. It is guessed that this excess is formed due to the annihilation of dark matter at the highly populated dark matter regions in the Universe like galactic center. From particle physics point of view, the processes like DM , $DM \rightarrow \gamma\gamma$, e^+e^- etc. have been used to explain such excess. These processes are model dependent. The WIMP dark matter with different mass and coupling of a pair of dark matter to the SM particle can be considered to explain these high energetic gamma-rays excess from the galactic center and positron excess in the cosmic ray.

In the following subsections, the gamma-ray excess and the positron excess will be discussed.

2.6.1 Gamma-ray Excess from Galactic Center

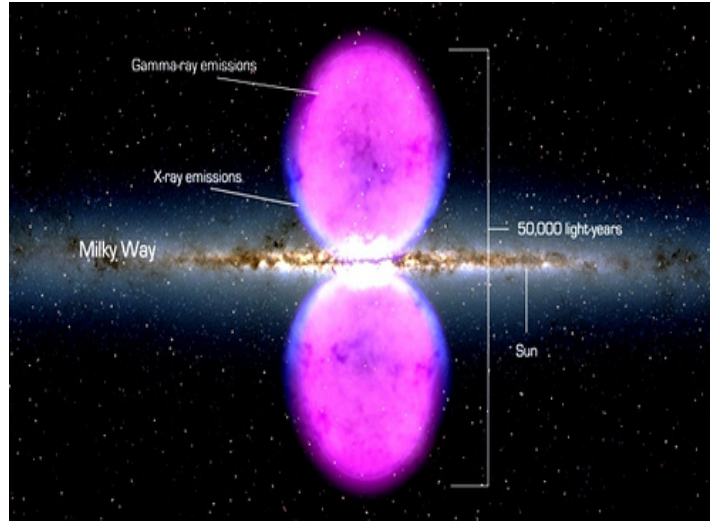


Figure 2.5: The Fermi bubble around the galactic center. Image credit: NASA/Fermi LAT.

Gamma-ray excess at the galactic center has been observed by Fermi Gamma-ray Space Telescope (FGST) [46]. The FGST is the space-based gamma-ray observatory, consisting of a Large Area Telescope (LAT) and a Gamma-ray Burst Monitor (GBM). The Fermi LAT contains the gamma-ray detector that can detect photons within the energy range of 20 MeV to 300 GeV. This detector first observed that the galactic center has the bubble shaped gamma-ray lobes, extending 25000 light-years above and below the galactic plane (see Fig. 2.5). The data from 1.25° to 10° around the galactic center can be explained with known sources of gamma-ray. But the gamma-ray spectrum within 1.25° shows an excess. The dark matter self-annihilations into the gamma-rays at the galactic center give an explanation of this excess [58].

2.6.2 Positron Excess in the Cosmic Ray

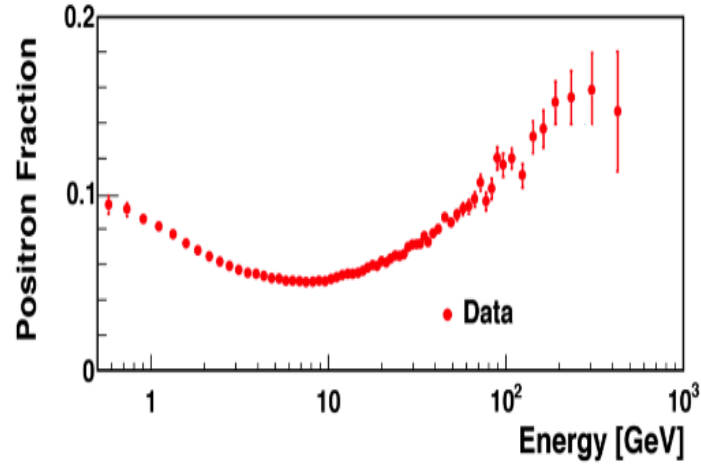


Figure 2.6: *The variations of fraction of positron flux with energy. Image credit: AMS-02. [47]*

Alpha Magnetic Spectrometer-02 [47] is placed at the International Space Station (ISS). It has the capability to detect photon, electron, positron, antiproton etc. in the cosmic rays. Also, it provides the information of the energy of the detected

particle. Presently it is detecting the particles in cosmic ray in the energy range of 0.5 GeV to 500 GeV. AMS has measured the positron fraction $\frac{\Phi_{e^+}}{\Phi_{e^+} + \Phi_{e^-}}$, where Φ are the flux of the particles in the cosmic ray. The most striking result is the observation of a rise in the positron fraction starting at ~ 10 GeV and extending at least to 350 GeV (see Fig. 2.6). A possible explanation for this observation can be the dark matter annihilations [59].

However, the cosmic particles backgrounds are still poorly understood and it is not possible at the moment to make a definite statement about the origin of this excess. In this work, the detailed study of the indirect detection of the dark matter is kept aside.

2.7 Summary

Current observations support a remarkably simple model of the Universe consisting of baryonic matter, dark matter, and dark energy. Several observations such as galactic rotation curves, gravitational lensing in bullet cluster, and the study of cosmic microwave background radiations support that the Universe contains unknown massive dark matter. The properties of dark matter are as much of a mystery now as they were in 1930's. In this chapter, the WIMPs and several other possible dark matter candidates which may contribute to the abundance of the dark matter in the Universe have been briefly discussed. The detailed relic density calculations of the WIMP dark matter have been reviewed. The direct and indirect detections of the dark matter have been shown. The density of the dark matter in the Universe, formation of large-scale structure, observed γ -, positron-excess etc. cannot be explained without extending the SM of particle physics. The simplest extensions involve dark matter, composed of the new particle(s) that may explain these observations.

In this thesis, the SM is extended with a $SU(2)_L$ singlet, doublet or triplet scalar. If

a discrete symmetry Z_2 is imposed on the extra scalar sector such that the standard model particles do not couple with an *odd* number of these extra scalars, then the lightest neutral stable scalar can serve as a viable dark matter candidate, which may fulfill the relic abundance of the Universe. The mass of the dark matter and the coupling of a pair of them to the standard model particle(s) correspond to a WIMP dark matter. The detailed study of the scalar dark matter candidate as WIMPs will be discussed in Chapter 6.

Chapter 3

Electroweak Symmetry Breaking in Extended Higgs sector

3.1 Introduction

In 2012, the ATLAS and CMS collaborations at the Large Hadron Collider (LHC) at the CERN announced the discovery of a new scalar resonance with a mass ~ 125 GeV. Although the properties of the scalar detected at LHC are consistent with the Higgs boson predicted by the Standard Model (SM), the experimental data still allow the extension of the SM Higgs sector with one or more $SU(2)_L$ scalar multiplets. The main goal of this thesis is to explore various models with extended scalar sectors using weak vector boson scattering processes and from the stability of the scalar potential. Imposing a discrete symmetry Z_2 on these models, the lightest neutral Z_2 -odd scalar can serve as a viable dark matter candidate which may fulfill the relic abundance of the dark matter in the Universe. In this chapter, the structure of the scalar potential in these new models and, how the new scalar fields interact with the SM particles and between one another will be discussed. Various theoretical and experimental bounds on the extended scalar sectors will be reviewed as well.

In the next section, the SM extended with a real singlet scalar will be discussed. With and without imposing an extra discrete symmetry Z_2 to the extended sectors,

how the particle gets masses through the electroweak symmetry breaking will be shown. In Sections 3.3, 3.4 and 3.5, similar studies of models extended with a doublet or a triplet scalar with hypercharges $Y = 0$ and 2 will be elaborated.

3.2 The Standard Model with a real singlet scalar

The simplest way to extend the Higgs sector of SM is to consider the addition of an extra real scalar S . The scalar S is a singlet under the SM gauge group. The Lagrangian, invariant under a Z_2 symmetry $S \rightarrow -S$, can be written as [60],

$$\mathcal{L} = (D_\mu \Phi)^\dagger (D^\mu \Phi) + \frac{1}{2} \partial_\mu S \partial^\mu S - V(\Phi, S),$$

with the scalar potential,

$$V(\Phi, S) = -m^2 |\Phi|^2 + \lambda |\Phi|^4 + \frac{1}{2} \overline{m}_S^2 S^2 + \frac{\kappa}{2} |\Phi|^2 S^2 + \frac{\lambda_S}{4!} S^4. \quad (3.1)$$

Φ is the SM complex doublet with vacuum expectation value (VEV) v_d ,

$$\Phi = \begin{pmatrix} \phi^+ \\ \phi^0 \end{pmatrix}, \quad \text{with} \quad \phi^0 = \frac{1}{\sqrt{2}}(h^0 + v_d + iG^0)$$

If the Z_2 symmetry break spontaneously then the singlet scalar also acquires VEV v_S such that $S = s + v_S$, i.e., the potential can have minimum at (v_d, v_S) in $h^0 s$ -plane.

The required conditions are,

$$\begin{aligned} m^2 &= \lambda v_d^2 + \frac{\kappa v_S^2}{2}, \\ \overline{m}_S^2 &= -\frac{\kappa v_d^2}{2} - \frac{\lambda_S v_S^2}{6}. \end{aligned}$$

The coefficient κ and the VEVs, v_d and v_S , govern the degree of mixing between s and h^0 of the SM doublet. The mass of the scalar fields are determined by the parameters, m , \overline{m}_S , λ , κ and the VEVs v_d , v_S . Using the minimization conditions we can write the mass matrix of h^0 and s ,

$$\begin{pmatrix} h^0 & s \end{pmatrix} \begin{pmatrix} A_{\phi\phi} & C_{\phi S} \\ C_{\phi S} & B_{SS} \end{pmatrix} \begin{pmatrix} h^0 \\ s \end{pmatrix} \quad (3.2)$$

with,

$$A_{\phi\phi} = 2\lambda v_d^2,$$

$$\begin{aligned}
B_{SS} &= \frac{1}{3}\lambda_S v_S^2, \\
C_{\phi S} &= \kappa v_d v_S.
\end{aligned}$$

The mass eigenstates are obtained by diagonalizing the mass matrix in eqn. 3.2 with a rotation of the $(h^0 \ s)$ basis,

$$\begin{pmatrix} h \\ H \end{pmatrix} = \begin{pmatrix} \cos \alpha' & \sin \alpha' \\ -\sin \alpha' & \cos \alpha' \end{pmatrix} \begin{pmatrix} h^0 \\ s \end{pmatrix}.$$

The mixing angle (α') between the scalars can be written as,

$$\tan 2\alpha' = \frac{2C_{\phi S}}{B_{SS} - A_{\phi\phi}}.$$

The masses of the scalars are,

$$\begin{aligned}
M_h^2 &= \frac{1}{2} \left[(B_{SS} + A_{\phi\phi}) - \sqrt{(B_{SS} - A_{\phi\phi})^2 + 4C_{\phi S}^2} \right], \\
M_H^2 &= \frac{1}{2} \left[(B_{SS} + A_{\phi\phi}) + \sqrt{(B_{SS} - A_{\phi\phi})^2 + 4C_{\phi S}^2} \right].
\end{aligned}$$

Here h is considered to be the observed Higgs-like scalar particle at ~ 125 GeV and H is a heavy scalar particle yet to be observed. The couplings of the Higgs-like scalar to the known fermions and gauge bosons are also modified. The new modified couplings are $\cos \alpha'$ times the couplings as in the SM. The couplings of the heavy Higgs to SM gauge bosons and fermions multiplied with $\sin \alpha'$: For example, $(\cos \alpha' g_2 M_W) hW^+W^-$, $(\sin \alpha' g_2 M_W) HW^+W^-$ etc.

3.2.1 Constraints on the SM+S model

The parameter space of this model is constrained by various kinds of theoretical considerations like absolute vacuum stability and unitarity of the scattering matrix. Also, the LHC puts severe constraints on this model. In the following, the constraints on the model will be discussed.

3.2.1.1 Constraints from stability of the scalar potential

The stability of the scalar potential requires that the potential should not become

unbounded from below, i.e, it should not approach negative infinity along any direction of the field space at large field values. At very large field the quadratic terms of the scalar potential in eqn. 3.1 are negligibly small compared to the quartic terms, so the scalar potential can be written as,

$$V(h^0, s) = \frac{1}{4}\lambda(h^0)^4 + \frac{\kappa}{4}(h^0)^2(s)^2 + \frac{1}{24}\lambda_S(s)^4.$$

We can further simplify the above equation as,

$$V(h^0, s) = \frac{1}{4} \left\{ \sqrt{\lambda}(h^0)^2 + \frac{\sqrt{\lambda_S}}{\sqrt{6}}(s)^2 \right\}^2 + \frac{1}{4} \left\{ \kappa + \sqrt{\frac{2\lambda\lambda_S}{3}} \right\} (h^0)^2(s)^2. \quad (3.3)$$

The scalar potential in eqn. 3.3 is bounded from below if,

$$\lambda(\Lambda) > 0, \quad \lambda_S(\Lambda) > 0 \quad \text{and} \quad \kappa(\Lambda) + \sqrt{\frac{2\lambda(\Lambda)\lambda_S(\Lambda)}{3}} > 0.$$

where the coupling constants are evaluated at a scale Λ using RG equations. If the scalar potential has a metastable electroweak vacuum, then the above conditions will be modified and are shown in Chapter 6.

3.2.1.2 Perturbativity constraints

To ensure that the radiatively improved scalar potential $V(\Phi, S)$ of the SM+S model remains perturbative at any given energy scale, one must impose the following upper bounds on the couplings λ, κ and λ_S of scalar potential $V(\Phi, S)$ as,

$$| \lambda(\Lambda), \kappa(\Lambda), \lambda_S(\Lambda) | \leq 4\pi.$$

3.2.1.3 Constraints from unitarity of the scattering matrix

The parameters of the scalar potential of this model are severely constrained by the unitarity of the scattering matrix (S-matrix) which consists of the quartic couplings of the scalar potential. At very high field values, one can obtain the scattering matrix by using various scalar-scalar, gauge boson-gauge boson, and scalar-gauge boson scatterings. The unitarity of the S-matrix demands that the eigenvalues of the scattering matrix should be less than 8π . In this model, the unitary bounds are

obtained from the scattering matrices as [61],

$$\lambda \leq 8\pi \quad \text{and} \quad \left| 12\lambda + \lambda_S \pm \sqrt{16\kappa^2 + (-12\lambda + \lambda_S)^2} \right| \leq 32\pi.$$

3.2.1.4 Constraints from the LHC

The signal strength measurement of the SM Higgs-like scalar with mass 125 GeV implies $\sin \alpha'$ less than 0.25 [62]. At the Large Hadron Collider, the direct searches of the heavy Higgs H boson in $gg \rightarrow H \rightarrow W^{*+}W^{*-}$ and $gg \rightarrow H \rightarrow Z^*Z^*$ ($W^{*\pm}, Z^*$ decay into fermions) channels put a stringent bound [62] on the mass of the heavy scalar. The mass range of 145 – 1000 GeV is thus excluded at 95% C.L.

3.2.2 Dark matter in SM+S

If the imposed Z_2 symmetry is exact then it prevents the extra scalar to acquire VEV. The potential can have minimum only along the Higgs field direction, i.e., the electroweak symmetry breaking driven only by the SM Higgs doublet. This extra scalar field does not mix with the SM Higgs and *odd* number of scalars do not couple with the SM particles. As a result, this scalar is stable and is considered to be a viable dark matter candidate. The dark matter studies in singlet extended SM will be taken up in Chapter 6.

3.3 Two Higgs doublet model

In this section, two Higgs doublet model will be briefly reviewed. In this model, an extra scalar doublet Φ' is added with the SM doublet Φ . Both of these fields possess hypercharge +1. Kinetic part of the Lagrangian of these two scalar fields, invariant under $SU(2)_L \times U(1)_Y$ gauge group, can be written as,

$$\mathcal{L}_{\text{Kinetic}}^{\text{2HDM}} = (D_\mu \Phi)^\dagger (D^\mu \Phi) + (D_\mu \Phi')^\dagger (D^\mu \Phi'),$$

where D_μ is the covariant derivative, given in eqn. 1.4.

The scalars are conventionally written as,

$$\Phi = \begin{pmatrix} \phi^+ \\ \phi^0 \end{pmatrix}, \quad \text{and} \quad \Phi' = \begin{pmatrix} \phi'^+ \\ \phi'^0 \end{pmatrix}.$$

The most general potential with these two scalar fields is given by [63],

$$\begin{aligned} V(\Phi, \Phi') = & m_{11}^2 (\Phi^\dagger \Phi) + m_{22}^2 (\Phi'^\dagger \Phi') - m_{12}^2 (\Phi^\dagger \Phi' + \Phi'^\dagger \Phi) + \lambda_1 (\Phi^\dagger \Phi)^2 \\ & + \lambda_2 (\Phi'^\dagger \Phi')^2 + \lambda_3 (\Phi^\dagger \Phi) (\Phi'^\dagger \Phi') + \lambda_4 (\Phi^\dagger \Phi') (\Phi'^\dagger \Phi) \\ & + \frac{\lambda_5}{2} [(\Phi^\dagger \Phi')^2 + (\Phi'^\dagger \Phi)^2] + \lambda_6 (\Phi^\dagger \Phi) (\Phi^\dagger \Phi' + \Phi'^\dagger \Phi) \\ & + \lambda_7 (\Phi'^\dagger \Phi') (\Phi^\dagger \Phi' + \Phi'^\dagger \Phi). \end{aligned} \quad (3.4)$$

The parameters m_{11}, m_{22} and λ_i ($i = 1, \dots, 4$) are real, whereas m_{12} , λ_5 , λ_6 and λ_7 could be complex in general. If these parameters are complex, then imaginary parts of these parameters give rise to explicit CP -violation in the Higgs sector, as not all the imaginary parts can be removed by re-phasing transformations. In this particular incarnation of 2HDM, a fermion can couple to both Φ and Φ' . However, this can lead to unacceptably large tree level flavor changing neutral currents (FCNC) [64–67]. One can avoid such FCNCs by imposing a Z_2 symmetry, namely $\Phi \rightarrow -\Phi$ and $\Phi' \rightarrow \Phi'$. The Z_2 symmetry is *exact* when m_{12} , λ_6 and λ_7 vanish. Here only λ_5 can be complex. But it becomes real after re-phasing one of the scalar doublets so that the scalar potential becomes CP -conserving. Furthermore, this symmetry is said to be broken *softly* if $m_{12} \neq 0$, i.e., it is violated in the quadratic terms only, but it is conserved in quartic terms i.e., $\lambda_6 = 0$ and $\lambda_7 = 0$. At this point, we would like to mention that we are interested in a specific scheme of coupling of fermions to the doublets. This scheme is known as the *Type-II* 2HDM, where the *down-type* quarks and the charged leptons couple to Φ and the *up-type* quarks, to Φ' [68]. This can be achieved by demanding $\Phi \rightarrow -\Phi$ and $\psi_R^i \rightarrow -\psi_R^i$ under the same Z_2 symmetry, where ψ stands for charged leptons or *down-type* quarks and i represents the generation index.

Expanding the neutral fields ϕ^0 and ϕ'^0 around their VEV,

$$\phi^0 = \frac{1}{\sqrt{2}}(v_d + h^0 + i\zeta_d), \quad (3.5)$$

$$\phi'^0 = \frac{1}{\sqrt{2}}(v'_d + h'^0 + i\zeta'_d). \quad (3.6)$$

After electroweak symmetry breaking (EWSB), we have the following minimizing conditions [69],

$$\begin{aligned} m_{11}^2 &= m_{12}^2 \tan \beta - \frac{1}{2}v^2 \left(2\lambda_1 \cos^2 \beta + (\lambda_3 + \lambda_4 + \lambda_5) \sin^2 \beta \right), \\ m_{22}^2 &= m_{12}^2 \cot \beta - \frac{1}{2}v^2 \left(2\lambda_2 \sin^2 \beta + (\lambda_3 + \lambda_4 + \lambda_5) \cos^2 \beta \right), \end{aligned}$$

with $\tan \beta = \frac{v'_d}{v_d}$. The two VEVs v_d and v'_d of the doublets contribute to the weakly interacting gauge boson masses at the tree-level and the masses of weak gauge bosons of 2HDM are given as:

$$M_W^2 = \frac{g_2^2}{4}v^2, \quad M_Z^2 = \frac{g_2^2}{4\cos^2 \theta_W}v^2, \quad \text{where } v^2 = (v_d^2 + v_d'^2) = (246 \text{ GeV})^2,$$

where θ_W is the Weinberg angle.

3.3.1 Scalar Masses and Mixing for 2HDM

After electroweak symmetry breaking, the squared mass matrix can be expressed as 8×8 for the scalars. This matrix composed of four 2×2 submatrices with bases, (ϕ^+, ϕ'^+) , (ϕ^-, ϕ'^-) , (h^0, h'^0) , (ζ_d, ζ'_d) . After rotating these fields into the mass basis, we get five physical mass eigenstates (H^\pm, h, H, A) and remaining three states are massless Goldstone bosons (G^\pm, G^0) eaten up to give mass to the SM gauge bosons W^\pm, Z . The mass eigenvalues for the physical scalar for 2HDM are given by,

$$\begin{aligned} M_A^2 &= \frac{m_{12}^2}{\sin \beta \cos \beta} - v^2 \lambda_5, \\ M_{H^\pm}^2 &= m_A^2 + \frac{1}{2}v^2 (\lambda_5 - \lambda_4), \\ M_h^2 &= \frac{1}{2} \left[(B + A) - \sqrt{(B - A)^2 + 4C^2} \right], \\ M_H^2 &= \frac{1}{2} \left[(B + A) + \sqrt{(B - A)^2 + 4C^2} \right], \\ \text{with } \tan 2\alpha &= \frac{2C}{B - A}, \end{aligned} \quad (3.7)$$

where we have defined,

$$\begin{aligned} A &= M_A^2 \sin^2 \beta + v^2(2\lambda_1 \cos^2 \beta + \lambda_5 \sin^2 \beta), \\ B &= M_A^2 \cos^2 \beta + v^2(2\lambda_2 \sin^2 \beta + \lambda_5 \cos^2 \beta), \\ C &= -M_A^2 \sin \beta \cos \beta + v^2(\lambda_3 + \lambda_4) \sin \beta \cos \beta. \end{aligned}$$

The mixing between the two doublets in the charged, CP -even and CP -odd scalar sectors for 2HDM are respectively given by,

$$\begin{aligned} \begin{pmatrix} G^\pm \\ H^\pm \end{pmatrix} &= \begin{pmatrix} \cos \beta & \sin \beta \\ -\sin \beta & \cos \beta \end{pmatrix} \begin{pmatrix} \phi^\pm \\ \phi'^\pm \end{pmatrix}, \\ \begin{pmatrix} h \\ H \end{pmatrix} &= \begin{pmatrix} \cos \alpha & \sin \alpha \\ -\sin \alpha & \cos \alpha \end{pmatrix} \begin{pmatrix} h^0 \\ h'^0 \end{pmatrix}, \\ \begin{pmatrix} G^0 \\ A \end{pmatrix} &= \begin{pmatrix} \cos \beta & \sin \beta \\ -\sin \beta & \cos \beta \end{pmatrix} \begin{pmatrix} \zeta_d \\ \zeta'_d \end{pmatrix}. \end{aligned} \tag{3.8}$$

3.3.2 Constraints on 2HDM

Varieties of considerations, stemming both from theoretical consistency conditions and from phenomenological bounds, constrain the 2HDM. In the following sections, various constraints such as vacuum stability, unitarity of scattering matrix and electroweak precision measurements on this model will be summarized.

3.3.2.1 Constraints from stability of the scalar potential

The tree-level scalar potential $V(\Phi_1, \Phi_2)$ is stable and bounded from below if [70]

$$\lambda_{1,2}(\Lambda) \geq 0, \quad \lambda_3(\Lambda) \geq -2\sqrt{\lambda_1(\Lambda)\lambda_2(\Lambda)}, \quad \lambda_{L,S}(\Lambda) \geq -\sqrt{\lambda_1(\Lambda)\lambda_2(\Lambda)} \tag{3.9}$$

where the coupling constants are evaluated at a scale Λ using RG equations. However, these conditions become nonfunctional if λ_1 becomes negative at some energy scale to render the EW vacuum metastable. Under such circumstances we need to handle metastability constraints on the potential differently, which we pursue in Chapter 6.

3.3.2.2 Perturbativity constraints

The radiatively improved scalar potential remain perturbative by requiring that all quartic couplings of $V(\Phi_1, \Phi_2)$ satisfy the following:

$$|\lambda_{1,2,3,4,5}(\Lambda)| \leq 4\pi. \quad (3.10)$$

These conditions put an upper bound on the couplings of the scalar potential at an energy scale Λ .

3.3.2.3 Constraints from unitarity of the scattering matrix

Unitarity bounds on λ_i are obtained considering scalar-scalar, gauge boson-gauge boson, and scalar-gauge boson scatterings [71]. The constraints come from the eigenvalues of the corresponding S-matrix [72]:

$$\begin{aligned} |\lambda_3 \pm \lambda_4| &\leq 8\pi, & |\lambda_3 \pm \lambda_5| &\leq 8\pi \\ |\lambda_3 + 2\lambda_4 \pm 3\lambda_5| &\leq 8\pi \\ \left| -\lambda_1 - \lambda_2 \pm \sqrt{(\lambda_1 - \lambda_2)^2 + \lambda_4^2} \right| &\leq 8\pi \\ \left| -3\lambda_1 - 3\lambda_2 \pm \sqrt{9(\lambda_1 - \lambda_2)^2 + (2\lambda_3 + \lambda_4)^2} \right| &\leq 8\pi \\ \left| -\lambda_1 - \lambda_2 \pm \sqrt{(\lambda_1 - \lambda_2)^2 + \lambda_5^2} \right| &\leq 8\pi. \end{aligned} \quad (3.11)$$

3.3.2.4 Constraints from electroweak precision experiments

In the 2HDM, the contributions to the S , T and U parameters can be written as in Ref. [73],

$$\begin{aligned} S_{2HDM} &= \frac{1}{\pi M_Z^2} \left[\sin^2(\beta - \alpha) \mathcal{B}_{22}(M_Z^2, M_H^2, M_A^2) - \mathcal{B}_{22}(M_Z^2, M_{H^\pm}^2, M_{H^\pm}^2) \right. \\ &\quad + \cos^2(\beta - \alpha) \left\{ \mathcal{B}_{22}(M_Z^2, M_h^2, M_A^2) + \mathcal{B}_{22}(M_Z^2, M_Z^2, M_H^2) - \mathcal{B}_{22}(M_Z^2, M_Z^2, M_h^2) \right. \\ &\quad \left. \left. - M_Z^2 \mathcal{B}_0(M_Z^2, M_Z^2, M_H^2) + M_Z^2 \mathcal{B}_0(M_Z^2, M_Z^2, M_h^2) \right\} \right], \\ T_{2HDM} &= \frac{1}{16\pi M_W^2 \sin^2 \theta_W} \left[F(M_{H^\pm}^2, M_A^2) + \sin^2(\beta - \alpha) \left\{ F(M_{H^\pm}^2, M_H^2) - F(M_A^2, M_H^2) \right\} \right] \end{aligned}$$

$$\begin{aligned}
& + \cos^2(\beta - \alpha) \left\{ F(M_{H^\pm}^2, M_h^2) - F(M_A^2, M_h^2) + F(M_W^2, M_H^2) - F(M_W^2, M_h^2) \right. \\
& - F(M_Z^2, M_H^2) + F(M_Z^2, M_h^2) + 4M_Z^2 \bar{B}_0(M_Z^2, M_H^2, M_h^2) \\
& \left. - 4M_W^2 \bar{B}_0(M_W^2, M_H^2, M_h^2) \right\}, \tag{3.12}
\end{aligned}$$

$$\begin{aligned}
U_{2HDM} = & -S_{2HDM} + \frac{1}{\pi M_Z^2} \left[\mathcal{B}_{22}(M_W^2, M_A^2, M_{H^\pm}^2) - 2\mathcal{B}_{22}(M_W^2, M_{H^\pm}^2, M_{H^\pm}^2) \right. \\
& + \sin^2(\beta - \alpha) \mathcal{B}_{22}(M_W^2, M_H^2, M_{H^\pm}^2) \\
& + \cos^2(\beta - \alpha) \left\{ \mathcal{B}_{22}(M_W^2, M_h^2, M_{H^\pm}^2) + \mathcal{B}_{22}(M_W^2, M_W^2, M_H^2) - \mathcal{B}_{22}(M_W^2, M_W^2, M_h^2) \right. \\
& \left. \left. - M_W^2 \mathcal{B}_0(M_W^2, M_W^2, M_H^2) + M_W^2 \mathcal{B}_0(M_W^2, M_W^2, M_h^2) \right\} \right],
\end{aligned}$$

where the functions \mathcal{B}_{22} , \mathcal{B}_0 , \bar{B}_0 and F are defined as follows,

$$\begin{aligned}
\mathcal{B}_{22}(q^2, m_1^2, m_2^2) = & \frac{q^2}{24} [2 \ln q^2 + \ln(x_1 x_2) - 6F(x_1, x_2) \\
& + \{(x_1 - x_2)^3 - 3(x_1^2 - x_2^2) + 3(x_1 - x_2)\} \ln \left(\frac{x_1}{x_2} \right) \\
& - \{2(x_1 - x_2)^2 - 8(x_1 + x_2) + \frac{10}{3}\} \\
& - \{(x_1 - x_2)^2 - 2(x_1 + x_2) + 1\} f(x_1, x_2)], \tag{3.13}
\end{aligned}$$

$$\begin{aligned}
\mathcal{B}_0(q^2, m_1^2, m_2^2) = & 1 + \frac{1}{2} \left\{ \frac{(x_1 + x_2)}{(x_1 - x_2)} - (x_1 - x_2) \right\} \ln \left(\frac{x_1}{x_2} \right) + \frac{1}{2} f(x_1, x_2), \\
f(x_1, x_2) = & \begin{cases} -2\sqrt{\Delta} \left\{ \arctan \frac{x_1 - x_2 + 1}{\sqrt{\Delta}} - \arctan \frac{x_1 - x_2 - 1}{\sqrt{\Delta}} \right\}, & (\Delta > 0) \\ 0, & (\Delta = 0) \\ \sqrt{-\Delta} \ln \frac{x_1 + x_2 - 1 + \sqrt{-\Delta}}{x_1 + x_2 - 1 - \sqrt{-\Delta}}, & (\Delta < 0), \end{cases} \tag{3.14}
\end{aligned}$$

with $\Delta = 2(x_1 + x_2) - (x_1 - x_2)^2 - 1$, $x_i \equiv m_i^2/q^2$ and

$$\begin{aligned}
\bar{B}_0(m_1^2, m_2^2, m_3^2) = & \frac{m_1^2 \ln m_1^2 - m_3^2 \ln m_3^2}{m_1^2 - m_3^2} - \frac{m_1^2 \ln m_1^2 - m_2^2 \ln m_2^2}{m_1^2 - m_2^2}, \\
F(m_1^2, m_2^2) = & F(m_2^2, m_1^2) = \frac{m_1^2 + m_2^2}{2} - \frac{m_1^2 m_2^2}{m_1^2 - m_2^2} \ln \left(\frac{m_1^2}{m_2^2} \right). \tag{3.15}
\end{aligned}$$

The experimental values of S , T and U parameters from the precision electroweak measurements for the fixed Higgs mass and top quark mass to be at 125 GeV and 173 GeV respectively is given in the Ref. [33].

$$\Delta S = 0.05 \pm 0.11, \quad \Delta T = 0.09 \pm 0.13, \quad \Delta U = 0.01 \pm 0.11, \tag{3.16}$$

with correlation coefficients of $+0.90$ between ΔS and ΔT , -0.59 between ΔS and ΔU , -0.83 between ΔT and ΔU . This would constrain the parameter space of 2HDM. If an exact Z_2 symmetry is imposed on the extra doublet then the eqn. 3.13 will be modified as eqn. 6.17 of Chapter 6.

3.3.2.5 Constraints from the LHC

Measured values of the Higgs signal strengths into different decay channels are consistent with the corresponding standard model expectations. Using the experimental data one gets $\sin(\beta - \alpha) \approx \pm 1$ with $\tan \beta = \frac{v_2}{v_1} \approx 4$. This limit is known as *alignment limit* of the 2HDM, in which the couplings of h to vector bosons are SM-like. In this limit, the nonstandard scalar masses are relatively unconstrained. B meson decay ($B \rightarrow X_s \gamma$, X_s denotes a strange hadronic final state) which receives contributions from the charged Higgs at one-loop, imposes a stringent constraint on the Higgs boson mass $M_{H^\pm} > 300$ GeV [74].

3.3.3 Dark Matter in 2HDM

In the above context of 2HDM, we have chosen Z_2 to be softly broken such that the quartic couplings, $\lambda_{6,7}$ are absent in the potential. The scalar fields of both the doublets can mix and also couple with the fermions. If the Z_2 symmetry is unbroken then the term m_{12} vanish and also this symmetry prevents the extra doublet to acquire a VEV, hence these scalar fields of the extra doublet do not mix with the fields of the SM scalar doublet. No SM particle can couple with an *odd* number of scalar fields of the extra doublet. The extra doublet $(\phi'^+, \phi'^0)^T$ can be taken as the physical basis $(H^+, (H + iA)/\sqrt{2})^T$. The lightest neutral particle of the new scalar sector can be considered as a viable dark matter candidate. The detailed analysis related to the dark matter issues and metastability scenario will be presented in Chapter 6.

3.4 Higgs triplet model with hypercharge $Y = 0$

In this model a real isospin $I = 1$ and hypercharge $Y = 0$ triplet $\tilde{\Phi}$ is added with the SM Higgs doublet Φ . This kind of model is known as Higgs triplet model (HTM). The kinetic part of the Lagrangian with these scalar fields is given by [75],

$$\mathcal{L}_{\text{Kinetic}}^{Y=0} = (D_\mu \Phi)^\dagger (D^\mu \Phi) + \frac{1}{2} (D_\mu \tilde{\Phi})^\dagger (D^\mu \tilde{\Phi}),$$

where

$$D_\mu \tilde{\Phi} = \left(\partial_\mu + ig_2 t_a W_\mu^a \right) \tilde{\Phi} \quad \text{with} \quad \tilde{\Phi} = \begin{pmatrix} \eta^+ \\ \eta^0 \\ -\eta^- \end{pmatrix}, \quad (3.17)$$

and

$$t_1 = \frac{1}{\sqrt{2}} \begin{pmatrix} 0 & 1 & 0 \\ 1 & 0 & 1 \\ 0 & 1 & 0 \end{pmatrix}, \quad t_2 = \frac{1}{\sqrt{2}} \begin{pmatrix} 0 & -i & 0 \\ i & 0 & -i \\ 0 & i & 0 \end{pmatrix}, \quad t_3 = \begin{pmatrix} 1 & 0 & 0 \\ 0 & 0 & 0 \\ 0 & 0 & -1 \end{pmatrix}.$$

The most general $SU(2)_L \times U(1)_Y$ scalar potential with SM Higgs doublet and a real scalar triplet is given by,

$$\begin{aligned} V(\Phi, \tilde{\Phi}) = & \mu_1^2 (\Phi^\dagger \Phi) + \frac{\mu_2^2}{2} (\tilde{\Phi}^\dagger \tilde{\Phi}) + \tilde{\lambda}_1 (\Phi^\dagger \Phi)^2 + \frac{\tilde{\lambda}_2}{4} (\tilde{\Phi}^\dagger \tilde{\Phi})^2 \\ & + \frac{\tilde{\lambda}_3}{2} (\Phi^\dagger \Phi) (\tilde{\Phi}^\dagger \tilde{\Phi}) + \tilde{\lambda}_4 \Phi^\dagger \sigma^a \Phi \tilde{\Phi}_a, \end{aligned} \quad (3.18)$$

where $\tilde{\Phi}_a = \left(\frac{1}{\sqrt{2}}(\eta^+ + \eta^-), \frac{1}{\sqrt{2}}(\eta^+ - \eta^-), \eta^0 \right)$.

Now expanding neutral component of the triplet field around the VEV v'_t and using eqn. 3.5 and after EWSB we have the following minimization conditions:

$$\begin{aligned} \mu_1^2 &= \frac{1}{2} \left(2\tilde{\lambda}_4 v'_t - (2\tilde{\lambda}_1 v_d^2 + \tilde{\lambda}_3 v_t'^2) \right), \\ \mu_2^2 &= \frac{1}{2v'_t} \left(\tilde{\lambda}_4 v_d^2 - \tilde{\lambda}_3 v_d^2 v'_t - 2\tilde{\lambda}_2 v_t'^3 \right). \end{aligned}$$

In this scenario the masses for W and Z bosons are given by,

$$M_W^2 = \frac{g_2^2}{4} v^2, \quad M_Z^2 = \frac{g_2^2}{4 \cos^2 \theta_W} v_d^2, \quad (3.19)$$

where VEVs are related to the SM VEV by $v^2 = v_d^2 + 4v_t'^2 = (246 \text{ GeV})^2$.

It is quite evident from eqn. 3.19 that this model violates custodial symmetry at

tree level, as,

$$\rho = \frac{M_W^2}{M_Z^2 \cos^2 \theta_W} = 1 + 4 \frac{v_t'^2}{v_d^2}.$$

The experimental value of ρ parameter is 1.0004 ± 0.00024 [10]. Hence, $\delta\rho \approx 0.0004 \pm 0.00024$. At tree-level, this puts a stringent constraint on the triplet scalar VEV, $v_t' < 4 \text{ GeV}$ at 3σ .

3.4.1 Scalar Masses and Mixing for HTM ($Y = 0$)

After spontaneous symmetry breaking, there are two physical neutral CP -even Higgs h, H , a pair of charged Higgs H^\pm and three Goldstone bosons $G^\pm, G^0 (\equiv \zeta_d)$. The masses of the physical particles are given by,

$$\begin{aligned} M_{H^\pm}^2 &= \tilde{\lambda}_4 \frac{(v_d^2 + 4v_t'^2)}{2v_t'}, \\ M_h^2 &= \frac{1}{2} \left[(\tilde{B} + \tilde{A}) - \sqrt{(\tilde{B} - \tilde{A})^2 + 4\tilde{C}^2} \right], \\ M_H^2 &= \frac{1}{2} \left[(\tilde{B} + \tilde{A}) + \sqrt{(\tilde{B} - \tilde{A})^2 + 4\tilde{C}^2} \right], \end{aligned} \quad (3.20)$$

where,

$$\begin{aligned} \tilde{A} &= 2\lambda_1 v_d^2, \\ \tilde{B} &= \frac{\lambda_4 v_d^2 + 4\lambda_2 v_t'^3}{2v_t'}, \\ \tilde{C} &= -\lambda_4 v_d + \lambda_3 v_d v_t'. \end{aligned} \quad (3.21)$$

The mixing between the SM doublet and the real triplet in the charged and CP -even scalar sectors for this scenario are respectively given by,

$$\begin{aligned} \begin{pmatrix} G^\pm \\ H^\pm \end{pmatrix} &= \begin{pmatrix} \cos \tilde{\beta} & \sin \tilde{\beta} \\ -\sin \tilde{\beta} & \cos \tilde{\beta} \end{pmatrix} \begin{pmatrix} \phi^\pm \\ \eta^\pm \end{pmatrix}, \\ \begin{pmatrix} h \\ H \end{pmatrix} &= \begin{pmatrix} \cos \gamma & \sin \gamma \\ -\sin \gamma & \cos \gamma \end{pmatrix} \begin{pmatrix} h^0 \\ \eta^0 \end{pmatrix}, \end{aligned}$$

with $\sin \gamma = \sqrt{\frac{\sqrt{(\tilde{B}-\tilde{A})^2+4\tilde{C}^2}-(\tilde{B}-\tilde{A})}{2\sqrt{(\tilde{B}-\tilde{A})^2+4\tilde{C}^2}}}$ and $\tan \tilde{\beta} = \frac{2v_t'}{v_d}$.

In large μ_2^2 and small v'_t limit $\sin \gamma$ and $\sin \tilde{\beta}$ can be written as,

$$\begin{aligned}\sin \gamma &= \sqrt{\frac{1}{2} - \frac{1}{2\sqrt{1 + 16\frac{v_t'^2}{v_d^2}}}} \approx 0, \\ \sin \tilde{\beta} &= \frac{2v'_t}{\sqrt{v_d^2 + 4v_t'^2}} \approx 0.\end{aligned}$$

In this limit the $\tilde{\lambda}$'s look like,

$$\begin{aligned}\tilde{\lambda}_1 &= \frac{M_h^2}{2v_d^2}, \\ \tilde{\lambda}_2 &= \frac{2(M_H^2 - M_{H^\pm}^2)}{v_d^2 \sin^2 \tilde{\beta}}, \\ \tilde{\lambda}_3 &= \frac{2(M_{H^\pm}^2 - (\sin \gamma / \sin \tilde{\beta}) M_H^2)}{v_d^2}, \\ \tilde{\lambda}_4 &= \frac{\sin \tilde{\beta} M_{H^\pm}^2}{v_d^2}.\end{aligned}$$

Also, in the same limit, if M_{H^\pm} and M_H are very heavy compared to M_h , then both the charged and heavy neutral particle masses should be degenerate (see eqns. 3.20 and 3.21). For large differences in M_{H^\pm} and M_H , the $\tilde{\lambda}_{2,3}$ become non-perturbative (see Section 3.4.2.2), and in addition it may violate the unitarity (Section 3.4.2.3) conditions.

3.4.2 Constraints on the HTM ($Y = 0$)

The parameter space of this model is constrained by theoretical considerations like absolute vacuum stability, perturbativity, and unitarity of the scattering matrix. In the following, these theoretical bounds and the bounds from the electroweak precision measurements on the HTM ($Y = 0$) will be discussed.

3.4.2.1 Constraints from stability of the scalar potential

A necessary condition for the stability of the vacuum comes from requiring that the scalar potential is bounded from below when the scalar fields become large in any direction of the field space. At the tree-level scalar potential $V(\Phi, \tilde{\Phi})$ is

bounded from below if

$$\tilde{\lambda}_1(\Lambda) \geq 0, \quad \tilde{\lambda}_2(\Lambda) \geq 0, \quad \tilde{\lambda}_3(\Lambda) \geq -2\sqrt{\tilde{\lambda}_1(\Lambda)\tilde{\lambda}_2(\Lambda)},$$

where Λ is an arbitrary energy scale. If the quantum corrections are included to the scalar potential, then the above conditions will be more complicated. The modification of the stability conditions of the scalar potential will be shown in Chapter 6.

3.4.2.2 Perturbativity bounds

The radiatively improved scalar potential remain perturbative by requiring that all quartic couplings of $V(\Phi, \tilde{\Phi})$ satisfy the following relations,

$$|\tilde{\lambda}_{1,2,3}(\Lambda)| \leq 4\pi \quad \text{and} \quad \left| \frac{\tilde{\lambda}_4(\Lambda)}{\Lambda} \right| \leq 4\pi.$$

On applying such conditions, one implies upper bounds on the values of the couplings $\tilde{\lambda}'$ s at low as well as high scales.

3.4.2.3 Constraints from unitarity of the scattering matrix

In this section, the derivation of unitary bounds on the quartic couplings of the scalar potential from the scattering matrix will be discussed. To the best of our knowledge, the full expressions of unitarity bounds on the scalar quartic couplings in this model have not yet been presented in the literature. It has been shown in Section 1.3.1.3 of Chapter 1 that the scattering matrix consists of only the quartic couplings of scalars, gauge bosons, and scalar-gauge bosons [71].

At very high energies, the equivalence theorem implies that the longitudinal modes of the gauge bosons are equivalent to the corresponding Goldstone bosons, e.g., the amplitude of $W_L^+ W_L^- \rightarrow W_L^+ W_L^-$ scattering is approximated by $G^+ G^- \rightarrow G^+ G^-$. In this energy limit, pure scalar scattering processes are considered to obtain the unitarity bound on the quartic couplings of the scalar potential. The scalar quartic couplings in the physical bases, G^\pm , G^0 , H^\pm , h , H , are complicated functions of $\tilde{\lambda}'$ s, γ , $\tilde{\beta}$. For example, the $hhhh$ vertex is $6(\lambda_1 \cos^4 \gamma + \lambda_3 \cos^2 \gamma \sin^2 \gamma + \lambda_2 \sin^4 \gamma)$. It

is difficult to calculate the unitary bounds in the physical bases. So to simplify the quartic coupling, one can consider the non-physical scalar fields before electroweak symmetry breaking, ϕ^\pm , η^\pm , ζ_d , h^0 , η^0 . Here the crucial point is that the S-matrix expressed in terms of the physical fields can be transformed into an S-matrix for the non-physical fields by making a unitary transformation [76].

Different quartic couplings in non-physical bases obtained by expanding the scalar potential of eqn. 3.18, are given by,

$$\begin{aligned}
\{\zeta_d \zeta_d \zeta_d \zeta_d\} &= 6\tilde{\lambda}_1, & \{\zeta_d \zeta_d \phi^+ \phi^-\} &= 2\tilde{\lambda}_1, \\
\{\phi^+ \phi^+ \phi^- \phi^-\} &= 4\tilde{\lambda}_1, & \{\zeta_d \zeta_d h^0 h^0\} &= 2\tilde{\lambda}_1, \\
\{\phi^+ \phi^- h^0 h^0\} &= 2\tilde{\lambda}_1, & \{h^0 h^0 h^0 h^0\} &= 6\tilde{\lambda}_1, \\
\{\zeta_d \zeta_d \eta^0 \eta^0\} &= \tilde{\lambda}_3, & \{\phi^+ \phi^- \eta^0 \eta^0\} &= \tilde{\lambda}_3, \\
\{h^0 h^0 \eta^0 \eta^0\} &= \tilde{\lambda}_3, & \{\eta^0 \eta^0 \eta^0 \eta^0\} &= 6\tilde{\lambda}_2, \\
\{\zeta_d \zeta_d \eta^+ \eta^-\} &= \tilde{\lambda}_3, & \{\phi^+ \phi^- \eta^+ \eta^-\} &= \tilde{\lambda}_3, \\
\{h^0 h^0 \eta^+ \eta^-\} &= \tilde{\lambda}_3, & \{\eta^0 \eta^0 \eta^+ \eta^-\} &= 2\tilde{\lambda}_2, \\
\{\eta^+ \eta^+ \eta^- \eta^-\} &= 4\tilde{\lambda}_2.
\end{aligned} \tag{3.22}$$

The full set of these non-physical scalar scattering processes can be expressed as a 16×16 S-matrix. This matrix is composed of three submatrices of dimensions 6×6 , 5×5 , and 5×5 which have different initial and final states.

The first 6×6 sub-matrix \mathcal{M}_1 corresponds to scattering processes whose initial and final states are one of these: $(h^0 \phi^+, \zeta_d \phi^+, \eta^0 \phi^+, h^0 \phi^+, \zeta_d \eta^+, \eta^0 \eta^+)$. Using the Feynman rules in eqn. 3.22, one can obtain \mathcal{M}_1 as, $\mathcal{M}_1 = \text{diag}(2\tilde{\lambda}_1, 2\tilde{\lambda}_1, 2\tilde{\lambda}_1, \tilde{\lambda}_3, \tilde{\lambda}_3, \tilde{\lambda}_3)$.

The sub-matrix \mathcal{M}_2 corresponds to scattering process with one of the following initial and final states: $(h^0 \zeta_d, \phi^+ \eta^-, \eta^+ \phi^-, \eta^0 \zeta_d, h^0 \eta^0)$. Similarly, one can calculate \mathcal{M}_2 , it take the following form: $\mathcal{M}_2 = \text{diag}(2\tilde{\lambda}_1, \tilde{\lambda}_3, \tilde{\lambda}_3, \tilde{\lambda}_3, \tilde{\lambda}_3)$.

The third sub-matrix corresponds to scattering with one of the following initial and final states $(\phi^+ \phi^-, \eta^+ \eta^-, \frac{\zeta_d \zeta_d}{\sqrt{2}}, \frac{h^0 h^0}{\sqrt{2}}, \frac{\eta^0 \eta^0}{\sqrt{2}})$. The factor $\frac{1}{\sqrt{2}}$ appeared due to statistics of identical particles. So one can find \mathcal{M}_3 with the help of the Feynman rules in eqn. 3.22 and is given by,

$$\mathcal{M}_3 = \begin{pmatrix} 4\tilde{\lambda}_1 & \tilde{\lambda}_3 & \sqrt{2}\tilde{\lambda}_1 & \sqrt{2}\tilde{\lambda}_1 & \frac{\tilde{\lambda}_3}{\sqrt{2}} \\ \tilde{\lambda}_3 & 4\tilde{\lambda}_2 & \frac{\tilde{\lambda}_3}{\sqrt{2}} & \frac{\tilde{\lambda}_3}{\sqrt{2}} & \sqrt{2}\tilde{\lambda}_2 \\ \sqrt{2}\tilde{\lambda}_1 & \frac{\tilde{\lambda}_3}{\sqrt{2}} & 3\tilde{\lambda}_1 & \tilde{\lambda}_1 & \frac{\tilde{\lambda}_3}{2} \\ \sqrt{2}\tilde{\lambda}_1 & \frac{\tilde{\lambda}_3}{\sqrt{2}} & \tilde{\lambda}_1 & 3\tilde{\lambda}_1 & \frac{\tilde{\lambda}_3}{2} \\ \frac{\tilde{\lambda}_3}{\sqrt{2}} & \sqrt{2}\tilde{\lambda}_2 & \frac{\tilde{\lambda}_3}{2} & \frac{\tilde{\lambda}_3}{2} & 3\tilde{\lambda}_2 \end{pmatrix}$$

The eigenvalues of \mathcal{M}_3 are : $\left\{ 2\tilde{\lambda}_1, 2\tilde{\lambda}_1, 2\tilde{\lambda}_2, \frac{1}{2} \left(6\tilde{\lambda}_1 + 5\tilde{\lambda}_2 \pm \sqrt{(6\tilde{\lambda}_1 - 5\tilde{\lambda}_2)^2 + 12\tilde{\lambda}_3^2} \right) \right\}$.

Unitary constraints of the scattering processes demand that the eigenvalues e_i 's ($i=1,..,16$) of the scattering-matrix should be less than 8π .

3.4.2.4 Constraints from electroweak precision experiments

Electroweak precision data has imposed bounds on new physics models via Peskin-Takeuchi [30] S , T , U parameters. The additional contributions from this model are given by [77, 78],

$$\begin{aligned} S_{\text{HTM}}^{Y=0} &\simeq 0, \\ T_{\text{HTM}}^{Y=0} &= \frac{1}{8\pi} \frac{1}{\sin^2 \theta_W \cos^2 \theta_W} \left[\frac{M_H^2 + M_{H^\pm}^2}{M_Z^2} - \frac{2M_{H^\pm}^2 M_H^2}{M_Z^2 (M_H^2 - M_{H^\pm}^2)} \log \left(\frac{M_H^2}{M_{H^\pm}^2} \right) \right] \\ &\simeq \frac{1}{6\pi} \frac{1}{\sin^2 \theta_W \cos^2 \theta_W} \frac{(\Delta M)^2}{M_Z^2}, \\ U_{\text{HTM}}^{Y=0} &= -\frac{1}{3\pi} \left(M_H^4 \log \left(\frac{M_H^2}{M_{H^\pm}^2} \right) \frac{(3M_{H^\pm}^2 - M_H^2)}{(M_H^2 - M_{H^\pm}^2)^3} + \frac{5(M_H^4 + M_{H^\pm}^4) - 22M_{H^\pm}^2 M_H^2}{6(M_H^2 - M_{H^\pm}^2)^2} \right) \\ &\simeq \frac{\Delta M}{3\pi M_{H^\pm}}. \end{aligned}$$

S is proportional to $\sin \tilde{\beta}$. In the limit $\tilde{\beta} \rightarrow 0$, the contribution to the S parameter from the triplet scalar fields is negligible. For $\tilde{\beta} \rightarrow 0$ and $M_{H^\pm, H} \gg M_h$ the charged particle H^\pm and heavier CP -even Higgs H are almost degenerate in mass, i.e., ΔM

is very small. Also the contributions to the T and U parameters from this model are negligible.

3.4.2.5 Constraints from the LHC

There is no direct search bound on the masses of the Higgs triplet model with hypercharge zero. One can get an indirect bound on the mass of the charged Higgs scalar from the diphoton excess. For $M_{H^\pm} < 200$ GeV, H^\pm will contribute significantly to the $\sigma(pp \rightarrow \gamma\gamma)$ and $\sigma(pp \rightarrow Z\gamma)$ cross-sections measured at the LHC.

3.4.3 Dark Matter in HTM ($Y = 0$)

Like in the case of an additional singlet or doublet scalars, if one imposes a discrete symmetry on the extra triplet scalar then the neutral component of the scalar triplet can be considered as a viable dark matter candidate. In Chapter 6, the detailed study of Z_2 -odd triplet scalar from metastability of electroweak vacuum as well as dark matter point of view will be discussed.

3.5 Higgs triplet model with hypercharge $Y = 2$

The detailed discussion of the Higgs triplet model with hypercharge $Y = 2$ will be provided in this section. The additional triplet is denoted by $\Delta = (\Delta_1, \Delta_2, \Delta_3)$, which can be written in the bi-doublet form as,

$$\Delta = \frac{\sigma^i}{\sqrt{2}} \Delta_i = \begin{pmatrix} \delta^+/\sqrt{2} & \delta^{++} \\ \delta^0 & -\delta^+/\sqrt{2} \end{pmatrix},$$

where $\Delta_1 = (\delta^{++} + \delta^0)/\sqrt{2}$, $\Delta_2 = i(\delta^{++} - \delta^0)/\sqrt{2}$, $\Delta_3 = \delta^+$. The Lagrangian of this model is given in the following,

$$\mathcal{L}^{Y=2} = \mathcal{L}_{\text{Yukawa}}^{Y=2} + \mathcal{L}_{\text{Kinetic}}^{Y=2} - V(\Phi, \Delta). \quad (3.23)$$

with the relevant kinetic and Yukawa interaction terms are respectively

$$\mathcal{L}_{\text{kinetic}}^{Y=2} = (D_\mu \Phi)^\dagger (D^\mu \Phi) + \text{Tr} \left[(D_\mu \Delta)^\dagger (D^\mu \Delta) \right], \quad (3.24)$$

$$\mathcal{L}_{\text{Yukawa}}^{Y=2} = \mathcal{L}_{\text{Yukawa}}^{\text{SM}} - \frac{1}{\sqrt{2}} (Y_\nu)_{ij} L_i^\top C i \sigma_2 \Delta L_j + \text{h.c.} . \quad (3.25)$$

Y_ν represents neutrino Yukawa coupling, and C is the charge conjugation operator.

Covariant derivative of the scalar triplet field is given by,

$$D_\mu \Delta = \partial_\mu \Delta + i \frac{g_2}{2} [\sigma^a W_\mu^a, \Delta] + i g_1 B_\mu \Delta \quad (a = 1, 2, 3).$$

The scalar potential in eqn. 3.23 is given by [79],

$$\begin{aligned} V(\Phi, \Delta) = & -m_\Phi^2 (\Phi^\dagger \Phi) + \frac{\lambda'_1}{4} (\Phi^\dagger \Phi)^2 + M_\Delta^2 \text{Tr}(\Delta^\dagger \Delta) + (\mu \Phi^\top i \sigma_2 \Delta^\dagger \Phi + \text{h.c.}) \\ & + \lambda'_2 [\text{Tr}(\Delta^\dagger \Delta)]^2 + \lambda'_3 \text{Tr}[(\Delta^\dagger \Delta)^2] + \lambda'_4 \Phi^\dagger \Delta \Delta^\dagger \Phi \\ & + \lambda'_5 (\Phi^\dagger \Phi) \text{Tr}(\Delta^\dagger \Delta). \end{aligned} \quad (3.26)$$

λ'_i ($i = 1, \dots, 5$) are real dimensionless coupling constants, while m_Φ , M_Δ and μ are real mass parameters of the above potential. Here μ term is the only term which can generate a CP -phase, as the other terms of the potential are self-conjugate. However, that phase can be absorbed by redefining the fields Φ and Δ . Furthermore, we assume that $m_\Phi^2 > 0$ for spontaneous symmetry breaking of above mentioned gauge group. After EWSB, the scalar potential (see eqn. 3.26) is expanded around the VEVs of neutral scalar CP -even scalar fields: around v_d as in eqn. 3.5 and around v_t as $\frac{1}{\sqrt{2}}(v_t + \xi^0 + i\zeta_t)$ respectively. At the minimum of the scalar potential, the following conditions[79] are satisfied.

$$\begin{aligned} m_\Phi^2 &= \frac{\lambda'_1 v_d^2}{4} - \sqrt{2} \mu v_t + \frac{(\lambda'_5 + \lambda'_4)}{2} v_t^2, \\ M_\Delta^2 &= \frac{2\mu v_d^2 - \sqrt{2}(\lambda'_5 + \lambda'_4) v_d^2 v_t - 2\sqrt{2}(\lambda'_2 + \lambda'_3) v_t^3}{2\sqrt{2} v_t}. \end{aligned}$$

Here the triplet VEV (v_t) contributes to the weakly interacting gauge boson masses at the tree-level as in the previous models. In this scenario the masses of weak gauge bosons are given as:

$$M_W^2 = \frac{g_2^2}{4} (v_d^2 + 2v_t^2), \quad M_Z^2 = \frac{g_2^2}{4 \cos^2 \theta_W} (v_d^2 + 4v_t^2). \quad (3.27)$$

In the following sections, the particle spectrum, the theoretical and experimental constraints on this model will be discussed.

3.5.1 Scalar Masses and Mixing for HTM ($Y = 2$)

After minimization of the scalar potential $V(\Phi, \Delta)$ in eqn. 3.26 with respect to the VEVs, a 10×10 squared mass matrix appeared for the scalars. This matrix is composed of four 2×2 and two 1×1 matrices. Among the ten eigenstates, seven are physical ($H^{\pm\pm}$, H^\pm , h , H , A) and they are massive. Remaining three states are massless Goldstone bosons G^\pm , G^0 , eaten up to give mass to the SM gauge bosons W^\pm , Z . The mass eigenvalues for the physical scalars are given by,

$$\begin{aligned}
M_{H^{\pm\pm}}^2 &= \frac{\sqrt{2}\mu v_d^2 - \lambda'_4 v_d^2 v_t - 2\lambda'_3 v_t^3}{2v_t}, \\
M_{H^\pm}^2 &= \frac{(v_d^2 + 2v_t^2)(2\sqrt{2}\mu - \lambda'_4 v_t)}{4v_t}, \\
M_A^2 &= \frac{\mu(v_d^2 + 4v_t^2)}{\sqrt{2}v_t}, \\
M_h^2 &= \frac{1}{2} \left(B' + A' - \sqrt{(B' - A')^2 + 4C'^2} \right), \\
M_H^2 &= \frac{1}{2} \left(B' + A' + \sqrt{(B' - A')^2 + 4C'^2} \right),
\end{aligned} \tag{3.28}$$

with $A' = \frac{\lambda'_1}{2} v_d^2$, $B' = \frac{\sqrt{2}\mu v_d^2 + 4(\lambda'_2 + \lambda'_3)v_t^3}{2v_t}$, $C' = v_d[-\sqrt{2}\mu + (\lambda'_5 + \lambda'_4)v_t]$.

The mixing between the doublet and triplet scalar fields in the charged, CP -even and CP -odd scalar sectors are respectively denoted by,

$$\begin{aligned}
\begin{pmatrix} G^\pm \\ H^\pm \end{pmatrix} &= \begin{pmatrix} \cos \beta' & \sin \beta' \\ -\sin \beta' & \cos \beta' \end{pmatrix} \begin{pmatrix} \phi^\pm \\ \delta^\pm \end{pmatrix}, \\
\begin{pmatrix} h \\ H \end{pmatrix} &= \begin{pmatrix} \cos \gamma' & \sin \gamma' \\ -\sin \gamma' & \cos \gamma' \end{pmatrix} \begin{pmatrix} \eta^0 \\ \xi^0 \end{pmatrix}, \\
\begin{pmatrix} G^0 \\ A \end{pmatrix} &= \begin{pmatrix} \cos \delta' & \sin \delta' \\ -\sin \delta' & \cos \delta' \end{pmatrix} \begin{pmatrix} \zeta_d \\ \zeta_t \end{pmatrix},
\end{aligned}$$

where the mixing angles are given by,

$$\begin{aligned}
\tan \beta' &= \frac{\sqrt{2}v_t}{v_d}, \\
\tan \delta' &= \frac{2v_t}{v_d},
\end{aligned}$$

$$\tan 2\gamma' = \frac{2C'}{B' - A'}.$$

3.5.2 Constraints on the HTM ($Y = 2$)

Let us summarize the constraints on the scalar potential of the $Y = 2$ triplet model given by eqn. 3.26 in order to sustain the stability of the electroweak vacuum, the conservation of the tree-level unitarity in various scattering processes, etc.

3.5.2.1 Constraints from stability of scalar potential

Stability of the electroweak vacuum of the scalar potential in eqn. 3.26 requires that it be bounded from below i.e., there is no direction in field space along which the potential tends to minus infinity. The necessary and sufficient conditions are [79]:

$$\begin{aligned} \lambda'_1(\Lambda) &\geq 0, \quad \lambda'_2(\Lambda) + \lambda'_3(\Lambda) \geq 0, \quad \lambda'_2(\Lambda) + \frac{\lambda'_3(\Lambda)}{2} \geq 0, \\ \lambda'_5(\Lambda) + \sqrt{\lambda'_1(\Lambda)(\lambda'_2(\Lambda) + \lambda'_3(\Lambda))} &\geq 0, \\ \lambda'_5(\Lambda) + \sqrt{\lambda'_1(\Lambda) \left(\lambda'_2(\Lambda) + \frac{\lambda'_3(\Lambda)}{2} \right)} &\geq 0, \\ \lambda'_5(\Lambda) + \lambda'_4(\Lambda) + \sqrt{\lambda'_1(\Lambda)(\lambda'_2(\Lambda) + \lambda'_3(\Lambda))} &\geq 0, \\ \text{and } \lambda'_5(\Lambda) + \lambda'_4(\Lambda) + \sqrt{\lambda'_1(\Lambda) \left(\lambda'_2(\Lambda) + \frac{\lambda'_3(\Lambda)}{2} \right)} &\geq 0. \end{aligned}$$

where the coupling constants are evaluated at an arbitrary running scale Λ .

3.5.2.2 Perturbativity constraints

For the HTM ($Y = 2$) to behave as a perturbative quantum field theory at any given scale, one must impose the conditions on the radiatively improved scalar potential $V(\Phi, \Delta)$ as,

$$|\lambda'_{1,2,3,4,5}(\Lambda)| \leq 4\pi, \quad \left| \frac{\mu(\Lambda)}{\Lambda} \right| \leq 4\pi.$$

These conditions imply an upper bound on the couplings λ' s and μ at an energy scale Λ .

3.5.2.3 Constraints from unitarity of the scattering matrix

The tree-level unitarity of the S-matrix for elastic scattering imposes the following constraints [79]:

$$\begin{aligned}
|\lambda'_5 + \lambda'_4| &\leq 8\pi, \quad |\lambda'_5| \leq 8\pi, \quad |2\lambda'_5 + 3\lambda'_4| \leq 16\pi, \\
|\lambda'_1| &\leq 16\pi, \quad |\lambda'_2| \leq 4\pi, \quad |\lambda'_2 + \lambda'_3| \leq 4\pi, \\
\left| \lambda'_1 + 4\lambda'_2 + 8\lambda'_3 \pm \sqrt{(\lambda'_1 - 4\lambda'_2 - 8\lambda'_3)^2 + 16\lambda_4'^2} \right| &\leq 32\pi, \\
\left| 3\lambda'_1 + 16\lambda'_2 + 12\lambda'_3 \pm \sqrt{(3\lambda'_1 - 16\lambda'_2 - 12\lambda'_3)^2 + 24(2\lambda'_5 + \lambda'_4)^2} \right| &\leq 32\pi, \\
|2\lambda'_5 - \lambda'_4| &\leq 16\pi \quad \text{and} \quad |2\lambda'_2 - \lambda'_3| \leq 8\pi.
\end{aligned}$$

3.5.2.4 Constraints from the neutrino mass and the electroweak precision experiments

Here we would like to discuss the constraints on the parameters coming from electroweak precision tests and from the neutrino mass. In this model, using eqn. 3.25, neutrino mass can be expressed as $(M_\nu)_{ij} = v_t (Y_\nu)_{ij}$. Consequently for realistic neutrino masses it calls for a tiny value of v_t or Y_ν or both.

If $Y_\nu \sim \mathcal{O}(1)$, then to satisfy sub-eV neutrino mass, v_t should be $\mathcal{O}(10^{-9})$ GeV. This can be achieved via the type-II seesaw mechanism. Using eqn. 3.27, for $v_t \ll v_d$, the triplet VEV can be expressed as $v_t \equiv \frac{\mu v_d^2}{M_\Delta^2}$. So one can choose a large M_Δ to get a neutrino mass of $\mathcal{O}(0.1)$ eV. This mechanism provides neutrino mass naturally. At this limit, the couplings of the new scalar particles with the SM particles are vanishingly small. One can take another extreme limit on v_t using ρ -parameter at the tree-level. In this model, the ρ -parameter can be calculated using the eqn. 3.27 and is given by,

$$\rho = \frac{M_W^2}{M_Z^2 \cos^2 \theta_W} = \frac{1 + \frac{2v_t^2}{v_d^2}}{1 + \frac{4v_t^2}{v_d^2}},$$

and thereby changing the ρ -parameter at the tree-level from its SM value $\rho = 1$. The electroweak precision measurements require the ρ -parameter to be very close to

unity 1.0004 ± 0.00024 [10]. This puts a severe restriction on the VEV of neutral CP -even component of the scalar triplet as, $v_t < 4$ GeV. In order to satisfy the neutrino mass, Y_ν should be $\mathcal{O}(10^{-9})$ for $v_t \sim \mathcal{O}(1)$ GeV. So in this limit, the explanation of neutrino masses is quite unnatural. In this case, the coupling of the new extra scalar particles to SM particles are not as small as in the previous case with $v_t \approx 10^{-9}$ GeV. The model benchmark points have been chosen with $v_t = 3$ GeV in Chapter 4.

At loop-level, the contributions of the scalar triplet with hypercharge $Y = 2$ to the S , T and U parameters are given by [32, 80],

$$\begin{aligned} S_{HTM}^{Y=2} &= -\frac{1}{3\pi} \ln \frac{m_{+1}^2}{m_{-1}^2} - \frac{2}{\pi} \sum_{T_3=-1}^{+1} (T_3 - Qs_W^2)^2 \xi \left(\frac{m_{T_3}^2}{m_Z^2}, \frac{m_{T_3}^2}{m_Z^2} \right), \\ T_{HTM}^{Y=2} &= \frac{1}{16\pi c_W^2 s_W^2} \sum_{T_3=-1}^{+1} (2 - T_3(T_3 - 1)) F \left(\frac{m_{T_3}^2}{m_Z^2}, \frac{m_{T_3-1}^2}{m_Z^2} \right), \\ U_{HTM}^{Y=2} &= \frac{1}{6\pi} \ln \frac{m_0^4}{m_{+1}^2 m_{-1}^2} + \frac{1}{\pi} \sum_{T_3=-1}^{+1} \left[2(T_3 - Qs_W^2)^2 \xi \left(\frac{m_{T_3}^2}{m_Z^2}, \frac{m_{T_3}^2}{m_Z^2} \right) \right. \\ &\quad \left. - (2 - T_3(T_3 - 1)) \xi \left(\frac{m_{T_3}^2}{m_W^2}, \frac{m_{T_3}^2}{m_W^2} \right) \right], \end{aligned}$$

where $m_{+1,0,-1} \equiv M_{H^{++}, H^+, H^0}$ and the function $\xi(x, y)$ is defined as [32],

$$\begin{aligned} \xi(x_1, x_2) &= \frac{4}{9} - \frac{5}{12}(x_1 + x_2) + \frac{1}{6}(x_1 - x_2)^2 \\ &\quad + \frac{1}{4} \left[x_1^2 - x_2^2 - \frac{1}{3}(x_1 - x_2)^3 - \frac{x_1^2 + x_2^2}{x_1 - x_2} \right] \ln \frac{x_1}{x_2} \\ &\quad - \frac{1}{12} \Delta(x_1, x_2) f(x_1, x_2). \end{aligned}$$

The definitions of Δ , f and F can be found in eqns. 3.14 and 3.15.

These parameters can be used for constraining the parameter space of this model from the electroweak precision data [33].

3.5.2.5 Constraints from the LHC

For $v_t \sim 1$ GeV, the direct search of $H^{\pm\pm}$ via $pp \rightarrow H^{++}H^{--}$, $H^{\pm\pm} \rightarrow W^{*\pm}W^{*\pm} \rightarrow$

$\mu^\pm \nu_\mu \mu^\pm \nu_\mu$ process at the LHC, puts a lower bound on $M_{H^{\pm\pm}} > 84$ GeV [81]. If constraints like the stability, unitarity, T -parameter and $\mu_{\gamma\gamma}$ at LHC are considered, then one can obtain the following lower bounds on the nonstandard scalar masses: $M_{H^+} > 130$ GeV, $M_{A,H} > 150$ GeV [82].

3.5.3 Dark matter in HTM ($Y = 2$)

If a discrete Z_2 symmetry is imposed on the triplet scalar such that the couplings of an *odd* number of scalar fields of the triplet with the SM particles are prohibited, then lightest of H and A can serve as a viable DM candidate which may saturate the measured DM relic density of the Universe. In this model, the dark matter candidate can annihilate to the SM particles via the exchange of a Higgs or a Z boson through s -channel diagrams and H , A and H^\pm mediated t - and u -channel diagrams. As the dark matter particle can interact with the nucleons through Higgs and Z mediated t -channel exchanges, the dark matter direct detection cross-sections rather large in this model. It was shown in Ref. [83], a significant portions of the parameter space is excluded [83] from direct detection experimental data from XENON and LUX.

3.6 Summary

In this chapter, several extensions of the scalar sector namely, SM+S, 2HDM, HTM with hypercharge $Y = 0, 2$ have been explored. At a time, it has been considered that one such extended sector as a new physics option beyond the SM. It is assumed that the electroweak symmetry breaking driven by the CP -even component the SM Higgs doublet and CP -even component of the extra scalar sector. In this case, both the CP -even scalar gets VEV and scalar field(s) of the extended sector can be mixed with the scalar fields of the SM Higgs doublet. The Goldstone boson, which is a combination of the scalar fields of the SM doublet and extra scalar sector, is the longitudinal component of corresponding vector boson. Also, it has been shown that the extra scalar fields can have direct couplings with the SM particles, or these may

get generated after the electroweak symmetry breaking. The other combinations become new physical scalar fields. It has been seen that depending on the isospin I and hypercharge Y , the models with extended scalar sectors have different numbers of neutral and charged scalar fields. Particle spectrum for different scalar extensions of the standard model has been calculated. For each extension of scalar sector of the standard model, various theoretical and phenomenological constraints have been shown. Using the above constraints, one can get allowed parameter space of these models. In this work, several benchmark points have been chosen, for which the vector boson scattering cross-section distributions with CM energy of these new models such as 2HDM, HTM with hypercharge $Y = 0, 2$ have been shown in Chapter 4. It has also been discussed in this chapter if one impose a discrete symmetry Z_2 on the extended scalar such that *odd* number of scalar fields do not couple with the SM particles then the lightest neutral scalar particle becomes stable. This scalar field can be taken as a dark matter candidate which may fulfill the relic abundance of the Universe that will be discussed in Chapter 6.

Chapter 4

Vector boson scattering in extended Higgs sector

4.1 Introduction

It has been discussed in the earlier Chapters that the measurement of properties of this scalar boson at Large Hadron Collider (LHC), is consistent with the minimal choice of the scalar sector, consisting of a single complex doublet. However, the data still allow an extended scalar sector, which, in turn, can accommodate a more elaborate mechanism for the EWSB. One immediate extension of this kind is the presence of either additional scalar doublet(s) or higher multiplet(s) of $SU(2)_L$. Even a marginal role of such scalars can in principle be probed in the upcoming experiments, utilizing their interaction with the electroweak gauge bosons.¹

If indeed there are additional scalars that couple with the W -and Z -bosons, longitudinal vector boson scattering (VBS) including scalar exchanges should provide a complementary way to direct search methods to probe into the scalar sector. In the SM, the Higgs boson helps preserve the unitarity of the S -matrix for the longitudinal electroweak vector boson scattering $V_L V_L \rightarrow V_L V_L$. The Higgs boson mediated diagram precisely cancels the residual s -dependence (where \sqrt{s} denotes the energy in

¹It should be noted that the new scalars may not always participate in the EWSB, *e.g.* as in the inert scalar model [15, 36].

the center-of-mass frame), thus taming the high energy behavior of the cross-section appropriately [84]. With an extended scalar sector, the preservation of unitarity could be a more complex process. Several factors then modify the \sqrt{s} -dependence of the $V_L V_L$ scattering. The first of these is the modification, albeit small, of the strength of the 125 GeV scalar to gauge boson pairs. Secondly, the extent of the influence of other scalars present in an extended scenario depends on their gauge quantum numbers and on the theoretical scenario in general. Thirdly, the observed mass of the 125 GeV scalar makes it kinematically impossible for it to participate as an s -channel resonance in $V_L V_L$ scattering processes. However, such resonant peaks may in general occur when heavier additional scalars enter into the arena.

One can thus expect that the \sqrt{s} -dependence of $V_L V_L$ scattering cross-sections will be modified with respect to SM-expectations as a result of the above effects. Such modifications have been formulated in terms of certain general parameters in some recent studies [85–88]. An apparent non-unitarity of the scattering matrix may be noticed here when the SM-like scalar with modified interaction strength is participating as the only scalar. However, unitarity is restored once the complete particle spectrum is taken into consideration. We emphasize here that the three effects mentioned above leave the signature of the specific non-standard EWSB sector in the modified energy-dependence, as long as the new scalars have their masses within or about the TeV-range.

To further elaborate our point, the purpose of writing this chapter is twofold. Using resonances at various $V_L V_L$ (where $V \equiv W^\pm$ or Z) scattering processes, we illustrate that it may be possible to distinguish between different extensions of the scalar sector, once the high-energy run of the LHC continues long enough. The shapes of the energy-dependence curves, especially the presence of resonant peaks, can shed light on the relevant scalar spectra of these models. We use for illustration some popular extensions like the Type-II two Higgs doublet model (2HDM) and real as

well as complex Higgs triplet models (HTM). It is shown in the ensuing study how the \sqrt{s} -dependence of the cross-sections reflect the characteristics of each of these scenarios so long as the additional scalars lie within about 2 TeV. This supplements rather faithfully other LHC-based phenomenology, and thus spurs the improvement of techniques to extract the dependence of $V_L V_L$ scattering cross-sections on \sqrt{s} . The other goal is to present analytical expressions for $V_L V_L$ scattering amplitudes in these otherwise well-motivated models. To the best of our knowledge, these full expressions have not yet been presented in the literature.

4.2 Polarization of Vector Bosons

To handle the electroweak sector, one of the main focus of this work is the polarization of the massive vector bosons W^\pm and Z . In this section, the longitudinal and transverse modes of the vector bosons will be defined.

The Lagrangian of a vector boson fields with mass m is given by,

$$\mathcal{L} = -\frac{1}{4}F^{\mu\nu}F_{\mu\nu} - \frac{m^2}{2}A^\mu A_\mu. \quad (4.1)$$

This Lagrangian is not gauge invariant because the mass term violates the $U(1)$ symmetry. The field strength tensor is given by, $F^{\mu\nu} = \partial^\mu A^\nu - \partial^\nu A^\mu$. Using the Euler-Lagrange equation $\partial^\mu \left(\frac{\partial \mathcal{L}}{\partial^\mu A^\nu} \right) - \frac{\partial \mathcal{L}}{\partial A^\nu} = 0$, the equation of motion of the gauge fields can be obtained for Lagrangian of eqn. 4.1 as,

$$-\partial^\mu F_{\mu\nu} - m^2 A_\nu = 0. \quad (4.2)$$

In the momentum space, these equations can be written as,

$$-p^2 A_\nu + p_\nu p^\mu A_\mu - m^2 A_\nu = 0.$$

Now multiply this equation with p^ν to get,

$$\begin{aligned} -p^2 p^\nu A_\nu + p^2 p^\mu A_\mu - m^2 p^\nu A_\nu &= 0 \\ \Rightarrow p^\nu A_\nu &= 0. \end{aligned}$$

This reduces the numbers of independent components of the polarization vector of a massive vector boson to three.

For the massless field, one write eqn. 4.2 as,

$$\partial^\mu F_{\mu\nu} = 0 \Rightarrow p^2 A_\nu - p_\nu p^\mu A_\mu = 0. \quad (4.3)$$

These are the Maxwell equations which also give, $p^\mu A_\mu = 0$, i.e., three degrees of freedom remains for a massless vector field. Masslessness of the photon demands the corresponding Lagrangian is invariant under a gauge transformation,

$$A_\mu \rightarrow A_\mu + \partial_\mu f, \quad (4.4)$$

where f is an function that satisfies $\square^2 f = 0$. Now, one can choose f such that $A_0(p) = 0$, which is not possible for massive vector fields. So for the massless photon, we have an extra constraint on the vector fields due to the gauge invariance. Thus, the photon has only two polarization vectors which are transverse to the three-momentum of the photon.

Now the polarization vector will be calculated in terms of momentum and energy for a massive vector boson. The components of the polarization vector in x -, y -, and z -directions are chosen as,

$$\begin{aligned} \epsilon_x^\mu &= (0, 1, 0, 0), \\ \epsilon_y^\mu &= (0, 0, 1, 0), \\ \epsilon_z^\mu &= (x_1, x_2, x_3, x_4). \end{aligned}$$

The polarization vector follows,

$$\epsilon_i \cdot \epsilon_j = -\delta_{ij}, \quad \text{and} \quad p \cdot \epsilon(p) = 0, \quad (4.5)$$

where $p_\mu = (E, p_x, p_y, p_z)$ is the four momentum of the vector boson. Using eqn. 4.5, we get, $x_2 = x_3 = 0$ and,

$$\begin{aligned} \epsilon_z \cdot \epsilon_z = -1 &\Rightarrow x_1^2 - x_4^2 = -1, \\ p \cdot \epsilon(p) = 0 &\Rightarrow p_x = 0, p_y = 0 \text{ and } x_4 = \frac{E}{p_z} x_1. \end{aligned}$$

Thus, we get $x_1 = \frac{|\mathbf{p}|}{m}$, with $|\mathbf{p}| = \sqrt{p_x^2 + p_y^2 + p_z^2}$ and $x_4 = \frac{E}{m}$. The polarization vector along the z -axis can be written as,

$$\epsilon_z = \left(\frac{|\mathbf{p}|}{m}, \frac{E}{m} \hat{p} \right). \quad (4.6)$$

This is the longitudinal component and the combinations $\epsilon^\pm = \frac{1}{\sqrt{2}}(\epsilon_x \pm i\epsilon_y)$ are the transverse components of the polarization vector corresponding to a massive vector.

From the above, it is evident that the longitudinal polarization of vector bosons grows with energy, whereas transverse components are independent of energy. Hence, at high energies $E \gg m$ one expects that longitudinal mode of the gauge bosons dominates over transverse modes. This is the difference between the longitudinal and transverse components of the gauge bosons.

4.3 Connection with Electroweak Symmetry Breaking

In the SM, after EWSB the charged scalar fields G^\pm and G^0 of the scalar doublet are eaten by the W^\pm and Z gauge bosons respectively, which become massive and also gain a third, longitudinal polarization. The longitudinal component of massive gauge boson is a Goldstone scalar field that belongs to the SM doublet. So through vector bosons scattering one can explore the Higgs sector.

In the extended scalar sectors such as doublet-, or triplet-extensions, one of the linear combination of charged scalar fields is eaten by the W boson which becomes massive, other combinations of fields become massive charged scalar fields. Similarly, a combination of pseudo scalars become the longitudinal part of massive Z gauge boson and the other combinations survive as physical pseudoscalars. One can use VBS processes to find the nature of the electroweak symmetry breaking in the presence of these extra scalars. In future colliders, if we find any direct signature of the extended scalar sector then this study will supplement our knowledge about these scalars obtained from direct searches.

In the following section, the study of the scattering cross-section using the partial wave analysis will be reviewed.

4.4 Scattering cross-section: Partial Wave Analysis

Let us consider a mono-energetic beam of particles being scattered by a target located at $(0, 0, 0)$. We will work here in the spherical coordinate system,

$$(r \sin \theta \cos \phi, r \sin \theta \sin \phi, r \cos \theta)$$

It is assumed that the detector covers a solid angle $d\Omega = \sin \theta d\theta d\phi$ in the direction (θ, ϕ) from the scattering center and the incoming beam travels along the z -axis.

The wave vector is given by,

$$\vec{k} = \frac{\sqrt{2mE}}{\hbar} \hat{z},$$

where E is the energy of the incident beam. The number of particles per unit time entering the detector is $N d\Omega$. The differential cross-section can be written as,

$$\frac{d\sigma}{d\Omega} = \frac{dn}{F_{in}}, \quad (4.7)$$

which is defined as the number dn of particles scattered into the direction (θ, ϕ) per unit time, per unit solid angle, normalized by the incident flux. Here F_{in} is the incident flux of the beam, which is defined as the number of particles per unit time, crossing a unit area placed normal to the direction of incidence. In the next, we will calculate the differential cross-section.

The plane wave of the incident particles are defined as $\psi = Ae^{ikz}$, with normalization A . The wave encounters a scattering potential producing an outgoing spherical wave. At large distances from the scattering center, one can decompose the wave function $\psi(r)$ into a part e^{ikz} describing the incident beam and a part ψ_{sc} for the scattered particles. As the collision is elastic, i.e., the energies of the incident and scattered particle are the same, one can write the wave function as,

$$\psi(r) \Big|_{r \rightarrow \infty} \approx e^{ikz} + \underbrace{f(\theta, \phi) \frac{e^{ikr}}{r}}_{\psi_{sc}}. \quad (4.8)$$

The function $f(\theta, \phi)$ represents the amplitude of the scattering and depends on the interaction of the incident particles. For momentum dependent coupling between

particles, the function f is expressed as $f \equiv f(k, \theta, \phi)$ to include dependence on the incident energy and momentum of the particles. If the target is azimuthally symmetric then f is independent of ϕ , thus $f \equiv f(k, \theta)$.

The current density is associated with the wave function, ψ , is given by,

$$\vec{J} = \frac{\hbar}{2m} [\psi^* \vec{\nabla} \psi - \psi \vec{\nabla} \psi^*] = \frac{1}{m} \text{Re} \left[\frac{\hbar}{i} \psi^* \vec{\nabla} \psi \right]. \quad (4.9)$$

Using eqn. 4.9, we can calculate both the incident flux and the number of scattered particles. The incident flux F_{in} with probability constant C , is given by,

$$F_{in} = C J_{in} = C \frac{\hbar k}{m}.$$

The scattered particle current density can be written as,

$$J_{sc} = \frac{1}{m} |f(\theta, \phi)|^2 \frac{\hbar k}{r^2}. \quad (4.10)$$

The number of scattered particles crossing the area $\vec{ds} = ds \hat{r}$ is given by,

$$\begin{aligned} dn &= C \vec{J}_{sc} \cdot \vec{ds} \\ &= C \frac{\hbar k}{m} |f(\theta, \phi)|^2 d\Omega \\ &= F_{in} |f(\theta, \phi)|^2 d\Omega, \end{aligned}$$

where $d\Omega = \frac{ds}{r^2}$ the solid angle subtended by the area ds . Comparing the above equation with eqn. 4.7, we get the differential cross-section as,

$$\frac{d\sigma}{d\Omega} = \frac{dn}{F_{in}} = |f(\theta, \phi)|^2.$$

The function, $f(\theta, \phi)$, actually gives us information about the probability amplitude for scattering processes in a direction (θ, ϕ) . In the following, the Schrödinger equation of the scattering particles will be solved to find the scattering amplitude.

Let us consider a target of fixed central potential $V(r)$. The angular momentum \vec{L} of the particles is constant under the central potential. There exists a stationary state which is a common eigenstate of the operator Hamiltonian H , angular momentum \vec{L} and z -component of angular momentum (L_z). We can write the wave function as ψ_{nlm} . This can be written as,

$$\psi_{nlm} = R_l(r) Y_l^m(\theta, \phi).$$

As we have considered the azimuthal symmetry, the above equation is independent of ϕ , i.e., $m = 0$. The spherical harmonics are then given by,

$$Y_l^0(\theta, \phi) = \sqrt{\frac{2l+1}{4\pi}} P_l(\cos \theta).$$

Let us now solve the radial part of the wave function. From the Schrödinger equation of the wave function ψ ,

$$\left[-\frac{\hbar^2}{2m} \nabla^2 + V(r) \right] \psi = E\psi$$

one gets,

$$\begin{aligned} \left[\frac{d^2}{dr^2} + \frac{2}{r} \frac{d}{dr} - \left\{ \frac{l(l+1)}{r^2} + \frac{2m}{\hbar^2} V(r) - k^2 \right\} \right] R_l(r) &= 0 \\ \Rightarrow \frac{d^2(rR_l(r))}{dr^2} - \left[\frac{l(l+1)}{r^2} + \frac{2m}{\hbar^2} V(r) - k^2 \right] (rR_l(r)) &= 0. \end{aligned}$$

The solution of the radial part $R_l(r)$ of the wave function can be written as,

$$R_l(r) = J_l j_l(kr) + N_l \eta_l(kr)$$

where $j_l(kr)$ and $\eta_l(kr)$ are the Bessel and Neumann functions. J_l and N_l are the normalization constants, independent of r . The scattering potential is assumed to be short-ranged, i.e., $V(r) \rightarrow 0$ at large distance r and the particles are free from the scattering potential. In the free region, $r \rightarrow \infty$, the Bessel and Neumann functions can be written as,

$$\lim_{r \rightarrow \infty} j_l(kr) \rightarrow \frac{\sin(kr - \frac{l\pi}{2})}{kr} \quad \text{and} \quad \lim_{r \rightarrow \infty} \eta_l(kr) \rightarrow \frac{\cos(kr - \frac{l\pi}{2})}{kr}. \quad (4.11)$$

Using eqns. 4.11, one gets the radial part of the wave function ψ ,

$$\lim_{r \rightarrow \infty} R_l(r) = C_l \frac{\sin(kr - \frac{l\pi}{2} + \delta_l)}{kr}.$$

The normalization constant C_l and phase δ_l are related with the J_l and N_l as,

$$C_l = \sqrt{J_l^2 + N_l^2} \quad \text{and} \quad \delta_l = -\frac{N_l}{J_l}.$$

$R_l(r)$ can be written in the form of incoming and outgoing waves as,

$$\begin{aligned} R_l(r) &\rightarrow \frac{1}{kr} C_l \frac{e^{(kr - \frac{l\pi}{2} + \delta_l)} - e^{-(kr - \frac{l\pi}{2} + \delta_l)}}{2i} \\ &= \frac{1}{2ikr} C_l e^{-i\delta_l} e^{-\frac{l\pi}{2}} (e^{kr} e^{2i\delta_l} - i^l e^{-kr}). \end{aligned}$$

The solution of the wave function of the free particle is given by

$$\psi_{nlm} = \frac{1}{2ikr} \sum_{l=0}^{\infty} C_l e^{-i\delta_l} e^{-\frac{l\pi}{2}} (e^{kr} e^{2i\delta_l} - i^l e^{-kr}) P_l(\cos \theta). \quad (4.12)$$

The wave function $\psi = e^{ikz}$ is independent of azimuthal angle ϕ so that only the Y_{lm} with $m = 0$, which are proportional to the Legendre polynomials $P_l(\cos \theta)$, can contribute to the expansion as,

$$\begin{aligned} e^{ikz} &= \sum_{l=0}^{\infty} i^l (2l+1) j_l(kr) P_l(\cos \theta) \\ &= \sum_{l=0}^{\infty} i^l (2l+1) \frac{\sin(kr - \frac{l\pi}{2})}{kr} P_l(\cos \theta), \quad \text{as } r \rightarrow \infty \\ &= \frac{1}{2ikr} \sum_{l=0}^{\infty} (2l+1) e^{-\frac{l\pi}{2}} (e^{kr} - i^l e^{-kr}) P_l(\cos \theta). \end{aligned} \quad (4.13)$$

Using eqn. 4.13 in eqn. 4.8, we get the wave function of the scattered particles as,

$$\begin{aligned} \psi(r) \Big|_{r \rightarrow \infty} &\approx e^{ikz} + f(\theta, \phi) \frac{e^{ikr}}{r} \\ &= \frac{1}{2ikr} \sum_{l=0}^{\infty} (2l+1) e^{-\frac{l\pi}{2}} (e^{kr} - i^l e^{-kr}) P_l(\cos \theta) + f(\theta, \phi) \frac{e^{ikr}}{r}. \end{aligned} \quad (4.14)$$

Comparing eqn. 4.12 and eqn. 4.14, one can get, $C_l = i^l (2l+1) e^{i\delta_l}$ and,

$$\begin{aligned} f(\theta, \phi) &= \frac{1}{2ik} \sum_{l=0}^{\infty} (2l+1) (e^{2i\delta_l} - 1) P_l(\cos \theta) \\ &= \frac{1}{k} \sum_{l=0}^{\infty} (2l+1) a_l P_l(\cos \theta). \end{aligned} \quad (4.15)$$

One can find a_l from the above equations as,

$$a_l = e^{2i\delta_l} - 1 = e^{i\delta_l} \sin \delta_l. \quad (4.16)$$

The real and imaginary part of a_l follows equation of the unitary circle (Fig. 4.1) as,

$$|a_l| \leq 1 \Rightarrow [Re(a_l)]^2 + \left[Im(a_l) - \frac{1}{2}\right]^2 \leq \left(\frac{1}{2}\right)^2. \quad (4.17)$$

So the scattering amplitude obeys the unitarity conditions. In the previous discussions, the quantum mechanical scattering cross-section has been calculated using the method of partial wave analysis. How this quantum mechanical scattering amplitude $f(\theta, \phi)$ is related to the Feynman amplitude in Quantum Field Theory (QFT)

will be shown now.

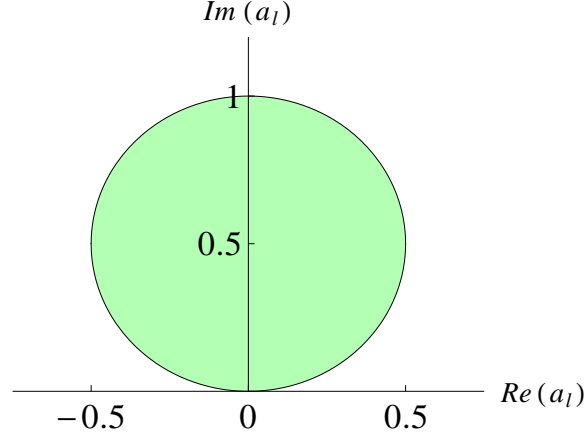


Figure 4.1: Argand diagram of the function a_l in $Re(a_l) - Im(a_l)$ plane is a unitary circle with radius 0.5.

Let us consider a scattering process for which the Feynman amplitude \mathcal{M} can be expressed as a function of CM energy \sqrt{s} and scattering angle θ or equivalently, of the Lorentz-invariant Mandelstam variables s , t and u . The differential cross-section is defined as,

$$\frac{d\sigma}{d\Omega} = \frac{1}{64\pi^2 s} |\mathcal{M}|^2 = |f(\theta, \phi)|^2, \quad (4.18)$$

where \mathcal{M} is the Feynman amplitude. Comparing with eqn. 4.15 one can write the following relation as,

$$\mathcal{M} = 16\pi \sum_{l=0}^{\infty} (2l+1) a_l P_l(\cos \theta). \quad (4.19)$$

Using eqn. 4.19 and putting into eqn. 4.18,

$$\begin{aligned} \frac{d\sigma}{d\Omega} &= \frac{1}{64\pi^2 s} (16\pi)^2 \sum_{l=0}^{\infty} (2l+1)^2 |a_l|^2 [P_l(\cos \theta)]^2 \\ &= \frac{4}{s} \sum_{l=0}^{\infty} (2l+1)^2 |a_l|^2 [P_l(\cos \theta)]^2. \end{aligned}$$

Now we get the total cross-section after integrating the differential cross-section over the solid angle ($d\Omega = -2\pi d(\cos \theta)$),

$$\sigma = \frac{8\pi}{s} \sum_{l=0}^{\infty} (2l+1)^2 |a_l|^2 \times \int_{-1}^1 [P_l(\cos \theta)]^2 d(\cos \theta)$$

$$\begin{aligned}
&= \frac{8\pi}{s} \sum_{l=0}^{\infty} (2l+1)^2 |a_l|^2 \times \frac{2}{(2l+1)} \\
&= \frac{16\pi}{s} \sum_{l=0}^{\infty} (2l+1) |a_l|^2.
\end{aligned} \tag{4.20}$$

Multiplying both sides of eqn. 4.19 with $P_l(\cos \theta)$ and integrating with respect to $\cos \theta$ from -1 to $+1$, one gets,

$$a_l = \frac{1}{32} \int_{-1}^{+1} \mathcal{M}(\theta) P_l(\cos \theta) d(\cos \theta). \tag{4.21}$$

where a_l are the partial wave coefficients corresponding to specific angular momentum values l . If the amplitude at tree level increases with energy then the unitary bound is violated after certain energy, then the theory becomes sick and can indicate the incompleteness of theory.

In the SM, various vector bosons scattering processes such as $W_L^\pm W_L^\mp \rightarrow W_L^\pm W_L^\mp$, $W_L^\pm W_L^\pm \rightarrow W_L^\pm W_L^\pm$, $W_L^\pm W_L^\mp \rightarrow Z_L Z_L$, $W_L^\pm Z_L \rightarrow W_L^\pm Z_L$ and $Z_L Z_L \rightarrow Z_L Z_L$ have been reviewed. It has been checked that without a Higgs boson, the unitarity condition is not fulfilled at high energies. The inclusion of Higgs-mediated diagrams restores unitarity rather spectacularly. Any extended scalar sector is in general expected to satisfy the unitarity condition, unless one can come to terms with strongly coupled physics controlling electroweak interactions at high energy. Thus the $V_L V_L$ scattering cross-sections in a ‘well-behaved’ new physics scenario should fall at high center-of-mass energies. However, if the scattering process involves the participation of an s -channel resonance at mass M , then one expects a peak at $\sqrt{s} = M$, above which the cross-section should die down gradually. The energy-dependence of the cross-sections, along with the appearance (or otherwise) of such resonant peaks should thus be computed if one has to verify the imprints of new physics in VBS when the appropriate measurements are feasible.

In this work, the amplitudes have been calculated in different models, using the exact expressions for polarization vectors (see appendix A.1), as we are dealing

with the energy range ($\sim 200 \text{ GeV} \rightarrow 2000 \text{ GeV}$). However, we have checked that at the high-energy limit, our results are consistent with calculations based on the equivalence theorem.

4.5 Benchmark points in different models for $V_L V_L$ scattering

In the Chapter 3 detailed theoretical and experimental constraints on extended scalar sectors namely type-II 2HDM, HTM ($Y = 0$), and HTM ($Y = 2$) had been discussed. Measurements of the couplings at LHC of SM-like Higgs with the vector bosons (see table 1.2 of Chapter 1) put indirect constraints on the models with an extended scalar sector. For example, a charged Higgs can contribute to $h\gamma\gamma$ at one loop. In our analysis, the heavier scalars are taken to be heavy so that $h\gamma\gamma$ constraints are not that important. hWW and hZZ coupling measurements at present agrees with SM values, thereby restricting couplings of the heavier scalars appreciably. As a result, 2HDM is pushed towards the alignment regime where couplings of heavier Higgs bosons with SM gauge bosons tend to vanish. We have taken care of all such constraints at 1σ in our analysis.

Benchmark points used for $V_L V_L$ scattering:

type-II 2HDM:

- (i) $\cos(\beta - \alpha) = 0.04$, $M_{H^\pm} \simeq M_H = 500 \text{ GeV}$, $\Gamma_{H^\pm} = 3.6 \text{ GeV}$, $\Gamma_H = 7 \text{ GeV}$
- (ii) $\cos(\beta - \alpha) = 0.08$, $M_{H^\pm} \simeq M_H = 500 \text{ GeV}$, $\Gamma_{H^\pm} = 3.7 \text{ GeV}$, $\Gamma_H = 6.7 \text{ GeV}$
- (iii) $\cos(\beta - \alpha) = 0.02$, $M_{H^\pm} \simeq M_H = 1500 \text{ GeV}$, $\Gamma_{H^\pm} = 25.4 \text{ GeV}$, $\Gamma_H = 26.8 \text{ GeV}$
- (iv) $\cos(\beta - \alpha) = 0.04$, $M_{H^\pm} \simeq M_H = 1500 \text{ GeV}$, $\Gamma_{H^\pm} = 101.9 \text{ GeV}$, $\Gamma_H = 106.7 \text{ GeV}$

HTM ($Y = 0$):

- (i) $\sin \gamma = 0.023$, $v'_t = 3 \text{ GeV}$, $M_{H^\pm} \simeq M_H = 500 \text{ GeV}$, $\Gamma_{H^\pm} = 0.167 \text{ GeV}$, $\Gamma_H = 0.12$

GeV

(ii) $\sin \gamma = 0.024$, $v'_t = 3$ GeV, $M_{H^\pm} \simeq M_H = 1500$ GeV, $\Gamma_{H^\pm} = 5.8$ GeV, $\Gamma_H = 4.8$ GeV

HTM ($Y = 2$):

(i) $\sin \gamma' = 0.025$, $v_t = 3$ GeV, $M_{H^{\pm\pm}} \simeq M_{H^\pm} \simeq M_H = 500$ GeV, $\Gamma_{H^{\pm\pm}} = 0.0001$ GeV, $\Gamma_{H^\pm} = 0.006$ GeV, $\Gamma_H = 0.023$ GeV

(ii) $\sin \gamma' = 0.024$, $v_t = 3$ GeV, $M_{H^{\pm\pm}} \simeq M_{H^\pm} \simeq M_H = 1500$ GeV, $\Gamma_{H^{\pm\pm}} = 0.0002$ GeV, $\Gamma_{H^\pm} = 0.023$ GeV, $\Gamma_H = 0.635$ GeV

N.B.: The similar notations have been followed for the above models as in the Chapter 3.

4.6 $V_L V_L$ scattering with extended scalar sectors

Next, we demonstrate how it is possible to distinguish among 2HDM, HTM ($Y = 0$) and HTM ($Y = 2$) using the five VBS processes: $W_L^+ W_L^- \rightarrow W_L^+ W_L^-$, $W_L^+ W_L^- \rightarrow Z_L Z_L$, $Z_L Z_L \rightarrow Z_L Z_L$, $W_L^+ W_L^+ \rightarrow W_L^+ W_L^+$ and $W_L^+ Z_L \rightarrow W_L^+ Z_L$. One can immediately see that the mediating scalar can be a neutral scalar, as also a singly or doubly charged Higgs. Thus the very constituents of 2HDM or triplet scenarios are potential players in the game.

Two things turn out to be crucial here: (a) nature of the energy-dependence, and (b) the center-of-mass energy at which the resonances occur. The shape of the resonance depends on the decay width, and hence, on the mass and the coupling of the resonating scalar. Thus an identification of the resonance can guide one to the theoretical scenario including the particle spectrum.

In any model with an extended scalar sector around a TeV, the very fact that the VVh interactions ($V \equiv W, Z$ and $h \equiv$ the 125 GeV scalar) are largely SM-like makes the non-resonant additional contributions small. In 2HDM, however, these

constraints allow enough parameter space for the heavier scalars to have a large decay width so that the effect of resonances can be felt for a wider range of \sqrt{s} . In HTM models, however, this is not the case and the resonances are narrow.

For a 2HDM scenario, the lighter CP -even scalar in the particle spectrum is usually interpreted as the SM-like Higgs. Going especially by the rate of decays into pairs of gauge bosons, the couplings of this state is expected to be ‘nearly SM-like’, implying that a 2HDM can be feasible largely in the ‘alignment limit’. Recent LHC data are by and large consistent with this limit [89]. Hence we have performed our analysis almost in that limit. Among the five scattering modes, we have resonant peaks for only three channels, namely, $W_L^+ W_L^- \rightarrow W_L^+ W_L^-$, $W_L^+ W_L^- \rightarrow Z_L Z_L$ and $Z_L Z_L \rightarrow Z_L Z_L$ (see Fig. 4.2) involving the heavier CP -even Higgs H . We have set its mass M_H of at two benchmark values (500 GeV and 1500 GeV) which are given in Section 4.5. The corresponding decay widths (Γ_H) can also be read off from the resonance peaks in Fig. 4.2. Using the high-energy scattering amplitudes given in Appendices A.1 and A.3, we should be able to predict the shapes of plots which contain such resonance peaks. It is quite evident from the plots, that apart from the occurrence of the peaks, the cross-sections are almost SM-like, as expected in the alignment limit.

Let us decompose the aforementioned amplitude² as $\mathcal{M} = \mathcal{M}_{gauge,h} + \mathcal{M}_H$, where \mathcal{M}_H is proportional to $1/(E_{CM}^2 - M_H^2)$. When $E_{CM} < M_H$, the H mediated diagram interferes constructively with the remaining terms, due to which the interference contributions to cross-section increases with energy. On the other hand, for $E_{CM} > M_H$, \mathcal{M}_H interferes destructively, and hence its contribution to the cross-section decreases. In the high-energy limit ($E_{CM} \gg M_H$), the amplitudes can be expressed as a power series in the energy (see eqn. A.9 of Appendix A.3). In this limit the terms

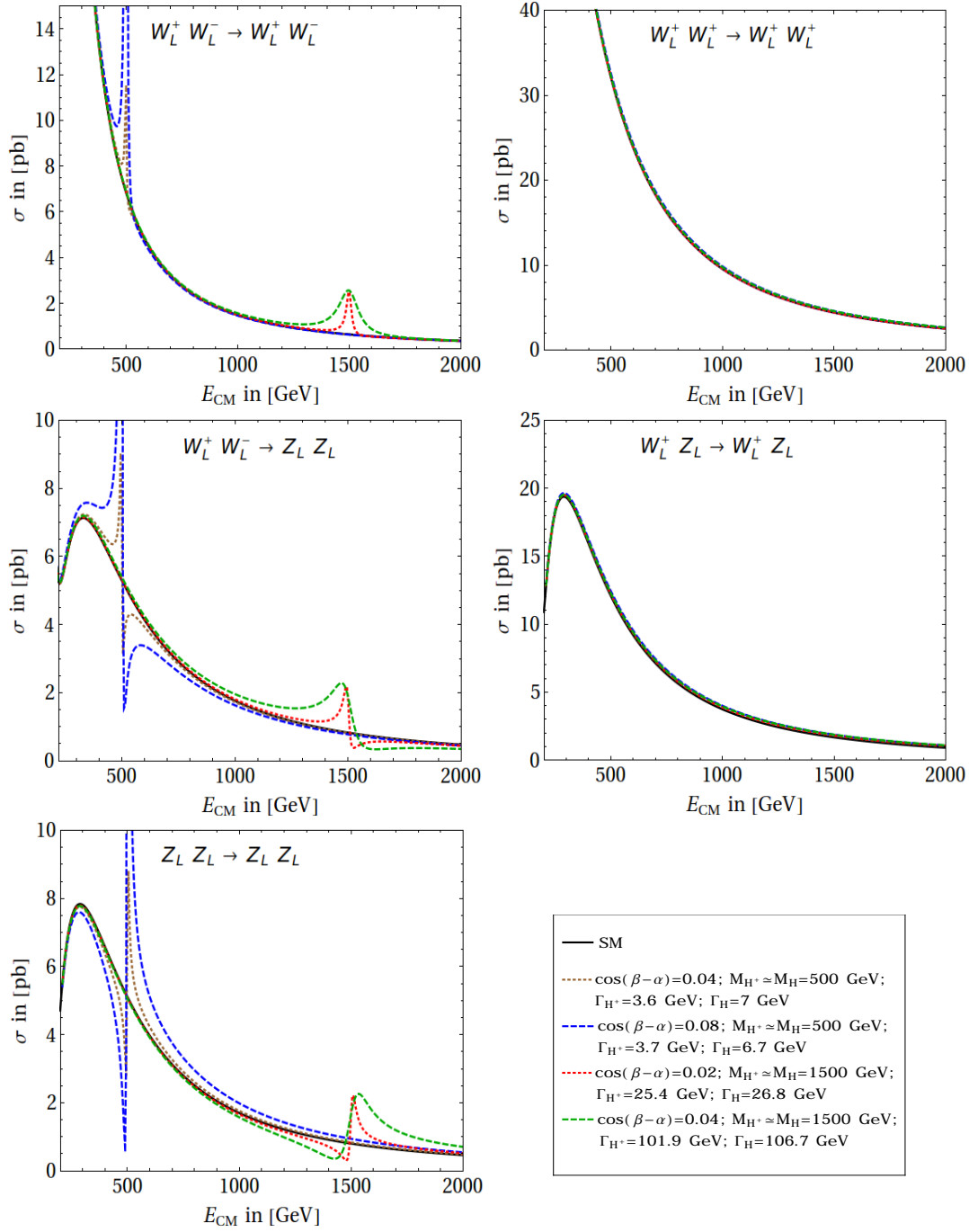
²This decomposition is not relevant for $Z_L Z_L \rightarrow Z_L Z_L$, since in this process there is no gauge boson mediated Feynman diagram.

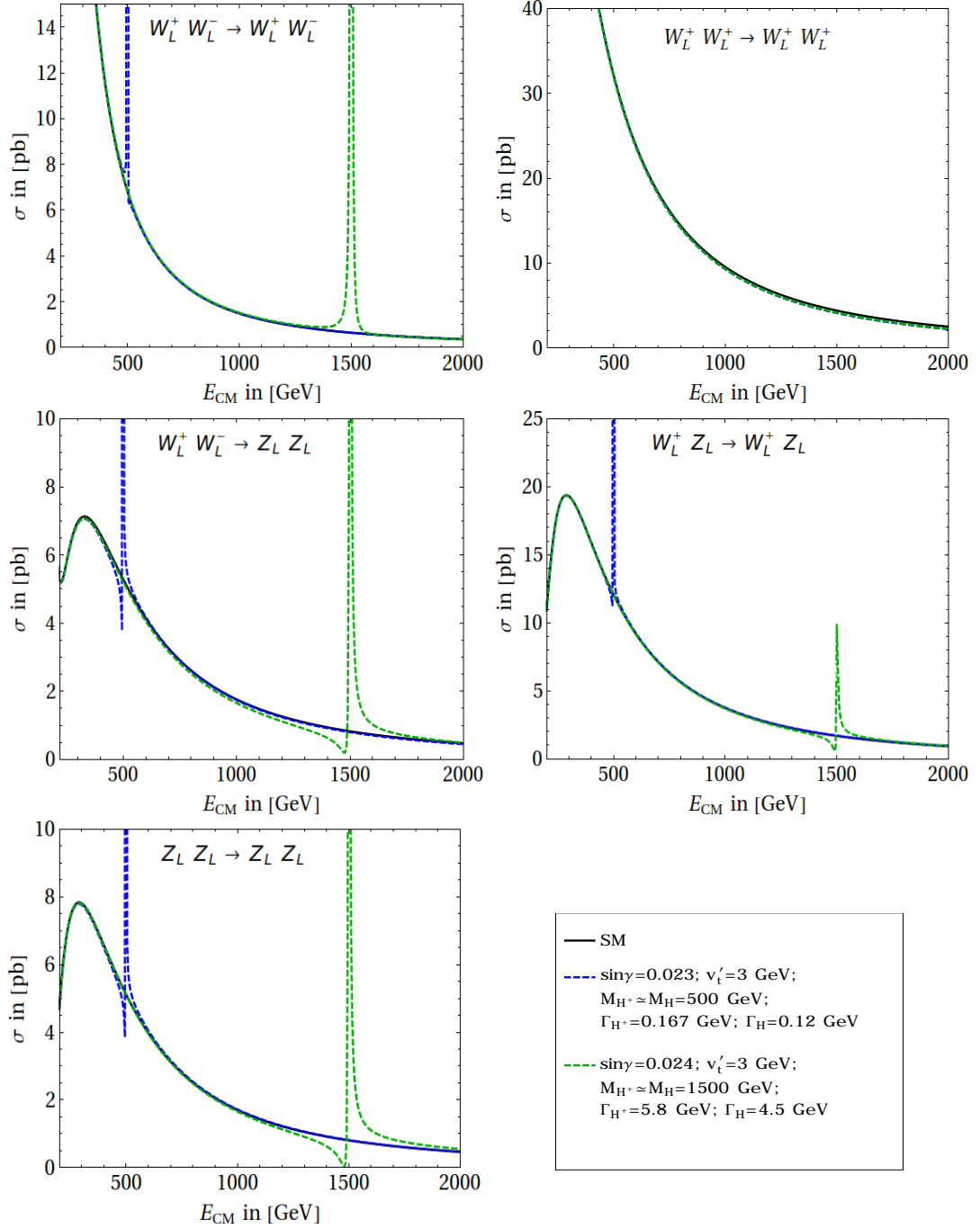
proportional E_{CM}^4 as well as E_{CM}^2 of the amplitude become zero. The remaining terms are either independent of energy or go in negative powers of energy, so that the cross-section decreases with rising energy, thus ensuring perturbative unitarity. It has been seen that in expansion of $|\mathcal{M}|^2$, square of the term \mathcal{M}_H which containing the factor $\frac{\Gamma_H^2 M_H^2}{(E_{CM}^2 - M_H^2)^2 + \Gamma_H^2 M_H^2}$, is always larger than the interference term that contains $\frac{(E_{CM}^2 - M_H^2)}{(E_{CM}^2 - M_H^2)^2 + \Gamma_H^2 M_H^2}$ near the pole. However, depending on the relative magnitudes of $\mathcal{M}_{gauge,h}$ and \mathcal{M}_H , the interference term may dominate over $|\mathcal{M}_H|^2$ away from the pole. It should be also noted here that due to the absence of $W^\pm Z H^\pm$ couplings in 2HDM, there are no Feynman diagrams mediated by H^\pm (s -channel) for $W_L^+ Z_L \rightarrow W_L^+ Z_L$. Moreover, 2HDM does not contain $H^{\pm\pm}$ which can mediated the process $W_L^+ W_L^+ \rightarrow W_L^+ W_L^+$. Therefore, for 2HDM we have no peaks for these two processes. The cross-sections for these processes are also similar to that of SM, due to the feeble coupling strength of H with gauge bosons.

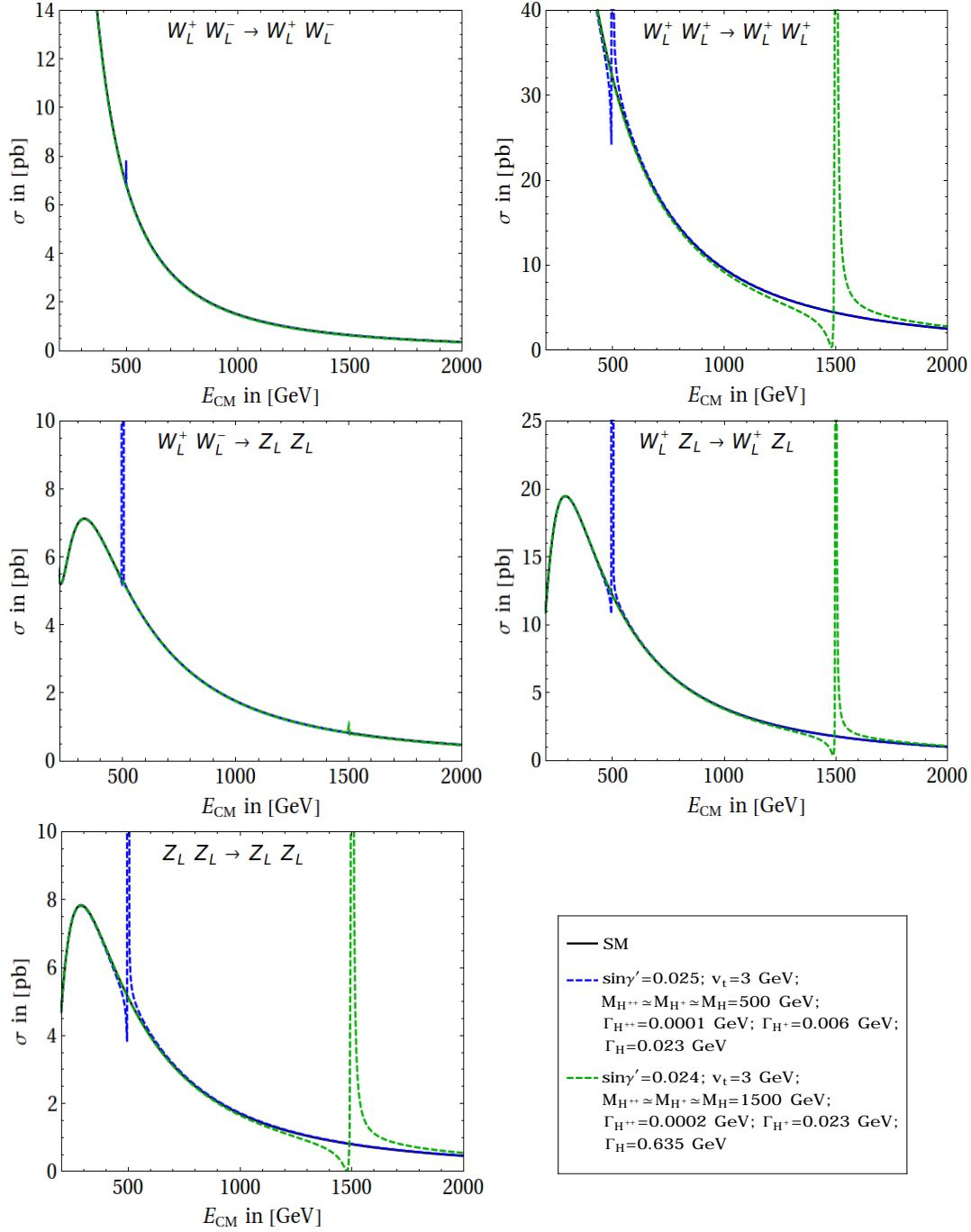
As has been mentioned already, we have also studied triplet models with two different values of the $U(1)$ hypercharge ($Y = 0$ and 2). In these models we can have interactions of charged scalars with pairs of gauge bosons.

Of these, we primarily focus on a $Y = 2$ HTM. This scenario is relevant in the context of the type-II seesaw mechanism of neutrino mass generation, and it also arises in left-right symmetric gauge theories. Now the question is how to isolate such a scenario from a $Y = 0$ HTM or even a type-II 2HDM models? our findings will be summarized in Table 5.1 which clearly indicates that HTM ($Y = 0$) and 2HDM can be distinguished via a s -channel H^+ resonance in $W_L^+ Z_L \rightarrow W_L^+ Z_L$ scattering process, as H^+ couples to W^+ and Z only in the triplet models.

The other aspect which might help in such a distinction is the width of the resonances: In 2HDM the allowed parameter space allows for a wider resonance than that in the HTM models. But width of the resonances does not help in identifying the hypercharge of the scalar triplet.

Figure 4.2: Plots for VV scattering in 2HDM.

Figure 4.3: *Plots for VV scattering in $Y=0$, HTM.*

Figure 4.4: Plots for VV scattering in $Y=2$, HTM.

Process	2HDM	HTM($Y = 0$)	HTM($Y = 2$)
$W_L^+ W_L^- \rightarrow W_L^+ W_L^-$	✓, (H)	✓, (H)	✓, (H)
$W_L^+ W_L^+ \rightarrow W_L^+ W_L^+$	✗	✗	✓, (H^{++})
$W_L^+ W_L^- \rightarrow Z_L Z_L$	✓, (H)	✓, (H)	✓, (H)
$W_L^+ Z_L \rightarrow W_L^+ Z_L$	✗	✓, (H^+)	✓, (H^+)
$Z_L Z_L \rightarrow Z_L Z_L$	✓, (H)	✓, (H)	✓, (H)

Table 4.1: *Different scattering processes and corresponding mediator particles for resonance in various extended scalar sectors. “✓” indicates presence of a resonance where as “✗” corresponds to no resonance peak.*

As HTM ($Y = 2$) contains a H^{++} that can couple to a pair of W^+ , in contrast to the 2HDM and HTM ($Y = 0$) models, the distinguishing feature of this model would be a s -channel H^{++} resonance in $W_L^+ W_L^+ \rightarrow W_L^+ W_L^+$ scattering process.

4.7 Summary

In this chapter, the elastic scattering of different modes of longitudinally polarized gauge bosons in various extended scalar sectors has been considered. The exact expression of longitudinal polarization vectors has been used to determine the scattering cross-sections. Generally, the idea of $V_L V_L$ scattering has been used for the proper understanding of the EWSB or in other words to perceive the importance of Higgs boson. In this analysis, a quantitative study of $V_L V_L$ scattering has been carried out to probe the various non-standard scalars in various BSM scenario at an intermediate energy-range.

In this analysis, the parameter space of these models has been scanned via several theoretical as well as phenomenological constraints. From the allowed parameter space, several benchmark points have been picked up for which the CM energy dependence of scattering cross-sections of different VBS modes in several models have been shown.

As far as model benchmark points are concerned, we have chosen only those regions of the parameter space which satisfy all the existing constraints. The present LHC data have allowed only a small portion of the parameter space of these models, thus we are compelled to execute our analysis in the restricted parameter space. As a result the cross-section is very much similar to the SM case away from the peaks. To differentiate between different extended scalar sectors from VBS one need to look for resonances at different VBS modes.

In this analysis to illustrate the effect of the non-standard scalar particles, two different masses have been chosen, ~ 500 GeV and other is at the relatively higher ~ 1500 GeV. Depending on the model parameters of a particular model and for a particular process the height and width of the peaks (if present) at the two different values of mass range of the heavier scalars are different from each other, as these are controlled by mass and corresponding decay width of those non-standard scalars which we want to probe via $V_L V_L$ scattering. If we consider a particular process then we can differentiate between the different models from the nature of these peaks. So this analysis provides an exclusive approach to discriminate the different extended scalar sectors.

Chapter 5

Metastability in Standard Model

5.1 Introduction

If one assumes the standard model is valid up to the Planck M_{Pl} scale then the Higgs potential develops a second minimum near M_{Pl} that is much deeper than the electroweak (EW) vacuum in which we live. This implies absolute stability of the EW vacuum (minimum) is excluded at a confidence level of about 3σ . For the measured experimental values of the SM parameters the instability (the Higgs quartic coupling λ becomes negative) occurs at scales larger than 10^{10} GeV. The instability problem does not necessarily lead to an inconsistency of our existence at the EW scale. The transition time from the EW vacuum to its deeper minimum is spectacularly greater than the lifetime of the Universe. New physics can change the stability of EW vacuum modifying the SM Higgs potential.

When extrapolating the known physics to higher energy scales, renormalization of the known parameters plays a crucial role. The parameters of the theory involved in a physical process, are dependent on the energy scales.

In this chapter, the metastability of the SM is revisited. The stability of the SM potential and mass bounds of the Higgs from the (meta)stability, instability, and perturbativity will be reviewed. Finally in the summary, the interpretation of the

instability problem and possible hints about the new physics at or below the instability scale will be discussed.

5.2 Effective Higgs potential in the Standard Model

In this section, the structure of the Higgs potential from the EW scale to the Planck scale M_{Pl} will be analyzed. In this study, the Higgs scalar potential up to two-loop quantum corrections is used and it has been improved by three-loop renormalization group running of the coupling parameters.

The SM tree-level Higgs potential is given by,

$$V_0^{\text{SM}}(\phi) = -\frac{1}{2}m^2\phi^2 + \frac{1}{4}\lambda\phi^4. \quad (5.1)$$

In Landau gauge using $\overline{\text{MS}}$ scheme, the SM Higgs potential up to two-loop can be found in Refs. [13, 90, 91]. The one-loop potential can be written as,

$$V_1^{\text{SM}}(\phi) = \sum_{i=1}^5 \frac{n_i}{64\pi^2} M_i^4(\phi) \left[\ln \frac{M_i^2(\phi)}{\mu^2(t)} - c_i \right], \quad (5.2)$$

where n_i is the number of degrees of freedom. For scalars and gauge bosons, n_i comes with a positive sign, whereas for fermions it is associated with a negative sign. Here $c_{H,G,f} = 3/2$, $c_{W,Z} = 5/6$ and $\mu(t)$ is related to the running parameter t as, $\mu(t) = M_Z \exp(t)$. $M_i(\phi)$ is given by,

$$M_i^2(\phi) = \kappa_i(t)\phi^2(t) - \kappa'_i(t),$$

n_i , κ_i and κ'_i can be found in eqn. (4) of Ref. [92] (see also Refs. [93–96]). It has been observed that the variation in the mass term m^2 of the Higgs potential from the EW scale to M_{Pl} is very small. One can neglect it for $\phi \gg 1$ TeV. Also, the β -functions of eqns. B.5–B.8 are independent of m^2 . In this work, the RGE of m^2 has not been considered. The running energy scale μ is replaced with the field ϕ in the potential [92] such that all the couplings of the SM remain within the perturbative domain. For $\phi \gg v$, the quantum corrections to $V(\phi)$, are reabsorbed in the effective running coupling λ_{eff} (see eqn. B.1) such that the effective potential becomes,

$$V_{\text{eff}}(\phi) \simeq \frac{1}{4}\lambda_{\text{eff}}\phi^4. \quad (5.3)$$

The matching conditions and RG evaluation of the SM couplings, which play an important role in the stability of the Higgs potential will be discussed in the next section.

5.2.1 Matching conditions and RG evaluation of the SM couplings

Using matching conditions one can evaluate the coupling constants at the highest mass scale of the SM namely the top quark mass M_t and then run them according to the RGEs up to the Planck scale. To know their values at M_t , one should take into account various threshold corrections up to M_t [97–99],

$$g_i(M_t) = g_i(M_Z) + \delta g_i(M_t). \quad (5.4)$$

$$\lambda(M_t) = \frac{M_h^2}{2v^2} (1 + \delta_H(M_t)). \quad (5.5)$$

$$y_t(M_t) = \frac{\sqrt{2}M_t}{v} (1 + \delta_t(M_t)). \quad (5.6)$$

All coupling constants are expressed in terms of pole masses (see table. 5.1). To calculate $g_1(M_t)$ and $g_2(M_t)$, one-loop RGEs are enough. For $g_3(M_t)$, first three-loop RGE running of α_s with five flavors excluding the top quark are used, and then the effect of top is included using prescriptions of an effective field theory. The leading term in four-loop RGE for α_s is also taken into account. Amongst all Yukawa couplings, the running of y_t is the most significant. $y_t(M_t)$ is related to the top pole mass M_t by the matching condition eqn. 5.6. In $\delta_t(M_t)$, three-loop QCD, one-loop EW, and two-loop $\mathcal{O}(\alpha\alpha_s)$ corrections are taken into account. Similarly, the relation between $\lambda(M_t)$ in $\overline{\text{MS}}$ scheme and Higgs pole mass M_h is given in eqn. 5.5. In $\delta_H(M_t)$, one-loop EW, two-loop $\mathcal{O}(\alpha\alpha_s)$, two-loop $\mathcal{O}(y_t^4 g_3^2)$ and two-loop $\mathcal{O}(y_t^6)$ corrections are considered. The loop effects considered in these matching conditions are comparable to Refs. [13, 100]. After knowing the values of various coupling constants at M_t , full three-loop SM RGEs are used to run them up to M_{Pl} .

Using these matching conditions one can estimate all the coupling constants at the

Physical Observable	Value	Reference
Pole mass of the W^\pm boson M_W	80.384 ± 0.014 GeV	[101]
Pole mass of the Z boson M_Z	91.1876 ± 0.0021 GeV	[102]
Pole mass of the Higgs M_h	125.7 ± 0.3 GeV	[103]
Pole mass of the top quark M_t	173.1 ± 0.6 GeV	[104]
VEV	246.21971 ± 0.00006 GeV	[105]
$\alpha_s(M_Z)$	0.1184 ± 0.0007	[106]

Table 5.1: *SM observables which can be taken as input to fix the SM fundamental parameters g_1, g_2, g_3, y_t and λ .*

scale M_t including the uncertainty in M_t , M_h and $\alpha_s(M_Z)$ (see table 5.1) as:

$$g_1(\mu = M_t) = 0.358725 + 0.000007 \left(\frac{M_t [\text{GeV}] - 173.1}{0.6} \right) \quad (5.7)$$

$$g_2(\mu = M_t) = 0.64818 - 0.00002 \left(\frac{M_t [\text{GeV}] - 173.1}{0.6} \right) \quad (5.8)$$

$$g_3(\mu = M_t) = 1.16449 - 0.0003 \left(\frac{M_t [\text{GeV}] - 173.1}{0.6} \right) + 0.0031 \left(\frac{\alpha_s(M_Z) - 0.1184}{0.0007} \right) \quad (5.9)$$

$$y_t(\mu = M_t) = 0.935643 + 0.0033 \left(\frac{M_t [\text{GeV}] - 173.1}{0.6} \right) - 0.0004 \left(\frac{\alpha_s(M_Z) - 0.1184}{0.0007} \right) - 0.00001 \left(\frac{M_h [\text{GeV}] - 125.7}{0.3} \right) \quad (5.10)$$

$$\lambda(\mu = M_t) = 0.127054 - 0.00003 \left(\frac{M_t [\text{GeV}] - 173.1}{0.6} \right) - 0.00001 \left(\frac{\alpha_s(M_Z) - 0.1184}{0.0007} \right) + 0.00061 \left(\frac{M_h [\text{GeV}] - 125.7}{0.3} \right) \quad (5.11)$$

As running of all the SM couplings is being considered up to the Planck scale, the values at very high energies are extremely sensitive to the initial values at M_t . These changes should be taken into account because it will also affect the stability of EW vacuum of Higgs potential. However, the stability of the Higgs potential does not alter due to the uncertainties in the other SM parameters at M_t . Setting all the couplings at M_t , using the RG-eqns. B.5-B.9, one can obtain the SM couplings at

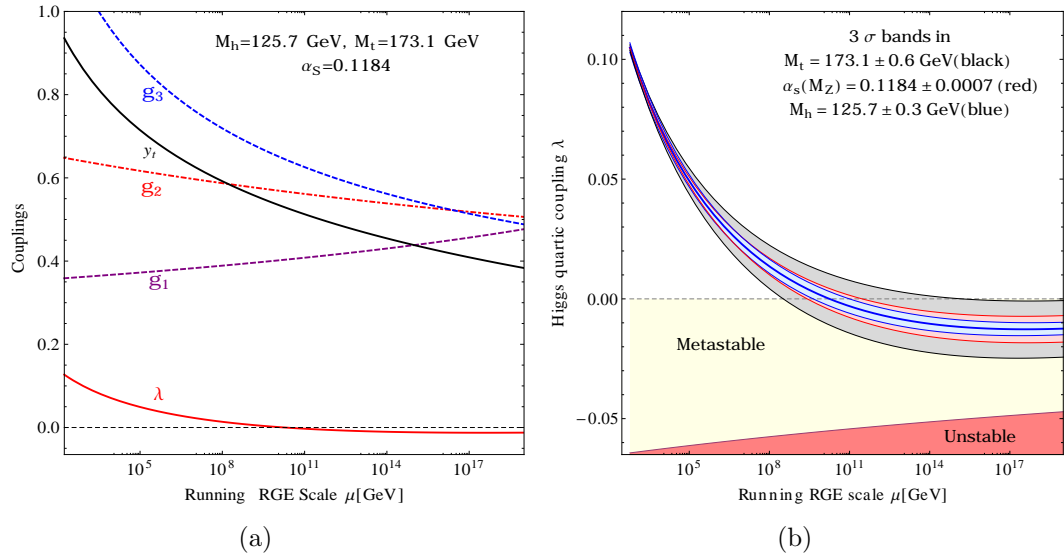


Figure 5.1: (a) RG evolution of the gauge couplings g_1, g_2, g_3 , top Yukawa coupling y_t , Higgs self-quartic coupling λ in $\overline{\text{MS}}$ scheme and (b) RG evolution of λ in the SM and in the 3σ bands for M_t , M_h and $\alpha_s(M_Z)$ are displayed.

M_{Pl} as:

$$\begin{aligned}
 g_1(\mu = M_{\text{Pl}}) = & 0.477685 + 0.00002 \left(\frac{M_t [\text{GeV}] - 173.1}{0.6} \right) \\
 & + 0.00001 \left(\frac{\alpha_s(M_Z) - 0.1184}{0.0007} \right) \\
 & + 10^{-8} \left(\frac{M_h [\text{GeV}] - 125.7}{0.3} \right)
 \end{aligned} \tag{5.12}$$

$$\begin{aligned}
 g_2(\mu = M_{\text{Pl}}) = & 0.505632 - 0.00001 \left(\frac{M_t [\text{GeV}] - 173.1}{0.6} \right) \\
 & - 0.00001 \left(\frac{\alpha_s(M_Z) - 0.1184}{0.0007} \right) \\
 & + 10^{-9} \left(\frac{M_h [\text{GeV}] - 125.7}{0.3} \right)
 \end{aligned} \tag{5.13}$$

$$\begin{aligned}
 g_3(\mu = M_{\text{Pl}}) = & 0.48714 - 0.00002 \left(\frac{M_t [\text{GeV}] - 173.1}{0.6} \right) \\
 & + 0.0002 \left(\frac{\alpha_s(M_Z) - 0.1184}{0.0007} \right)
 \end{aligned} \tag{5.14}$$

$$+10^{-9} \left(\frac{M_h[\text{GeV}] - 125.7}{0.3} \right) \quad (5.15)$$

$$\begin{aligned} y_t(\mu = M_{\text{Pl}}) = & 0.38227 + 0.00304 \left(\frac{M_t [\text{GeV}] - 173.1}{0.6} \right) \\ & + 0.0009 \left(\frac{\alpha_S(M_Z) - 0.1184}{0.0007} \right) \\ & - 8 \times 10^{-6} \left(\frac{M_h[\text{GeV}] - 125.7}{0.3} \right) \end{aligned} \quad (5.16)$$

$$\begin{aligned} \lambda(\mu = M_{\text{Pl}}) = & -0.0122748 - 0.003935 \left(\frac{M_t [\text{GeV}] - 173.1}{0.6} \right) \\ & - 0.00209 \left(\frac{\alpha_S(M_Z) - 0.1184}{0.0007} \right) \\ & + 0.0008 \left(\frac{M_h[\text{GeV}] - 125.7}{0.3} \right) \end{aligned} \quad (5.17)$$

The couplings g_1, g_2, g_3, y_t and λ have been plotted with the running energy in Fig. 5.1(a) and only the Higgs quartic coupling λ has been shown in Fig. 5.1(b). In Fig. 5.1(b), the blue solid line corresponds to the measured central values of M_t , M_h and $\alpha_S(M_Z)$, the blue band belongs to the 3σ deviation in M_h , whereas the red and black correspond to the deviation in $\alpha_S(M_Z)$ and M_t respectively. As the running of the Yukawa couplings of the other quarks and leptons are very small, these are not included in this analysis.

As defined in eqn. 5.3, λ_{eff} differs from λ as it takes care of quantum corrections. It has been observed that for high energy scale $\phi \gg v$, the difference in λ_{eff} and λ is not appreciable (see Fig. 5.2). In the stability analysis, λ_{eff} has been used instead of λ .

The Higgs quartic coupling, λ or λ_{eff} becomes negative after $\mu \sim 10^{10}$ GeV. This corresponds to the metastability of the EW vacuum. The detailed study of the metastability of the Higgs potential will be carried out in the next section.

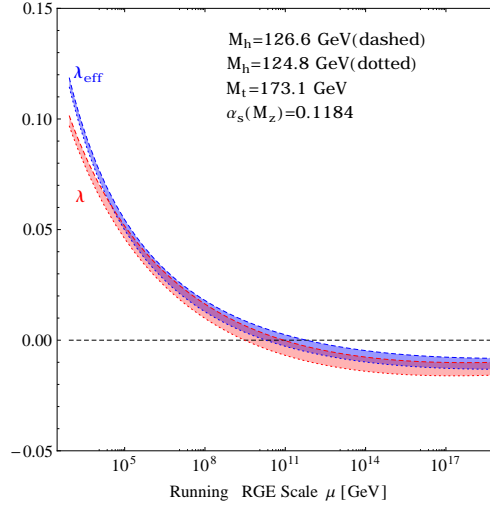


Figure 5.2: *Higgs quartic coupling λ and effective λ_{eff} -function as a function of running RGE scale.*

5.2.2 Metastability and Tunneling Probability

The Higgs quartic coupling determines the shape of the Higgs potential $V(\phi)$. How it changes with the running energy and why an extra deeper minimum in the Higgs potential is located near the Planck scale, will be discussed in the following.

One can realize from the β -function of the coupling constants of eqns. B.5-B.8 and Fig. 5.1 that except the gauge coupling g_1 , the other SM couplings are the decreasing functions of the running energy. The top Yukawa coupling y_t decreases due to the dominant contributing term $-\frac{8y_t g_3^2}{16\pi^2}$, which is present in β_{y_t} . Similarly in the β -function of the gauge couplings g_2 and g_3 , the dominant contributions are $-\frac{7g_3^2}{16\pi^2}$ and $-\frac{19g_2^2}{96\pi^2}$ respectively. But the running of the Higgs quartic coupling is of different nature than the other SM couplings.

In Fig. 5.3, for the central values (including the other SM parameters) of $M_t = 173.1$ GeV, $M_h = 125.7$ GeV and $\alpha_s(M_Z) = 0.1184$, the variation of Higgs quartic coupling λ (blue) and corresponding β -function (red) with the running energy scale have been

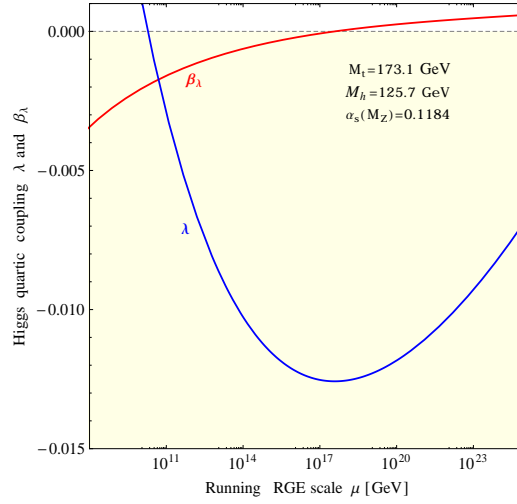


Figure 5.3: *Higgs quartic coupling λ and corresponding β -function as a function of the running RGE scale.*

shown. The λ decreases up to $\sim 10^{17}$ GeV because β_λ remains negative as it contains the dominant term, $-\frac{6y_t^4}{16\pi^2}$ (see eqn. B.9). As y_t also decreases with the running energy, β_λ is an increasing function of the running energy. It crosses zero around the energy $\mu_{min} \sim 10^{17}$ GeV. λ increases after this energy scale. Therefore, the Higgs potential $V(\phi)$ has one extra minimum at that particular scale. The depth of the minimum is $\sim \frac{1}{4}|\lambda(\mu_{min})|\mu_{min}^4$, much deeper than the depth of the EW vacuum. So the false minimum, i.e., the EW vacuum could tunnel to the true (deeper) minimum.

The vacuum tunneling probability of EW vacuum to the true minimum at the present epoch is given by [14, 107, 108]

$$\mathcal{P}_0 = 0.15 \frac{\Lambda_B^4}{H_0^4} e^{-S(\Lambda_B)}, \quad (5.18)$$

where $H_0 = 1.44 \times 10^{-42}$ GeV (natural units) is the Hubble parameter and $S(\Lambda_B)$ is the minimum action of the Higgs potential at energy Λ_B . Now one can calculate the action S of the Higgs potential using semi-classical approach. The Euclidean

equations of motion of ϕ can be written as [14, 107, 108],

$$-\partial_\mu \partial^\mu \phi + \frac{\partial V_{\text{eff}}(\phi)}{\partial \phi} = 0 \quad (5.19)$$

$$-\phi'' - \frac{3}{r} \phi' + |\lambda_{\text{eff}}| \phi^3 = 0, \quad (5.20)$$

where $r = x_\mu x^\mu$ and the eqn. 5.20 satisfies the following boundary conditions,

$$\phi'(0) = 0 \quad \text{and} \quad \phi(\infty) = v \rightarrow 0. \quad (5.21)$$

Here the Euclidean solution of ϕ starting and end point is $\phi = v$ at Euclidean time $\tau (\equiv it) = \mp \infty$. The choice of the origin for the Euclidean time τ can be made in such a way that the turning point $\phi = 0$ is reached at $\tau = 0$. Such a solution is called a “bounce”. With this boundary conditions, the Euclidean equation of motion can be solved analytically and the solution of eqn. 5.20 is given by,

$$\phi(r) = \sqrt{\frac{2}{|\lambda_{\text{eff}}|}} \frac{2R}{r^2 + R^2}, \quad (5.22)$$

where R is some arbitrary parameter, generally it is called the size of the bounce.

Action of the Higgs potential given by,

$$S = \int d^4x \left(\frac{1}{2} (\nabla \phi)^2 - V_{\text{eff}}(\phi) \right). \quad (5.23)$$

Here $d^4x = 2\pi^2 r^3 dr$ is the volume element of 4-dimensional sphere, using eqn. 5.22, one can get

$$\begin{aligned} S &= \frac{16R^2}{|\lambda_{\text{eff}}|} \int_0^\infty 2\pi^2 r^3 dr \frac{(r^2 - R^2)}{(r^2 + R^2)^4} \\ &= \frac{8\pi^2}{3 |\lambda_{\text{eff}}|}. \end{aligned} \quad (5.24)$$

One can calculate tunneling time from EW vacuum to new deeper minimum using the eqn. 5.18. The lifetime τ_{EW} is given by [14],

$$\tau_{\text{EW}} = \left(\frac{55}{3\pi} \right)^{1/4} \frac{e^{S(\Lambda_B)/4}}{\Lambda_B} \approx \frac{T_U}{\mathcal{P}_0^{1/4}}, \quad (5.25)$$

where, $T_U \approx \frac{0.96}{H_0} \approx 13.7$ billion years is the lifetime of the Universe.

The minimum action of the Higgs potential is needed to calculate the EW vacuum decay time. For $\beta_{\lambda_{\text{eff}}} = 0$, λ_{eff} is minimum and negative, i.e., S of eqn. 5.24 become minimum. In this calculation the loop correction to the action is neglected, as in

Ref. [108] it had been argued that setting the running scale to R^{-1} significantly restricts the size of such corrections. Also the gravitational corrections [17, 109] to the action is neglected as in Ref. [15]. In Ref. [108] it was pointed out that thermal corrections are important at very high temperatures. Finite temperature effects to EW vacuum stability in the context of SM have been calculated in [110]. It had been claimed in Ref. [111] that the parameter space corresponding to EW metastability gets further reduced. In this work zero temperature field theory has been used however.

If τ_{EW} is greater than the lifetime of the universe T_U , then the EW vacuum is called metastable, i.e., $0 < \mathcal{P}_0 < 1$. This ensuing bounds on the effective Higgs quartic coupling [15, 108] as,

$$\lambda_{\text{eff}}(\Lambda_B) < 0 \quad \text{and} \quad \lambda_{\text{eff}}(\Lambda_B) > \lambda_{\text{min}}(\Lambda_B) = \frac{-0.06488}{1 - 0.00986 \ln(v/\Lambda_B)}. \quad (5.26)$$

On the other hand, if $\lambda_{\text{eff}}(\Lambda_B) < \lambda_{\text{min}}(\Lambda_B)$, then the vacuum is unstable, implies no existence of the Universe. If $\lambda_{\text{eff}}(\Lambda_B) > 0$, i.e., $\mathcal{P}_0 = 0$, no transition will take place, i.e., the EW vacuum is stable. But the recent experimental data suggest that the EW vacuum remains in the metastable state, considering there is no new physics up to the Planck scale. Therefore, the EW vacuum could transit to the other minimum and such a transition can release an enormous amount of energy and which will destroy the present Universe.

The variations of the tunneling probability against the top mass M_t has been shown in Fig. 5.4. It is clear from the figure that the tunneling probability decreases with the decrease of M_t , i.e., the lifetime of EW vacuum increases. For $M_t \lesssim 171$ the lifetime of EW vacuum become infinite as $\lambda > 0$ at all scales, i.e., the EW vacuum of the Higgs potential become absolutely stable. One can obtain from Fig. 5.4 that the experimental favored data imply that the lifetime of EW vacuum is $\sim 10^{100} - 10^{500}$ years, much greater than the lifetime of our present Universe.

The stability of EW vacuum is best displayed with the aid of phase diagrams. One

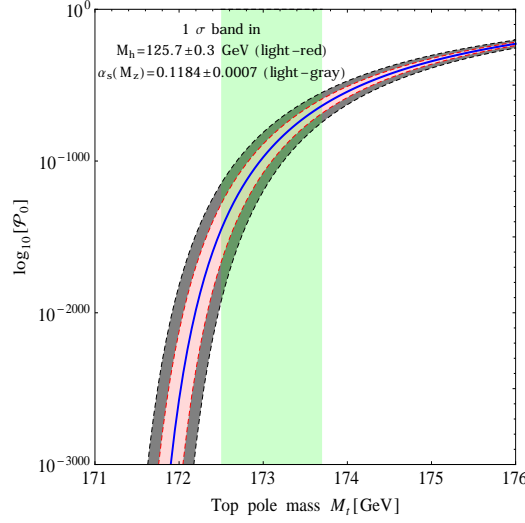


Figure 5.4: Tunneling probability \mathcal{P}_0 dependence on M_t in SM. Light-green band stands for M_t at $\pm 1\sigma$. The solid blue line corresponds to the central values of M_h and $\alpha_s(M_Z)$, whereas the light-red band corresponds to the 1σ deviation in Higgs mass and light-gray band for $\alpha_s(M_Z)$.

can also identify the regions of EW stability and metastability in $M_t - M_h$ plane of Fig. 5.5 and in $\alpha_s(M_Z) - M_t$ plane of Fig. 5.6. In these figures, the unstable (red) and the metastable (yellow) region is separated by instability line which occurs when $\lambda(\mu) = \lambda_{\min}$. The criticality ($\beta_\lambda(\mu) = \lambda(\mu) = 0$) line separated the metastable and stable (green) regions. The red region (right-side) of Fig. 5.5(a) is excluded as the theory becomes non-perturbative at the Planck scale. The Fig. 5.5(a) illustrates the remarkable coincidence for which the EW vacuum in the SM appears to live right in between the stable and unstable regions. The Fig. 5.5(b) is zoomed version of the Fig. 5.5(a), here the gray ellipses are experimentally preferred range of M_h and M_t at 1, 2 and 3σ . From these figures one can conclude that for the Higgs mass $M_h < 125.7$ GeV, the stability of the EW vacuum up to the Planck mass is excluded at 98% C.L. (one-sided).

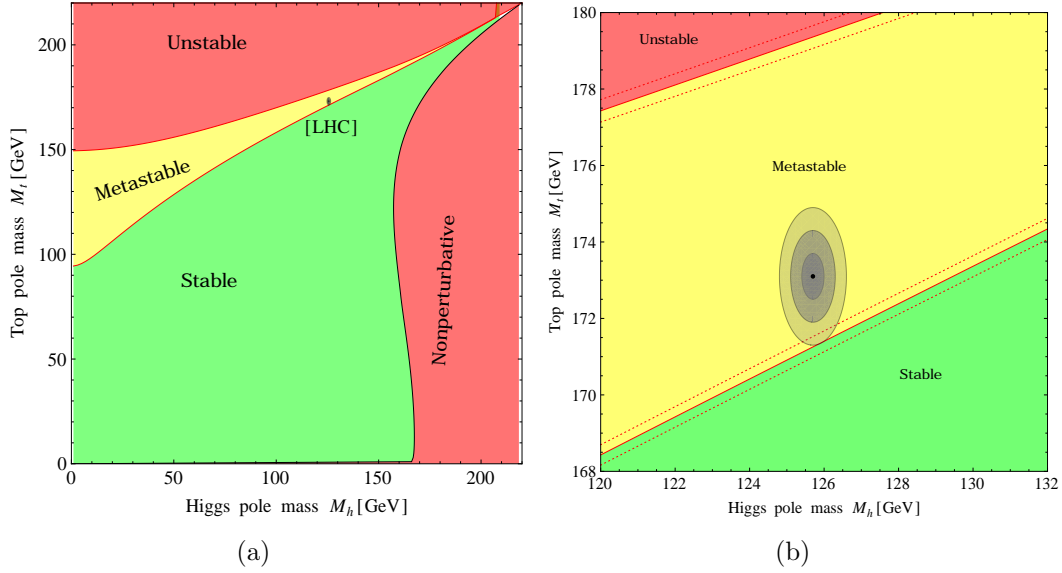


Figure 5.5: (a) In SM, regions of absolute stability (green), metastability (yellow), instability (red) of the EW vacuum in the $M_h - M_t$ plane phase diagram. (b) Zoomed in the region of the preferred experimental range of M_h and M_t . The boundary lines (red) correspond to 1σ variation in $\alpha_s(M_Z)$. The gray areas denote the experimentally favored zones for M_h and M_t at 1, 2 and 3σ .

5.2.3 Bounds on the Higgs mass from metastability and perturbativity

As it has been seen from Fig. 5.5, the measured values of M_h and M_t appear to be rather special, in the sense that they place the SM EW vacuum in a near-critical condition, i.e., at the border between stability and metastability. The vacuum stability bound on the Higgs mass approximated as,

$$M_h [\text{GeV}] > 129.46 + 1.12 \left(\frac{M_t [\text{GeV}] - 173.1}{0.6} \right) - 0.56 \left(\frac{\alpha_s(M_Z) - 0.1184}{0.0007} \right), \quad (5.27)$$

is obtained from the requirement $\lambda = \beta_\lambda = 0$. One can see from eqn. 5.27 that the main uncertainty comes from the top mass, M_t , so any improvement in the measurement of the top mass is of great importance for the question of EW vacuum stability.

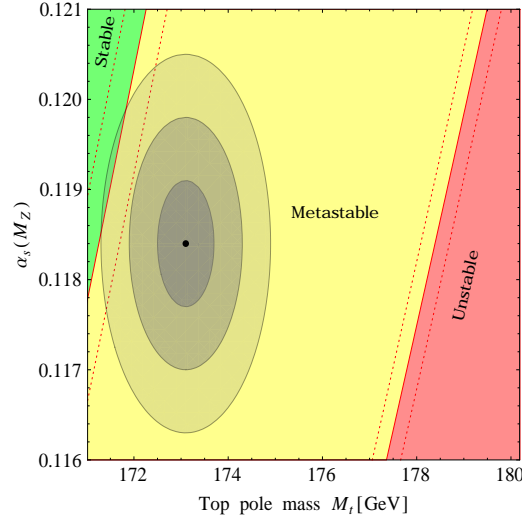


Figure 5.6: Phase diagram in $M_t - \alpha_s(M_Z)$ plane in SM. Regions of absolute stability (green), metastability (yellow), instability (red) of the EW vacuum are marked. The dotted lines correspond to $\pm 3\sigma$ variation in M_h and the gray areas denote the experimental allowed region for M_t and $\alpha_s(M_Z)$ at 1, 2 and 3σ .

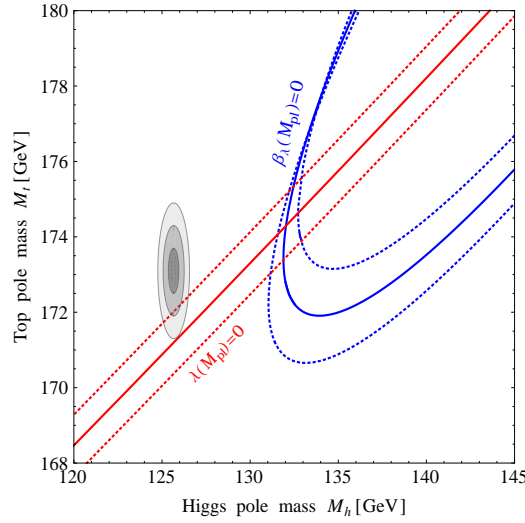


Figure 5.7: Contour plot for $\lambda(M_{Pl}) = 0$ (red line) and $\beta_\lambda(M_{Pl}) = 0$ (blue line). Dotted lines correspond to $\pm 3\sigma$ variation in $\alpha_s(M_Z)$. The gray areas denote the experimental allowed region for M_h and M_t at 1, 2 and 3σ .

The metastability bound is given by,

$$M_h \text{ [GeV]} > 109.73 + 1.84 \left(\frac{M_t \text{ [GeV]} - 173.1}{0.6} \right) - 0.88 \left(\frac{\alpha_S(M_Z) - 0.1184}{0.0007} \right), \quad (5.28)$$

comes from the requirement $\beta_\lambda = 0$ and $\lambda = \lambda_{\min}$. To ensure perturbativity, one demand $\lambda(M_{\text{Pl}}) < 4\pi$, which leads to

$$M_h \text{ [GeV]} < 172.23 + 0.36 \left(\frac{M_t \text{ [GeV]} - 173.1}{0.6} \right) - 0.12 \left(\frac{\alpha_S(M_Z) - 0.1184}{0.0007} \right). \quad (5.29)$$

Note that these bound are scheme independent, while the higher order RG equations, the potential calculation including radiative corrections or the threshold matching conditions are scheme and gauge dependent. The instability scale Λ_I in Landau gauge with $\overline{\text{MS}}$ scheme has been found as,

$$\begin{aligned} \log_{10} \left(\frac{\Lambda_I}{\text{GeV}} \right) = & 10.277 - 0.82 \left(\frac{M_t \text{ [GeV]} - 173.1}{0.6} \right) + 0.33 \left(\frac{\alpha_S(M_Z) - 0.1184}{0.0007} \right) \\ & + 0.23 \left(\frac{M_h \text{ [GeV]} - 125.7}{0.3} \right). \end{aligned} \quad (5.30)$$

5.2.4 Asymptotic safety in SM

Shaposhnikov and Wetterich predicted [112] mass of the Higgs boson of 126 GeV imposing the constraint $\lambda(M_{\text{Pl}}) = \beta_\lambda(M_{\text{Pl}}) = 0$, in a scenario known as asymptotic safety of gravity. This corresponds to the fact that both the EW minimum and new minimum residing at the Planck scale, are degenerate. From Fig. 5.7, it clear that the present experimental data of the SM parameters does not allow this condition to be realized in the SM. This condition is satisfied at $M_h = 132.033$ GeV and $M_t = 174.294$ GeV for fixed central values of the other SM parameters.

5.2.5 Veltman's conditions in SM

The Higgs mass with quadratic divergence term in cutoff regularization scheme is given by,

$$\begin{aligned} m_h^2 &= m_{h,bare}^2 + \frac{\Lambda_{cut}^2}{16\pi^2 v^2} STr(\mathcal{M}^2). \\ STr(\mathcal{M}^2) &= 3(m_h^2 + m_Z^2 + 2m_W^2 - 4m_t^2). \end{aligned} \quad (5.31)$$

The quadratic divergences part gives rise to the hierarchy problem related to the Higgs mass. The condition for the absence of the quadratic divergences at one loop, $STr(\mathcal{M}^2) = 0$, is known as the Veltman's condition (VC). For high energy $\phi \gg v$ eqn. 5.31 can be written as,

$$\frac{STr(\mathcal{M}^2)}{\phi^2} = 6\lambda_1 + \frac{9}{4}g_2^2 + \frac{3}{4}g_1^2 - 12y_t^2 = 0.$$

Due to the large negative contribution from the term containing the top Yukawa coupling, it is not possible to satisfy VC at M_{Pl} given the experimental measurements of M_t and M_h . It has been seen that if one consider Higgs mass $M_h \approx 135 \pm 2.5$ GeV with top mass $M_t = 173.1 \pm 0.6$ GeV, the VCs in the SM at M_{Pl} can be satisfied, which is excluded at more than 5σ . For $M_h \approx 135 \pm 2.5$ GeV the quadratic divergence part may cancel at one-loop but if two-loop corrections are included then the problem arises again. Also, the VCs may be satisfied at a given scale but a nonzero quadratic divergence part in the Higgs mass may reappear for a different cut-off scale. This implies that the hierarchy problem is not solvable in the SM using the VC.

5.3 Summary

In this chapter, it has been shown that the ground state of the Higgs potential depends on the SM parameters. With the present experimental values of the SM parameters, it has been observed that the Higgs quartic coupling λ , together with all other SM coupling constants, remains perturbative in the entire energy domain between the EW and the Planck scales. It has also been seen that assuming the validity of the SM up to the Planck scale M_{Pl} , the measured value of $M_h \simeq 125$ GeV

is near-critical, i.e., it places the EW vacuum right at the border between absolute stability and metastability. The absolute stability of the EW vacuum of the Higgs potential is excluded at about 98% confidence level.

In the SM, with the present measured values of the SM parameters, the asymptotic safety of gravity at the Planck scale M_{Pl} is not realized. Also the possible solution of hierarchy problem related to the Higgs mass, i.e., Veltman's condition cannot be achieved at any scale between EW and M_{Pl} . At M_{Pl} this condition is fulfilled for the Higgs mass $M_h > 130$ GeV, which is excluded at more than 5σ C.L.

New physics can modify the effective Higgs potential through the quantum corrections as well as the stability of the EW vacuum will also alter. In the next chapter, the detailed modifications of stability of the Higgs potential in the presence of new physics in the form of an additional scalar multiplet will be discussed.

Chapter 6

Metastability in Extended Scalar Sectors of the Standard Model

6.1 Introduction

It has been seen in the previous chapter that life time of the Universe is finite in the SM. It is important to explore if the new extra scalar field(s) of an extended scalar sector has an answer to this puzzle in its reserve. In this work a $SU(2)_L$ singlet [36] or a doublet [15] or a hyperchargeless triplet [37] scalar is added to the SM and a Z_2 -symmetry is imposed on these new models such that the *odd* number of new scalar fields do not couple with the SM particles. As the lightest neutral particle of the additional scalar sector cannot decay, it becomes stable and serves as a viable dark matter candidate which may saturate the relic abundance of the dark matter in the Universe. As these new models contain various kinds of new scalar fields, the structure of scalar potential and the absolute stability bounds of the EW vacuum of the scalar potential which had been shown in Chapter 3 are rather complicated than that in the SM due to the involvement of more parameters.

In this work, a detailed study of the metastability of the EW vacuum of Higgs potential in the extended scalar sector will be presented. Various kinds of phase diagrams will be drawn to illustrate the region of absolute stability, metastability, instability

and the non-perturbativity on different parameter spaces of these extended scalar sectors. In the Section 6.2, the stability of the EW vacuum in the presence of a real singlet scalar will be discussed. In Sections 6.3 and 6.4, similar studies for the inert doublet model (IDM) and inert triplet model (ITM) will be elaborated.

6.2 Singlet scalar extension of SM

Recent cosmological and astrophysical evidences suggest presence of cold dark matter (DM). A simple choice is to add a gauge singlet real scalar S to the SM [113]. An additional Z_2 symmetry ensures the stability of S . The scalar modifies the Higgs effective potential, and can ensure vacuum stability up to M_{Pl} . Such extensions of SM have been discussed in the literature [114–129] in the context of vacuum stability.

In the context of SM, detailed studies of metastability has shown in Chapter 5. Along the same line, in this section, the studies of the metastable vacuum has been extended to the SM+ S model [15].

6.2.1 Effective potential and RGE running

In this model, an extra real scalar singlet field S , odd under Z_2 symmetry, is added to the SM, providing a suitable candidate for dark matter. The corresponding Lagrangian density is given by,

$$\mathcal{L}_S = \frac{1}{2}(\partial_\mu S)(\partial^\mu S) - V_0^S$$

with,

$$V_0^S = \frac{1}{2}\bar{m}_S^2 S^2 + \frac{\kappa}{2}|\Phi|^2 S^2 + \frac{\lambda_S}{4!}S^4, \quad (6.1)$$

where,

$$\Phi = \begin{pmatrix} G^+ \\ (h + v + iG^0)/\sqrt{2} \end{pmatrix}.$$

After spontaneous EW symmetry breaking, DM mass M_S is expressed as $M_S^2 = \bar{m}_S^2 + \kappa v^2/2$.

SM tree level Higgs potential

$$V_0^{\text{SM}}(\phi) = -\frac{1}{2}m^2h^2 + \frac{1}{4}\lambda h^4$$

is augmented by the SM+ S one-loop Higgs potential in Landau gauge using $\overline{\text{MS}}$ scheme, which is written as

$$V_1^{\text{SM}+S}(h) = V_1^{\text{SM}}(h) + V_1^S(h).$$

The expression of $V_1^{\text{SM}}(h)$ is given¹ in eqn. 5.2 and the one loop contribution of the singlet scalar can be written as [119, 130],

$$V_1^S(h) = \frac{1}{64\pi^2} M_S^4(h) \left[\ln \left(\frac{M_S^2(h)}{\mu^2(t)} \right) - \frac{3}{2} \right],$$

where,

$$M_S^2(h) = \overline{m}_S^2(t) + \kappa(t)h^2(t)/2.$$

SM contributions are taken at two-loop level [13, 14, 90, 91], whereas the scalar contributions are considered at one-loop only.

For $h \gg v$, the effective potential can be approximated as

$$V_{\text{eff}}^{\text{SM}+S}(h) \simeq \lambda_{\text{eff}}(h) \frac{h^4}{4}, \quad (6.2)$$

with

$$\lambda_{\text{eff}}(h) = \lambda_{\text{eff}}^{\text{SM}}(h) + \lambda_{\text{eff}}^S(h), \quad (6.3)$$

where $\lambda_{\text{eff}}^{\text{SM}}(h)$ can be found in eqn. B.1 and,

$$\lambda_{\text{eff}}^S(h) = e^{4\Gamma(h)} \left[\frac{\kappa^2}{64\pi^2} \left(\ln \left(\frac{\kappa}{2} \right) - \frac{3}{2} \right) \right]. \quad (6.4)$$

As quartic scalar interactions do not contribute to wave function renormalization at one-loop level, S does not alter $\gamma(\mu)$ of SM and anomalous dimension of S is zero [117]. All running coupling constants are evaluated at $\mu = h$.

The beta functions for the new physics parameters κ and λ_S are given in eqn. B.12. \overline{m}_S also evolves with energy. But as the beta functions of other parameters do not involve \overline{m}_S , its beta function is not considered in this discussion. Here, new physics effects are included in the RGEs at one-loop only.

¹Here h is used instead of ϕ , representing the SM-like Higgs field.

6.2.2 Singlet Scalar as a dark matter candidate

As it has already been discussed that the new extended real singlet scalar is odd under Z_2 symmetry, i.e., under this symmetry, $S \rightarrow -S$, but Standard Model particles are invariant. Due to Z_2 symmetry *odd* numbers of the scalar fields S do not couple with the SM particles. The particle S is stable and it can be considered as a viable dark matter candidate. This model can provide dark matter with almost all possible mass ranges which allowed from the relic density constraints of WMAP [20] and Planck [21] data.

After EW symmetry breaking one can write the potential (see eqn. 6.1) explicitly as,

$$V_0^S = \frac{1}{2} \left(\overline{m}_S^2 + \frac{\kappa v^2}{2} \right) S^2 + \frac{kv}{2} h S^2 + \frac{\kappa}{4} h^2 S^2 + \frac{\lambda_S}{24} S^4. \quad (6.5)$$

S is the scalar singlet under the SM gauge symmetry so there are no 4-point coupling like, $SSXX$ (X is the SM vector boson or a fermion). The scalar field can annihilate to SM particles only *via* Higgs exchange. S is called a Higgs portal dark matter. LHC has put a stringent bounds on the Higgs invisible decay width [131]. The decay width of h to pair of S is given by,

$$\Gamma(h \rightarrow SS) = \frac{v^2}{32\pi M_h} \kappa^2 \left(1 - \frac{4M_{\text{DM}}^2}{M_h^2} \right)^{1/2}. \quad (6.6)$$

Also the direct detection experiments, XENON 100 [50, 51] and LUX [53] puts a bound on the dark matter mass from the non-observation of dark matter-nucleon scattering. DM direct detection involve the h -mediated t -channel process, $SN \rightarrow SN$. The scattering cross-section is given by,

$$\sigma_{S,N} = \frac{m_r^2}{4\pi} f_N^2 m_N^2 \left(\frac{\kappa}{M_{\text{DM}} M_h^2} \right)^2 \quad (6.7)$$

where $f_N \approx 0.3$ is the form factor of the nucleus. m_r represents the reduced mass of the nucleus and the scattered dark matter particle.

With the invisible Higgs decay width at LHC and non-observation of dark matter in the direct detection experiment at the LUX and including indirect Fermi-LAT

bounds, it has been shown in Refs. [132, 133] that the dark matter mass below 50 GeV and 70 – 110 GeV are excluded. In the table 6.1, few benchmark points have been shown for low dark matter mass less than the half of the Higgs mass. **FeynRules** [134] along with **micrOMEGAs** [135, 136] have been used to compute relic density of scalar DM in SM+ S model. The main dominant contributions to the relic density in these region is $SS \rightarrow b\bar{b}$.

M_{DM} (GeV)	κ	Relic density	σ_{SI} (cm ²)	Br($h \rightarrow SS$) in %
55	0.007	0.1242	1.3×10^{-46}	1.83
56	0.0045	0.1182	5.5×10^{-47}	0.72
58	0.0018	0.1199	8.2×10^{-48}	0.121
60	0.00075	0.1203	1.3×10^{-48}	0.013

Table 6.1: *Benchmark points with dark matter mass $M_{DM} < M_h/2$, which is allowed from the relic density constraint on the DM of WMAP and Planck, $\Omega h^2 = 0.1198 \pm 0.0026$ within 3σ confidence level, direct detection LUX (2013) and Higgs invisible decay width from the LHC.*

In Fig. 6.1, how the relic density changes with the dark matter mass in this model, has been shown. The plot generated for three different Higgs portal coupling $\kappa(M_Z) = 0.05$ (black), $\kappa(M_Z) = 0.10$ (brown), and $\kappa(M_Z) = 0.15$ (red). Here the blue band corresponds to the relic density constraints from WMAP and Planck data allowed at 3σ confidence level. The light red band region is excluded from the Higgs invisible decay width. For the $\kappa(M_Z) = 0.05$, one can see that there are four regions in dark matter mass which cross the blue band, i.e., satisfy the relic density in the right ballpark.

The dark matter mass near the 50 GeV, the dominant part in the annihilation of relic density is $SS \rightarrow b\bar{b}$ (79%), $SS \rightarrow W^\pm W^{\mp*2}$ (8%), $SS \rightarrow c\bar{c}$ (7%), however these regions are not allowed from Higgs invisible decay width as well as from the direct detection data. For 70 GeV, the process $SS \rightarrow b\bar{b}$ is about 52% and $SS \rightarrow W^\pm W^{\mp*}$

²The virtual $W^{\pm*}$ can decay to quarks and leptons.

is 40% of total annihilation cross-section. Whereas for the dark matter mass around 160 GeV, the dominant contributions in the annihilation are, $SS \rightarrow W^\pm W^\mp$ (48%), $SS \rightarrow hh$ (30%) and in $SS \rightarrow ZZ$ (22%) are allowed from direct searches. Similarly for other values of $\kappa(M_Z)$, the relic density in the right ballpark can be found near the dark matter mass 400 GeV and 500 GeV. In this case dominant contributions are $SS \rightarrow hh, t\bar{t}$.

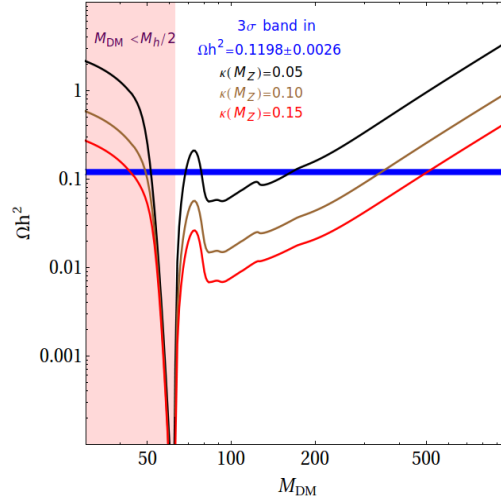


Figure 6.1: Dark matter relic density Ωh^2 as a function of the dark matter mass $M_{DM} (\equiv M_S)$ for different values of the portal coupling: $\kappa(M_Z) = 0.05$ (black), $\kappa(M_Z) = 0.10$ (brown), and $\kappa(M_Z) = 0.15$ (red). The thin blue band corresponds to the relic density of the dark matter, $\Omega h^2 = 0.1198 \pm 0.0026$ (3σ) of the present the Universe.

In Fig. 6.2, the relic density in $\kappa(M_Z) - M_{DM}$ plane for the high dark matter masses have been plotted. In this plot the blue line (upper dotted) corresponds to the relic density $\Omega h^2 = 0.112$ (minimum relic density allowed from WMAP and Planck) and other two belong to $\Omega h^2 = 0.1198$ and $\Omega h^2 = 0.1276$ (maximum) respectively. The relic density band is almost like a straight line because for $M_{DM} > M_W, M_h$, the annihilation cross-section is proportional to $\frac{\kappa^2}{M_{DM}^2}$.

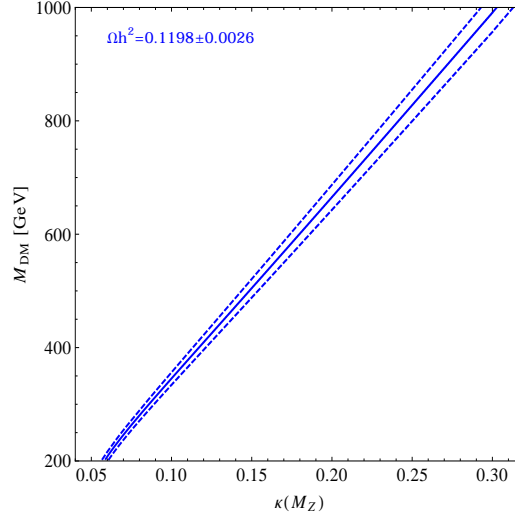


Figure 6.2: SM+S allowed parameter space in the $\kappa(M_Z) - M_{DM}$ plane in agreement with the relic density constraints, direct and indirect detection. Where the upper dotted, solid in the middle and the lower dotted blue line correspond to the relic density $\Omega h^2 = 0.112, 0.1198$ and 0.1276 respectively.

6.2.3 RGE running from $\mu = M_t$ to M_{Pl} in SM+S

The similar technique of the matching conditions of Section 5.2.1 has been used to calculate all the coupling at $\mu = M_t$. After knowing the values of various coupling constants at M_t , full three-loop SM RGEs and one-loop RGEs for the scalar S have been used to run them up to M_{Pl} .

M_S (GeV)	$\kappa(M_Z)$	$\lambda_S(M_Z)$	g_1	g_2	g_3	y_t	λ	κ	λ_S
620	0.185	1	0.478	0.506	0.487	0.382	-0.0029	0.424	4.66
795	0.239	0.389	0.478	0.506	0.487	0.382	0	0.412	1

Table 6.2: Values of all SM+S coupling constants at $M_{Pl} = 1.2 \times 10^{19}$ GeV with $M_t = 173.1$ GeV, $M_h = 125.7$ GeV and $\alpha_S(M_Z) = 0.1184$.

For SM+S, the running B.12 depends on the extra parameters M_S , $\kappa(M_Z)$ and $\lambda_S(M_Z)$. Assuming the values of SM parameters at M_t as given in eqns. 5.7– 5.11, for two different sets of M_S , $\kappa(M_Z)$ and $\lambda_S(M_Z)$, the values of all parameters at M_{Pl} in SM+S model in Table 6.2 has been presented. The first set stands for

our benchmark point, as described later. For this choice, $\lambda(M_{\text{Pl}})$ is negative. The second set is chosen such that $\lambda(M_{\text{Pl}}) = 0$. Note that as the running of new physics parameters is not considered till M_S , in this case it is all the same to specify these parameters either at M_Z or at M_t .

In the SM, the gauge couplings g_1, g_2, g_3 , top Yukawa coupling y_t do not vanish at M_{Pl} . The same is true in SM+S model [116], since running of these couplings are hardly affected by S , as displayed in Fig. 6.3. Higgs portal coupling κ and scalar self-quartic coupling λ_S increase with energy. The rise of λ_S is so rapid that it may render the theory nonperturbative at higher energies. For example, if $\lambda_S(M_Z) > 1.3$, λ_S becomes nonperturbative before M_{Pl} . Higgs self-quartic coupling λ also gets affected by inclusion of S . But the change is not visible in Fig. 6.3.

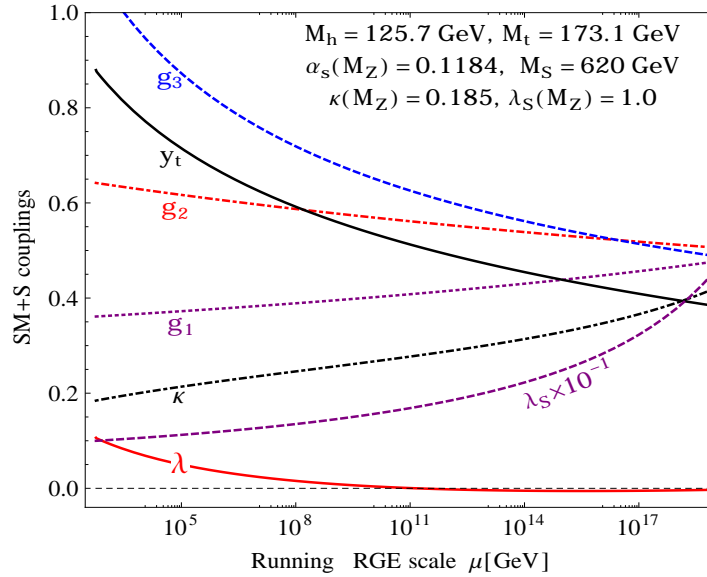


Figure 6.3: SM+S RG evolution of the gauge couplings g_1, g_2, g_3 , top Yukawa coupling y_t , Higgs self-quartic coupling λ , Higgs portal coupling κ and scalar self-quartic coupling λ_S in $\overline{\text{MS}}$ scheme.

As the issue of stability hinges on the value of λ at higher energies, the running of λ is focused for SM+S model in Fig. 6.4 as for the SM in Fig. 5.1(b), for a *benchmark*

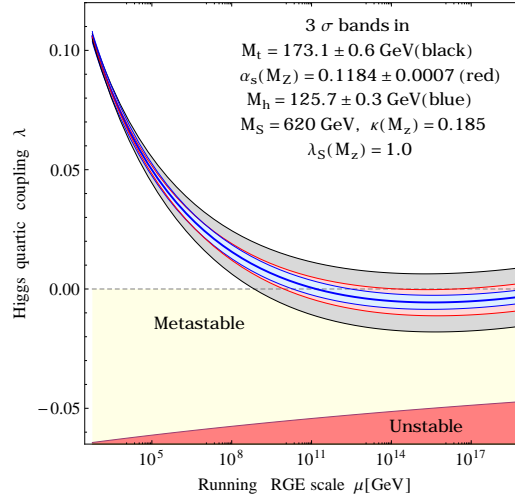


Figure 6.4: *RG evolution of λ in the SM+S for our benchmark point. 3σ bands for M_t , M_h and $\alpha_s(M_Z)$ are displayed.*

point $M_S = 620$ GeV, $\kappa(M_Z) = 0.185$ and $\lambda_S(M_Z) = 1$. It has been observed that the behavior of λ running might change significantly, modifying instability scale Λ_I to 1.68×10^{11} GeV, whereas in SM $\Lambda_I \sim 1.9 \times 10^{10}$ GeV (see eqn. 5.30). It has the potential to push out the EW vacuum from metastability to a stable vacuum. The benchmark point was chosen keeping in mind that the new physics effects are clearly visible, yet the vacuum is still in metastable state. This point also satisfies the WMAP and Planck imposed DM relic density constraint $\Omega h^2 = 0.1198 \pm 0.0026$ [21].

As defined in eqn. 6.3, λ_{eff} differs from λ as it takes care of loop corrections. In the SM, in Fig. 5.2, one can see that the difference $\lambda_{\text{eff}} - \lambda$ is always positive and negligible near M_{Pl} . Similar features has also been seen in SM+S model (see Fig. 6.5(a)). However, the instability scale Λ_I changes significantly if λ_{eff} instead of λ is chosen to work: In SM, the instability scale changes to 1.25×10^{11} GeV and in SM+S, it becomes 1.7×10^{12} GeV. Also β_λ has been plotted to show that at high energies, λ , λ_{eff} and β_λ all seem to vanish.

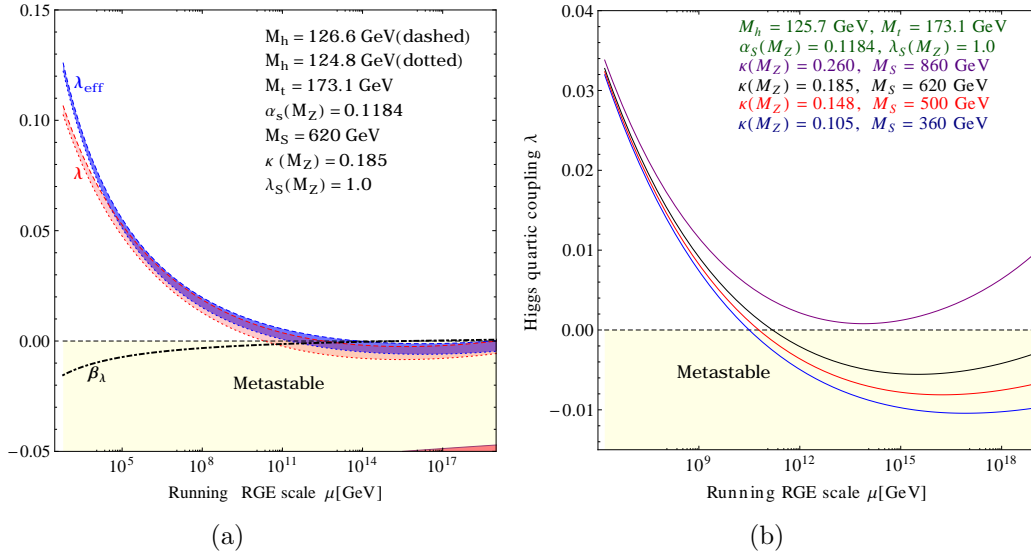


Figure 6.5: (a) *RG evolution of λ (red band), λ_{eff} (blue band) and β_λ (dot-dashed black) in SM+S for our benchmark point.* (b) *Evolution of λ for different $\kappa(M_Z)$. Each $\kappa(M_Z)$ corresponds to a specific M_S to satisfy DM relic density $\Omega h^2 \approx 0.1198$.*

In Fig. 6.5(b) the RGE running of λ for various new physics parameters has been displayed to explicitly demonstrate that as $\kappa(M_Z)$ increases, for a given energy, λ assumes a higher value [115, 137]. Finally, for some parameter space, λ never turns negative, implying stability of the EW vacuum. It happens due to the $\kappa^2/2$ term in β_λ . Due to this positive contribution, the presence of the scalar never drives EW vacuum towards instability. Next, the tunneling probability will be calculated to demonstrate stability issues with EW vacuum in this model SM+S.

6.2.4 Tunneling probability and Metastability in SM+S

The present data on M_h and M_t indicate that the Universe might be residing in a false vacuum in SM, waiting for a quantum tunneling to a true vacuum lying close to the Planck scale.

The vacuum decay probability \mathcal{P}_0 of EW vacuum at the present epoch is given in

eqn. 5.18. In $S(\Lambda_B) = \frac{8\pi^2}{3|\lambda(\Lambda_B)|}$, the effective Higgs quartic coupling as given in eqn. 6.3 has been used. The metastability and perturbativity constraints in this

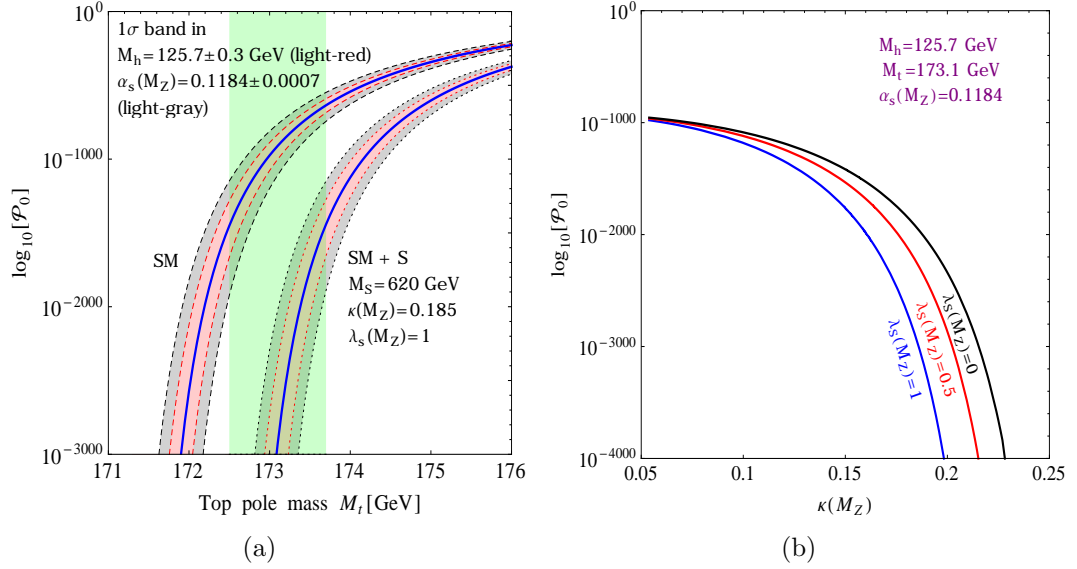


Figure 6.6: (a) Tunneling probability \mathcal{P}_0 as a function of M_t . The left band corresponds to SM and the right one to SM+S for our benchmark point. Light-green band stands for M_t at $\pm 1\sigma$. (b) \mathcal{P}_0 as a function of $\kappa(M_Z)$ for various $\lambda_S(M_Z)$.

model are shown here.

- If $\lambda(\Lambda_B) > \frac{4\pi}{3}$, $|\kappa| > 8\pi$, $|\lambda_S| > 8\pi$, then the theory is nonperturbative.
- If $\lambda(\Lambda_B) > 0$, then the vacuum is stable.
- If $0 > \lambda(\Lambda_B) > \lambda_{\min}(\Lambda_B)$, then the vacuum is metastable.
- If $\lambda(\Lambda_B) < \lambda_{\min}(\Lambda_B)$, then the vacuum is unstable.
- If $\lambda_S < 0$, the potential is unbounded from below along the S -direction.
- If $\kappa < 0$, the potential is unbounded from below along a direction in between S and H .

In Fig. 6.6 tunneling probability \mathcal{P}_0 as a function of M_t has been plotted. To calculate \mathcal{P}_0 , the minimum value of λ_{eff} (see eqn. 6.3) has been found and put the same in $S(\Lambda_B)$. The right band corresponds to the tunneling probability for our benchmark point. For comparison, the same plot for SM as the left band in Fig. 6.6(a) is shown. 1σ error bands in α_S and in M_h are also displayed. The error due to α_S is clearly more significant than that due to M_h . It has been observed that for a given M_t , these new physics effects lower the tunneling probability. It bolsters our earlier observation that scalar S helps the EW vacuum to come out of metastability. It has been demonstrated in Fig. 6.6(b), where \mathcal{P}_0 as a function of $\kappa(M_Z)$ for different choices of $\lambda_S(M_Z)$ has been plotted, assuming central values for M_h , M_t and α_S . It has been seen that for low values of $\kappa(M_Z)$, \mathcal{P}_0 tends to coincide with its SM value. For a given $\kappa(M_Z)$, for higher $\lambda_S(M_Z)$, \mathcal{P}_0 gets smaller, making the EW vacuum more stable.

6.2.5 Phase diagrams in SM+ S

The phase diagrams in different parameter planes for this model has been presented to demonstrate the stability of the EW vacuum.

In the SM, the phase diagram in $M_h - M_t$ plane is given in Fig. 5.5. Given the measured errors on M_t and M_h , the SM phase diagram indicates that the stability of EW vacuum is excluded³ at $\sim 3\sigma$. However, the extra scalar in this model modifies these findings, as illustrate by the phase diagram in the $M_h - M_t$ plane for SM+ S in Fig. 6.7. For our benchmark point, it has been seen that the boundaries shift towards higher values of M_t , so that the EW vacuum stability is excluded only at 1.1σ , indicated by the blue-dashed ellipse. For $M_S = 360$ GeV, $\kappa(M_Z) = 0.105$ and $\lambda_S(M_Z) = 1.6$, the plot is redrawn to highlight the fact that λ_S might turn out to be too large, so that the theory becomes nonperturbative (marked as the orange region in Fig. 6.7(b)). Here EW vacuum stability is excluded at 2σ . All these boundaries

³In a mass dependent renormalization scheme, such exclusion happens at 3.5σ [138].

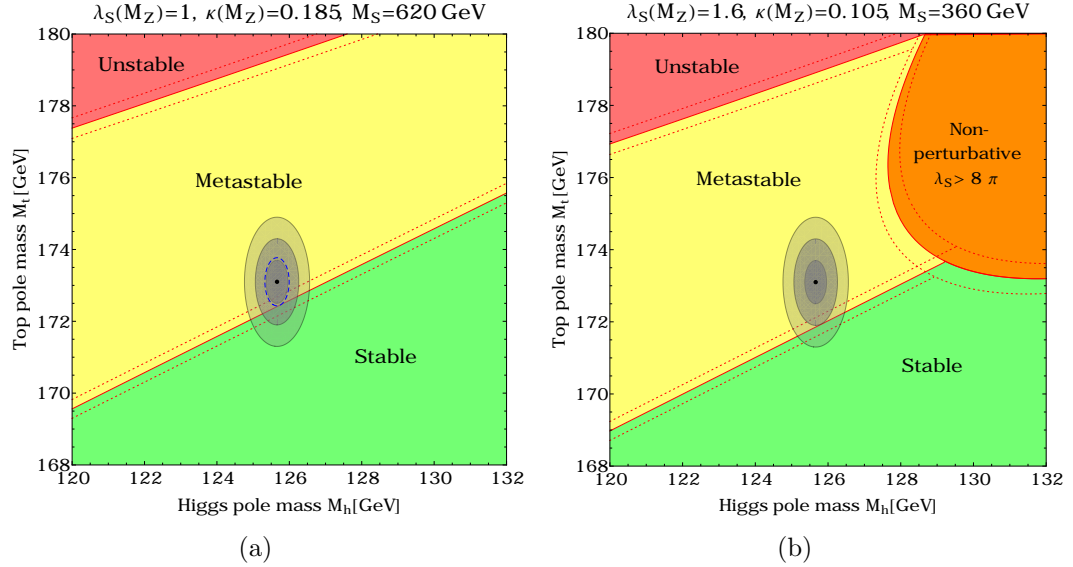


Figure 6.7: (a) In SM+S, regions of absolute stability (green), metastability (yellow), instability (red) of the EW vacuum in the $M_h - M_t$ plane phase diagram is presented for the benchmark point $M_S = 620$ GeV, $\kappa(M_Z) = 0.185$ and $\lambda_S(M_Z) = 1$. (b) Similar plot for $M_S = 360$ GeV, $\kappa(M_Z) = 0.105$ and $\lambda_S(M_Z) = 1.6$. The orange region corresponds to nonperturbative zone for λ_S . The three boundary lines (dotted, solid and dotted red) correspond to $\alpha_s(M_Z) = 0.1184 \pm 0.0007$. The gray areas denote the experimentally favored zones for M_h and M_t at 1, 2 and 3 σ .

separating various stability regions in the phase diagram depend on α_S . 1 σ bands for the same is also displayed in these figures.

Given the sizable error on $\alpha_S(M_Z)$, it is instructive to draw the phase diagram in the $M_t - \alpha_S(M_Z)$ plane as well. This diagram for SM is available in Fig. 5.6. The same is presented in Fig. 6.8 for this model using our benchmark point. With increase of $\kappa(M_Z)$ and/or $\lambda_S(M_Z)$, the boundaries between different stability regions shift towards right, allowing the EW vacuum to be more stable.

The phase diagram for $\kappa(M_Z) - M_S$ plane is displayed in Fig. 6.9. As addition of the scalar does not drive the EW vacuum towards instability, there is no unstable region marked on the plot. Between the dashed lines, the allowed region is marked

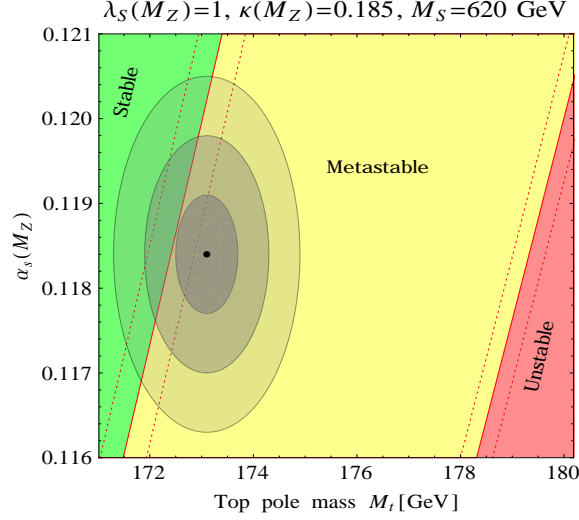


Figure 6.8: Phase diagram in $M_t - \alpha_S(M_Z)$ plane in SM+S model for our benchmark point. Regions of absolute stability (green), metastability (yellow), instability (red) of the EW vacuum are marked. The dotted lines correspond to $\pm 3\sigma$ variation in M_h and the gray areas denote the experimental allowed region for M_t and $\alpha_S(M_Z)$ at 1, 2 and 3σ .

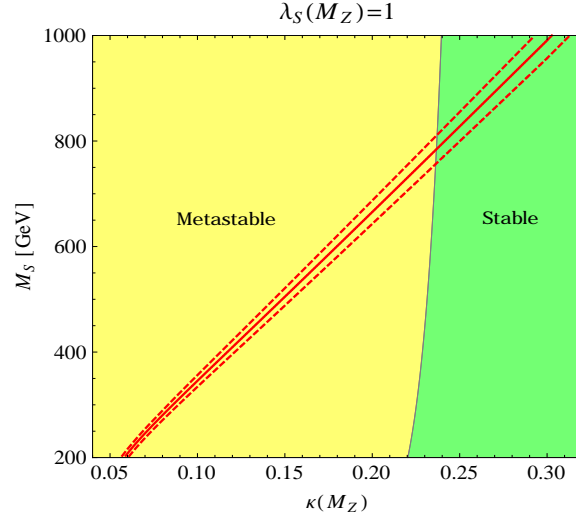


Figure 6.9: Phase diagram in $\kappa(M_Z) - M_S$ plane in SM+S. Regions of absolute stability (green), metastability (yellow) of the EW vacuum for $\lambda_S(M_Z) = 1$ are shown. The red solid line corresponds to $\Omega h^2 \approx 0.1198$. The red dashed lines correspond to 3σ error on Ωh^2 .

ensuing from relic density constraints.

In SM, the vacuum stability, metastability and perturbativity bound are given in eqns. 5.27– 5.29. In SM+ S model, change in M_h bounds with respect to $\kappa(M_Z)$ was considered in Refs. [117,129] for different cut-off scales, considering stability aspects only. As shown in Fig. 6.10, in presence of the scalar S , these bounds shift to lower values for larger $\kappa(M_Z)$. For large values of $\kappa(M_Z)$, depending on the choice of λ_S at M_Z , $\lambda_S(M_{\text{Pl}})$ may become so large that the theory becomes nonperturbative. This imposes further constraints on the parameter space, shown as the curved line representing $\lambda_S(M_{\text{Pl}}) = 8\pi$. As before, for a given $\kappa(M_Z)$, M_S is chosen in such a way that $\Omega h^2 \approx 0.1198$ for $M_h = 125.7$ GeV. However, in the plot, as M_h changes, Ωh^2 also changes. But this variation is contained within 3σ .

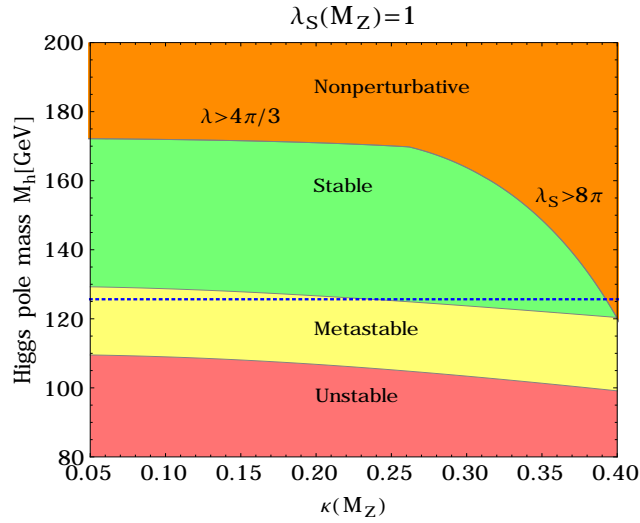


Figure 6.10: Phase diagram in $\kappa(M_Z) - M_h$ plane in SM+ S . Regions of absolute stability (green), metastability (yellow) and instability (red) of the EW vacuum for $\lambda_S(M_Z) = 1$ are displayed. λ and/or λ_S are/is nonperturbative in the orange region. The blue dashed line corresponds to $M_h = 125.7$ GeV.

6.2.6 Confidence level of vacuum stability in SM+S

As new physics effects do change the stability of EW vacuum, it is important to show the change in the confidence level at which stability is excluded or allowed. In Fig. 6.11, the confidence level against $\kappa(M_Z)$ has been plotted for $M_t = 173.1$ GeV, $M_h = 125.7$ GeV and $\alpha_S(M_Z) = 0.1184$. M_S is dictated by $\kappa(M_Z)$ to satisfy $\Omega h^2 \approx 0.1198$. For $\lambda_S(M_Z) = 1$, It has been seen that the EW vacuum becomes stable for $\kappa(M_Z) = 0.24$ onward. For a lower $\lambda_S(M_Z)$, this point shifts to a higher value. If $\lambda_S(M_Z) = 0$, stability is assured for $\kappa(M_Z) \geq 0.27$. Note that as κ dependence in RGE running of λ creeps in through the term $\kappa^2/2$ in β_λ , the stability strongly depends on $\kappa(M_Z)$. However, as β_λ depends on λ_S only *via* κ running, although λ_S running is relatively strong, the stability of EW vacuum does not change appreciably when $\lambda_S(M_Z)$ is varied from 0 to 1.

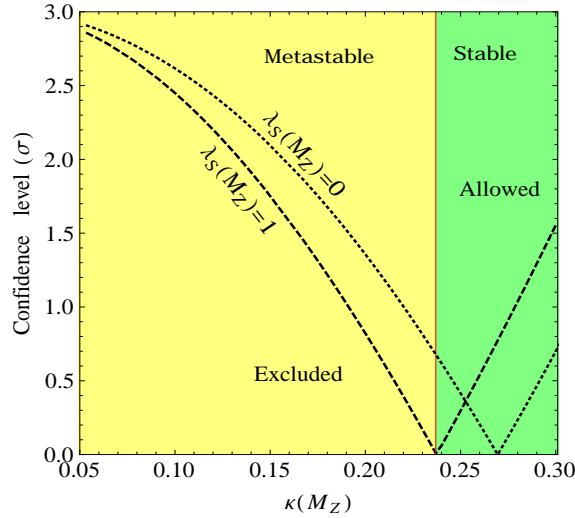


Figure 6.11: Dependence of confidence level (one-sided) at which EW vacuum stability is excluded/allowed on $\kappa(M_Z)$ in SM+S. Regions of absolute stability (green) and metastability (yellow) of EW vacuum are shown.

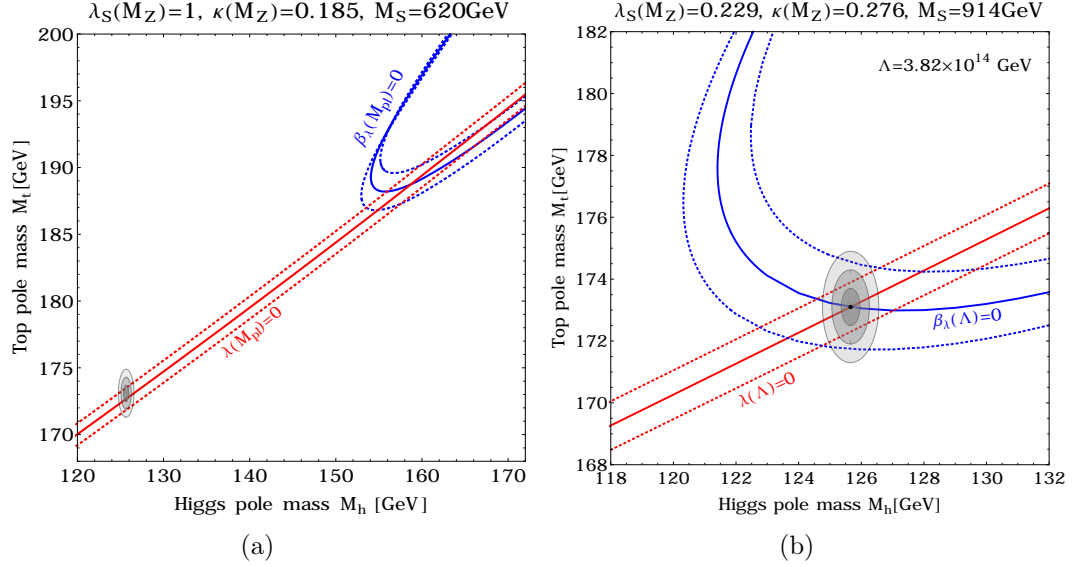


Figure 6.12: In SM+S model, **(a)** Contour plot for $\lambda(M_{\text{Pl}}) = 0$ (red line) and $\beta_\lambda(M_{\text{Pl}}) = 0$ (blue line) for our benchmark point. **(b)** Similar plot for $\lambda(\Lambda) = 0$ and $\beta_\lambda(\Lambda) = 0$, where $\Lambda = 3.8 \times 10^{14}$ GeV. Dotted lines correspond to $\pm 3\sigma$ variation in $\alpha_s(M_Z)$. The gray areas denote the experimental allowed region for M_h and M_t at 1, 2 and 3σ .

6.2.7 Asymptotic safety in SM+S

Shaposhnikov and Wetterich predicted [112] mass of the Higgs boson of 126 GeV imposing the constraint $\lambda(M_{\text{Pl}}) = \beta_\lambda(M_{\text{Pl}}) = 0$, in a scenario known as asymptotic safety of gravity. As mentioned before, this corresponds to two degenerate vacua. In Fig. 5.7, it has been shown that the present error in M_t and M_h does not allow this condition to be realised in SM. In SM+S model, the situation worsens [114] and it has demonstrated in Fig. 6.12(a) for our benchmark point. In presence of the scalar, the values of M_t and M_h , required to satisfy this condition, are pushed far away from the experimentally favored numbers: For our benchmark point this condition is satisfied at $M_h = 140.8$ GeV and $M_t = 179.5$ GeV.

However, it is possible to meet this condition at a lower energy than at M_{Pl} . In Fig. 6.12(b), it is demonstrated that at a different point in the parameter space:

$M_S = 914$ GeV, $\kappa(M_Z) = 0.276$ and $\lambda_S(M_Z) = 0.229$, the condition $\lambda(\Lambda) = \beta_\lambda(\Lambda) = 0$ is indeed satisfied at $\Lambda = 3.8 \times 10^{14}$ GeV and is also consistent with experimentally allowed range for M_t and M_h . The value of Λ decreases with $\lambda_S(M_Z)$ and $\kappa(M_Z)$. The corresponding value of M_S is chosen to satisfy relic density of DM constraints. Also, it is difficult to simultaneously satisfy Veltman condition at M_{Pl} [114]. All these observations indicate that some new physics could be operational at very high energies to take care of such issues.

6.3 Doublet scalar extension of SM

The model is popularly known in the literature as the inert doublet (ID) model, first proposed by Deshpande and Ma [70].

In previous Section 6.2, stability analysis, including NNLO corrections, has done for extended singlet scalar DM model. The stability of the EW vacuum was shown to depend on new physics parameters. In this section such an analysis has been extended to the ID model. It has been assumed that ID DM is the only DM particle which saturates the entire DM relic density. In this context, the constraints on the parameters of the ID model have been reviewed.

A detailed study on the ID parameter space was performed in Refs. [89, 139–147] indicating bounds from absolute EW vacuum stability, perturbativity, collider study, EW precision tests (EWPT), etc. In this work [36], the new parameter spaces have been found allowing the metastability of the Higgs potential.

6.3.1 Inert Doublet Model

In this model, the standard model is extended by adding an extra $SU(2)_L$ doublet scalar, odd under an additional discrete Z_2 symmetry. The Z_2 symmetry prohibits the inert doublet to acquire a vacuum expectation value.

The scalar potential of eqn. 3.4 at the tree level with exact Z_2 symmetry, is given⁴ by,

$$V(\Phi_1, \Phi_2) = m_{11}^2 |\Phi_1|^2 + \lambda_1 |\Phi_1|^4 + m_{22}^2 |\Phi_2|^2 + \lambda_2 |\Phi_2|^4 \\ + \lambda_3 |\Phi_1|^2 |\Phi_2|^2 + \lambda_4 |\Phi_1^\dagger \Phi_2|^2 + \frac{\lambda_5}{2} [(\Phi_1^\dagger \Phi_2)^2 + h.c.] , \quad (6.8)$$

where the SM Higgs doublet Φ_1 and the inert doublet Φ_2 are given by

$$\Phi_1 = \begin{pmatrix} G^+ \\ \frac{1}{\sqrt{2}}(v + h + iG^0) \end{pmatrix}, \quad \Phi_2 = \begin{pmatrix} H^+ \\ \frac{1}{\sqrt{2}}(H + iA) \end{pmatrix}.$$

Φ_2 contains a CP even neutral scalar H , a CP odd neutral scalar A , and a pair of charged scalar fields H^\pm . The Z_2 symmetry prohibits these particles to decay entirely to SM particles. The lightest of H and A can then serve as a DM candidate.

After EW symmetry breaking, the scalar potential is given by

$$V(h, H, A, H^\pm) = \frac{1}{4} [2m_{11}^2 (h + v)^2 + \lambda_1 (h + v)^4 + 2m_{22}^2 (A^2 + H^2 + 2H^+ H^-) \\ + \lambda_2 (A^2 + H^2 + 2H^+ H^-)^2] \\ + \frac{1}{2} (h + v)^2 [\lambda_3 H^+ H^- + \lambda_S A^2 + \lambda_L H^2] \quad (6.9)$$

where,

$$\lambda_{L,S} = \frac{1}{2} (\lambda_3 + \lambda_4 \pm \lambda_5) . \quad (6.10)$$

Masses of these scalars are given by,

$$M_h^2 = m_{11}^2 + 3\lambda_1 v^2, \\ M_H^2 = m_{22}^2 + \lambda_L v^2, \\ M_A^2 = m_{22}^2 + \lambda_S v^2, \\ M_{H^\pm}^2 = m_{22}^2 + \frac{1}{2} \lambda_3 v^2.$$

For $\lambda_4 - \lambda_5 < 0$ and $\lambda_5 > 0$ ($\lambda_4 + \lambda_5 < 0$ and $\lambda_5 < 0$), A (H) is the lightest Z_2 odd particle (LOP). In this work, A has been taken as the LOP and hence, as a viable DM candidate. Choice of H as LOP will lead to similar results.

For large DM mass, $M_A \gg M_Z$, appropriate relic density of DM is obtained if

⁴Here the notation of Higgs quartic coupling λ_1 is used instead of λ .

M_A , M_H , and M_{H^\pm} are nearly degenerate that will be explained latter. Hence, in anticipation, one can define,

$$\begin{aligned}\Delta M_H &= M_H - M_A, \\ \Delta M_{H^\pm} &= M_{H^\pm} - M_A.\end{aligned}$$

so that the new independent parameters for the ID model become $\{M_A, \Delta M_H, \Delta M_{H^\pm}, \lambda_2, \lambda_S\}$. Here λ_S is chosen as A is treated as the DM particle.

The one-loop effective potential for h in the $\overline{\text{MS}}$ scheme and the Landau gauge is given by

$$V_1^{\text{SM+ID}}(h) = V_1^{\text{SM}}(h) + V_1^{\text{ID}}(h) \quad (6.11)$$

The SM one-loop effective Higgs potential $V_1^{\text{SM}}(h)$ can be found in eqn. 5.2 and the additional contribution to the one-loop effective potential due to the inert doublet is given by [145]

$$V_1^{\text{ID}}(h) = \sum_{j=H,A,H^+,H^-} \frac{1}{64\pi^2} M_j^4(h) \left[\ln \left(\frac{M_j^2(h)}{\mu^2(t)} \right) - \frac{3}{2} \right] \quad (6.12)$$

where,

$$M_j^2(h) = \frac{1}{2} \lambda_j(t) h^2(t) + m_{22}^2(t) \quad (6.13)$$

with $\lambda_A(t) = 2\lambda_S(t)$, $\lambda_H(t) = 2\lambda_L(t)$, and $\lambda_{H^\pm}(t) = \lambda_3(t)$.

In the present work, in the Higgs effective potential, SM contributions are taken at the two-loop level, whereas the ID scalar contributions are considered at one loop only.

For $h \gg v$, the Higgs effective potential can be approximated as

$$V_{\text{eff}}^{\text{SM+ID}}(h) \simeq \lambda_{1,\text{eff}}(h) \frac{h^4}{4}, \quad (6.14)$$

with

$$\lambda_{1,\text{eff}}(h) = \lambda_{1,\text{eff}}^{\text{SM}}(h) + \lambda_{1,\text{eff}}^{\text{ID}}(h), \quad (6.15)$$

where $\lambda_{1,\text{eff}}^{\text{SM}}$ can be found in eqn. B.1 and,

$$\lambda_{1,\text{eff}}^{\text{ID}}(h) = \sum_{j=L,S,3} e^{4\Gamma(h)} \left[\frac{\delta_j \lambda_j^2}{64\pi^2} \left(\ln(\delta_j \lambda_j) - \frac{3}{2} \right) \right]. \quad (6.16)$$

Here $\delta_j = 1$ when $j = L, S$; $\delta_j = \frac{1}{2}$ for $j = 3$; and anomalous dimension $\gamma(\mu)$ of the Higgs field takes care of its wave function renormalization (see the Appendix). As quartic scalar interactions do not contribute to wave function renormalization at the one-loop level, ID does not alter $\gamma(\mu)$ of the SM. All running coupling constants are evaluated at $\mu = h$.

If DM mass M_A is larger than M_t , then the ID starts to contribute after the energy scale M_A . For $M_A < M_t$, the contributions of ID to the β -functions (see eqns. B.14–B.18) are rather negligible for the running from M_A to M_t , as is evident from the expressions.

To compute the RG evolution of all the couplings, all the couplings with threshold corrections at M_t has been calculated. In Table 6.3 a specific set of values of λ_i at $M_t = 173.1$ GeV and at $M_{\text{Pl}} = 1.2 \times 10^{19}$ GeV for $M_h = 125.7$ GeV and $\alpha_s(M_Z) = 0.1184$ have been provided. In Fig. 6.13 the running of the scalar couplings (λ_i) has been shown for this set of parameters. It has been seen that for this specific choice of parameters, λ_1 assumes a small negative value leading to a metastable EW vacuum as discussed in the following sections. This set is chosen to reproduce the DM relic density in the right ballpark.

	λ_S	λ_L	λ_2	λ_3	λ_4	λ_5	λ_1
M_t	0.001	0.039	0.10	0.0399	0.00003	0.038	0.127
M_{Pl}	0.046	0.082	0.127	0.090	0.038	0.036	−0.009

Table 6.3: A set of values of all ID model coupling constants at M_t and M_{Pl} for $M_A = 573$ GeV, $\Delta M_{H^\pm} = 1$ GeV, $\Delta M_H = 2$ GeV, and $\lambda_S(M_Z) = 0.001$.

6.3.2 Constraints on ID model

ID model parameter space is constrained from theoretical considerations like absolute vacuum stability, perturbativity and unitarity of the scattering matrix. EW precision measurements and direct search limits at LEP, LHC put severe restric-

tions on the model. The recent measurements of Higgs decay width at the LHC put additional constraints. The requirement that the ID DM saturates the DM relic density all alone restricts the allowed parameter space considerably. The tree level vacuum stability bound of the ID model can be found in eqn. 3.9. The unitary (eqn. 3.12) and perterbativity (eqn. 3.10) bounds up to the M_{Pl} have also been taken into account.

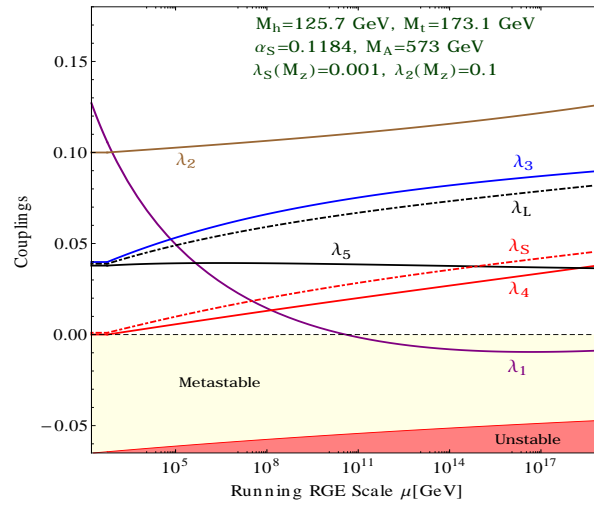


Figure 6.13: IDM RG evolution of the couplings λ_i ($i = 1, \dots, 5$), λ_L , λ_S for the set of parameters in Table 6.3.

6.3.2.1 Bounds from electroweak precision experiments

Bounds ensuing from electroweak precision experiments are imposed on new physics models *via* Peskin-Takeuchi [30] S , T , U parameters. The additional contributions from 2HDM can be found in eqn. 3.13, which are modified for ID model [72, 148] as,

$$\Delta S = \frac{1}{2\pi} \left[\frac{1}{6} \ln \left(\frac{M_H^2}{M_{H^\pm}^2} \right) - \frac{5}{36} + \frac{M_H^2 M_A^2}{3(M_A^2 - M_H^2)^2} + \frac{M_A^4 (M_A^2 - 3M_H^2)}{6(M_A^2 - M_H^2)^3} \ln \left(\frac{M_A^2}{M_H^2} \right) \right],$$

$$\Delta T = \frac{1}{32\pi^2 \alpha v^2} \left[F(M_{H^\pm}^2, M_A^2) + F(M_{H^\pm}^2, M_H^2) - F(M_A^2, M_H^2) \right] \quad (6.17)$$

The NNLO global electroweak fit results of ΔS , ΔT and ΔU are given eqn. 3.16 have been used, with a correlation coefficient of +0.91, fixing ΔU to zero. The contribution of the scalars in the ID model to ΔU is rather negligible. To assess the

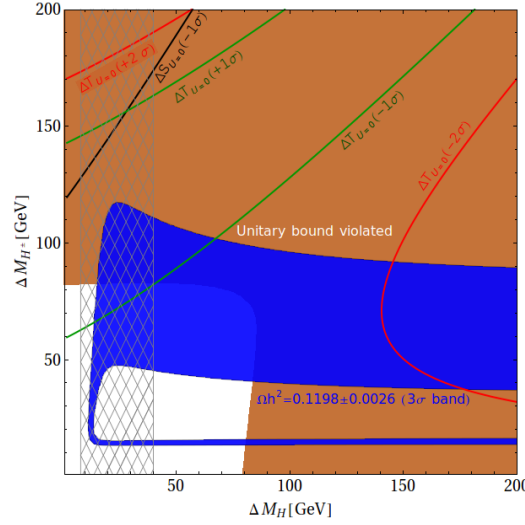


Figure 6.14: Allowed parameter space in $\Delta M_{H^\pm} - \Delta M_H$ plane for $M_A = 70$ GeV and $\lambda_S = 0.007$ in IDM. Constraints from S and T parameters are shown by solid black, green and red lines. The blue band corresponds the 3σ variation in $\Omega h^2 = 0.1198 \pm 0.0026$ [21]. On the brown region the unitarity bound is violated on or before M_{Pl} . The cross-hatched region is excluded from LEP II data.

implications of S and T constraints on the ID model, in Fig. 6.14, in the $\Delta M_{H^\pm} - \Delta M_H$ plane, various constraints is displayed for $M_A = 70$ GeV and $\lambda_S = 0.007$. This is the maximum value of λ_S for the given DM mass, allowed by LUX [53] direct detection data at 1σ . The blue region allowed by relic density constraints shifts upwards for smaller λ_S . Constraints on ΔS and ΔT , as mentioned in eqn. 3.16, are marked as black, green, and red solid lines. It has been seen that the 1σ bound on ΔT is the most stringent one. The black line corresponding to the lower limit on ΔS at 1σ can also be interesting. But the LEP II bounds, represented by the cross-hatched bar, take away a considerable part. The line representing the ΔS upper limit is beyond the region considered and lies towards the bottom-right corner of

the plot. In this plot, increasing M_H enhances S , but T gets reduced. In addition, if one demand unitarity constraints to be respected up to M_{Pl} , assuming no other new physics shows up in between, the parameter space gets severely restricted. In this plot, a small window is allowed by ΔT only at 2σ , which satisfies DM relic density constraints. As mentioned earlier, this window gets further reduced with smaller λ_S (the relic density band takes an “L” shape as shown in Fig. 6.18).

6.3.2.2 Direct search limits from LEP and LHC

The decays $Z \rightarrow AH$, $Z \rightarrow H^+H^-$, $W^\pm \rightarrow AH^\pm$, and $W^\pm \rightarrow HH^\pm$ are restricted from Z and W^\pm decay widths at LEP. It implies $M_A + M_H \geq M_Z$, $2M_{H^\pm} \geq M_Z$, and $M_{H^\pm} + M_{H,A} \geq M_W$. More constraints on the ID model can be extracted from chargino [149] and neutralino [150] search results at LEP II: The charged Higgs mass $M_{H^\pm} \geq 70$ GeV. The bound on M_A is rather involved: If $M_A < 80$ GeV, then ΔM_H should be less than ~ 8 GeV, or else M_H should be greater than ~ 110 GeV (see Fig. 6.17). The Run 1 of LHC data provide significant constraints on the ID parameter space through the direct searches in final states with two leptons plus missing transverse energy [151]. These analyses exclude inert scalar masses of up to about 55 GeV. For $M_{H^\pm} = 85$ GeV and $M_A = 55$ GeV, the $M_H \lesssim 145$ GeV are excluded at 4σ and for $M_A > 60$ GeV all masses of H are allowed. For $M_{H^\pm} > 150$ GeV with $M_A = 55$ GeV, $115 \lesssim M_H \lesssim 160$ GeV region is excluded and $M_A > 80$ GeV all masses of H are allowed.

6.3.2.3 Bounds from LHC diphoton signal strength

In the ID model, Higgs to diphoton signal strength $\mu_{\gamma\gamma}$ is defined as

$$\mu_{\gamma\gamma} = \frac{\sigma(gg \rightarrow h \rightarrow \gamma\gamma)}{\sigma(gg \rightarrow h \rightarrow \gamma\gamma)_{\text{SM}}} \approx \frac{Br(h \rightarrow \gamma\gamma)_{\text{ID}}}{Br(h \rightarrow \gamma\gamma)_{\text{SM}}} \quad (6.18)$$

using the narrow width approximation for the production cross-section of $\sigma(gg \rightarrow h \rightarrow \gamma\gamma)$ and the fact that $\sigma(gg \rightarrow h)$ in both the SM and ID are the same.

Now if the ID particles have masses less than $M_h/2$, $h \rightarrow \text{ID}$, ID decays are allowed.

In that case,

$$\mu_{\gamma\gamma} = \frac{\Gamma(h \rightarrow \gamma\gamma)_{\text{ID}}}{\Gamma(h \rightarrow \gamma\gamma)_{\text{SM}}} \frac{\Gamma_{\text{tot}}(h \rightarrow \text{SM}, \text{SM})}{\Gamma_{\text{tot}}(h \rightarrow \text{SM}, \text{SM}) + \Gamma_{\text{tot}}(h \rightarrow \text{ID}, \text{ID})}, \quad (6.19)$$

where [152]

$$\Gamma(h \rightarrow \text{ID}, \text{ID}) = \frac{v^2}{16\pi M_h} \lambda_{\text{ID}}^2 \left(1 - \frac{4M_{\text{ID}}^2}{M_h^2}\right)^{1/2}, \quad (6.20)$$

where for $\text{ID} = A, H, H^\pm$, $\lambda_{\text{ID}} = \lambda_S, \lambda_L, \sqrt{2}\lambda_3$.

In this case, the ID particles are heavier than $M_h/2$,

$$\mu_{\gamma\gamma} = \frac{\Gamma(h \rightarrow \gamma\gamma)_{\text{ID}}}{\Gamma(h \rightarrow \gamma\gamma)_{\text{SM}}}. \quad (6.21)$$

In the ID model, the H^\pm gives additional contributions at one loop. The analytical expression is given by [153–155]

$$\Gamma(h \rightarrow \gamma\gamma)_{\text{ID}} = \frac{\alpha^2 m_h^3}{256\pi^3 v^2} \left| \sum_f N_f^c Q_f^2 y_f F_{1/2}(\tau_f) + y_W F_1(\tau_W) + Q_{H^\pm}^2 \frac{v \mu_{hH^+H^-}}{2m_{H^\pm}^2} F_0(\tau_{H^\pm}) \right|^2 \quad (6.22)$$

where $\tau_i = m_i^2/4m_h^2$. Q_f, Q_{H^\pm} denote electric charges of corresponding particles. N_f^c is the color factor. y_f and y_W denote Higgs couplings to $f\bar{f}$ and WW . $\mu_{hH^+H^-} = \lambda_3 v$ stands for the coupling constant of the hH^+H^- vertex. The loop functions $F_{(0,1/2,1)}$ are defined as

$$F_0(\tau) = -[\tau - f(\tau)]\tau^{-2},$$

$$F_{1/2}(\tau) = 2[\tau + (\tau - 1)f(\tau)]\tau^{-2},$$

$$F_1(\tau) = -[2\tau^2 + 3\tau + 3(2\tau - 1)f(\tau)]\tau^{-2},$$

where,

$$f(\tau) = \begin{cases} (\sin^{-1} \sqrt{\tau})^2, & \tau \leq 1 \\ -\frac{1}{4}[\ln 1 + \frac{\sqrt{1-\tau^{-1}}}{1} - \sqrt{1-\tau^{-1}} - i\pi]^2, & \tau > 1 \end{cases}, \quad (6.23)$$

From the diphoton decay channel of the Higgs at the LHC, the measured values are $\mu_{\gamma\gamma} = 1.17 \pm 0.27$ from ATLAS [156] and $\mu_{\gamma\gamma} = 1.14_{-0.23}^{+0.26}$ from CMS [157].

One can see that a positive λ_3 leads to a destructive interference between SM and ID contributions in eqn. 6.22 and *vice versa*. Hence, for ID particles heavier than $M_h/2$, $\mu_{\gamma\gamma} < 1$ ($\mu_{\gamma\gamma} > 1$) when λ_3 is positive (negative). However, if these ID particles

happen to be lighter than $M_h/2$, they might contribute to the invisible decay of the Higgs boson. Using the global fit result [131] that such an invisible branching ratio is less than $\sim 20\%$, in eqn. 6.19, the second ratio provides a suppression of $\sim 0.8 - 1$.

Now can negative λ_3 is allowed in the ID model? It will be discussed at the end of this section. The benchmark points with positive λ_3 is used here, allowed at 1σ by both CMS and ATLAS experiments.

6.3.2.4 Constraints from dark matter relic density and direct search limits

As it has been seen that Higgs can decay to pair of inert particles (see eqns. 6.9, 6.20), so most of the parameter spaces with dark matter mass less than $M_h/2$, are strictly restricted from the Higgs invisible decay width of LHC and also from the direct detection experimental data. In this model the dark matter mass below 50 GeV are excluded from these constraints. In Table 6.4, few benchmark points for IDM with the dark matter mass, $M_A(\equiv M_{DM}) < M_h/2$ have been shown.

The heavy CP -even and charge Higgs mass have been fixed at 180 and 200 GeV respectively. The relic density, dark matter-nucleon cross-section, as well as the branching ratio of Higgs to pair of dark matter particles have been shown in the same table. For all these points, it has been seen that the dominant process in the dark matter annihilation is $AA \rightarrow b\bar{b}$.

The ID dark matter candidate A can self-annihilate into SM fermions. Once the DM mass is greater than the W^\pm -mass, so that the DM can annihilate into a pair of W^\pm bosons, the cross-section increases significantly, thereby reducing DM relic density. Hence, it becomes difficult to saturate Ωh^2 after ~ 75 GeV with positive λ_S , although for $M_A < 75$ GeV, both signs of λ_S can be allowed to arrive at the right DM relic density Ωh^2 .

$M_{DM}(\equiv M_A)$ (GeV)	λ_S	Relic density	σ_{SI} (cm ²)	Br($h \rightarrow SS$) in %
54.7	0.004	0.1263	1.78×10^{-46}	3.67
56	0.0022	0.1197	3.47×10^{-48}	1.05
58.8	0.0006	0.1222	2.4×10^{-48}	0.06
60	0.00035	0.1236	1.13×10^{-48}	0.017

Table 6.4: *Benchmark points with dark matter mass $M_{DM} < M_h/2$, with $M_{H^\pm} = 200$ GeV and $M_{H^\pm} = 180$ GeV, which is allowed from the relic density constraint of WMAP and Planck, $\Omega h^2 = 0.1198 \pm 0.0026$ within 3σ confidence level, direct detection LUX (2013) and Higgs invisible decay width from the LHC.*

The role of the sign of λ_S can be understood from the contributing diagrams to the $AA \rightarrow W^+W^-$ annihilation processes. Four diagrams contribute: the AAW^+W^- vertex driven point interaction diagram (henceforth referred to as the p -channel diagram), H^+ -mediated t - and u -channel diagrams, and the h -mediated s -channel diagram. For $AA \rightarrow ZZ$ annihilation, the t - and u -channel diagrams are mediated by H . A negative λ_S induces a destructive interference between the s -channel diagram with the rest, thereby suppressing $AA \rightarrow W^+W^-, ZZ$ processes. For DM masses of $75 - 100$ GeV, this can be used to get the appropriate Ωh^2 [140, 158]. To avoid large contributions from t - and u -channel diagrams and coannihilation diagrams, the values of M_H and M_{H^\pm} can be pushed to be rather large $\gtrsim 500$ GeV. However, to partially compensate the remaining p -channel diagram by the s -channel one, λ_S assumes a large negative value ~ -0.1 , which is ruled out by the DM direct detection experiments. That is why in the ID model, DM can be realized below 75 GeV, a regime designated as the “low” DM mass region.

At “high” DM mass $M_A \gtrsim 500$ GeV, one can get the right Ωh^2 due to a partial cancellation between different diagrams contributing to the $AA \rightarrow W^+W^-$ and $AA \rightarrow ZZ$ annihilation processes. For example, in $AA \rightarrow W^+W^-$, the p -channel diagram tends to cancel with the H^+ -mediated t - and u -channel diagrams [142, 159] in the limit $M_A \gg M_W$, and the sum of amplitudes of these diagrams in this

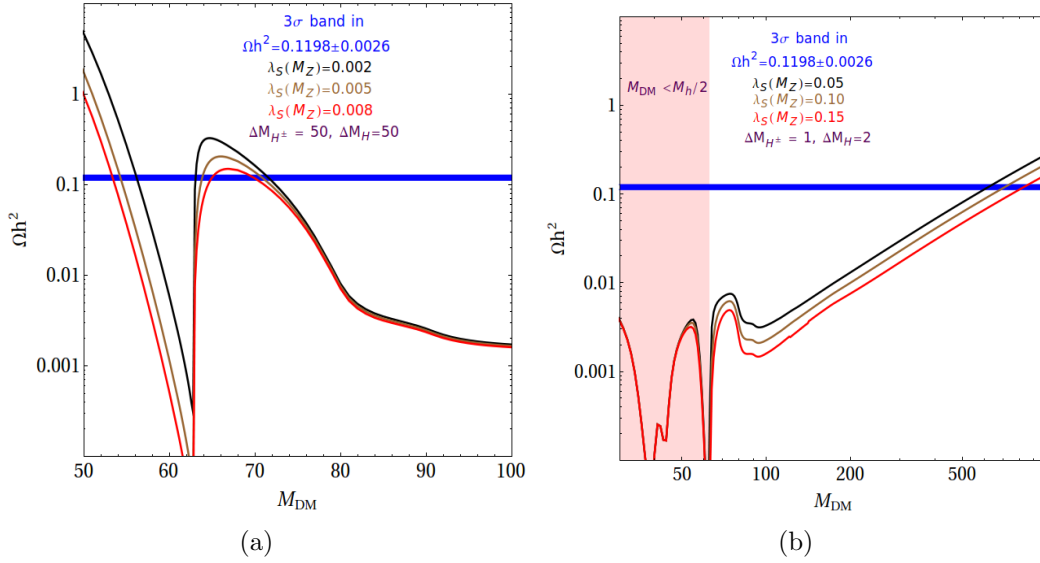


Figure 6.15: In IDM, (a) Dark matter relic density Ωh^2 as a function of the dark matter mass $M_{DM} (\equiv M_A)$ for different values of the Higgs portal coupling: $\lambda_S(M_Z) = 0.002$ (black), $\lambda_S(M_Z) = 0.005$ (brown), and $\lambda_S(M_Z) = 0.008$ (red), with $\Delta M_{H^\pm} = \Delta M_H = 50$ GeV. (b) For Higgs portal coupling: $\lambda_S(M_Z) = 0.05$ (black), $\lambda_S(M_Z) = 0.10$ (brown), and $\lambda_S(M_Z) = 0.15$ (red), with $\Delta M_{H^\pm} = 1$ GeV and $\Delta M_H = 2$ GeV. The thin blue band corresponds to the relic density of the dark matter, $\Omega h^2 = 0.1198 \pm 0.0026$ (3σ) of the present the Universe. Light red band is disallowed from the Higgs invisible decay width.

limit is proportional to $M_{H^\pm}^2 - M_A^2$. Hence, at high M_A , a partial cancellation between these diagrams is expected for nearly degenerate M_{H^\pm} and M_A . Similarly, for $AA \rightarrow ZZ$, a cancellation is possible when the masses M_H and M_A are close by. For $M_A \gtrsim 500$ GeV, keeping the mass differences of M_{H^\pm} and M_H with M_A within 8 GeV, such cancellations help reproduce the correct Ωh^2 . It is nevertheless worth mentioning that such nearly degenerate masses will lead to coannihilation of these Z_2 odd ID scalars [160] to SM particles. Despite such near-degeneracy, both H and H^+ , being charged under the same Z_2 as A , decay promptly to the LOP A , so that they do not become relics. **FeynRules** [134] along with **micrOMEGAs** [135, 136] used to compute the relic density of A .

In Fig. 6.15, the relic density against the dark matter mass have been shown. For Fig. 6.15(a), $\Delta M_{H^\pm} = \Delta M_H = 50$ GeV have been chosen, so the relic density is mainly dominated by the self-annihilation of the dark matter candidate. For three different values of Higgs portal coupling, $\lambda_S = 0.002, 0.005, 0.008$, the relic density turns out in the right ballpark for the dark matter mass $65 - 70$ GeV. The dominant annihilation channels are, $AA \rightarrow b\bar{b}, W^\pm W^\mp$. Fig. 6.15(b), the relic density is in the right ballpark with dark matter mass around 600 GeV. In this case both the co-annihilation and annihilation of the dark matter play important role. In this region inert particles annihilate mainly to $W^\pm W^\mp, ZZ, hh$. The blue band corresponds to the constraints coming from the WMAP and Planck data. The region which is allowed from the relic density is also allowed from the direct search of the dark matter.

DM direct detection experiments involve the h -mediated t -channel process $AN \rightarrow AN$ with a cross-section proportional to λ_S^2/M_A^2 in the limit $M_A \gg m_N$:

$$\sigma_{A,N} = \frac{m_r^2}{\pi} f_N^2 m_N^2 \left(\frac{\lambda_S}{M_A M_h^2} \right)^2 \quad (6.24)$$

where $f_N \approx 0.3$ is the form factor of the nucleus. m_r represents the reduced mass of the nucleus and the scattered dark matter particle.

Thus, λ_S is constrained from non observation of DM signals at XENON100 [50, 51] and LUX [53]. For $M_A = 70$ GeV, the ensuing bound from LUX [52, 53] data at 1σ is $|\lambda_S| < 0.007$.

The constraint on λ_S from DM direct detection experiments gets diluted with M_A [see eqn. 6.24]. Hence, for low DM mass, direct detection bounds are more effective. At high mass, the relic density constraints are likely to supersede these bounds. For example, for $M_{DM} = 573$ GeV, the upper limit on $|\lambda_S|$ is 0.138 from LUX. However, to satisfy the relic density constraints from the combined data of WMAP and Planck within 3σ , λ_S can be as large as 0.07 only.

Within the framework of the ID model, it is possible to explain the observations in various indirect DM detection experiments [143, 161] for some regions of the parameter space. In this work, such details have not included as such estimations involve proper understanding of the astrophysical backgrounds and an assumption of the DM halo profile which contain some arbitrariness. For a review of constraints on the ID model from astrophysical considerations see, for example, Ref. [162].

Sign of λ_3

Whether λ_3 can be taken as positive or negative depends on the following:

- If the ID model is not the answer to the DM puzzle, so that both relic density and direct detection constraints can be evaded, no restriction exists on the possible sign of $\lambda_3(M_Z)$. Otherwise, the following two cases need be considered:

- A negative $\lambda_3(M_Z)$ implies

$$\lambda_S(M_Z) < -\frac{1}{v^2}(M_{H^\pm}^2 - M_A^2).$$

As A is considered as the DM candidate, so that $M_A < M_{H^\pm}$, $\lambda_S(M_Z)$ is always negative when $\lambda_3(M_Z) < 0$. For low DM mass, the splitting $(M_{H^\pm} - M_A) \gtrsim 10$ GeV, as otherwise DM coannihilation processes cause an inappreciable depletion in Ωh^2 . For $M_A = 70$ GeV, this implies a lower bound $\lambda_S(M_Z) \lesssim -0.025$, which violates the DM direct detection bound $|\lambda_S| < 0.007$. Hence, for low DM mass, a negative $\lambda_3(M_Z)$ is not feasible.

- For high mass DM, the right relic density can be obtained when the splitting $(M_{H^\pm} - M_A) \sim$ a few GeV or less. The above logic then implies that a negative λ_3 does not put any severe restriction on λ_S to contradict DM direct detection bounds as earlier. Hence, for a high DM mass, $\lambda_3(M_Z)$

can assume both the signs. Moreover, due to propagator suppression for large M_{H^\pm} in the $h\gamma\gamma$ vertex, the ID contribution to $\mu_{\gamma\gamma}$ is negligibly small and hence, the sign of $\lambda_3(M_Z)$ is not constrained by measurements on $\mu_{\gamma\gamma}$ as well.

- If at any scale, λ_3 is negative while $\lambda_1 > 0$, then the bound (3.9) must be respected.
- If at some scale, $\lambda_1 < 0$, then a negative λ_3 makes the potential unbounded from below, as mentioned in the following section. This means one can start with a negative $\lambda_3(M_Z)$, but with RG evolution when λ_1 turns negative, λ_3 evaluated at that scale must be positive. Such parameter space does exist. Here, a significant deviation has been found of this analysis from earlier analyses which did not allow a negative λ_1 . For example, in Ref. [142] a negative $\lambda_3(M_Z)$ was not allowed from stability of the Higgs potential if the theory has to be valid up to 10^{16} GeV together with relic density considerations.

6.3.3 Tunneling Probability and Metastability in IDM

The presence of the inert doublet induces additional contributions to β_{λ_1} (see eqn. B.14). As a result, which is generic for all scalars, λ_1 receives a positive contribution compared to the SM, which pushes a metastable vacuum towards stability, implying a lower \mathcal{P}_0 (see eqn. 5.18).

Electroweak metastability in the ID model has been explored earlier in the literature, albeit in a different context [163–166]. If H^+ gets a VEV, there could exist another charge-violating minimum. If instead, A receives a VEV, another CP -violating minimum could pop up. But these vacua always lie higher than the usual EW vacuum. If Z_2 is broken by introducing additional soft terms in the Lagrangian, then the new Z_2 -violating minimum can be lower than the usual Z_2 -preserving EW minimum. As in this work, Z_2 is an exact symmetry of the scalar potential, so such

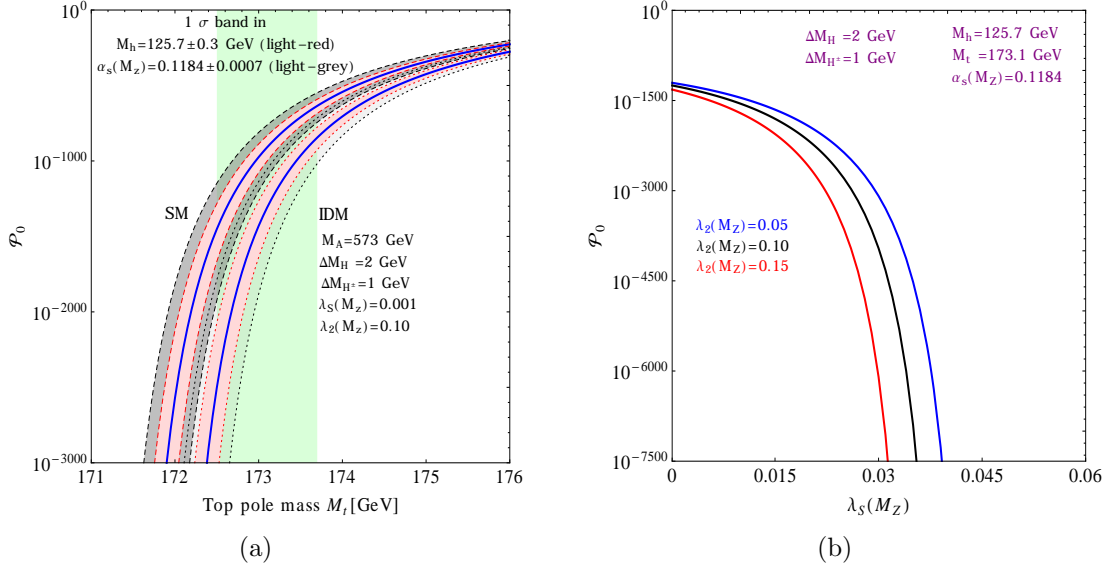


Figure 6.16: (a) Tunneling probability \mathcal{P}_0 dependence on M_t . The left band (between dashed lines) corresponds to SM. The right one (between dotted lines) is for ID model for DM mass $M_A = 573$ GeV. Constraints from WMAP and Planck measured relic density, as well as XENON100 and LUX DM direct detection null results are respected for these specific choice of parameters. Light-green band stands for M_t at $\pm 1\sigma$. (b) \mathcal{P}_0 is plotted against Higgs dark matter coupling $\lambda_S(M_Z)$ for different values of $\lambda_2(M_Z)$.

cases need not be considered. However, as mentioned earlier, if at some scale before M_{Pl} , the sign of λ_1 becomes negative, there might exist a deeper minimum which is charge-, CP - and Z_2 -preserving and lying in the SM Higgs h direction.

The EW vacuum is metastable or unstable, depends on the minimum value of λ_1 before M_{Pl} , which can be understood as follows. For EW vacuum metastability, the decay lifetime should be greater than the lifetime of the Universe, implying $\mathcal{P}_0 < 1$ (eqn. 5.26). Hence the vacuum stability constraints on the ID model can now be reframed, when $\lambda_{1,\text{eff}}$ runs into negative values, implying metastability of the EW vacuum. It is reminded to the reader that in the ID model, instability of the EW vacuum cannot be realized as addition of the scalars only improves the stability of

the vacuum.

- If $0 > \lambda_{1,\text{eff}}(\Lambda_B) > \lambda_{1,\text{min}}(\Lambda_B)$, then the vacuum is metastable.
- If $\lambda_{1,\text{eff}}(\Lambda_B) < \lambda_{1,\text{min}}(\Lambda_B)$, then the vacuum is unstable.
- If $\lambda_2 < 0$, then the potential is unbounded from below along the H, A and H^\pm direction.
- If $\lambda_3(\Lambda_I) < 0$, the potential is unbounded from below along a direction in between H^\pm and h .
- If $\lambda_L(\Lambda_I) < 0$, the potential is unbounded from below along a direction in between H and h .
- If $\lambda_S(\Lambda_I) < 0$, the potential is unbounded from below along a direction in between A and h .

In the above, Λ_I represents any energy scale for which $\lambda_{1,\text{eff}}$ is negative and the conditions for unboundedness of the potential follow from eqn. 6.9. At this point note the significant deviations are being made in the allowed parameter space compared to the usual vacuum stability conditions: According to eqn. 3.9, $\lambda_{3,L,S}$ can take slightly negative values. But at a scale where $\lambda_{1,\text{eff}}$ is negative, with the new conditions $\lambda_{3,L,S}$ have to be positive.

The tunneling probability \mathcal{P}_0 is computed by putting the minimum value of $\lambda_{1,\text{eff}}$ in eqn. 5.24 to minimize $S(\Lambda_B)$. In Fig. 6.16(a), \mathcal{P}_0 has been plotted as a function of M_t . The right band corresponds to the tunneling probability for our benchmark point as in Table 6.3. For comparison, \mathcal{P}_0 has been plotted for SM as the left band in Fig. 6.16(a). 1σ error bands in α_s and M_h are also shown. As expected, for a given M_t , the presence of ID lowers tunneling probability. This is also reflected in Fig. 6.16(b), where \mathcal{P}_0 has been plotted as a function of $\lambda_S(M_Z)$ for different choices

of $\lambda_2(M_Z)$, assuming $M_h = 125.7$ GeV, $M_t = 173.1$ GeV, and $\alpha_s = 0.1184$. Here DM mass M_A is also varied with λ_S to get $\Omega h^2 = 0.1198$. For a given $\lambda_S(M_Z)$, the higher the value of $\lambda_2(M_Z)$, the smaller \mathcal{P}_0 gets, leading to a more stable EW vacuum.

6.3.4 Phase diagrams in IDM

The stability of EW vacuum depends on the value of parameters at low scale, chosen to be M_Z . In order to show the explicit dependence of EW stability on various parameters, it is customary to present phase diagrams in various parameter spaces. In Fig. 6.17 the LEP constraints has been shown in the $M_H - M_A$ plane as in

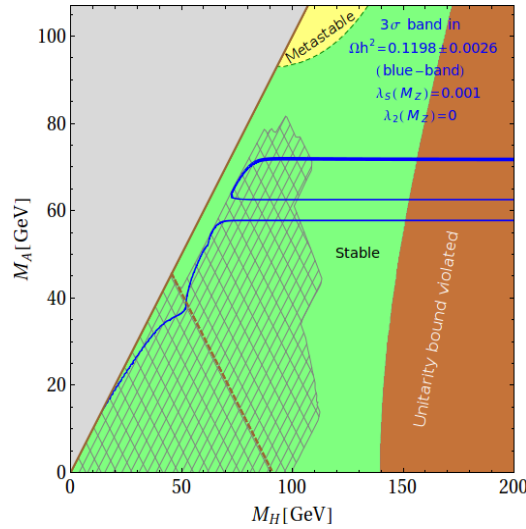


Figure 6.17: Constraints in $M_H - M_A$ plane in IDM. The cross-hatched region is excluded from LEP [150]. Choosing $M_{H\pm} = 120$ GeV and $\lambda_S(M_Z) = 0.001$, relic density constraint is satisfied at 3σ on the blue band. The green (yellow) region corresponds to EW vacuum stability (metastability). The solid brown line correspond to $M_H = M_A$. The gray area on the left to it is of no interest to us as $M_H > M_A$ has been chosen. The dashed brown line shows the LEP1 limit. On the brown region, unitarity constraints are violated before M_{P1} .

Ref. [150]. Identifying regions of EW stability and metastability, the plot has been updated here. As a scenario is being considered where the ID model is valid till

M_{P1} , there are further limits from unitarity. The relic density constraint imposed by WMAP and Planck combined data is represented by the thin blue band. The choice of $\lambda_2(M_Z)$ does not have any impact on relic density calculations, but affects EW stability as expected. In this plot, for higher values of $\lambda_2(M_Z)$, the region corresponding to EW metastability will be smaller. The chosen parameters satisfy the LUX direct detection bound.

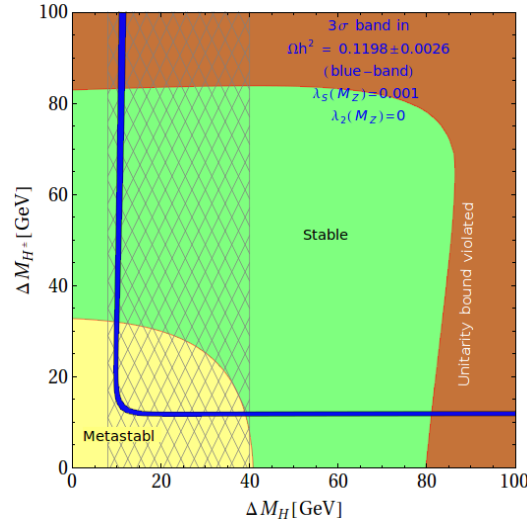


Figure 6.18: Phase diagram in $\Delta M_H - \Delta M_{H^\pm}$ plane for $M_A = 70$ GeV in IDM. The green and yellow regions correspond to EW vacuum stability and metastability respectively. The cross-hatched band is excluded from LEP. The brown region suffers from unitarity violation before M_{P1} . The blue band reflects relic density constraint at 3σ .

As small splitting among M_A , M_H , and M_{H^\pm} leads to some cancellations among diagrams contributing to DM annihilation, ΔM_{H^\pm} and ΔM_H are often used as free parameters in the ID model. In Fig. 6.18, constraints on this parameter space for $M_A = 70$ GeV has been presented. As before, the brown region corresponds to unitarity violation before M_{P1} . For small ΔM_{H^\pm} and ΔM_H , $\lambda_{3,4,5}$ are required to be small, which leads to little deviation from SM metastability. The metastable region is shown by the yellow patch, which shrinks for larger λ_2 . The blue band

reflects the relic density constraint for $\lambda_S(M_Z) = 0.001$. For such small $\lambda_S(M_Z)$, the h -mediated s -channel diagram in $AA \rightarrow WW$ or $AA \rightarrow ZZ$ contributes very little. H^+ - or H -mediated t - and u -channel diagrams are also less important than the quartic vertex driven diagram due to propagator suppression. This explains the “L” shape of the blue band. For higher values of $\lambda_S(M_Z)$, the shape of the band changes and ultimately leads to a closed contour. It appears that due to LEP constraints, EW vacuum metastability is almost ruled out. Although the LEP constraint permits $\Delta M_H < 8$ GeV, allowing a narrow strip towards the left, the relic density constraints cannot be satisfied on this strip as it leads to an increased rate of DM coannihilation processes, leading to a dip in Ωh^2 . But as it will be seen later, if M_t and α_s are allowed to deviate from their respective central values, for some region in this parameter space, it is possible to realize a metastable EW vacuum.

To delineate the role of M_H in EW vacuum stability, in Figs. 6.17 and 6.18, $\lambda_2(M_Z)$ is chosen to be small. To demonstrate the effect of λ_S , phase diagrams will be presented in Fig. 6.19 in the $\lambda_S(M_Z) - M_A$ plane. Panel (a) deals with low DM masses. For $\Delta M_{H^\pm} = 40$ GeV and $\Delta M_H = 40$ GeV, part of the allowed relic density band (blue) is allowed from LEP constraints (cross-hatched band). The entire parameter space corresponds to EW vacuum stability. Choosing small ΔM_{H^\pm} and ΔM_H , which imply small values of $\lambda_{3,4,5}$, can lead to metastability. But those regions are excluded by LEP. Again, metastability can creep in if M_t and α_s are allowed to deviate from their central values.

In Fig. 6.19(b), the same parameter space has been studied for high DM masses. As mentioned before, to obtain the correct relic density, smaller mass splitting among various ID scalars needs to be chosen. For $\Delta M_{H^\pm} = 1$ GeV and $\Delta M_H = 2$ GeV, the 3σ relic density constraint is shown as the blue band. The blue dashed line demarcates the boundary between stable (green) and metastable (yellow) phases of EW vacuum. The choice of small values of ΔM_{H^\pm} and ΔM_H , in turn, leads to a

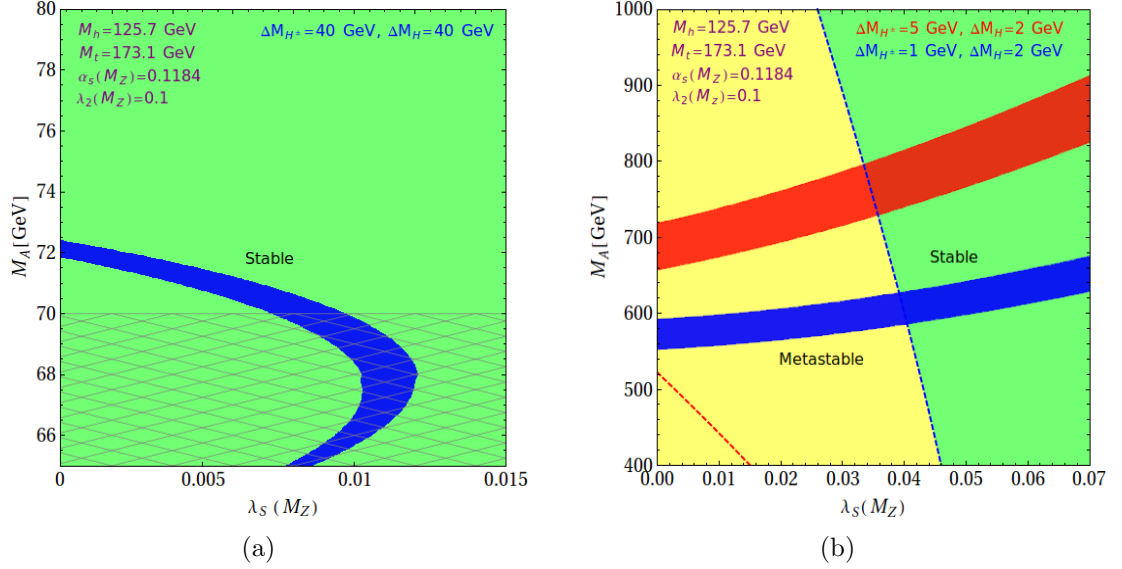


Figure 6.19: Phase diagram in $\lambda_S(M_Z) - M_A$ plane for $\lambda_2(M_Z) = 0.1$ in IDM. Panel (a) stands for ‘low’ DM mass. The blue band corresponds the 3σ variation in Ωh^2 when $\Delta M_{H^\pm} = 40$ GeV and $\Delta M_H = 40$ GeV. LEP direct search constraints are represented by the cross-hatched band at the bottom. Entire green region imply EW vacuum stability. Panel (b) stands for ‘high’ DM masses. The relic density band (blue) now correspond to $\Delta M_{H^\pm} = 1$ GeV and $\Delta M_H = 2$ GeV. The corresponding stable and metastable phases for EW vacuum are represented by green and yellow patches respectively. The relic density band (red) corresponds to $\Delta M_{H^\pm} = 5$ GeV and $\Delta M_H = 2$ GeV. For this, the boundary separating the EW phases is denoted by the red dashed line.

large region pertaining to EW metastability.

To illustrate the sensitivity to the mass splitting, in Fig. 6.19(b), another relic density band (red) has been presented for $\Delta M_{H^\pm} = 5$ GeV and $\Delta M_H = 2$ GeV. The corresponding boundary between the phases is denoted by the red dashed line. The region on the right implies EW stability (the green and yellow regions do not apply to this case). As for high DM masses, EW metastability can be attained for a sizable amount of the parameter space; $\lambda_2(M_Z)$ need not be chosen to be very small to maximize the metastable region for the sake of demonstration.

The fact that for SM the EW vacuum stability is ruled out at $\sim 3\sigma$, is demonstrated by a phase space diagram in the $M_t - M_h$ plane [13,14]. In Ref. [15], similar diagrams were presented for a singlet scalar extended SM. To demonstrate the impact of ID scalars to uplift the EW vacuum metastability, phase diagrams have been presented in the $M_t - M_h$ plane for two sets of benchmark points in Fig. 6.20. Panel (a) is drawn for $M_A = 70$ GeV, $\Delta M_{H^\pm} = 11.8$ GeV, $\Delta M_H = 45$ GeV, $\lambda_S(M_Z) = 0.001$, and $\lambda_2(M_Z) = 0.1$. For panel (b) the set of parameters in Table 6.3 is being used. Both sets of parameters are chosen so that they respect the WMAP

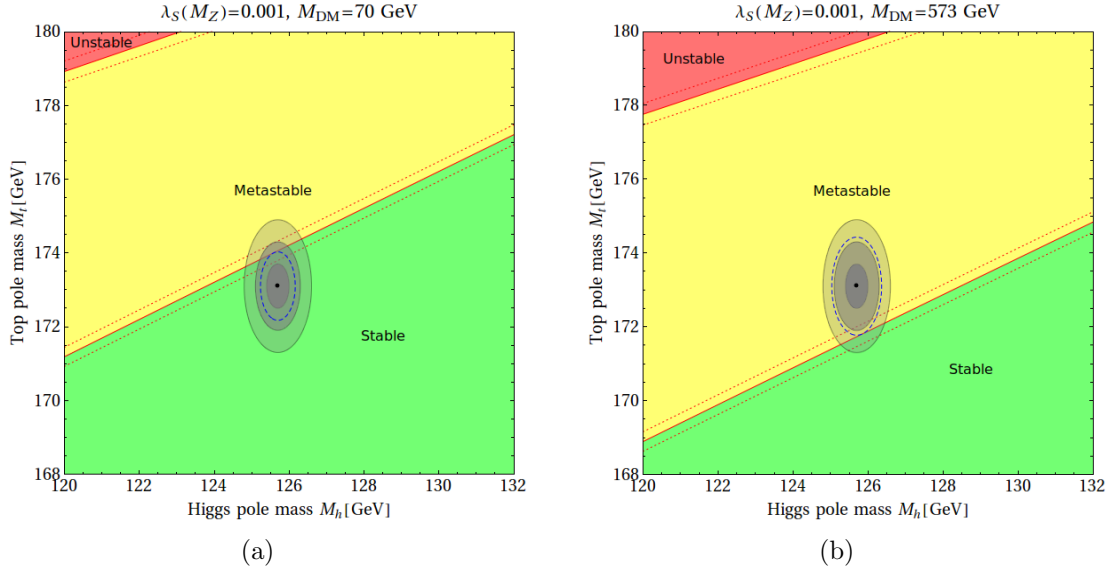


Figure 6.20: Phase diagrams in $M_h - M_t$ plane in IDM. Panels (a) and (b) stand for ‘low’ and ‘high’ DM masses respectively. Regions of absolute stability (green), metastability (yellow), instability (red) of the EW vacuum are also marked. The gray zones represent error ellipses at 1, 2 and 3σ . The three boundary lines (dotted, solid and dotted red) correspond to $\alpha_s(M_Z) = 0.1184 \pm 0.0007$. Details of benchmark points are available in the text.

and Planck combined results on DM relic density and the direct detection bounds from XENON 100 and LUX. As in Ref. [15], the line demarcating the boundary between stable and metastable phases of EW vacuum is obtained by demanding

that the two vacua be at the same depth, implying $\lambda_1(\Lambda_B) = \beta_{\lambda_1}(\Lambda_B) = 0$. The line separating the metastable phase from the unstable one is drawn using the conditions $\beta_{\lambda_1}(\Lambda_B) = 0$ and $\lambda_1(\Lambda_B) = \lambda_{1,\min}(\Lambda_B)$, as in eqn. 5.26. The variations due to uncertainty in the measurement of α_s are marked as dotted red lines. In each panel, the dot representing central values for M_h and M_t is encircled by 1σ , 2σ , and 3σ ellipses representing errors in their measurements. According to Fig. 6.20(a), EW vacuum stability is allowed at 1.5σ , whereas in Fig. 6.20(b), it is excluded at 2.1σ , indicated by blue-dashed ellipses.

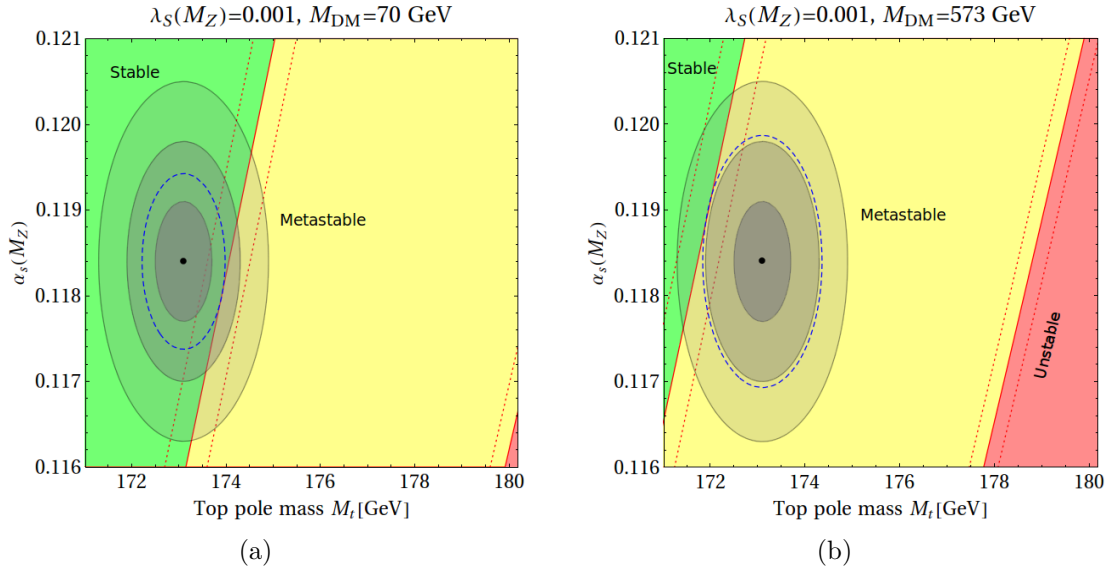


Figure 6.21: Phase diagrams in $M_t - \alpha_s(M_Z)$ plane in IDM for the same sets of benchmark points as in Fig. 6.20. Notations used are also the same as in Fig. 6.20.

As in the literature SM EW phase diagrams are also presented in the $\alpha_s(M_Z) - M_t$ plane [100, 167], the same is done in the ID model as well. In Fig. 6.21, the same sets of benchmark parameters has been used as in Fig. 6.20. As a consistency check, one can note that the EW vacuum is allowed or ruled out at the same confidence levels.

To study the impact of nonzero ID couplings, however, it is instructive to study the

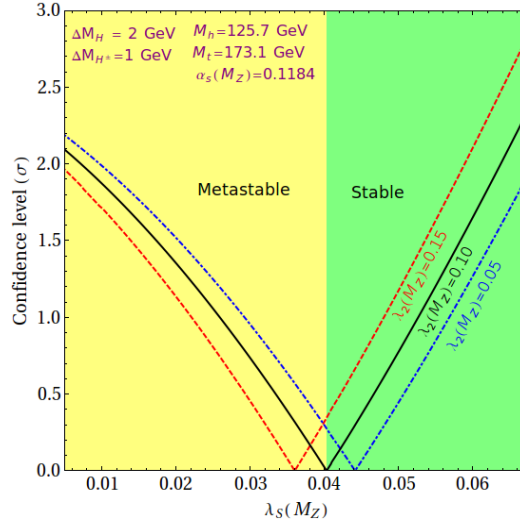


Figure 6.22: Dependence of confidence level at which EW vacuum stability is excluded (one-sided) or allowed on $\lambda_S(M_Z)$ and $\lambda_2(M_Z)$ in IDM. Regions of absolute stability (green) and metastability (yellow) of EW vacuum are shown for $\lambda_2(M_Z) = 0.1$. The positive slope of the line corresponds to the stable EW vacuum and negative slope corresponds to the metastability.

change in the confidence level (σ) at which EW stability is modified with respect to these couplings. As in Ref. [15], In Fig. 6.22 σ has been plotted against $\lambda_S(M_Z)$ for different values of $\lambda_2(M_Z)$. M_A is varied along with $\lambda_S(M_Z)$ to keep DM relic density fixed at $\Omega h^2 = 0.1198$ throughout the plot. Note that changing $\lambda_2(M_Z)$ does not alter Ωh^2 . The masses of other ID particles are determined using $\Delta M_{H^\pm} = 1$ GeV and $\Delta M_H = 2$ GeV. The parameter space considered does not yield too large DM-nucleon cross-section, inconsistent with XENON 100 and LUX DM direct detection null results. For a specific value of $\lambda_2(M_Z) = 0.1$, with the increase of $\lambda_S(M_Z)$, the confidence level at which EW is metastable (yellow region) gets reduced and becomes zero at $\lambda_S(M_Z) \simeq 0.04$. After this, EW vacuum enters in the stable phase (green). With further increases in $\lambda_S(M_Z)$, the confidence level at which EW is stable keeps increasing. Two other values in the same plot is used to illustrate the role of $\lambda_2(M_Z)$. The value of $\lambda_S(M_Z)$ at which the EW vacuum enters in the

stable phase increases with decreases in $\lambda_2(M_Z)$, as expected. The yellow and green marked regions are not applicable when $\lambda_2(M_Z) = 0.05, 0.15$.

6.3.5 Veltman's conditions in IDM

As the validity of the ID model have been extended till M_{Pl} , it is interesting to explore whether Veltman's condition (VC) can be satisfied in this model at any scale on or before M_{Pl} . It has been shown in Section 5.2.5, if one imposes VC in the SM at M_{Pl} , then the top mass measurement $M_t = 173.1 \pm 0.6$ GeV implies $M_h \approx 135 \pm 2.5$ GeV, which is excluded at more than 5σ .

Veltman's condition implies that the quadratic divergences in the radiative corrections to the Higgs mass can be handled if the coefficient multiplying the divergence somehow vanishes [168, 169]. VC includes the contributions from the infrared degrees of freedom of the theory and does not carry any special information about the ultraviolet divergences. In SM, it suggests the combination

$$6\lambda_1 + \frac{9}{4}g_2^2 + \frac{3}{4}g_1^2 - 12y_t^2 = 0.$$

Due to the large negative contribution from the term containing the top Yukawa coupling, it is not possible to satisfy VC till M_{Pl} given the experimental measurements of M_t and M_h within the context of SM.

In the ID model, as more scalars are added a possibility opens up to satisfy VC, as their contributions can offset the large negative contribution from the top quark.

The above VC for the SM associated with m_{11} is promoted in the ID model to [148, 170]

$$6\lambda_1 + 2\lambda_3 + \lambda_4 + \frac{9}{4}g_2^2 + \frac{3}{4}g_1^2 - 12y_t^2 = 0. \quad (6.25)$$

If $2\lambda_3 + \lambda_4$ is positive, then it has been checked with the RG improved coupling constants, and it is possible to satisfy the above VC at a scale before M_{Pl} .

However, in the ID model m_{22} also receives quadratically divergent radiative correc-

tions. The corresponding VC reads as

$$6\lambda_2 + 2\lambda_3 + \lambda_4 + \frac{9}{4}g_2^2 + \frac{3}{4}g_1^2 = 0. \quad (6.26)$$

Note that it lacks the Yukawa contribution as the unbroken Z_2 forbids fermionic interactions of the inert doublet Φ_2 . As $2\lambda_3 + \lambda_4$ is already positive, this VC can be satisfied if λ_2 is negative. But a negative λ_2 renders the potential unbounded from below as evident from the earlier discussions. Note that amongst our RG improved coupling constants λ_1 can be driven to negative values at high scales. But this makes the required cancellations for VCs even worse. Hence, it is not possible to satisfy Veltman's conditions in a scenario where only the ID model reigns the entire energy regime up to the M_{Pl} .

6.4 Triplet ($Y = 0$) scalar extension of the SM

In this case, the SM is extended by an additional hyperchargeless $SU(2)_L$ scalar triplet. This triplet is odd under a discrete Z_2 symmetry, whereas, the standard model fields are even. Also this symmetry prohibits the inert triplet to acquire a vacuum expectation value.

The tree-level scalar potential of eqn. 3.18 with additional Z_2 -symmetry, can be written⁵ as,

$$V_0(\Phi, T) = \mu_1^2 |\Phi|^2 + \lambda_1 |\Phi|^4 + \frac{\mu_2^2}{2} \text{tr}|T|^2 + \frac{\lambda_2}{4} \text{tr}|T|^4 + \frac{\lambda_3}{2} |\Phi|^2 \text{tr}|T|^2, \quad (6.27)$$

where the SM Higgs doublet Φ and the inert scalar triplet T are given by,

$$\Phi = \begin{pmatrix} G^+ \\ \frac{1}{\sqrt{2}}(v + h + iG^0) \end{pmatrix}, \quad T = \begin{pmatrix} H/\sqrt{2} & -H^+ \\ -H^- & -H/\sqrt{2} \end{pmatrix}, \quad (6.28)$$

T contains a neutral scalar H and a pair of charged scalar fields H^\pm . The Z_2 symmetry prohibits these particles to decay entirely to SM particles. The neutral particle H can then serve as a DM candidate.

⁵Here T is denoted as the scalar triplet, which is equivalent to $\tilde{\Phi}$ of eqn. 3.17 and the λ_i 's are equivalent to $\tilde{\lambda}_i$ of the eqn. 3.18.

After electroweak symmetry breaking the scalar potential can be written as,

$$V(h, H, H^\pm) = \frac{1}{4} [2\mu_1^2(h+v)^2 + \lambda_1(h+v)^4 + 2\mu_2^2(H^2 + 2H^+H^-) + \lambda_2(H^2 + 2H^+H^-)^2 + \lambda_3(h+v)^2(H^2 + 2H^+H^-)].$$

Masses of these scalars are given by,

$$\begin{aligned} M_h^2 &= \mu_1^2 + 3\lambda_1 v^2, \\ M_H^2 &= \mu_2^2 + \frac{\lambda_3}{2} v^2, \\ M_{H^\pm}^2 &= \mu_2^2 + \frac{\lambda_3}{2} v^2. \end{aligned}$$

At the tree level both the neutral and charged particle masses are the same. If we include one-loop radiative correction then the charged particles become slightly heavier [171, 172] than neutral ones.

$$\Delta M = (M_{H^\pm} - M_H)_{1-loop} = \frac{\alpha M_H}{4\pi s_W^2} \left[f\left(\frac{M_W}{M_H}\right) - c_W^2 f\left(\frac{M_Z}{M_H}\right) \right]$$

where,

$$f(x) = -\frac{x}{4} \left[2x^3 \log(x) + (x^2 - 4)^{\frac{3}{2}} \log\left[\frac{1}{2}(x^2 - 2 - x\sqrt{x^2 - 4})\right] \right].$$

One-loop effective Higgs potential in $\overline{\text{MS}}$ scheme in the Landau gauge is given by

$$V_1^{\text{SM+IT}}(h) = V_1^{\text{SM}}(h) + V_1^{\text{IT}}(h) \quad (6.29)$$

$V_1^{\text{SM}}(h)$ can be found in eqn. 5.2. The additional contribution to the one-loop effective potential due to the inert triplet is given by [77],

$$V_1^{\text{IT}}(h) = \sum_{j=H, H^+, H^-} \frac{1}{64\pi^2} M_j^4(h) \left[\ln\left(\frac{M_j^2(h)}{\mu^2(t)}\right) - \frac{3}{2} \right] \quad (6.30)$$

where,

$$M_j^2(h) = \frac{1}{2} \lambda_j(t) h^2(t) + \mu_2^2(t) \quad (6.31)$$

with $\lambda_{H, H^\pm}(t) = \lambda_3(t)$. In the present work, in the Higgs effective potential, SM contributions are taken at two-loop level and the IT scalar contributions are considered at one-loop only.

Similarly for large field value $h \gg v$, the Higgs effective potential can be approxi-

mated as

$$V_{\text{eff}}^{\text{SM+IT}}(h) \simeq \lambda_{1,\text{eff}}(h) \frac{h^4}{4}, \quad (6.32)$$

with

$$\lambda_{1,\text{eff}}(h) = \lambda_{1,\text{eff}}^{\text{SM}}(h) + \lambda_{1,\text{eff}}^{\text{IT}}(h), \quad (6.33)$$

where $\lambda_{\text{eff}}^{\text{SM}}(\phi)$ same as in eqn. B.1 and,

$$\lambda_{1,\text{eff}}^{\text{IT}}(h) = e^{4\Gamma(h)} \left[\frac{3\lambda_3^2}{256\pi^2} \left(\ln \left(\frac{\lambda_3}{2} \right) - \frac{3}{2} \right) \right]. \quad (6.34)$$

To compute the RG evolution of all the couplings in these model, we first calculate

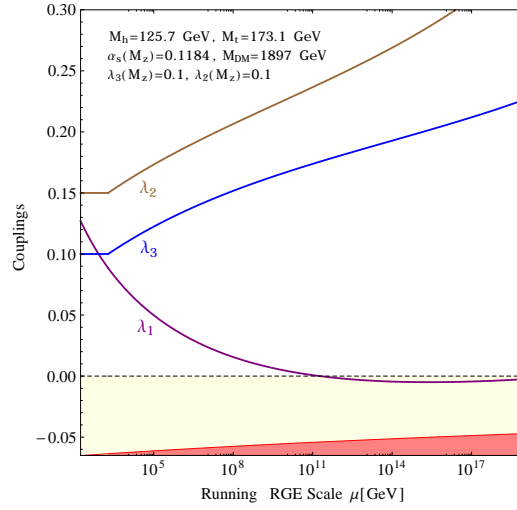


Figure 6.23: ITM *RG evolution of the couplings* $\lambda_1, \lambda_2, \lambda_3$ *for the set of parameters in Table 6.5.*

	λ_1	λ_2	λ_3
M_t	0.127054	0.10	0.10
M_{Pl}	-0.00339962	0.267706	0.206306

Table 6.5: A set of values of all ITM coupling constants at M_t and M_{Pl} for $M_{DM} = 1897$ GeV.

all couplings with threshold corrections at M_t and using the RG-eqns. B.19–B.22, one can obtain the couplings $\lambda_{1,2,3}$ at M_{Pl} . For a specific set of values of λ_i at $M_t = 173.1$ GeV, their values at $M_{\text{Pl}} = 1.2 \times 10^{19}$ GeV for $M_h = 125.7$ GeV and

$\alpha_s(M_Z) = 0.1184$ have been provided in Table 6.5. In Fig. 6.23 we explicitly show running of the scalar couplings (λ_i) for this set of parameters. It has been found that for the specific choice of parameters, λ_1 assumes a small negative value leading to a metastable EW vacuum as discussed in the previous sections.

6.4.1 Constraints on ITM

The absolute stability of the EW vacuum of the scalar potential (eqn. 6.27), unitarity of scattering matrix, perturbativity and the EW precision measurements puts a stringent bound on the ITM parameter space which had been shown in Chapter 3.

Constraints from LHC diphoton signal strength and dark matter will be discussed in the following subsections.

6.4.1.1 Bounds from LHC diphoton signal strength

The Higgs to diphoton signal strength $\mu_{\gamma\gamma}$ can be defined similar to eqn. 6.19. If the IT particles have masses greater than $M_h/2$, i.e., $\Gamma(h \rightarrow \text{IT}, \text{IT}) = 0$ then,

$$\mu_{\gamma\gamma} = \frac{\Gamma(h \rightarrow \gamma\gamma)_{\text{IT}}}{\Gamma(h \rightarrow \gamma\gamma)_{\text{SM}}}. \quad (6.35)$$

In ITM, the additional contributions to $\mu_{\gamma\gamma}$ at one-loop due to the H^\pm can be found in eqn. 6.22, where $\mu_{hH^+H^-} = \lambda_3 v$ stands for the coupling constant of hH^+H^- vertex. One can see that a positive λ_3 leads to a destructive interference between SM and IT contributions in eqn. 6.22 and *vice versa*. Hence, for IT particles heavier than $M_h/2$, $\mu_{\gamma\gamma} < 1$ ($\mu_{\gamma\gamma} > 1$) when λ_3 is positive (negative). One can see from the eqn. 6.22, the contribution to the Higgs diphoton channel is proportional to $\frac{\lambda_3}{M_{H^\pm}^2}$. It has been seen, if the charged scalar mass is greater than 300 GeV then the contributions of inert triplet model to the diphoton signal is negligible.

6.4.1.2 Constraints from dark matter relic density

In Fig. 6.24, we have plotted the relic density as a function of dark matter mass for ITM. Here in this plot, the Higgs portal coupling $\lambda_3(M_Z) = 0.10$ has been used.

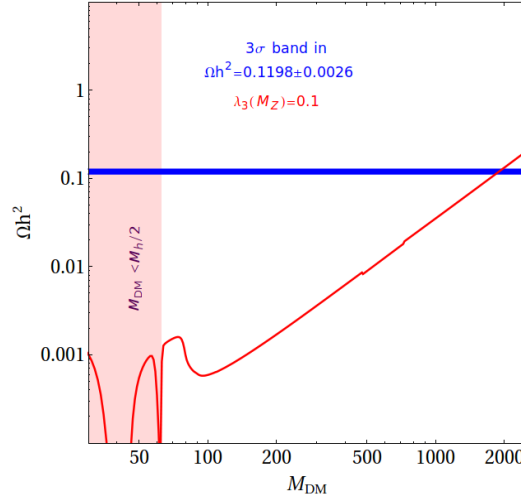


Figure 6.24: Dark matter relic density Ωh^2 as a function of the dark matter mass $M_{DM}(\equiv M_H)$ for the portal coupling: $\lambda_3(M_Z) = 0.10$ (red) in ITM. The thin blue band corresponds the relic density, $\Omega h^2 = 0.1198 \pm 0.0026$ (3σ).

The light red band is excluded from the Higgs invisible decay width data from the LHC. It has been seen that from eqn. 6.29, the mass difference between the neutral and charged particles is ~ 150 MeV [171, 172]. The co-annihilation cross-section of the dark matter H with charged (H^\pm) particles are very large. It has been seen that for 500 GeV, the total cross-section is $\langle \sigma v \rangle \sim 10^{-25} \text{ cm}^3 \text{ s}^{-1}$ and so the relic density becomes ~ 0.01 which corresponds to under-abundance. For dark matter mass greater than 1.8 TeV, one can get relic density of the dark matter in the right ballpark.

6.4.2 Tunneling Probability and Metastability in ITM

The tunneling probability \mathcal{P}_0 (see eqn. 5.18) is computed by putting the minimum value of $\lambda_{1,\text{eff}}$ of eqn. 6.33 in eqn. 5.24. In Fig. 6.25(a), we have plotted \mathcal{P}_0 as a function of M_t . The right band corresponds to the tunneling probability for our benchmark point as in Table 6.5. For comparison, we plot \mathcal{P}_0 for SM as the left band in Fig. 6.25(a). 1σ error bands in α_s and M_h are also shown. We plot \mathcal{P}_0

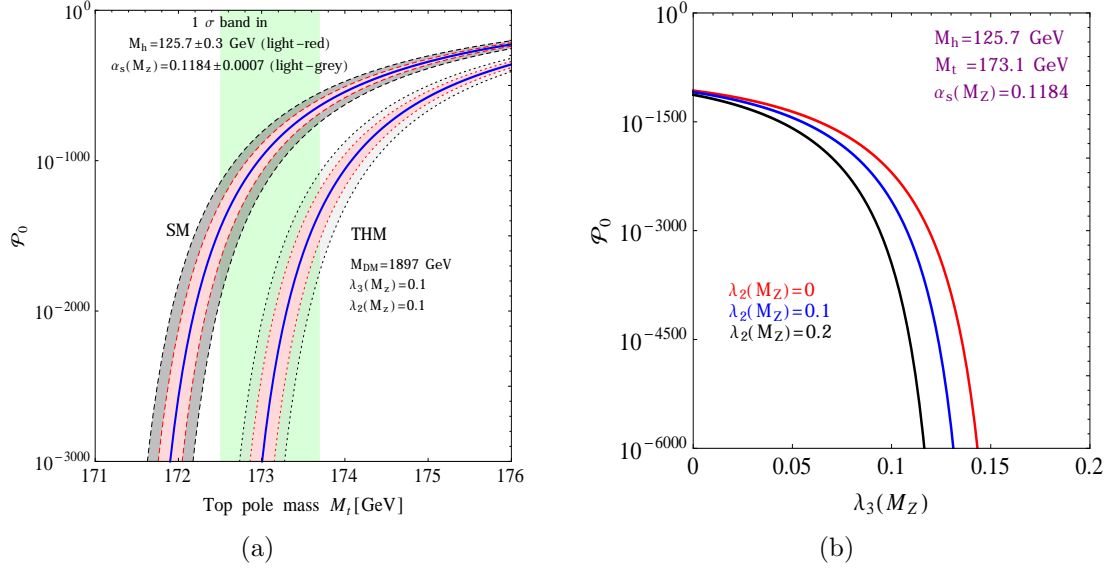


Figure 6.25: (a) Tunneling probability \mathcal{P}_0 dependence on M_t . The left band (between dashed lines) corresponds to SM. The right one (between dotted lines) is for IT model for DM mass $M_H = 1897$ GeV. Dark matter constraints are respected for these specific choices of parameters. Light-green band stands for M_t at $\pm 1\sigma$. (b) \mathcal{P}_0 is plotted against Higgs dark matter coupling $\lambda_3(M_Z)$ for different values of $\lambda_2(M_Z)$.

as a function of $\lambda_3(M_Z)$ in Fig. 6.25(b) for different choices of $\lambda_2(M_Z)$, assuming $M_h = 125.7$ GeV, $M_t = 173.1$ GeV and $\alpha_s = 0.1184$. Here DM mass M_{DM} is also varied with λ_3 to get $\Omega h^2 = 0.1198$.

The modified vacuum stability conditions are,

- If $0 > \lambda_1(\Lambda_B) > \lambda_{1,\min}(\Lambda_B)$, then the vacuum is metastable.
- If $\lambda_1(\Lambda_B) < \lambda_{1,\min}(\Lambda_B)$, then the vacuum is unstable.
- If $\lambda_2 < 0$, the potential is unbounded from below along the H and H^\pm -direction.
- If $\lambda_3(\Lambda_I) < 0$, the potential is unbounded from below along a direction in between H and h also H^\pm and h .

In the above, Λ_I represents any energy scale for which λ_1 is negative.

6.4.3 Phase diagrams in ITM

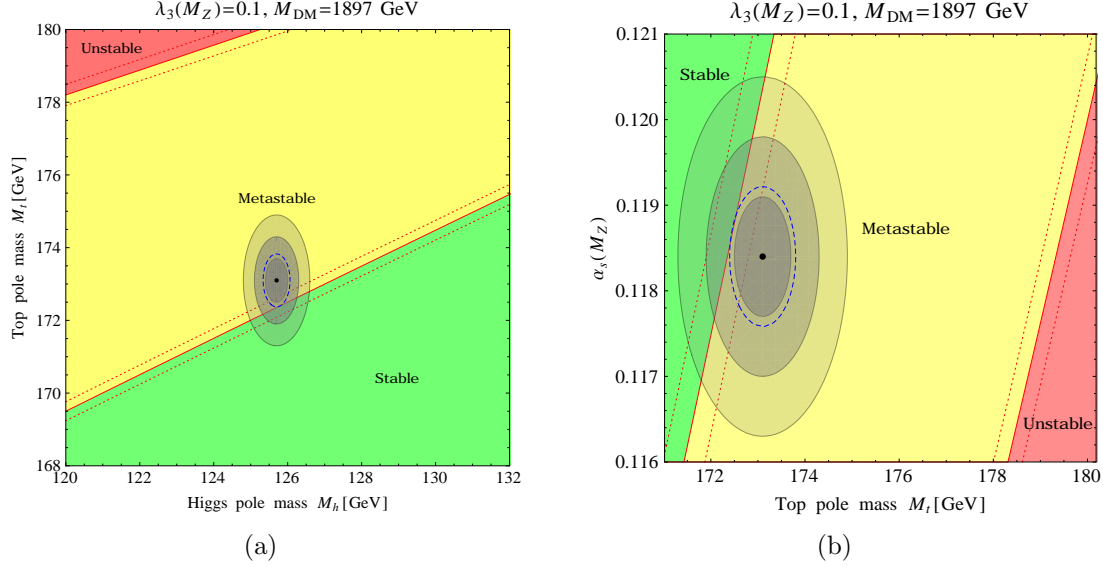


Figure 6.26: Phase diagrams in (a) $M_h - M_t$ plane and (b) $M_t - \alpha_s(M_Z)$ plane ITM. Regions of absolute stability (green), metastability (yellow), instability (red) of the EW vacuum are also marked. The gray zones represent error ellipses at 1, 2 and 3σ . The three boundary lines (dotted, solid and dotted red) correspond to $\alpha_s(M_Z) = 0.1184 \pm 0.0007$.

To explain the impact of inert triplet scalars to uplift the EW vacuum metastability, in Fig. 6.26 phase diagram in $M_t - M_h$ and $\alpha_s(M_Z) - M_t$ plane has been presented for the benchmark points $M_{DM} = 1897$ GeV, $\lambda_2(M_Z) = 0.10$ and $\lambda_3(M_Z) = 0.10$. For this points one can see from the phase diagram in Fig. 6.26 that the stability electroweak is excluded at 1.2σ (one-sided).

The confidence level vs $\lambda_3(M_Z)$ diagram like Fig. 6.11 of SM+S and Fig. 6.22 of IDM is presented in Fig. 6.27 for the inert triplet model. If the ITM is valid up to the Planck scale, which may saturate the relic abundance of the dark matter of the Universe then this phase diagram becomes important to realize where the

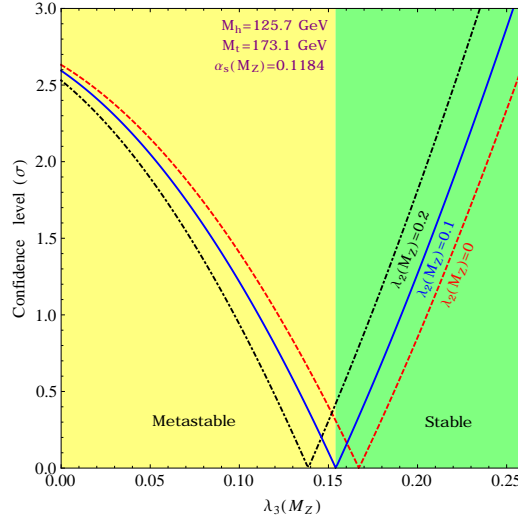


Figure 6.27: Dependence of confidence level at which EW vacuum stability is excluded (one-sided) or allowed on $\lambda_3(M_Z)$ and $\lambda_2(M_Z)$ in ITM. Regions of absolute stability (green) and metastability (yellow) of EW vacuum are shown for $\lambda_2(M_Z) = 0.1$.

present EW vacuum is residing. Along the line (black, blue and red) in the Fig. 6.27 the dark matter mass change in such a way that the relic density $\Omega h^2 = 0.1198$ remains same. One can see that with the increase of $\lambda_{2,3}(M_Z)$, the EW vacuum approaches the stability. In this model, the electroweak vacuum becomes absolutely stable after $\lambda_3(M_Z) = 0.154$ for $\lambda_2(M_Z) \approx 0.10$ (see blue line in the Fig. 6.27). This phase diagram has been presented for central values of M_h , M_t and $\alpha_s(M_Z)$. However, if we increase the top mass or decrease the Higgs mass or decrease $\alpha_s(M_Z)$ within experimental uncertainties then the size of the region corresponding to the metastability of the EW vacuum increases. With a maximum top mass $M_t = 174.9$ GeV and a minimum $M_h = 124.8$ GeV and a minimum $\alpha_s(M_Z) = 0.1163$, allowed at 3σ , the EW vacuum the Higgs potential becomes absolutely stable for the dark matter mass more than 1912 GeV with $\lambda_3(M_Z)$ greater than 0.31 for fixed $\lambda_2(M_Z) = 0.1$.

In Fig. 6.28, we have shown the valid parameter spaces in $\lambda_3(M_Z) - M_H$ plane for central value of M_t , M_h and $\alpha(M_Z)$. Here the lower (red) region are excluded, as the scalar potential becomes unbounded from below along the direction in between H^\pm and h . In this region the effective Higgs quartic coupling is negative and form a local minima along the Higgs h direction near the Planck scale and at the same time λ_3 remains negative up to the Planck scale. It has been found that the parameter spaces with negative $\lambda_3(M_Z)$ is also allowed from the metastability. In this case λ_3 becomes positive at the scale Λ_B of global minimum and remains positive up to the Planck scale. The green region implies that the EW vacuum is absolutely stable. In the upper red region the unitary bounds are violated. In the plot, the right-side of the black dotted line are viable from $\mu_{\gamma\gamma}$ at 1σ .

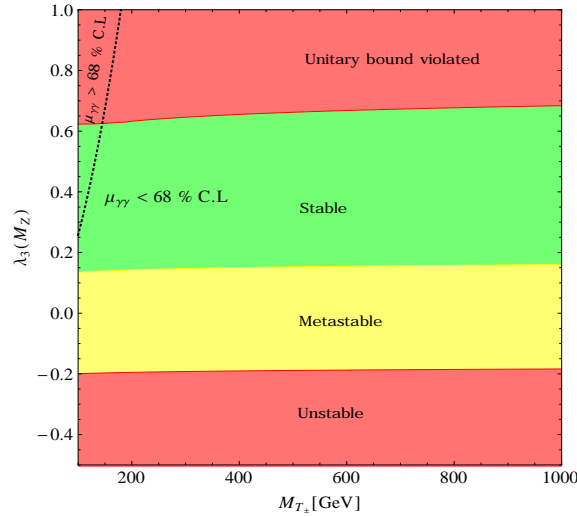


Figure 6.28: Phase diagram in $\lambda_3(M_Z) - M_H$ plane in ITM. Right side of the black-dotted line is allowed from the signal strength ratio of $\mu_{\gamma\gamma}$ within 68% confidence level. and the left side is excluded at 1σ . In the metastable region, the Higgs portal coupling $\lambda_3(M_Z)$ is negative, however, beyond the scale Λ_B it is greater than zero.

6.5 Summary

According to the standard model of particle physics with the present measured values of the SM parameters, the electroweak vacuum is lying right in between stability and instability, as if it is ready to tunnel into a regime of absolute instability. Nevertheless, the transition time required for this is safely beyond the present lifetime of the Universe. Still, the question is, what prompts such a near-criticality? In this chapter, we did not try to find an answer to this question. But we explored the validity of this question in the context of the different models containing extra scalar field(s) that also offers a solution to the dark matter puzzle.

Near-criticality is best explained with the help of phase diagrams which were used in the Chapter 5 for the SM. A similar endeavor has been made in this chapter for various kinds of extended scalar sectors namely SM+ S , inert doublet and inert triplet models. The next-to-next-to-leading order corrections have been included in the SM calculations. The effects due to the extra scalar(s) were incorporated up to two-loop.

In this chapter, various kinds of dark matter models have been chosen to illustrate changes in EW vacuum stability as apart from neutrino masses, the presence of dark matter in the Universe is the most striking signature of new physics beyond the standard model of particle physics.

In these models, for some specific choice of parameter space, the scalar field(s) can rescue the EW vacuum from metastability, making it absolutely stable, so that λ never turns negative. But as the DM direct detection experiments or collider searches are yet to confirm the exact nature of the DM candidate, the parameter space allowed by DM relic density constraints, dictated by the cosmic microwave background radiation experiments such as Planck or WMAP, have been considered. It has been checked that in these considerations, the related DM-nucleon cross-

sections are beyond the present sensitivity of direct-detection experiments such as XENON100 and LUX.

The addition of scalar multiplet does not help in realizing the asymptotic safety scenario of gravity. But it is possible to have two degenerate vacua at somewhat lower energy (shown for the SM+ S model), which depends on the parameter space under consideration.

In short, near-criticality of EW vacuum indicates the presence of new dynamics other than the SM at a very high energy. In this chapter, new scalars physics have been introduced at EW scale to demonstrate the influence of such scalars in shaping the minimum (if any) of the potential lying close to M_{Pl} .

Chapter 7

Summary and Conclusions

The Higgs signal strength data is consistent with the theoretical predictions of the SM with small uncertainties. The LHC is yet to find any convincing signal suggesting the existence of any new physics beyond the standard model of particle physics. There are several well-motivated possibilities for an enlarged scalar sector that go far beyond the minimalistic one doublet scenario of the standard model. Small uncertainty in Higgs signal data at LHC does allow physics beyond the SM. Other experimental evidences point towards the existence of dark matter, which so far could have escaped detection in colliders and DM direct detection experiments.

In this thesis, several extended scalar sectors of the SM have been discussed. The SM has been extended with either a $SU(2)$ singlet or doublet or triplet with different hypercharges. It has been considered that the extra scalar fields transform under same standard model gauge group.

This work has two aspects. In the first case, it has been considered that both the SM doublet and the extra scalar field are responsible for the electroweak symmetry breaking, i.e., both the neutral CP -even component of SM doublet and extra scalar fields are getting vacuum expectation values. In other words, the minima of the combined scalar potential form on the plane containing the CP -even components. These components mix and form a Higgs-like particle and extra heavy scalar parti-

cles. The different extended scalar sectors contain different kinds of scalar particles such as charged, or neutral CP -even and CP -odd scalar(s). These scalars can couple to the vector bosons. In this point of view, various kinds of vector boson scattering processes have been calculated for the three models such as (i) type-II two Higgs doublet model, (ii) Higgs triplet model with a hyperchargeless scalar triplet, and (iii) Higgs triplet model with a scalar triplet with hypercharge $Y = 2$. The exact expressions of longitudinal polarization vectors have been used to determine the scattering cross-sections. Generally, the idea of vector boson scattering has been used for a better understanding of EWSB. A generic expression of the amplitude of the vector boson scattering has been given for these models. From this analysis, it is revealed that away from resonance the cross-sections are not significantly different from that of the SM. This is quite expected because only those parameter spaces have been chosen which satisfy all the existing constraints. One can differentiate these three models from the standard model and between one another, looking for the resonance peaks in different modes of vector boson scattering. In future, if we observe any signature of these new scalars in the future collider experiments, then this study will help in revealing the characteristics of the extended scalar sector.

If the standard model is valid up to the Planck scale, the present measurements on the masses of the top quark and Higgs indicate the presence of a deeper minimum of the scalar potential at a very high energy scale, threatening the stability of the present electroweak vacuum. State of the art NNLO calculations performed to evaluate the probability that the present EW vacuum will tunnel into the deeper vacuum lying close to M_{Pl} suggest that the present EW vacuum is metastable at $\sim 3\sigma$. As a part of this thesis, this has been reproduced. The lack of stability might be the artifact of the incompleteness of the SM.

It is important to look into the problem of EW stability in a scenario which addresses the issue of DM as well. In this case, at a time an extended scalar sector has been

taken which provides a viable dark matter candidate. In the presence of these new scalar sectors, the detailed study of the Higgs potential has been discussed. Assuming these models valid up to the M_{Pl} scale and allowing the metastability of the electroweak vacuum, new viable parameter spaces have been found. As new extra scalar sector introduces a few new parameters and fields, the study of the parameter space is quite involved when one considers radiatively improved scalar potentials containing SM NNLO corrections and two-loop new sector contributions. Inclusion of these NNLO corrections is mandatory to reproduce the correct confidence level at which EW vacuum is metastable in the SM. In these models, the formation of the extra minimum near the M_{Pl} scale have been described. The detailed calculation of transition probability from the EW minimum to the new minimum at the Planck scale has also been shown. In the presence of new scalar sectors, the conditions for absolute stability of the EW vacuum have been reviewed in this work. If one allows the metastable EW vacuum then new metastability conditions arise which have also been shown for these extended scalar sectors of the SM.

As extra scalar sectors can provide a viable dark matter candidate which may fulfill the relic abundance of the dark matter in the Universe, in this context, it is instructive to explore whether these extra scalars can also extend the lifetime of the Universe. This study will help in estimating the mean lifetime of the EW vacuum, especially if it still remains in the metastable state in models with extended scalar sectors.

Appendices

Appendix A

Analytical expressions for vector boson scattering

A.1 Amplitudes for different modes of $V_L V_L$ scattering

Let p_1, p_2 are the four momenta of initial state gauge bosons and k_1, k_2 are that for the final state gauge bosons. $\epsilon_\mu(p)$ be the polarization four vector of a gauge bosons $V(\equiv W^\pm, Z)$ with four momentum p . It can be written as, $\epsilon_\mu(p) \equiv \{\frac{|\mathbf{p}|}{M_V}, \frac{E_V}{M_V}\hat{p}\}$, where $E_V = \sqrt{|\mathbf{p}|^2 + M_V^2}$ is the energy of the gauge boson. Here, M_V is the mass of V . We use the shorthand notations $\epsilon_1 \equiv \epsilon(p_1)$, $\epsilon_2 \equiv \epsilon(p_2)$, $\epsilon_3 \equiv \epsilon(k_1)$, $\epsilon_4 \equiv \epsilon(k_2)$, $c_W \equiv \cos \theta_W$ and $s_W \equiv \sin \theta_W$ and $x \equiv \cos \theta$, where θ is the scattering angle. Mandelstam variables are defined as: $s = (p_1 + p_2)^2$; $t = (p_1 - k_1)^2$; $u = (p_1 - k_2)^2$.

A.1.1 $W_L^+(p_1) + W_L^-(p_2) \rightarrow W_L^+(k_1) + W_L^-(k_2)$

Scattering amplitudes in terms of longitudinal polarization vectors and four momenta:

$$\begin{aligned}
 (a) \quad \mathcal{M}_p &= g_2^2 \{2(\epsilon_1 \cdot \epsilon_3)(\epsilon_2 \cdot \epsilon_4) - (\epsilon_1 \cdot \epsilon_2)(\epsilon_3 \cdot \epsilon_4) - (\epsilon_1 \cdot \epsilon_4)(\epsilon_2 \cdot \epsilon_3)\}. \\
 (b) \quad \mathcal{M}_s^{\gamma+Z} &= -g_2^2 \left(\frac{s_W^2}{s} + \frac{c_W^2}{s - M_Z^2} \right) \{ (p_1 - p_2)^\mu (\epsilon_1 \cdot \epsilon_2) + 2(p_2 \cdot \epsilon_1) \epsilon_2^\mu - 2(p_1 \cdot \epsilon_2) \epsilon_1^\mu \} \\
 &\quad \{ (k_2 - k_1)_\mu (\epsilon_3 \cdot \epsilon_4) - 2(k_2 \cdot \epsilon_3) \epsilon_{4\mu} - 2(k_1 \cdot \epsilon_4) \epsilon_{3\mu} \}. \\
 (c) \quad \mathcal{M}_t^{\gamma+Z} &= -g_2^2 \left(\frac{s_W^2}{t} + \frac{c_W^2}{t - M_Z^2} \right) \{ (p_1 + k_1)^\mu (\epsilon_1 \cdot \epsilon_3) - 2(k_1 \cdot \epsilon_1) \epsilon_3^\mu - 2(p_1 \cdot \epsilon_3) \epsilon_1^\mu \} \\
 &\quad \{ (p_2 + k_2)_\mu (\epsilon_2 \cdot \epsilon_4) - 2(k_2 \cdot \epsilon_2) \epsilon_{4\mu} - 2(p_2 \cdot \epsilon_4) \epsilon_{2\mu} \}.
 \end{aligned}$$

$$(d) \quad \mathcal{M}_s^S = - \frac{(C g_2 M_W)^2}{s - M_S^2} (\epsilon_1 \cdot \epsilon_2) (\epsilon_3 \cdot \epsilon_4).$$

$$(e) \quad \mathcal{M}_t^S = - \frac{(C g_2 M_W)^2}{t - M_S^2} (\epsilon_1 \cdot \epsilon_3) (\epsilon_2 \cdot \epsilon_4).$$

$$(f) \quad \mathcal{M}_u^{H^{++}} = - \frac{(\hat{C} g_2 M_W)^2}{u - M_{H^{++}}^2} (\epsilon_1 \cdot \epsilon_4) (\epsilon_2 \cdot \epsilon_3).$$

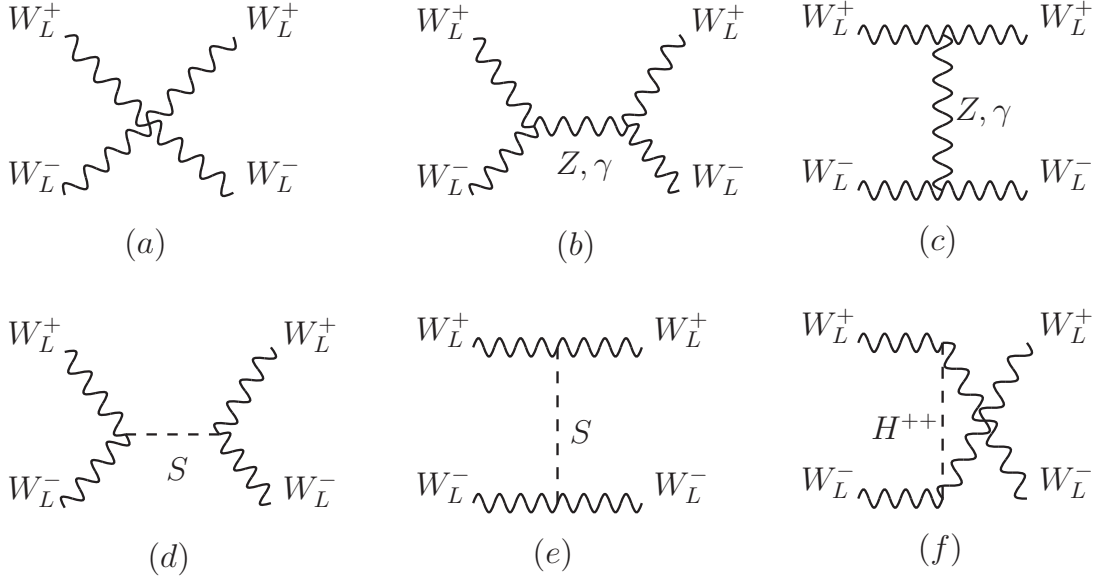


Figure A.1: Generic Feynman diagrams for $W_L^+(p_1) + W_L^-(p_2) \rightarrow W_L^+(k_1) + W_L^-(k_2)$ scattering

Scattering amplitudes in terms of center of momentum energy and scattering angle:

$$(a) \quad \mathcal{M}_p = \frac{E_{CM}^2 g_2^2}{16M_W^4} \{ 8M_W^2(1 - 3x) + E_{CM}^2(-3 + 6x + x^2) \}.$$

$$(b) \quad \mathcal{M}_s^{\gamma+Z} = - \frac{g_2^2}{4M_W^4} \left(\frac{s_W^2}{s} + \frac{c_W^2}{s - M_Z^2} \right) (E_{CM}^6 - 12E_{CM}^2 M_W^4 - 16M_W^6)x.$$

$$(c) \quad \mathcal{M}_t^{\gamma+Z} = - \frac{g_2^2}{32M_W^4} \left(\frac{s_W^2}{t} + \frac{c_W^2}{t - M_Z^2} \right) \{ -64M_W^6(1 + x) + E_{CM}^6(-1 + x)^2(3 + x) \\ + 16E_{CM}^2 M_W^4(1 - 7x + 10x^2) - 4E_{CM}^4 M_W^2(3 - 13x + 9x^2 + x^3) \}.$$

$$(d) \quad \mathcal{M}_s^S = - \frac{(C g_2 M_W)^2}{s - M_S^2} \frac{(E_{CM}^2 - 2M_W^2)^2}{4M_W^4}.$$

$$(e) \quad \mathcal{M}_t^S = - \frac{(C g_2 M_W)^2}{t - M_S^2} \frac{\{4M_W^2 + E_{CM}^2(-1+x)\}^2}{16M_W^4}.$$

$$(f) \quad \mathcal{M}_u^{H^{++}} = - \frac{(\hat{C} g_2 M_W)^2}{u - M_{H^{++}}^2} \frac{\{-4M_W^2 + E_{CM}^2(1+x)\}^2}{16M_W^4}.$$

Here, $E_{CM} = \sqrt{s}$ is the center of momentum energy.

A.1.2 $W_L^+(p_1) + W_L^+(p_2) \rightarrow W_L^+(k_1) + W_L^+(k_2)$

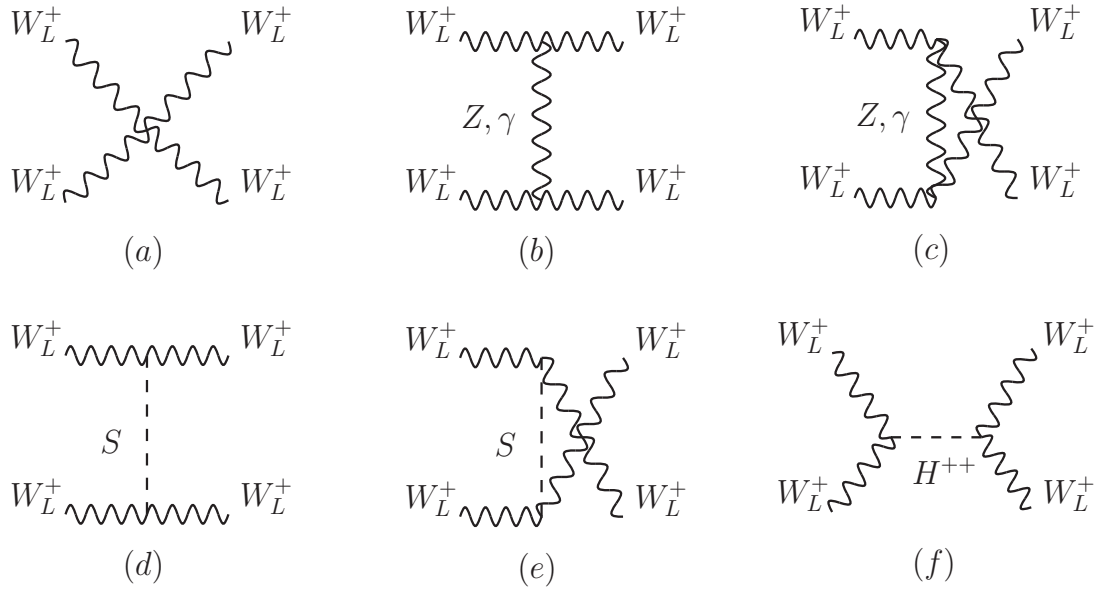


Figure A.2: *Generic Feynman diagrams for $W_L^+(p_1) + W_L^+(p_2) \rightarrow W_L^+(k_1) + W_L^+(k_2)$ scattering.*

Scattering amplitudes in terms of longitudinal polarization vectors and four momenta:

$$(a) \quad \mathcal{M}_p = g_2^2 \{2(\epsilon_1 \cdot \epsilon_2)(\epsilon_3 \cdot \epsilon_4) - (\epsilon_1 \cdot \epsilon_3)(\epsilon_2 \cdot \epsilon_4) - (\epsilon_1 \cdot \epsilon_4)(\epsilon_2 \cdot \epsilon_3)\}.$$

$$(b) \quad \mathcal{M}_t^{\gamma+Z} = g_2^2 \left(\frac{s_W^2}{t} + \frac{c_W^2}{t - M_Z^2} \right) \{ (p_1 + k_1)^\mu (\epsilon_1 \cdot \epsilon_3) - 2(k_1 \cdot \epsilon_1) \epsilon_3^\mu - 2(p_1 \cdot \epsilon_3) \epsilon_1^\mu \} \\ \{ (p_2 + k_2)_\mu (\epsilon_2 \cdot \epsilon_4) - 2(k_2 \cdot \epsilon_2) \epsilon_{4\mu} - 2(p_2 \cdot \epsilon_4) \epsilon_{2\mu} \}.$$

$$(c) \quad \mathcal{M}_u^{\gamma+Z} = g_2^2 \left(\frac{s_W^2}{u} + \frac{c_W^2}{u - M_Z^2} \right) \{ (p_1 + k_2)^\mu (\epsilon_1 \cdot \epsilon_4) - 2(k_2 \cdot \epsilon_1) \epsilon_4^\mu - 2(p_1 \cdot \epsilon_4) \epsilon_1^\mu \} \\ \{ (p_2 + k_1)_\mu (\epsilon_2 \cdot \epsilon_3) - 2(k_1 \cdot \epsilon_2) \epsilon_{3\mu} - 2(p_2 \cdot \epsilon_3) \epsilon_{2\mu} \}.$$

$$(d) \quad \mathcal{M}_t^S = - \frac{(C g_2 M_W)^2}{t - M_h^2} (\epsilon_1 \cdot \epsilon_3)(\epsilon_2 \cdot \epsilon_4).$$

$$(e) \quad \mathcal{M}_u^S = - \frac{(C g_2 M_W)^2}{u - M_h^2} (\epsilon_1 \cdot \epsilon_4)(\epsilon_2 \cdot \epsilon_3).$$

$$(f) \quad \mathcal{M}_s^{H^{++}} = - \frac{(\hat{C} g_2 M_W)^2}{s - M_{H^{++}}^2} (\epsilon_1 \cdot \epsilon_2)(\epsilon_3 \cdot \epsilon_4).$$

Scattering amplitudes in terms of center of momentum energy and scattering angle:

$$(a) \quad \mathcal{M}_p = - \left(\frac{g^2}{8M_W^4} \right) \{ 8E_{CM}^2 M_W^2 + E_{CM}^4 (-3 + x^2) \}.$$

$$(b) \quad \mathcal{M}_t^{\gamma+Z} = \frac{g_2^2}{32M_W^4} \left(\frac{s_W^2}{t} + \frac{c_W^2}{t - M_Z^2} \right) \{ -64M_W^6(1+x) + E_{CM}^6(-1+x)^2(3+x) \\ + 16E_{CM}^2 M_W^4 (1-7x+10x^2) - 4E_{CM}^4 M_W^2 (3-13x+9x^2+x^3) \}.$$

$$(c) \quad \mathcal{M}_u^{\gamma+Z} = \frac{g_2^2}{32M_W^4} \left(\frac{s_W^2}{u} + \frac{c_W^2}{u - M_Z^2} \right) \{ 64M_W^6(-1+x) - E_{CM}^6(-3+x)(1+x)^2 \\ + 16E_{CM}^2 M_W^4 (1+7x+10x^2) + 4E_{CM}^4 M_W^2 (-3-13x-9x^2+x^3) \}.$$

$$(d) \quad \mathcal{M}_t^h = - \frac{(C g_2 M_W)^2}{t - M_h^2} \frac{\{ 4M_W^2 + E_{CM}^2(-1+x) \}^2}{16M_W^4}.$$

$$(e) \quad \mathcal{M}_u^h = - \frac{(C g_2 M_W)^2}{u - M_h^2} \frac{\{ -4M_W^2 + E_{CM}^2(1+x) \}^2}{16M_W^4}.$$

$$(f) \quad \mathcal{M}_s^{H^{++}} = - \frac{(\hat{C} g_2 M_W)^2}{s - M_{H^{++}}^2} \frac{(E_{CM}^2 - 2M_W^2)^2}{4M_W^4}.$$

A.1.3 $W_L^+(p_1) + W_L^-(p_2) \rightarrow Z_L(k_1) + Z_L(k_2)$

Scattering amplitudes in terms of longitudinal polarization vectors and four momenta:

$$(a) \quad \mathcal{M}_p = - g_2^2 c_W^2 \{ 2(\epsilon_1 \cdot \epsilon_2)(\epsilon_3 \cdot \epsilon_4) - (\epsilon_1 \cdot \epsilon_3)(\epsilon_2 \cdot \epsilon_4) - (\epsilon_1 \cdot \epsilon_4)(\epsilon_2 \cdot \epsilon_3) \}.$$

$$(b) \quad \mathcal{M}_t^W = - \frac{g_2^2 c_W^2}{t - M_W^2} \left[\{ (p_1 + k_1)^\mu (\epsilon_1 \cdot \epsilon_3) - 2(k_1 \cdot \epsilon_1) \epsilon_3^\mu - 2(p_1 \cdot \epsilon_3) \epsilon_1^\mu \} \right. \\ \left. \{ (p_2 + k_2)_\mu (\epsilon_2 \cdot \epsilon_4) - 2(k_2 \cdot \epsilon_2) \epsilon_{4\mu} - 2(p_2 \cdot \epsilon_4) \epsilon_{2\mu} \} \right. \\ \left. + \frac{(M_W^2 - M_Z^2)^2}{M_W^2} (\epsilon_1 \cdot \epsilon_3)(\epsilon_2 \cdot \epsilon_4) \right].$$

$$(c) \quad \mathcal{M}_u^W = - \frac{g_2^2 c_W^2}{u - M_W^2} \left[\{ (p_1 + k_2)^\mu (\epsilon_1 \cdot \epsilon_4) - 2(k_2 \cdot \epsilon_1) \epsilon_4^\mu - 2(p_1 \cdot \epsilon_4) \epsilon_1^\mu \} \right. \\ \left. \{ (p_2 + k_1)_\mu (\epsilon_2 \cdot \epsilon_3) - 2(k_1 \cdot \epsilon_2) \epsilon_{3\mu} - 2(p_2 \cdot \epsilon_3) \epsilon_{2\mu} \} \right]$$

$$\begin{aligned}
& + \frac{(M_W^2 - M_Z^2)^2}{M_W^2} (\epsilon_1 \cdot \epsilon_4) (\epsilon_2 \cdot \epsilon_3) \Big]. \\
(d) \quad \mathcal{M}_s^S &= - \frac{(C g_2 M_W)(C' \frac{g_2 M_Z}{c_W})}{s - M_S^2} (\epsilon_1 \cdot \epsilon_2) (\epsilon_3 \cdot \epsilon_4). \\
(e) \quad \mathcal{M}_t^{H^+} &= - \frac{(\tilde{C} \frac{g_2 M_Z}{c_W})^2}{t - M_{H^+}^2} (\epsilon_1 \cdot \epsilon_3) (\epsilon_2 \cdot \epsilon_4). \\
(f) \quad \mathcal{M}_u^{H^+} &= - \frac{(\tilde{C} \frac{g_2 M_Z}{c_W})^2}{u - M_{H^+}^2} (\epsilon_1 \cdot \epsilon_4) (\epsilon_2 \cdot \epsilon_3).
\end{aligned}$$

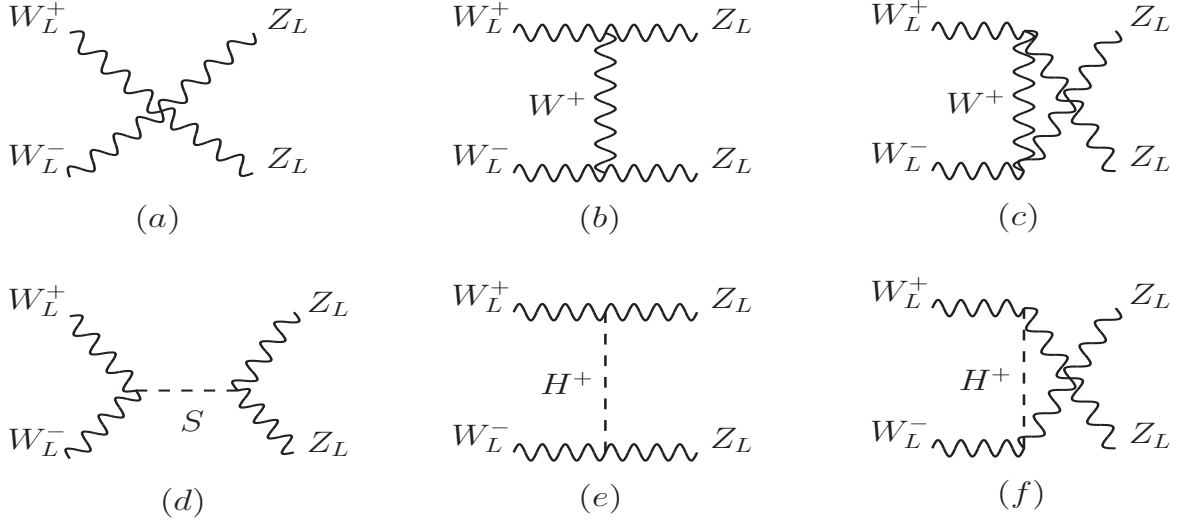


Figure A.3: Generic Feynman diagrams for $W_L^+(p_1) + W_L^-(p_2) \rightarrow Z_L(k_1) + Z_L(k_2)$ scattering.

Scattering amplitudes in terms of center of momentum energy and scattering angle:

$$\begin{aligned}
(a) \quad \mathcal{M}_p &= \frac{E_{CM}^2 g_2^2 c_W^2}{8M_W^2 M_Z^2} \{ 4(M_W^2 + M_Z^2) + E_{CM}^2 (-3 + x^2) \}. \\
(b) \quad \mathcal{M}_t^W &= - \frac{c_W^2 g_2^2}{32M_W^4 M_Z^2 (t - M_W^2)} \{ 3E_{CM}^6 M_W^2 - 4E_{CM}^4 M_W^4 - 10E_{CM}^4 M_W^2 M_Z^2 \\
&\quad + 8E_{CM}^2 M_W^4 M_Z^2 + 2E_{CM}^4 M_Z^4 + 16E_{CM}^2 M_W^2 M_Z^4 - 96M_W^4 M_Z^4 \\
&\quad - 8E_{CM}^2 M_Z^6 + 32M_W^2 M_Z^6 + x(E_{CM}^4 M_W^2 x^2 - 5E_{CM}^4 M_W^2 \\
&\quad + 12E_{CM}^2 M_W^4 + 24E_{CM}^2 M_W^2 M_Z^2 + 16M_W^4 M_Z^2
\end{aligned}$$

$$\begin{aligned}
& -4E_{CM}^2 M_Z^4 \sqrt{(-E_{CM}^2 + 4M_W^2)(-E_{CM}^2 + 4M_Z^2)} + E_{CM}^6 M_W^2 x^2 \\
& -16E_{CM}^4 M_W^4 x^2 + 32E_{CM}^2 M_W^6 x^2 - 22E_{CM}^4 M_W^2 M_Z^2 x^2 \\
& + 96E_{CM}^2 M_W^4 M_Z^2 x^2 + 2E_{CM}^4 M_Z^4 x^2 + 32E_{CM}^2 M_W^2 M_Z^4 x^2 \}. \\
(c) \quad \mathcal{M}_u^W = & -\frac{c_W^2 g_2^2}{32M_W^4 M_Z^2 (u - M_W^2)} \{ 3E_{CM}^6 M_W^2 - 4E_{CM}^4 M_W^4 - 10E_{CM}^4 M_W^2 M_Z^2 \\
& + 8E_{CM}^2 M_W^4 M_Z^2 + 2E_{CM}^4 M_Z^4 + 16E_{CM}^2 M_W^2 M_Z^4 - 96M_W^4 M_Z^4 \\
& - 8E_{CM}^2 M_Z^6 + 32M_W^2 M_Z^6 - x(E_{CM}^4 M_W^2 x^2 - 5E_{CM}^4 M_W^2 \\
& + 12E_{CM}^2 M_W^4 + 24E_{CM}^2 M_W^2 M_Z^2 + 16M_W^4 M_Z^2 \\
& - 4E_{CM}^2 M_Z^4) \sqrt{(-E_{CM}^2 + 4M_W^2)(-E_{CM}^2 + 4M_Z^2)} + E_{CM}^6 M_W^2 x^2 \\
& - 16E_{CM}^4 M_W^4 x^2 + 32E_{CM}^2 M_W^6 x^2 - 22E_{CM}^4 M_W^2 M_Z^2 x^2 \\
& + 96E_{CM}^2 M_W^4 M_Z^2 x^2 + 2E_{CM}^4 M_Z^4 x^2 + 32E_{CM}^2 M_W^2 M_Z^4 x^2 \}. \\
(d) \quad \mathcal{M}_s^S = & -\frac{(C g_2 M_W)(C' \frac{g_2 M_Z}{c_W})}{s - M_S^2} \frac{(E_{CM}^2 - 2M_W^2)(E_{CM}^2 - 2M_Z^2)}{4M_W^2 M_Z^2}. \\
(e) \quad \mathcal{M}_t^{H^+} = & -\frac{(\tilde{C} \frac{g_2 M_Z}{c_W})^2}{t - M_{H^+}^2} \frac{\{ \sqrt{(E_{CM}^2 - 4M_W^2)(E_{CM}^2 - 4M_Z^2)} - E_{CM}^2 x \}^2}{16M_W^2 M_Z^2}. \\
(f) \quad \mathcal{M}_u^{H^+} = & -\frac{(\tilde{C} \frac{g_2 M_Z}{c_W})^2}{u - M_{H^+}^2} \frac{\{ \sqrt{(E_{CM}^2 - 4M_W^2)(E_{CM}^2 - 4M_Z^2)} + E_{CM}^2 x \}^2}{16M_W^2 M_Z^2}.
\end{aligned}$$

A.1.4 $W_L^+(p_1) + Z_L(p_2) \rightarrow W_L^+(k_1) + Z_L(k_2)$

Scattering amplitudes in terms of longitudinal polarization vectors and four momenta:

$$\begin{aligned}
(a) \quad \mathcal{M}_p = & -c_W^2 g_2^2 \{ 2(\epsilon_1 \cdot \epsilon_3)(\epsilon_2 \cdot \epsilon_4) - (\epsilon_1 \cdot \epsilon_4)(\epsilon_2 \cdot \epsilon_3) - (\epsilon_1 \cdot \epsilon_2)(\epsilon_3 \cdot \epsilon_4) \}. \\
(b) \quad \mathcal{M}_s^W = & \frac{g_2^2 c_W^2}{s - M_W^2} \left[\{ (p_1 - p_2)^\mu (\epsilon_1 \cdot \epsilon_2) + 2(p_2 \cdot \epsilon_1) \epsilon_2^\mu - 2(p_1 \cdot \epsilon_2) \epsilon_1^\mu \} \right. \\
& \{ (k_2 - k_1)_\mu (\epsilon_3 \cdot \epsilon_4) - 2(k_2 \cdot \epsilon_3) \epsilon_{4\mu} - 2(k_1 \cdot \epsilon_4) \epsilon_{3\mu} \} \\
& \left. - \frac{(M_W^2 - M_Z^2)^2}{M_W^2} (\epsilon_1 \cdot \epsilon_2)(\epsilon_3 \cdot \epsilon_4) \right]. \\
(c) \quad \mathcal{M}_u^W = & -\frac{g_2^2 c_W^2}{u - M_W^2} \left[\{ (p_1 + k_2)^\mu (\epsilon_1 \cdot \epsilon_4) - 2(k_2 \cdot \epsilon_1) \epsilon_4^\mu - 2(p_1 \cdot \epsilon_4) \epsilon_1^\mu \} \right. \\
& \{ (p_2 + k_1)_\mu (\epsilon_2 \cdot \epsilon_3) - 2(k_1 \cdot \epsilon_2) \epsilon_{3\mu} - 2(p_2 \cdot \epsilon_3) \epsilon_{2\mu} \}
\end{aligned}$$

$$\begin{aligned}
& - \frac{(M_W^2 - M_Z^2)^2}{M_W^2} (\epsilon_1 \cdot \epsilon_4) (\epsilon_2 \cdot \epsilon_3) \Big]. \\
(d) \quad \mathcal{M}_t^S &= - \frac{(C g_2 M_W)(C' \frac{g_2 M_Z}{c_W})}{t - M_S^2} (\epsilon_1 \cdot \epsilon_3) (\epsilon_2 \cdot \epsilon_4). \\
(e) \quad \mathcal{M}_s^{H^+} &= - \frac{(\tilde{C} \frac{g_2 M_Z}{c_W})^2}{s - M_{H^+}^2} (\epsilon_1 \cdot \epsilon_2) (\epsilon_3 \cdot \epsilon_4). \\
(f) \quad \mathcal{M}_u^{H^+} &= - \frac{(\tilde{C} \frac{g_2 M_Z}{c_W})^2}{u - M_{H^+}^2} (\epsilon_1 \cdot \epsilon_4) (\epsilon_2 \cdot \epsilon_3).
\end{aligned}$$

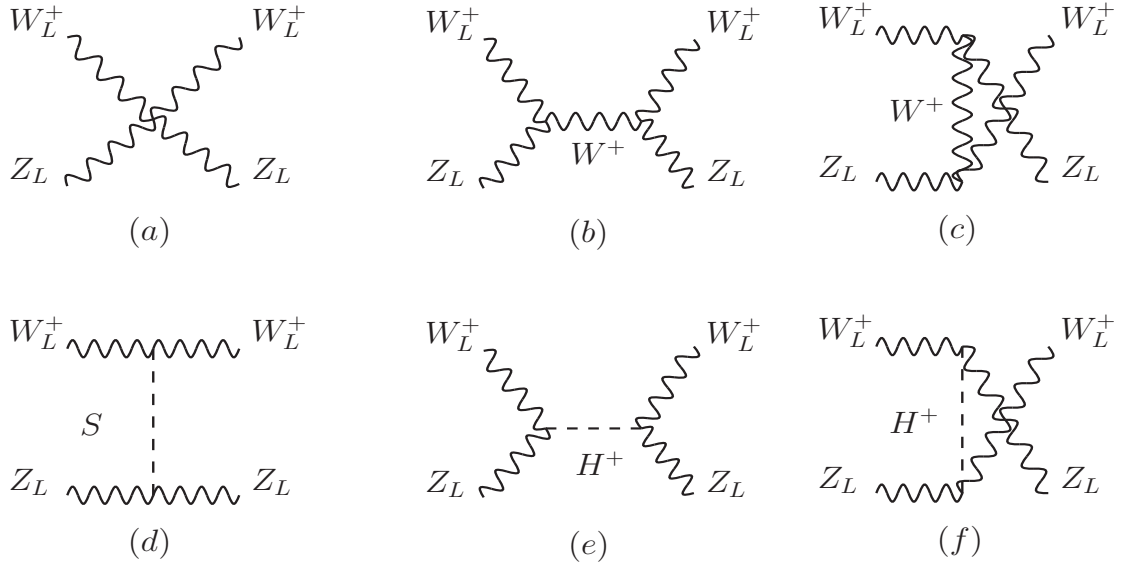


Figure A.4: *Generic Feynman diagrams for $W_L^+(p_1) + Z_L(p_2) \rightarrow W_L^+(k_1) + Z_L(k_2)$ scattering.*

Scattering amplitudes in terms of center of momentum energy and scattering angle:

$$\begin{aligned}
(a) \quad \mathcal{M}_p &= - \frac{c_W^2 g^2}{16 E_{CM}^4 M_W^2 M_Z^2} \{ 4 E_{CM}^2 (M_W^2 - M_Z^2)^2 (M_W^2 + M_Z^2) (-1 + x) \\
& \quad + (M_W^2 - M_Z^2)^4 (-1 + x)^2 \\
& \quad + 4 E_{CM}^6 (M_W^2 + M_Z^2) (1 + 3x) + E_{CM}^8 (-3 - 6x + x^2) \\
& \quad - 2 E_{CM}^4 (M_W^2 - M_Z^2)^2 (-1 + 4x + x^2) \}.
\end{aligned}$$

$$\begin{aligned}
(b) \quad \mathcal{M}_s^W = & - \frac{c_W^2 g^2}{4E_{CM}^2 M_W^4 M_Z^2 (s - M_W^2)} \left[E_{CM}^6 (M_W^2 - M_Z^2)^2 + (M_W^5 - M_W M_Z^4)^2 (-1 + x) \right. \\
& + E_{CM}^8 M_W^2 x - E_{CM}^4 \{ 2M_Z^6 + 4M_W^4 M_Z^2 (-1 + 2x) \\
& + M_W^2 M_Z^4 (-1 + 2x) + M_W^6 (3 + 2x) \} \\
& + E_{CM}^2 \{ M_W^2 + M_Z^2 \} (3M_W^6 + M_W^2 M_Z^4 + M_Z^6 \\
& \left. - M_W^4 M_Z^2 (5 + 8x) \} \right].
\end{aligned}$$

$$\begin{aligned}
(c) \quad \mathcal{M}_u^W = & \frac{M_Z^2 c_W^2 g^2}{32E_{CM}^6 M_W^4 (u - M_W^2)} \left[\{ M_W^2 (M_W^2 - M_Z^2)^6 (-1 + x)^3 \right. \\
& + E_{CM}^{12} M_W^2 (-3 + x)(1 + x)^2 \\
& - 2E_{CM}^2 (M_W^2 - M_Z^2)^4 (-1 + x)^2 (-M_Z^4 + M_W^4 x + \\
& + M_W^2 M_Z^2 (3 + x)) \} + 2E_{CM}^{10} \{ M_Z^4 (1 + x)^2 \\
& + M_W^2 M_Z^2 (1 + 9x + 7x^2 - x^3) + M_W^4 (4 + 15x + 10x^2 - x^3) \} \\
& + 4E_{CM}^6 \{ -M_Z^8 (-3 + x^2) - M_W^6 M_Z^2 (-9 + 9x + 7x^2 + x^3) \\
& + M_W^8 (-2 + x + 10x^2 + x^3) + M_W^2 M_Z^6 (-9 + x + 15x^2 + x^3) \\
& - M_W^4 M_Z^4 (-15 + 9x + 17x^2 + x^3) \} \\
& - E_{CM}^4 (M_W^2 - M_Z^2)^2 \{ -8M_Z^6 (-1 + x) \\
& + M_W^6 (-7 - 5x + 11x^2 + x^3) \\
& + M_W^2 M_Z^4 (-23 + 11x + 11x^2 + x^3) \\
& - 2M_W^4 M_Z^2 (-3 - 25x + 27x^2 + x^3) \} - E_{CM}^8 \{ 8M_Z^6 (1 + x) \\
& + 2M_W^4 M_Z^2 (9 + 25x + 31x^2 - x^3) \\
& + M_W^2 M_Z^4 (-13 + 19x + 49x^2 + x^3) \\
& \left. + M_W^6 (3 + 35x + 49x^2 + x^3) \} \right].
\end{aligned}$$

$$\begin{aligned}
(d) \quad \mathcal{M}_t^S = & - \frac{(C \ g_2 M_W)(C' \ \frac{g_2 M_Z}{c_W})}{t - M_S^2} \left(\frac{1}{16E_{CM}^4 M_W^2 M_Z^2} \right) \left[\{ E_{CM}^4 (-1 + x) \right. \\
& + (M_W^2 - M_Z^2)^2 (-1 + x) \\
& + 2E_{CM}^2 (-M_Z^2 (-1 + x) + M_W^2 (1 + x)) \} \{ E_{CM}^4 (-1 + x) \\
& \left. + (M_W^2 - M_Z^2)^2 (-1 + x) + 2E_{CM}^2 (-M_W^2 (-1 + x) \right.
\end{aligned}$$

$$\begin{aligned}
& + M_Z^2(1+x)) \} \}. \\
(e) \quad \mathcal{M}_u^{H^+} = & - \frac{(\tilde{C} \frac{g_2 M_Z}{c_W})^2}{u - M_{H^+}^2} \left(\frac{1}{16 E_{CM}^4 M_W^2 M_Z^2} \right) \{ 2 E_{CM}^2 (M_W^2 + M_Z^2) \\
& + (M_W^2 - M_Z^2)^2 (-1+x) - E_{CM}^4 (1+x) \}^2. \\
(f) \quad \mathcal{M}_s^{H^+} = & - \frac{(\tilde{C} \frac{g_2 M_Z}{c_W})^2}{s - M_{H^+}^2} \frac{(-E_{CM}^2 + M_W^2 + M_Z^2)^2}{4 M_W^2 M_Z^2}.
\end{aligned}$$

A.1.5 $Z_L(p_1) + Z_L(p_2) \rightarrow Z_L(k_1) + Z_L(k_2)$

Scattering amplitudes in terms of longitudinal polarization vectors and four momenta:

$$\begin{aligned}
(a) \quad \mathcal{M}_s^S = & - \frac{(C' \frac{g_2 M_Z}{c_W})^2}{(s - M_S^2)} (\epsilon_1 \cdot \epsilon_2) (\epsilon_3 \cdot \epsilon_4). \\
(b) \quad \mathcal{M}_t^S = & - \frac{(C' \frac{g_2 M_Z}{c_W})^2}{(t - M_S^2)} (\epsilon_1 \cdot \epsilon_3) (\epsilon_2 \cdot \epsilon_4). \\
(c) \quad \mathcal{M}_u^S = & - \frac{(C' \frac{g_2 M_Z}{c_W})^2}{(u - M_S^2)} (\epsilon_1 \cdot \epsilon_4) (\epsilon_2 \cdot \epsilon_3).
\end{aligned}$$

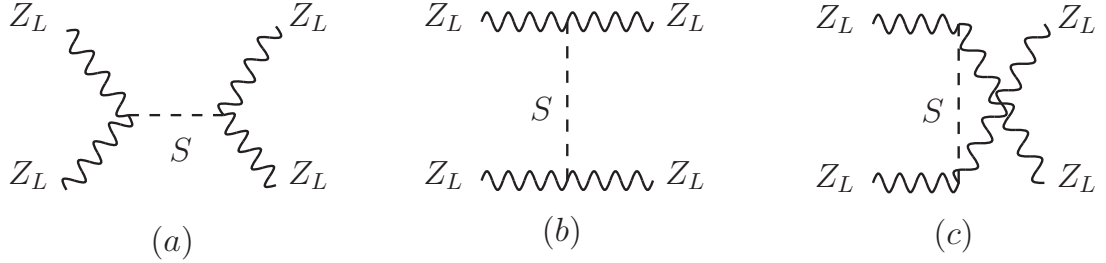


Figure A.5: Generic Feynman diagrams for $Z_L(p_1) + Z_L(p_2) \rightarrow Z_L(k_1) + Z_L(k_2)$ scattering.

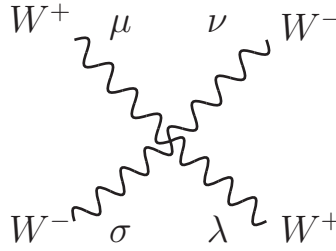
Scattering amplitudes in terms of center of momentum energy and scattering angle:

$$\begin{aligned}
(a) \quad \mathcal{M}_s^S = & - \frac{(C' \frac{g_2 M_Z}{c_W})^2}{(s - M_S^2)} \frac{(E_{CM}^2 - 2 M_Z^2)^2}{4 M_Z^4}. \\
(b) \quad \mathcal{M}_t^S = & - \frac{(C' \frac{g_2 M_Z}{c_W})^2}{(t - M_S^2)} \frac{\{ 4 M_Z^2 + E_{CM}^2 (-1+x) \}^2}{16 M_Z^4}.
\end{aligned}$$

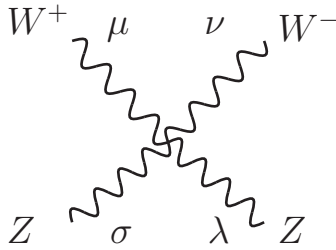
$$(c) \quad \mathcal{M}_u^{S=} = -\frac{(C' \frac{g_2 M_Z}{c_W})^2}{(u - M_S^2)} \frac{\{-4M_Z^2 + E_{CM}^2(1+x)\}^2}{16M_Z^4}.$$

A.2 Required Feynman rules for VV scattering

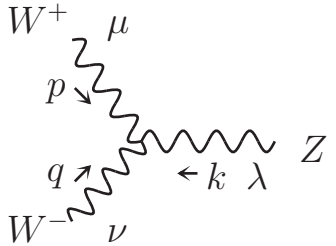
The Feynman rules for the different vertices with the assumption that all momenta and fields are incoming.



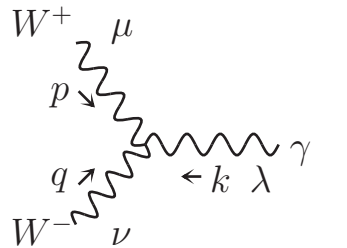
$$: i g_2^2 (2g^{\mu\lambda} g^{\sigma\nu} - g^{\mu\sigma} g^{\nu\lambda} - g^{\sigma\lambda} g^{\mu\nu}). \quad (\text{A.1})$$



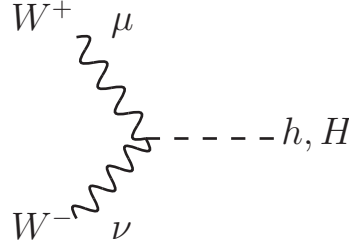
$$: -i g_2^2 c_W^2 (2g^{\mu\nu} g^{\sigma\lambda} - g^{\nu\sigma} g^{\mu\lambda} - g^{\nu\lambda} g^{\mu\sigma}). \quad (\text{A.2})$$



$$: i g_2 c_W \{(p - q)^\lambda g^{\mu\nu} + (q - k)^\mu g^{\lambda\nu} + (k - p)^\nu g^{\mu\lambda}\}. \quad (\text{A.3})$$



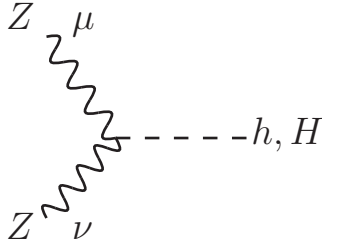
$$: i g_2 s_W \{(p - q)^\lambda g^{\mu\nu} + (q - k)^\mu g^{\lambda\nu} + (k - p)^\nu g^{\mu\lambda}\}. \quad (\text{A.4})$$



$$W^+ \mu \quad \text{---} \quad \text{---} \quad h, H \quad : ig_2 M_W g_{\mu\nu} C, \text{ where } C \text{ is given by:}$$

$$W^- \nu$$

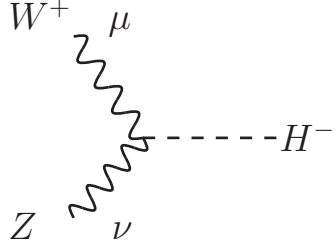
$$\begin{aligned}
 \text{SM :} & \quad \begin{cases} \text{for } h, & C = 1, \\ \text{for } H, & C = 0, \end{cases} \\
 \text{2HDM :} & \quad \begin{cases} \text{for } h, & C = \sin(\beta - \alpha), \\ \text{for } H, & C = \cos(\beta - \alpha), \end{cases} \\
 Y = 0 \text{ HTM :} & \quad \begin{cases} \text{for } h, & C = (\cos \tilde{\beta} \cos \gamma + 2 \sin \tilde{\beta} \sin \gamma), \\ \text{for } H, & C = (-\cos \tilde{\beta} \sin \gamma + 2 \sin \tilde{\beta} \cos \gamma), \end{cases} \\
 Y = 2 \text{ HTM :} & \quad \begin{cases} \text{for } h, & C = (\cos \beta' \cos \gamma' + \sqrt{2} \sin \beta' \sin \gamma'), \\ \text{for } H, & C = (-\cos \beta' \sin \gamma' + \sqrt{2} \sin \beta' \cos \gamma'). \end{cases}
 \end{aligned} \tag{A.5}$$



$$Z \mu \quad \text{---} \quad \text{---} \quad h, H \quad : \frac{ig_2 M_Z}{c_W} g_{\mu\nu} C', \text{ where } C' \text{ is given by:}$$

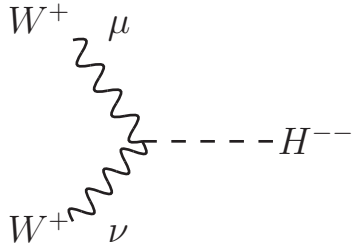
$$Z \nu$$

$$\begin{aligned}
 \text{SM :} & \quad \begin{cases} \text{for } h, & C' = 1, \\ \text{for } H, & C' = 0, \end{cases} \\
 \text{2HDM :} & \quad \begin{cases} \text{for } h, & C' = \sin(\beta - \alpha), \\ \text{for } H, & C' = \cos(\beta - \alpha), \end{cases} \\
 Y = 0 \text{ HTM :} & \quad \begin{cases} \text{for } h, & C' = \cos \gamma, \\ \text{for } H, & C' = -\sin \gamma, \end{cases} \\
 Y = 2 \text{ HTM :} & \quad \begin{cases} \text{for } h, & C' = (\cos \delta' \cos \gamma' + 2 \sin \delta' \sin \gamma'), \\ \text{for } H, & C' = (-\cos \delta' \sin \gamma' + 2 \sin \delta' \cos \gamma'). \end{cases}
 \end{aligned} \tag{A.6}$$



$$: \frac{ig_2 M_Z}{c_W} g_{\mu\nu} \tilde{C}, \text{ where } \tilde{C} \text{ is given by:}$$

$$\begin{aligned}
\text{SM :} & \quad \tilde{C} = 0, \\
\text{2HDM :} & \quad \tilde{C} = 0, \\
Y = 0 \text{ HTM :} & \quad \tilde{C} = \sin \tilde{\beta} \cos \tilde{\beta} \frac{M_W}{M_Z}, \\
Y = 2 \text{ HTM :} & \quad \tilde{C} = c_W \left\{ \sin \beta' \cos \delta' s_W^2 - \frac{(1 + s_W^2)}{\sqrt{2}} \cos \beta' \sin \delta' \right\}.
\end{aligned} \tag{A.7}$$



$$: ig_2 M_W g_{\mu\nu} \hat{C}, \text{ where } \hat{C} \text{ is given by:}$$

$$\begin{aligned}
\text{SM :} & \quad \hat{C} = 0, \\
\text{2HDM :} & \quad \hat{C} = 0, \\
Y = 0 \text{ HTM :} & \quad \hat{C} = 0, \\
Y = 2 \text{ HTM :} & \quad \hat{C} = 2 \sin \beta'.
\end{aligned} \tag{A.8}$$

A.3 Restoration of unitarity in extended scalar sectors

Generally when $E_{CM} \gg M_i$ ($i \equiv W, Z, h, H, H^+, H^{++}$), one can express $V_L V_L \rightarrow V_L V_L$ scattering amplitude as,

$$\mathcal{M} = A_4 E_{CM}^4 + A_2 E_{CM}^2 + A_0 + A_{-2} E_{CM}^{-2} + \dots \tag{A.9}$$

If $A_{4,2} \neq 0$ then the scattering cross-section will increase with E_{CM} . The $SU(2)_L \times U(1)_Y$ gauge symmetry implies that $A_4 = 0$ from the gauge mediated and cross diagrams. We need the scalar particles in the model so A_2 becomes exactly zero for $E_{CM} \gg M_i$ and theory become unitarized, i.e., the cross-section will decrease with energy.

The gauge and scalar contributions to A_2 and A_0 are denoted as,

$$A_2 = A_{2,g} + \sum_S A_{2,S}, \quad S = h, H, H^+, H^{++}, \quad (\text{A.10})$$

and

$$A_0 = A_{0,g} + A_{0,S}. \quad (\text{A.11})$$

The expressions for $A_{2,g}$, $A_{2,S}$, $A_{0,g}$ and $A_{0,S}$ of different vector bosons scattering processes are presented for different models of extended scalar sector.

1. $W_L^+ W_L^- \rightarrow W_L^+ W_L^-$

	SM	2HDM	HTM($Y = 0$)	HTM($Y = 2$)
$A_{2,g}$	$\frac{g_2^2(4M_W^2 - 3c_W^2 M_Z^2)(1+x)}{2M_W^4}$	$\frac{g_2^2(4M_W^2 - 3c_W^2 M_Z^2)(1+x)}{2M_W^4}$	$\frac{g_2^2(4M_W^2 - 3c_W^2 M_Z^2)(1+x)}{2M_W^4}$	$\frac{g_2^2(4M_W^2 - 3c_W^2 M_Z^2)(1+x)}{2M_W^4}$
$A_{2,S}(S \equiv h, H)$	$-\frac{g_2^2}{2M_W^2} C^2 (1+x)$	$-\frac{g_2^2}{2M_W^2} C^2 (1+x)$	$-\frac{g_2^2}{2M_W^2} C^2 (1+x)$	$-\frac{g_2^2}{2M_W^2} C^2 (1+x)$
$A_{2,S}(S \equiv H^+)$	0	0	0	0
$A_{2,S}(S \equiv H^{++})$	0	0	0	$\frac{g_2^2}{2M_W^2} \hat{C}^2 (1+x)$

Table A.1: $A_{2,g}$ and $A_{2,S}$ for $W_L^+ W_L^- \rightarrow W_L^+ W_L^-$ process. C and \hat{C} can be found in Appendix A.2.

$$A_{0,g} = \frac{g_2^2}{4M_W^4(-1+x)} \left\{ -c_W^2 M_Z^4(3+x^2) - 2c_W^2 M_W^2 M_Z^2(-3-6x+x^2) + 4M_W^4(-1-4x+x^2) \right\} \quad (\text{A.12})$$

$$A_{0,S} = -\frac{1}{4M_W^4} \left[(g_2 M_W \hat{C})^2 \{ M_{H^{++}}^2 - 2M_W^2(-1+x) \} + 2 \sum_{S=h,H} (g_2 M_W C)^2 \{ M_S^2 + M_W^2(-1+x) \} \right] \quad (\text{A.13})$$

2. $W_L^+ W_L^+ \rightarrow W_L^+ W_L^+$

	SM	2HDM	HTM($Y = 0$)	HTM($Y = 2$)
$A_{2,g}$	$\frac{g_2^2(3c_W^2 M_Z^2 - 4M_W^2)}{M_W^4}$	$\frac{g_2^2(3c_W^2 M_Z^2 - 4M_W^2)}{M_W^4}$	$\frac{g_2^2(3c_W^2 M_Z^2 - 4M_W^2)}{M_W^4}$	$\frac{g_2^2(3c_W^2 M_Z^2 - 4M_W^2)}{M_W^4}$
$A_{2,S}(S \equiv h, H)$	$\frac{g_2^2}{M_W^2} C^2$	$\frac{g_2^2}{M_W^2} C^2$	$\frac{g_2^2}{M_W^2} C^2$	$\frac{g_2^2}{M_W^2} C^2$
$A_{2,S}(S \equiv H^+)$	0	0	0	0
$A_{2,S}(S \equiv H^{++})$	0	0	0	$-\frac{g_2^2}{M_W^2} \hat{C}^2$

Table A.2: $A_{2,g}$ and $A_{2,S}$ for $W_L^+ W_L^+ \rightarrow W_L^+ W_L^+$ process. C and \hat{C} can be found in Appendix A.2.

$$A_{0,g} = \frac{g_2^2}{2M_W^4(-1+x^2)} \left\{ c_W^2 M_Z^4(3+x^2) + 4M_W^4(1+3x^2) - 2c_W^2 M_W^2 M_Z^2(3+5x^2) \right\} \quad (\text{A.14})$$

$$A_{0,S} = -\frac{1}{4M_W^4} \left\{ (g_2 M_W \hat{C})^2 (M_{H^{++}}^2 - 4M_W^2) + 2 \sum_{S=h,H} (g_2 M_W C)^2 (M_S^2 + 2M_W^2) \right\} \quad (\text{A.15})$$

3. $W_L^+ W_L^- \rightarrow Z_L Z_L$

	SM	2HDM	HTM($Y = 0$)	HTM($Y = 2$)
$A_{2,g}$	$\frac{g_2^2 c_W^2 M_Z^2}{M_W^4}$	$\frac{g_2^2 c_W^2 M_Z^2}{M_W^4}$	$\frac{g_2^2 c_W^2 M_Z^2}{M_W^4}$	$\frac{g_2^2 c_W^2 M_Z^2}{M_W^4}$
$A_{2,S}(S \equiv h, H)$	$-\frac{g_2^2}{c_W M_W M_Z} C C'$	$-\frac{g_2^2}{c_W M_W M_Z} C C'$	$-\frac{g_2^2}{c_W M_W M_Z} C C'$	$-\frac{g_2^2}{c_W M_W M_Z} C C'$
$A_{2,S}(S \equiv H^+)$	0	0	$\frac{g_2^2}{c_W^2 M_W^2} \tilde{C}^2$	$\frac{g_2^2}{c_W^2 M_W^2} \tilde{C}^2$
$A_{2,S}(S \equiv H^{++})$	0	0	0	0

Table A.3: $A_{2,g}$ and $A_{2,S}$ for $W_L^+ W_L^- \rightarrow Z_L Z_L$ process. C, C' and \tilde{C} can be found in Appendix A.2.

$$A_{0,g} = -\frac{c_W^2 g_2^2 M_Z^2}{2M_W^4(-1+x^2)} \left\{ M_Z^2(-1+x^2) + 2M_W^2(1+x^2) \right\} \quad (\text{A.16})$$

$$A_{0,S} = \frac{1}{4M_W^2 M_Z^2} \left[-2 \left(\frac{g_2 M_Z}{c_W} \tilde{C} \right)^2 (M_{H^+}^2 + M_W^2 + M_Z^2) \right]$$

$$+ \sum_{S=h,H} (g_2 M_W C) \left(\frac{g_2 M_Z}{c_W} C' \right) \{ -M_S^2 + 2(M_W^2 + M_Z^2) \} \Big\} \quad (\text{A.17})$$

4. $W_L^+ Z_L \rightarrow W_L^+ Z_L$

	SM	2HDM	HTM($Y=0$)	HTM($Y=2$)
$A_{2,g}$	$-\frac{g_2^2 c_W^2 M_Z^2 (1-x)}{8M_W^4}$	$-\frac{g_2^2 c_W^2 M_Z^2 (1-x)}{8M_W^4}$	$-\frac{g_2^2 c_W^2 M_Z^2 (1-x)}{8M_W^4}$	$-\frac{g_2^2 c_W^2 M_Z^2 (1-x)}{8M_W^4}$
$A_{2,S}(S \equiv h, H)$	$\frac{g_2^2 (1-x)}{8c_W M_W M_Z} C C'$	$\frac{g_2^2 (1-x)}{8c_W M_W M_Z} C C'$	$\frac{g_2^2 (1-x)}{8c_W M_W M_Z} C C'$	$\frac{g_2^2 (1-x)}{8c_W M_W M_Z} C C'$
$A_{2,S}(S \equiv H^+)$	0	0	$-\frac{g_2^2}{8c_W^2 M_W^2} (1-x) \tilde{C}^2$	$\frac{g_2^2}{8c_W^2 M_W^2} (1-x) \tilde{C}^2$
$A_{2,S}(S \equiv H^{++})$	0	0	0	0

Table A.4: $A_{2,g}$ and $A_{2,S}$ for $W_L^+ Z_L \rightarrow W_L^+ Z_L$ process. C, C' and \tilde{C} can be found in Appendix A.2.

$$A_{0,g} = \frac{c_W^2 g_2^2 M_Z^2}{4M_W^4 (1+x)} \{ 2M_W^2 (-1+x) + M_Z^2 (1+x)^2 \} \quad (\text{A.18})$$

$$A_{0,S} = -\frac{1}{4M_W^2 M_Z^2} \left[\left(\frac{g_2 M_Z}{c_W} \tilde{C} \right)^2 \{ 2M_{H^+}^2 - (M_W^2 + M_Z^2)(1+x) \} \right. \\ \left. + \sum_{S=h,H} (g_2 M_W C) \left(\frac{g_2 M_Z}{c_W} C' \right) \{ (M_S^2 + (M_W^2 + M_Z^2)(1+x)) \} \right] \quad (\text{A.19})$$

5. $Z_L Z_L \rightarrow Z_L Z_L$

There are no gauge contributions in this process so $A_{2,V} = 0$ and the contributions to A_0 are given as follows:

$$A_{0,V} = 0, \quad (\text{no gauge contributions}), \quad (\text{A.20})$$

$$A_{0,S} = -\frac{3}{4M_Z^4} \sum_{S=h,H} \left(\frac{g_2 M_Z}{c_W} C' \right)^2 M_S^2. \quad (\text{A.21})$$

Appendix B

Effective Higgs quartic coupling and RG -equations for SM

B.1 Effective Higgs quartic coupling for SM

The Higgs effective quartic coupling including one-loop and two-loop radiative corrections[14].

$$\lambda_{\text{eff}}^{\text{SM}}(\phi) = e^{4\Gamma(\phi)}[\lambda(\mu = \phi) + \lambda_{\text{eff}}^{(1)}(\mu = \phi) + \lambda_{\text{eff}}^{(2)}(\mu = \phi)] \quad (\text{B.1})$$

Here,

$$\begin{aligned} (16\pi^2) \lambda_{\text{eff}}^{(1)} = & \frac{3}{8}g_2^4 \left(\ln \frac{g_2^2}{4} - \frac{5}{6} + 2\Gamma \right) + \frac{3}{16}(g_1^2 + g_2^2)^2 \left(\ln \frac{g_1^2 + g_2^2}{4} - \frac{5}{6} + 2\Gamma \right) \\ & - 3y_t^4 \left(\ln \frac{y_t^2}{2} - \frac{3}{2} + 2\Gamma \right) + 3\lambda^2 (4 \ln \lambda - 6 + 3 \ln 3 + 8\Gamma) \end{aligned} \quad (\text{B.2})$$

and

$$\begin{aligned} (16\pi^2)^2 \lambda_{\text{eff}}^{(2)} = & \frac{1}{576}g_1^4 g_2^2 \left\{ 4359 + 218\pi^2 - 36 \left(2\Gamma + \ln \frac{g_2^2}{4} \right) - 153 \left(2\Gamma + \ln \frac{g_2^2}{4} \right)^2 \right. \\ & - 4080 \left(2\Gamma + \ln \frac{g_1^2 + g_2^2}{4} \right) + 306 \left(2\Gamma + \ln \frac{g_2^2}{4} \right) \left(2\Gamma + \ln \frac{g_1^2 + g_2^2}{4} \right) \\ & + 924 \left(2\Gamma + \ln \frac{g_1^2 + g_2^2}{4} \right)^2 + 132 \left(2\Gamma + \ln \frac{g_1^2 + g_2^2}{4} \right) \left(2\Gamma + \ln \frac{y_t^2}{2} \right) \\ & \left. - 66 \left(2\Gamma + \ln \frac{y_t^2}{2} \right)^2 \right\} + \frac{1}{192}g_1^2 g_2^4 \left\{ 817 + 46\pi^2 + 213 \left(2\Gamma + \ln \frac{g_2^2}{4} \right)^2 \right. \\ & - 6 \left(2\Gamma + \ln \frac{g_2^2}{4} \right) (50 + 53 \left(2\Gamma + \ln \frac{g_1^2 + g_2^2}{4} \right)) \\ & \left. + 4 \left(2\Gamma + \ln \frac{g_1^2 + g_2^2}{4} \right) \left(-91 + 57(2\Gamma + \ln \frac{g_1^2 + g_2^2}{4}) \right) \right\} \end{aligned}$$

$$\begin{aligned}
& +12\left(2\Gamma + \ln \frac{g_1^2 + g_2^2}{4}\right)\left(2\Gamma + \ln \frac{y_t^2}{2}\right) - 6\left(2\Gamma + \ln \frac{y_t^2}{2}\right)^2 \Big\} \\
& +8g_3^2 y_t^4 \left\{ 9 - 8\left(2\Gamma + \ln \frac{y_t^2}{2}\right) + 3\left(2\Gamma + \ln \frac{y_t^2}{2}\right)^2 \right\} \\
& +\frac{1}{8}g_1^2 g_2^2 y_t^2 \left\{ -57 + 44\left(2\Gamma + \ln \frac{g_1^2 + g_2^2}{4}\right) + 4\left(2\Gamma + \ln \frac{y_t^2}{2}\right) \right. \\
& \left. -18\left(2\Gamma + \ln \frac{g_1^2 + g_2^2}{4}\right)\left(2\Gamma + \ln \frac{y_t^2}{2}\right) + 9\left(2\Gamma + \ln \frac{y_t^2}{2}\right)^2 \right\} \\
& +\frac{1}{48}g_1^4 y_t^2 \left\{ 189 - 28\left(2\Gamma + \ln \frac{g_1^2 + g_2^2}{4}\right) - 68\left(2\Gamma + \ln \frac{y_t^2}{2}\right) \right. \\
& \left. -54\left(2\Gamma + \ln \frac{g_1^2 + g_2^2}{4}\right)\left(2\Gamma + \ln \frac{y_t^2}{2}\right) + 27\left(2\Gamma + \ln \frac{y_t^2}{2}\right)^2 \right\} \\
& +\frac{1}{576}g_1^6 \left\{ 2883 + 206\pi^2 - 9\left(2\Gamma + \ln \frac{g_2^2}{4}\right)^2 + 708\left(2\Gamma + \ln \frac{g_1^2 + g_2^2}{4}\right)^2 \right. \\
& \left. -102\left(2\Gamma + \ln \frac{y_t^2}{2}\right)^2 + 6\left(2\Gamma + \ln \frac{g_1^2 + g_2^2}{4}\right)\left(-470 + 3\left(2\Gamma + \ln \frac{g_2^2}{4}\right) \right. \right. \\
& \left. \left. +34\left(2\Gamma + \ln \frac{y_t^2}{2}\right)\right)\right\} +\frac{1}{6}y_t^6 \left\{ -9g_2^2\left(1 - \ln \frac{g_2^2}{4} + \ln \frac{y_t^2}{2}\right) + 4g_1^2\left(9 - 8\left(2\Gamma \right. \right. \right. \\
& \left. \left. + \ln \frac{y_t^2}{2}\right) + 3\left(2\Gamma + \ln \frac{y_t^2}{2}\right)^2\right)\right\} +\frac{1}{192}g_2^6 \left\{ -2067 + 90\pi^2 + 1264\left(2\Gamma \right. \right. \\
& \left. \left. + \ln \frac{g_2^2}{4}\right) + 69\left(2\Gamma + \ln \frac{g_2^2}{4}\right)^2 + 632\left(2\Gamma + \ln \frac{g_1^2 + g_2^2}{4}\right) - 414\left(2\Gamma + \ln \frac{g_2^2}{4}\right)\left(2\Gamma \right. \right. \\
& \left. \left. + \ln \frac{g_1^2 + g_2^2}{4}\right) + 156\left(2\Gamma + \ln \frac{g_1^2 + g_2^2}{4}\right)^2 + 36\left(2\Gamma + \ln \frac{g_1^2 + g_2^2}{4}\right)\left(2\Gamma + \ln \frac{y_t^2}{2}\right) \right. \\
& \left. 54\left(2\Gamma + \ln \frac{y_t^2}{2}\right)^2 - 144\left(-\ln \frac{g_2^2}{4} + \ln \frac{y_t^2}{2}\right)\left(2\Gamma + \ln \frac{g_2^2 y_t^2}{4}\right)\right\} \\
& +\frac{1}{2}y_t^6 \left\{ -69 - \pi^2 + 48\left(2\Gamma + \ln \frac{y_t^2}{2}\right) - 6\left(2\Gamma + \ln \frac{g_2^2}{4}\right)\left(2\Gamma + \ln \frac{y_t^2}{2}\right) \right. \\
& \left. -3\left(2\Gamma + \ln \frac{y_t^2}{2}\right)^2 - 6\left(-\ln \frac{g_2^2}{4} + \ln \frac{y_t^2}{2}\right)\left(2\Gamma + \ln \frac{g_2^2 y_t^2}{4}\right)\right\}
\end{aligned}$$

$$\begin{aligned}
& + \frac{3}{16} g_2^4 y_t^2 \left\{ 15 + 2\pi^2 + 8 \left(2\Gamma + \ln \frac{g_2^2}{4} \right) + 4 \left(2\Gamma + \ln \frac{g_1^2 + g_2^2}{4} \right) - 12 \left(2\Gamma + \ln \frac{y_t^2}{2} \right) \right. \\
& - 6 \left(2\Gamma + \ln \frac{g_1^2 + g_2^2}{4} \right) \left(2\Gamma + \ln \frac{y_t^2}{2} \right) - 3 \left(2\Gamma + \ln \frac{y_t^2}{2} \right)^2 \\
& \left. + 12 \left(-\ln \frac{g_2^2}{4} + \ln \frac{y_t^2}{2} \right) \left(2\Gamma + \ln \frac{g_2^2 y_t^2}{4} \right) \right\} + \frac{3}{4} \left(g_2^6 - 3g_2^4 y_t^2 + 4y_t^6 \right) \text{Polylog}_2 \left[\frac{g_2^2}{2y_t^2} \right] \\
& + \frac{1}{64} g_2^2 \left(g_1^4 + 18g_1^2 g_2^2 - 51g_2^4 - \frac{48g_2^6}{g_1^2 + g_2^2} \right) \sqrt{-\frac{4(g_1^2 + g_2^2)}{g_2^2} + \frac{(g_1^2 + g_2^2)^2}{g_2^4}} \left\{ \frac{\pi^2}{3} \right. \\
& - \ln \left[\frac{g_1^2 + g_2^2}{g_2^2} \right]^2 + 2 \ln \left[\frac{1}{2} - \frac{1}{2} \sqrt{-3 + \frac{4g_1^2}{g_1^2 + g_2^2}} \right]^2 \\
& \left. - 4 \text{Polylog}_2 \left[\frac{1}{2} - \frac{1}{2} \sqrt{-3 + \frac{4g_1^2}{g_1^2 + g_2^2}} \right] \right\} + \frac{1}{96} \sqrt{(g_1^2 + g_2^2)(g_1^2 + g_2^2 - 8y_t^2)} \left(17g_1^4 \right. \\
& - 6g_1^2 g_2^2 + 9g_2^4 + 2 \left(7g_1^2 - 73g_2^2 + \frac{64g_2^2}{g_1^2 + g_2^2} y_t^2 \right) \left\{ \frac{\pi^2}{3} - \ln \left[\frac{g_1^2 + g_2^2}{2y_t^2} \right]^2 \right. \\
& \left. \left. + 2 \ln \left[\frac{1}{2} \left(1 - \sqrt{1 - \frac{8y_t^2}{g_1^2 + g_2^2}} \right) \right]^2 - 4 \text{Polylog}_2 \left[\frac{1}{2} \left(1 - \sqrt{1 - \frac{8y_t^2}{g_1^2 + g_2^2}} \right) \right] \right\} \right\}, \quad (\text{B.3})
\end{aligned}$$

where,

$$\Gamma(\phi) = \int_{M_t}^{\phi} \gamma(\mu) d \ln \mu.$$

Anomalous $\gamma(\mu)$ function of the Higgs field takes care of its wave function renormalization.

$$\begin{aligned}
\gamma = & \frac{1}{16\pi^2} \left\{ \frac{3g_1^2}{4} + \frac{9g_2^2}{4} - 3y_t^2 \right\} + \frac{1}{(16\pi^2)^2} \left\{ -\frac{431g_1^4}{96} - \frac{9g_1^2 g_2^2}{16} + \frac{271g_2^4}{32} - 6\lambda^2 \right. \\
& \left. + y_t^2 \left(-\frac{85g_1^2}{24} - \frac{45g_2^2}{8} - 20g_3^2 + \frac{27y_t^2}{4} \right) \right\} + \frac{1}{(16\pi^2)^3} \left\{ -\frac{1315g_1^6}{54} + \frac{193g_1^4 g_2^2}{36} + \frac{181g_1^2 g_2^4}{60} \right. \\
& - \frac{15851g_2^6}{100} + \frac{419g_1^4 g_3^2}{36} + \frac{2857g_2^4 g_3^2}{100} + \frac{107g_1^4 \lambda}{36} + \frac{119}{20} g_1^2 g_2^2 \lambda + \frac{223g_2^4 \lambda}{25} \\
& - 15g_1^2 \lambda^2 - 45g_2^2 \lambda^2 + 36\lambda^3 + \frac{1499g_1^4 y_t^2}{36} - \frac{1321}{60} g_1^2 g_2^2 y_t^2 + \frac{117g_2^4 y_t^2}{5} \\
& \left. - \frac{291}{20} g_1^2 g_3^2 y_t^2 - \frac{757}{100} g_2^2 g_3^2 y_t^2 - \frac{4462g_3^4 y_t^2}{25} + \frac{135\lambda^2 y_t^2}{2} + \frac{471g_1^2 y_t^4}{20} + \frac{4011g_2^2 y_t^4}{100} \right\}
\end{aligned}$$

$$+\frac{1581g_3^2y_t^4}{20}-45\lambda y_t^4-\frac{6013y_t^6}{13}\Big\}$$

B.2 Standard Model β -functions

The beta functions of the coupling parameters χ ($\chi \equiv g_1, g_2, g_3, y_f, \lambda$ and m^2) for the SM are defined as,

$$\beta_\chi = \frac{\partial \chi}{\partial \ln \mu}. \quad (\text{B.4})$$

Beta function of the standard model coupling constants and the mass term up to three loop are presented here for completeness [14, 173–177],

$$\begin{aligned} \beta_{g_1} = & g_1^3 \left[\frac{1}{16\pi^2} \left(\frac{41}{6} \right) + \frac{1}{(16\pi^2)^2} \left\{ \frac{1}{18} (199g_1^2 + 81g_2^2 + 264g_3^2 - 51y_t^2) \right. \right. \\ & + \frac{1}{(16\pi^2)^3} \left\{ -\frac{388613g_1^4}{5184} + \frac{1315g_2^4}{64} + 99g_3^4 - 3\lambda^2 - \frac{29g_3^2y_t^2}{3} \right. \\ & + \frac{315y_t^4}{16} + \frac{1}{864}g_1^2(1845g_2^2 - 4384g_3^2 + 1296\lambda - 8481y_t^2) \\ & \left. \left. + g_2^2 \left(-g_3^2 + \frac{3\lambda}{2} - \frac{785y_t^2}{32} \right) \right\} \right] \end{aligned} \quad (\text{B.5})$$

$$\begin{aligned} \beta_{g_2} = & g_2^3 \left[\frac{1}{16\pi^2} \left(-\frac{19}{6} \right) + \frac{1}{(16\pi^2)^2} \left\{ \frac{1}{6} (9g_1^2 + 35g_2^2 + 72g_3^2 - 9y_t^2) \right\} \right. \\ & + \frac{1}{(16\pi^2)^3} \left\{ -\frac{5597g_1^4}{576} + \frac{324953g_2^4}{1728} + 81g_3^4 - 3\lambda^2 - 7g_3^2y_t^2 \right. \\ & + \frac{147y_t^4}{16} + \frac{1}{96}g_1^2(873g_2^2 - 32g_3^2 + 48\lambda - 593y_t^2) \\ & \left. \left. + g_2^2 \left(39g_3^2 + \frac{3\lambda}{2} - \frac{729y_t^2}{32} \right) \right\} \right] \end{aligned} \quad (\text{B.6})$$

$$\begin{aligned} \beta_{g_3} = & g_3^3 \left[\frac{1}{16\pi^2} \left(-7 \right) + \frac{1}{(16\pi^2)^2} \left\{ \frac{11g_1^2}{6} + \frac{9g_2^2}{2} - 2(13g_3^2 + y_t^2) \right\} \right. \\ & + \frac{1}{(16\pi^2)^3} \left\{ -\frac{2615g_1^4}{216} + \frac{109g_2^4}{8} + \frac{65g_3^4}{2} - 40g_3^2y_t^2 + 15y_t^4 \right. \end{aligned}$$

$$\left. + g_2^2 \left(21g_3^2 - \frac{93y_t^2}{8} \right) - \frac{1}{72} g_1^2 (9g_2^2 - 616g_3^2 + 303y_t^2) \right\} \Bigg] \quad (\text{B.7})$$

$$\begin{aligned} \beta_{y_t} = & y_t \left[\frac{1}{16\pi^2} \left\{ \frac{1}{12} (-17g_1^2 - 27g_2^2 - 96g_3^2 + 54y_t^2) \right\} + \frac{1}{(16\pi^2)^2} \left\{ \frac{1187g_1^4}{216} - \frac{23g_2^4}{4} \right. \right. \\ & + g_1^2 \left(-\frac{3g_2^2}{4} + \frac{19g_3^2}{9} + \frac{131y_t^2}{16} \right) + g_2^2 \left(9g_3^2 + \frac{225y_t^2}{16} \right) \\ & \left. \left. - 6(18g_3^4 - \lambda^2 - 6g_3^2y_t^2 + 2\lambda y_t^2 + 2y_t^4) \right\} \right. \\ & + \frac{1}{(16\pi^2)^3} \frac{1}{24} \left\{ 24g_3^2(16\lambda y_t^2 - 157y_t^4) \right. \\ & + 4g_3^4y_t^2(3827 - 1368\zeta(3)) + 16g_3^6(-2083 + 960\zeta(3)) \\ & \left. \left. + 9(-96\lambda^3 + 10\lambda^2y_t^2 + 528\lambda y_t^4 + y_t^6(113 + 36\zeta(3))) \right\} \right] \quad (\text{B.8}) \end{aligned}$$

$$\begin{aligned} \beta_\lambda = & \left[\frac{1}{16\pi^2} \left\{ \frac{3}{8} (2g_2^4 + (g_1^2 + g_2^2)^2) + 24\lambda^2 - 6y_t^4 - 3\lambda(g_1^2 + 3g_2^2 - 4y_t^2) \right\} \right. \\ & + \frac{1}{(16\pi^2)^2} \frac{1}{48} \left\{ -379g_1^6 - 559g_1^4g_2^2 - 289g_1^2g_2^4 + 915g_2^6 \right. \\ & + 48\lambda \left(\frac{629g_1^4}{24} - \frac{73g_2^4}{8} + 108g_2^2\lambda - 312\lambda^2 + g_1^2 \left(\frac{39g_2^2}{4} + 36\lambda \right) \right) \\ & - 4(57g_1^4 - 2g_1^2(63g_2^2 + 85\lambda) + 3(9g_2^4 - 90g_2^2\lambda + 64\lambda(-5g_3^2 + 9\lambda)))y_t^2 \\ & \left. \left. - 16(8g_1^2 + 96g_3^2 + 9\lambda)y_t^4 + 1440y_t^6 \right\} + \frac{1}{(16\pi^2)^3} \frac{1}{12} \left\{ 20952\lambda^3y_t^2 \right. \right. \\ & + 288\lambda^4(299 + 168\zeta(3)) \\ & - y_t^4(g_3^4(2128 - 768\zeta(3)) + 48g_3^2y_t^2(19 - 120\zeta(3)) + 9y_t^4(533 + 96\zeta(3))) \\ & + 108\lambda^2y_t^2(16g_3^2(-17 + 16\zeta(3)) + y_t^2(191 + 168\zeta(3))) \\ & + \lambda y_t^2(27y_t^4(13 - 176\zeta(3)) - 32g_3^4(-311 + 36\zeta(3)) \\ & \left. \left. - 24g_3^2y_t^2(-895 + 1296\zeta(3))) \right\} + 0.0000133607g_3^6y_t^4 \right] \quad (\text{B.9}) \end{aligned}$$

$$\beta_{m^2} = m^2 \left[\frac{1}{(16\pi^2)} \left\{ 6\lambda + 3y_t^2 - \frac{9g_2^2}{4} - \frac{3g_1^2}{4} \right\} + \frac{1}{(16\pi^2)^2} \left\{ \lambda(-30\lambda - 36y_t^2 + 36g_2^2 + 12g_1^2) \right. \right.$$

$$\begin{aligned}
& +y_t^2 \left(-\frac{27y_t^2}{4} + 20g_3^2 + \frac{45g_2^2}{8} + \frac{85g_1^2}{24} \right) + \left(-\frac{145}{32}g_2^4 + \frac{557}{96}g_1^4 + \frac{15g_2^2g_1^2}{16} \right) \\
& + \frac{1}{(16\pi^2)^3} \left\{ \lambda^2(1026\lambda + 148.5y_t^2 - 192.822g_2^2 - 64.273g_1^2) + \lambda y_t^2(347.394y_t^2 \right. \\
& + 80.385g_3^2 - 318.591g_2^2 - 99.498g_1^2) + \lambda(-64.5145g_2^4 - 182.79g_1^4 \\
& - 63.0385g_2^2g_1^2) + y_t^4(154.405y_t^2 - 209.24g_3^2 - 3.82928g_2^2 - 12.5128g_1^2) \\
& + y_t^2(178.484g_3^4 - 102.627g_2^4 - 77.0028g_1^4 + 7.572g_3^2g_2^2 + 14.545g_3^2g_1^2 \\
& + 19.1167g_2^2g_1^2) + g_2^4(-28.572g_3^2 + 301.724g_2^2 + 16.552g_1^2) + g_1^4(-11.642g_3^2 \\
& \left. + 27.161g_2^2 + 38.786g_1^2) \right\} \Bigg] \tag{B.10}
\end{aligned}$$

B.3 β -functions for singlet scalar extended SM

As a discrete Z_2 symmetry have been imposed on the extra singlet scalar, *odd* number of scalars do not couple with the standard model particles. So the β -functions of g_1, g_2, g_3 and Yukawa couplings remain unchanged. Only the Higgs quartic coupling β_λ gets modified. At one loop, we have to add $\frac{k^2/2}{16\pi^2}$ with β_λ of eqn. B.4. The β -functions of λ_S and κ are given by [15, 114, 118, 178],

$$\beta_\kappa = \begin{cases} 0 & \text{for } \mu < M_S \\ \frac{\kappa}{16\pi^2} [4\kappa + 12\lambda + 6y^2 - \frac{3}{2}(g'^2 + 3g^2) + \lambda_S] & \text{for } \mu \geq M_S \end{cases}, \tag{B.11}$$

$$\beta_{\lambda_S} = \begin{cases} 0 & \text{for } \mu < M_S \\ \frac{1}{16\pi^2} [3\lambda_S^2 + 12\kappa^2] & \text{for } \mu \geq M_S \end{cases}. \tag{B.12}$$

B.4 β -functions for inert doublet extended SM

As in inert doublet model pseudoscalar A has been taken as a lightest particle, the expressions of β -functions at one loop are given as follows [36],

For $\mu < M_A$,

$$\beta_{\lambda_1} = \beta_\lambda^{SM} \quad \text{and} \quad \beta_{\lambda_{2,3,4,5}} = 0, \tag{B.13}$$

and for $\mu > M_A$

$$\begin{aligned}\beta_{\lambda_1} = & \frac{1}{16\pi^2} [24\lambda_1^2 + 2\lambda_3^2 + 2\lambda_3\lambda_4 + \lambda_4^2 + \lambda_5^2 \\ & + \frac{3}{8} (3g_2^4 + g_1^4 + 2g_2^2g_1^2) - 3\lambda_1 (3g_2^2 + g_1^2) \\ & + 4\lambda_1 (y_\tau^2 + 3y_b^2 + 3y_t^2) - 2 (y_\tau^4 + 3y_b^4 + 3y_t^4)],\end{aligned}\quad (\text{B.14})$$

$$\begin{aligned}\beta_{\lambda_2} = & 24\lambda_2^2 + 2\lambda_3^2 + 2\lambda_3\lambda_4 + \lambda_4^2 + \lambda_5^2 \\ & + \frac{3}{8} (3g_2^4 + g_1^4 + 2g_2^2g_1^2) - 3\lambda_2 (3g_2^2 + g_1^2)],\end{aligned}\quad (\text{B.15})$$

$$\begin{aligned}\beta_{\lambda_3} = & \frac{1}{16\pi^2} [4(\lambda_1 + \lambda_2)(3\lambda_3 + \lambda_4) + 4\lambda_3^2 + 2\lambda_4^2 + 2\lambda_5^2 \\ & + \frac{3}{4} (3g_2^4 + g_1^4 - 2g_2^2g_1^2) - 3\lambda_3 (3g_2^2 + g_1^2) \\ & + 2\lambda_3 (y_\tau^2 + 3y_t^2 + 3y_b^2)],\end{aligned}\quad (\text{B.16})$$

$$\begin{aligned}\beta_{\lambda_4} = & \frac{1}{16\pi^2} [4\lambda_4(\lambda_1 + \lambda_2 + 2\lambda_3 + \lambda_4) + 8\lambda_5^2 \\ & + 3g_2^2g_1^2 - 3\lambda_4 (3g_2^2 + g_1^2) \\ & + 2\lambda_4 (y_\tau^2 + 3y_t^2 + 3y_b^2)],\end{aligned}\quad (\text{B.17})$$

$$\begin{aligned}\beta_{\lambda_5} = & \frac{1}{16\pi^2} [4\lambda_5(\lambda_1 + \lambda_2 + 2\lambda_3 + 3\lambda_4) \\ & - 3\lambda_5 (3g_2^2 + g_1^2) \\ & + 2\lambda_5 (y_\tau^2 + 3y_t^2 + 3y_b^2)].\end{aligned}\quad (\text{B.18})$$

In this case the symbol λ_1 is the same as Higgs quartic coupling λ . Let us note the y_t dependence of these expressions. While β_{λ_1} is dominated by the y_t^4 term, β_{λ_2} does not depend on y_t . The y_t dependence of other β_{λ_i} s are softened by the corresponding λ_i multiplying the y_t^2 terms. Two-loop RGEs used in this work have been generated using SARAH [179].

B.5 β -functions for inert triplet ($Y = 0$) extended SM

Similarly for β -functions for inert triplet model at one-loop given as follows [77]:

For $\mu < M_H$,

$$\beta_{\lambda_1} = \beta_{\lambda}^{SM} \quad \text{and} \quad \beta_{\lambda_{2,3}} = 0, \quad (\text{B.19})$$

and for $\mu > M_H$

$$\begin{aligned} \beta_{\lambda_1} = & \frac{1}{16\pi^2} \left[24\lambda_1^2 + \frac{3}{2}\lambda_3^2 + \frac{3}{8}(3g_2^4 + g_1^4 + 2g_2^2g_1^2) - 3\lambda_1(3g_2^2 + g_1^2) \right. \\ & \left. + 4\lambda_1(y_\tau^2 + 3y_b^2 + 3y_t^2) - 2(y_\tau^4 + 3y_b^4 + 3y_t^4) \right], \end{aligned} \quad (\text{B.20})$$

$$\beta_{\lambda_2} = \frac{1}{16\pi^2} [22\lambda_2^2 + 2\lambda_3^2 + 12g_2^4 - 24g_2^2\lambda_2], \quad (\text{B.21})$$

$$\beta_{\lambda_3} = \frac{1}{16\pi^2} [6g_2^4 + 12\lambda_1\lambda_3 + 10\lambda_2\lambda_3 + 4\lambda_3^2 + \lambda_3(6y_t^2 - \frac{33}{2}g_2^2 - \frac{3}{2}g_1^2)]. \quad (\text{B.22})$$

In this work two-loop RGEs are used for the extra scalar sectors.

References

- [1] Aad G. *et al.* (2012), Observation of a new particle in the search for the Standard Model Higgs boson with the ATLAS detector at the LHC, Phys. Lett. B 716, 1-29 (DOI: 10.1016/j.physletb.2012.08.020).
- [2] Chatrchyan S. *et al.* (2012), Observation of a new boson at a mass of 125 GeV with the CMS experiment at the LHC, Phys. Lett. B 716, 30-61 (DOI: 10.1016/j.physletb.2012.08.021).
- [3] Figure taken from the website “https://en.wikipedia.org/wiki/Standard_Model”.
- [4] Higgs P. W. (1964), Broken Symmetries and the Masses of Gauge Bosons, Phys. Rev. Lett. 13, 508-509 (DOI: 10.1103/PhysRevLett.13.508).
- [5] Higgs P. W. (1966), Spontaneous Symmetry Breakdown without Massless Bosons, Phys. Rev. 145, 1156-1163 (DOI: 10.1103/PhysRev.145.1156).
- [6] Englert F. and Brout R. (1964), Broken Symmetry and the Mass of Gauge Vector Mesons, Phys. Rev. Lett. 13, 321-323 (DOI: 10.1103/PhysRevLett.13.321).
- [7] Higgs P. W. (1964), Broken symmetries, massless particles and gauge fields, Phys. Lett. 12, 132-133 (DOI: 10.1016/0031-9163(64)91136-9).
- [8] Cabibbo N. (1963), Unitary Symmetry and Leptonic Decays, Phys. Rev. Lett. 10, 531-533 (DOI: 10.1103/PhysRevLett.10.531).

-
- [9] Kobayashi M. and Maskawa T. (1973), CP Violation in the Renormalizable Theory of Weak Interaction, *Prog. Theor. Phys.* 49, 652-657 (DOI: 10.1143/PTP.49.652).
 - [10] Olive K. A. *et al.* (2014), Review of Particle Physics, *Chin. Phys. C* 38, 090001 (DOI: 10.1088/1674-1137/38/9/090001).
 - [11] Abada A. *et al.* (2007), Low energy effects of neutrino masses, *JHEP* 0712, 061 (DOI: 10.1088/1126-6708/2007/12/061).
 - [12] A. Zee (1980), A Theory of Lepton Number Violation, Neutrino Majorana Mass, and Oscillation, *Phys. Lett. B* 93, 389 (DOI: 10.1016/0370-2693(80)90193-8).
 - [13] Degrandi G. *et al.* (2012), Higgs mass and vacuum stability in the Standard Model at NNLO, *JHEP* 1208, 098 (DOI: 10.1007/JHEP08(2012)098).
 - [14] Buttazzo D. *et al.* (2013), Investigating the near-criticality of the Higgs boson, *JHEP* 1312, 089 (DOI: 10.1007/JHEP12(2013)089).
 - [15] Khan N. and Rakshit S. (2014), Study of electroweak vacuum metastability with a singlet scalar dark matter, *Phys. Rev. D* 90, 113008 (DOI: 10.1103/PhysRevD.90.113008).
 - [16] Masina I. and Notari A. (2012), The Higgs mass range from Standard Model false vacuum Inflation in scalar-tensor gravity, *Phys. Rev. D* 85, 123506 (DOI: 10.1103/PhysRevD.85.123506).
 - [17] Isidori G. *et al.* (2008), Gravitational corrections to standard model vacuum decay, *Phys. Rev. D* 77, 025034 (DOI: 10.1103/PhysRevD.77.025034).
 - [18] Bezrukov F. L. and Shaposhnikov M. (2008), The Standard Model Higgs boson as the inflaton, *Phys. Lett. B* 659, 703 (DOI: 10.1016/j.physletb.2007.11.072).

- [19] Kamada K. *et al.* (2012), Generalized Higgs inflation, Phys. Rev. D 86, 023504 (DOI: 10.1103/PhysRevD.86.023504).
- [20] Bennett C. L. *et al.* (2013), Nine-Year Wilkinson Microwave Anisotropy Probe (WMAP) Observations: Final Maps and Results, Astrophys. J. Suppl. 208, 20 (DOI: 10.1088/0067-0049/208/2/20).
- [21] Ade P. A. R. *et al.* (2014), Planck 2013 results. XVI. Cosmological parameters, Astron. Astrophys. 571, A 16 (DOI: 10.1051/0004-6361/201321591).
- [22] Rich J., Lloyd D. Owen and Spiro M. (1987), Experimental Particle Physics Without Accelerators, Phys. Rept. 151, 239 (DOI:10.1016/0370-1573(87)90055-X), Smith P. F. (1988), Terrestrial Searches for New Stable Particles, Contemp. Phys. 29, 159. (DOI:10.1080/00107518808213759), Olive K. A. (2009), Dark Energy and Dark Matter, Conf. Proc. C 0908171, 257 (DOI:10.3204/DESY-PROC-2010-04/35).
- [23] Sakharov A. D. (1967, 1991), Violation of CP Invariance, C Asymmetry, and Baryon Asymmetry of the Universe, Pisma Zh. Eksp. Teor. Fiz. 5, 32-35, JETP Lett. 5, 24-27, Sov. Phys. Usp. 34, 392-393, Usp. Fiz. Nauk. 161, 61-64 (DOI: 10.1070/PU1991v034n05ABEH002497).
- [24] CMS Collaboration (2015), Measurements of the Higgs boson production and decay rates and constraints on its couplings from a combined ATLAS and CMS analysis of the LHC pp collision data at $\sqrt{s} = 7$ and 8 TeV, (CMS-PAS-HIG-15-002).
- [25] Aaboud M. *et al.* (2016), Search for resonances in diphoton events at $\sqrt{s}=13$ TeV with the ATLAS detector, arXiv:1606.03833 [hep-ex]. Diphoton searches in CMS. <https://indico.in2p3.fr/event/12279/session/12/contribution/218/>.

-
- [26] Schael S. *et al.* (2006), Precision electroweak measurements on the Z resonance, Phys. Rept. 427, 257 (DOI: 10.1016/j.physrep.2005.12.006).
- [27] Abe K. *et al.* (2000), A High precision measurement of the left-right Z boson cross-section asymmetry, Phys. Rev. Lett. 84, 5945 (DOI: 10.1103/PhysRevLett.84.5945).
- [28] Lee B. W. (1972), Perspectives on theory of weak interactions, NAL-THY-92 (FERMILAB-CONF-72-092-T).
- [29] Khan N. *et al.* (2016), Exploring the extended scalar sector with resonances in vector boson scattering, [arXiv:1608.05673 [hep-ph]](under review).
- [30] Peskin M. E. and Takeuchi T. (1992), Estimation of oblique electroweak corrections, Phys. Rev. D 46, 381-409 (DOI: 10.1103/PhysRevD.46.381).
- [31] Altarelli G. and Barbieri R. (1991), Vacuum polarization effects of new physics on electroweak processes, Phys. Lett. B 253, 161 (DOI: 10.1016/0370-2693(91)91378-9).
- [32] Lavoura L. and Li L. F. (1994), Making the small oblique parameters large, Phys. Rev. D 49, 1409-1416 (DOI: 10.1103/PhysRevD.49.1409).
- [33] Baak M. *et al.* (2014), The global electroweak fit at NNLO and prospects for the LHC and ILC, Eur. Phys. J. C 74, 3046 (DOI: 10.1140/epjc/s10052-014-3046-5).
- [34] Chakraborty J. *et al.* (2014), Copositive Criteria and Boundedness of the Scalar Potential, Phys. Rev. D 89, 095008 (DOI: 10.1103/PhysRevD.89.095008).
- [35] Yao Y. P. and Yuan C. P. (1988), Modification of the Equivalence Theorem Due to Loop Corrections, Phys. Rev. D 38, 2237 (DOI: 10.1103/PhysRevD.38.2237),

- Veltman H. G. J. (1990), The Equivalence Theorem, Phys. Rev. D 41, 2294 (DOI: 10.1103/PhysRevD.41.2294), He H. J. *et al.* (1992), On the precise formulation of equivalence theorem, Phys. Rev. Lett. 69, 2619 (DOI: 10.1103/PhysRevLett.69.2619).
- [36] Khan N. and Rakshit S. (2015), Constraints on inert dark matter from the metastability of the electroweak vacuum, Phys. Rev. D 92, 055006 (DOI: 10.1103/PhysRevD.92.055006).
- [37] Khan N. (2016), Exploring Hyperchargeless Higgs Triplet Model up to the Planck Scale,[arXiv:1610.03178 [hep-ph]] (under review).
- [38] Freese K. (2009), Review of Observational Evidence for Dark Matter in the Universe and in upcoming searches for Dark Stars, EAS Publ. Ser. 36, 113-126 (DOI: 10.1051/eas/0936016).
- [39] Clowe D. *et al.* (2006), A direct empirical proof of the existence of dark matter, Astrophys. J. 648, L 109-L 113 (DOI: 10.1086/508162).
- [40] Alcock C. *et al.* (1998), EROS and MACHO combined limits on planetary mass dark matter in the galactic halo, Astrophys. J. 499, L 9 (DOI: 10.1086/311355).
- [41] Tisserand P. *et al.* (2007), Limits on the Macho Content of the Galactic Halo from the EROS-2 Survey of the Magellanic Clouds, Astron. Astrophys. 469, 387-404 (DOI: 10.1051/0004-6361:20066017).
- [42] Doe P. J. *et al.* (2013), Project 8: Determining neutrino mass from tritium beta decay using a frequency-based method, arXiv:1309.7093 [nucl-ex] (C13-07-29.2).
- [43] Murayama H. (2007), Physics Beyond the Standard Model and Dark Matter, arXiv:0704.2276 [hep-ph] (C06-07-31.1).

-
- [44] Lin D. N. C. and Faber S. M. (1983), Some implications of nonluminous matter in dwarf spheroidal galaxies, *Astrophys. J.* 266, L 21-L 25 (DOI: 10.1086/183971).
- [45] Hwang J. C. (1997), Roles of a coherent scalar field on the evolution of cosmic structures, *Phys. Lett. B* 401, 241-246 (DOI: 10.1016/S0370-2693(97)00400-0).
- [46] Abdo A. A. *et al.* (2009), Measurement of the Cosmic Ray e^+ plus e^- spectrum from 20 GeV to 1 TeV with the Fermi Large Area Telescope, *Phys. Rev. Lett.* 102, 181101 (DOI: 10.1103/PhysRevLett.102.181101).
- [47] Aguilar M. *et al.* (2013), First Result from the Alpha Magnetic Spectrometer on the International Space Station: Precision Measurement of the Positron Fraction in Primary Cosmic Rays of 0.5–350 GeV, *Phys. Rev. Lett.* 110, 141102 (DOI: 10.1103/PhysRevLett.110.141102).
- [48] Adriani O. *et al.* (2013), Measurement of the flux of primary cosmic ray antiprotons with energies of 60-MeV to 350-GeV in the PAMELA experiment, *JETP Lett.* 96, 621-627, *Pisma Zh. Eksp. Teor. Fiz.* 96, 693-699 (DOI: 10.1134/S002136401222002X).
- [49] Savage C. *et al.* (2009), Compatibility of DAMA/LIBRA dark matter detection with other searches, *JCAP* 0904, 010 (DOI: 10.1088/1475-7516/2009/04/010).
- [50] Aprile E. *et al.* (2012), Dark Matter Results from 225 Live Days of XENON100 Data, *Phys. Rev. Lett.* 109, 181301 (DOI: 10.1103/PhysRevLett.109.181301).
- [51] Aprile E. *et al.* (2011), Dark Matter Results from 100 Live Days of XENON100 Data, *Phys. Rev. Lett.* 107, 131302 (DOI: 10.1103/PhysRevLett.107.131302).
- [52] <http://dendera.berkeley.edu/plotter/entryform.html>, <http://dmtools.brown.edu>.

-
- [53] Akerib D. S. *et al.* (2014), First results from the LUX dark matter experiment at the Sanford Underground Research Facility, *Phys. Rev. Lett.* 112, 091303 (DOI: 10.1103/PhysRevLett.112.091303).
- [54] Agrawal P. *et al.* (2010), A Classification of Dark Matter Candidates with Primarily Spin-Dependent Interactions with Matter, arXiv:1003.1912 [hep-ph] (UMD-PP-10-004).
- [55] Bernabei R. *et al.* (2010), New results from DAMA/LIBRA, *Eur. Phys. J. C* 67, 39-49 (DOI: 10.1140/epjc/s10052-010-1303-9).
- [56] Aalseth C. E. *et al.* (2013), CoGeNT: A Search for Low-Mass Dark Matter using p-type Point Contact Germanium Detectors, *Phys. Rev. D* 88, 012002 (DOI: 10.1103/PhysRevD.88.012002).
- [57] Agnese R. *et al.* (2013), Silicon Detector Dark Matter Results from the Final Exposure of CDMS II, *Phys. Rev. Lett.* 111, 251301 (DOI: 10.1103/PhysRevLett.111.251301).
- [58] Hooper D. and Goodenough L. (2011), Dark Matter Annihilation in The Galactic Center As Seen by the Fermi Gamma Ray Space Telescope, *Phys. Lett. B* 697, 412-428 (DOI: 10.1016/j.physletb.2011.02.029).
- [59] Geng C. Q. *et al.* (2015), Revisiting multicomponent dark matter with new AMS-02 data, *Phys. Rev. D* 91, 095006 (DOI: 10.1103/PhysRevD.91.095006).
- [60] McDonald J. (1994), Gauge singlet scalars as cold dark matter, *Phys. Rev. D* 50, 3637-3649 (DOI: 10.1103/PhysRevD.50.3637).
- [61] Cynolter G. *et al.* (2005), Note on unitarity constraints in a model for a singlet scalar dark matter candidate, *Acta Phys. Polon. B* 36, 827-832 (ITP-BUDAPEST-614).

-
- [62] Pelliccioni M. (2015), CMS High mass WW and ZZ Higgs search with the complete LHC Run1 statistics, arXiv:1505.03831 (C15-03-14).
- [63] Branco G. C. *et al.* (2012), Theory and phenomenology of two-Higgs-doublet models, Phys. Rept. 516, 1-102 (DOI: 10.1016/j.physrep.2012.02.002).
- [64] Glashow S. L. and Weinberg S. (1977), Natural Conservation Laws for Neutral Currents, Phys. Rev. D 15, 1958 (DOI: 10.1103/PhysRevD.15.1958).
- [65] Paschos E. A. (1977), Diagonal Neutral Currents, Phys. Rev. D 15, 1966 (DOI: 10.1103/PhysRevD.15.1966).
- [66] Arhrib A. (2005), Top and Higgs flavor changing neutral couplings in two Higgs doublets model, Phys. Rev. D 72, 075016 (DOI: 10.1103/PhysRevD.72.075016).
- [67] Dery A. *et al.* (2013), Higgs couplings to fermions: 2HDM with MFV, JHEP 1308, 006 (DOI: 10.1007/JHEP08(2013)006).
- [68] Pich A. and Tuzon P. (2009), Yukawa Alignment in the Two-Higgs-Doublet Model, Phys. Rev. D 80, 091702 (DOI: 10.1103/PhysRevD.80.091702).
- [69] Eriksson D. *et al.* (2010), 2HDMC: Two-Higgs-Doublet Model Calculator Physics and Manual, Comput. Phys. Commun. 181, 189-205 (DOI: 10.1016/j.cpc.2009.09.011).
- [70] Deshpande N. G. and Ma E. (1978), Pattern of Symmetry Breaking with Two Higgs Doublets, Phys. Rev. D 18, 2574 (DOI: 10.1103/PhysRevD.18.2574).
- [71] Lee B. W. *et al.* (1977), Weak Interactions at Very High-Energies: The Role of the Higgs Boson Mass, Phys. Rev. D 16, 1519 (DOI: 10.1103/PhysRevD.16.1519).
- [72] Arhrib A. *et al.* (2012), $H \rightarrow \gamma\gamma$ in Inert Higgs Doublet Model, Phys. Rev. D 85, 095021 (DOI: 10.1103/PhysRevD.85.095021).

- [73] He H. J. *et al.* (2001), Extra families, Higgs spectrum and oblique corrections, Phys. Rev. D 64, 053004 (DOI: 10.1103/PhysRevD.64.053004).
- [74] Mahmoudi F. and Stal O. (2010), Flavor constraints on the two-Higgs-doublet model with general Yukawa couplings, Phys. Rev. D 81, 035016 (DOI: 10.1103/PhysRevD.81.035016).
- [75] Chen M. C. *et al.* (2008), Higgs Triplets, Decoupling, and Precision Measurements, Phys. Rev. D 78, 093001 (DOI: 10.1103/PhysRevD.78.093001).
- [76] Kanemura S. *et al.* (1993), Lee-Quigg-Thacker bounds for Higgs boson masses in a two doublet model, Phys. Lett. B 313, 155-160 (DOI: 10.1016/0370-2693(93)91205-2).
- [77] Forshaw J. R. *et al.* (2003), Mass bounds in a model with a triplet Higgs, JHEP 0306, 059 (DOI: 10.1088/1126-6708/2003/06/059).
- [78] Forshaw J. R. *et al.* (2001), Higgs mass bounds in a triplet model, JHEP 0110, 007 (DOI: 10.1088/1126-6708/2001/10/007).
- [79] Arhrib A. *et al.* (2011), The Higgs Potential in the Type II Seesaw Model, Phys. Rev. D 84, 095005 (DOI: 10.1103/PhysRevD.84.095005).
- [80] Chun E. J. *et al.* (2013), Vacuum Stability, Perturbativity, EWPD and Higgs-to-diphoton in Type II Seesaw, arXiv:1305.0329 (C13-02-13.1).
(2015), (DOI: 10.1007/JHEP03(2015)041).
- [81] Kanemura S. *et al.* (2015), LHC Run-I constraint on the mass of doubly charged Higgs bosons in the same-sign diboson decay scenario, PTEP2015, 051B02 (DOI: 10.1093/ptep/ptv071).
- [82] Das D. and Santamaria A. (2016), Updated scalar sector constraints in Higgs triplet model, Phys. Rev. D 94, 015015 (DOI: 10.1103/PhysRevD.94.015015).

-
- [83] Araki T. *et al.* (2011), Dark Matter in Inert Triplet Models, Phys. Rev. D 83, 075014 (DOI: 10.1103/PhysRevD.83.075014).
 - [84] Dawson S. (1998), Introduction to electroweak symmetry breaking, hep-ph/9901280 (C98-06-29.8).
 - [85] Bhattacharyya G. *et al.* (2013), Modified Higgs couplings and unitarity violation, Phys. Rev. D 87, 011702, (DOI: 10.1103/PhysRevD.87.011702).
 - [86] Choudhury D. *et al.* (2013), Anomalous Higgs Couplings as a Window to New Physics, Phys. Rev. D 88, 013014 (DOI: 10.1103/PhysRevD.88.013014).
 - [87] Chang J. *et al.* (2013), WW scattering in the era of post-Higgs-boson discovery, Phys. Rev. D 87, 093005 (DOI: 10.1103/PhysRevD.87.093005).
 - [88] Cheung K. *et al.* (2008), Partially Strong WW Scattering, Phys. Rev. D 78, 051701 (DOI: 10.1103/PhysRevD.78.051701).
 - [89] Das D. and Saha I. (2015), Search for a stable alignment limit in two-Higgs-doublet models, Phys. Rev. D 91, 095024 (DOI: 10.1103/PhysRevD.91.095024).
 - [90] Ford C. *et al.* (1992), The Standard model effective potential at two loops, Nucl. Phys. B 387, 373-390, (DOI: 10.1016/0550-3213(92)90165-8).
 - [91] Martin S. P. (2002), Two loop effective potential for a general renormalizable theory and softly broken supersymmetry Phys. Rev. D 65, 116003 (DOI: 10.1103/PhysRevD.65.116003).
 - [92] Casas J. A. *et al.* (1995), Improved Higgs mass stability bound in the standard model and implications for supersymmetry, Phys. Lett. B 342, 171-179 (DOI: 10.1016/0370-2693(94)01404-Z).

-
- [93] Altarelli G. and Isidori G. (1994), Lower limit on the Higgs mass in the standard model: An Update, Phys. Lett. B 337, 141-144 (DOI: 10.1016/0370-2693(94)91458-3).
- [94] Casas J. A. *et al.* (1995), The Lightest Higgs boson mass in the minimal supersymmetric standard model, Nucl. Phys. B 436, 3-29, (DOI: 10.1016/0550-3213(95)00057-Y).
- [95] Casas J. A. *et al.* (1996), Standard model stability bounds for new physics within LHC reach, Phys. Lett. B 382, 374-382 (DOI: 10.1016/0370-2693(96)00682-X).
- [96] Quiros M. (1997), Constraints on the Higgs boson properties from the effective potential, hep-ph/9703412 (IEM-FT-153-97).
- [97] Sirlin A. and Zucchini R. (1986), Dependence of the Quartic Coupling $H(m)$ on $M(H)$ and the Possible Onset of New Physics in the Higgs Sector of the Standard Model, Nucl. Phys. B 266, 389-409 (DOI: 10.1016/0550-3213(86)90096-9).
- [98] Melnikov K. and Ritbergen T. V. (2000), The Three loop relation between the \overline{MS} and the pole quark masses, Phys. Lett. B 482, 99-108 (DOI: 10.1016/S0370-2693(00)00507-4).
- [99] Holthausen M. *et al.* (2012), Planck scale Boundary Conditions and the Higgs Mass, JHEP 1202, 037 (DOI: 10.1007/JHEP02(2012)037).
- [100] Bezrukov F. *et al.* (2012), Higgs Boson Mass and New Physics, JHEP 1210, 140 (DOI: 10.1007/JHEP10(2012)140).
- [101] J. Alcaraz *et al.* (2006), A Combination of preliminary electroweak measurements and constraints on the standard model, hep-ex/0612034 (CERN-PH-EP/2006-042).

-
- [102] J. Beringer *et al.* (2012), Review of Particle Physics (RPP), Phys. Rev. D 86, 010001 (DOI: 10.1103/PhysRevD.86.010001).
- [103] Giardino P. P. *et al.*, The universal Higgs fit, JHEP 1405, 046 (2014) (DOI: 10.1007/JHEP05(2014)046).
- [104] ATLAS and CDF and CMS and D0 Collaborations (2014), First combination of Tevatron and LHC measurements of the top-quark mass, arXiv:1403.4427 (ATLAS-CONF-2014-008, CDF-NOTE-11071, CMS-PAS-TOP-13-014, D0-NOTE-6416, FERMILAB-TM-2582-E).
- [105] Tishchenko V. *et al.* (2013), Detailed Report of the MuLan Measurement of the Positive Muon Lifetime and Determination of the Fermi Constant, Phys. Rev. D 87, 052003 (DOI: 10.1103/PhysRevD.87.052003).
- [106] Bethke S. (2013), World Summary of α_s (2012), Nucl. Phys. Proc. Suppl. 234, 229-234 (DOI: 10.1016/j.nuclphysbps.2012.12.020).
- [107] Coleman S. R. (1977), The Fate of the False Vacuum. 1. Semiclassical Theory, Phys. Rev. D 15, 2929-2936 (DOI: 10.1103/PhysRevD.16.1248).
- [108] Isidori G. *et al.* (2001), On the metastability of the standard model vacuum, Nucl. Phys. B 609, 387-409 (DOI: 10.1016/S0550-3213(01)00302-9).
- [109] Coleman S. R. and Luccia F. De (1980), Gravitational Effects on and of Vacuum Decay, Phys. Rev. D 21, 3305 (DOI: 10.1103/PhysRevD.21.3305).
- [110] Rose L. D. *et al.* (2016), On the fate of the Standard Model at finite temperature, JHEP 1605, 050 (DOI: 10.1007/JHEP05(2016)050).
- [111] Espinosa J. R. and Quiros M. (1995), Improved metastability bounds on the standard model Higgs mass, Phys. Lett. B 353, 257-266 (DOI: 10.1016/0370-2693(95)00572-3).

-
- [112] Shaposhnikov M. and Wetterich C. (2010), Asymptotic safety of gravity and the Higgs boson mass, *Phys. Lett. B* 683, 196-200 (DOI: 10.1016/j.physletb.2009.12.022).
- [113] Burgess C. P. *et al.* (2001), The Minimal model of nonbaryonic dark matter: A Singlet scalar, *Nucl. Phys. B* 619, 709-728 (DOI: 10.1016/S0550-3213(01)00513-2).
- [114] Haba N. *et al.* (2014), Planck scale boundary conditions in the standard model with singlet scalar dark matter, *JHEP* 1404, 029 (DOI: 10.1007/JHEP04(2014)029).
- [115] Kadastik M. *et al.* (2012), Implications of the 125 GeV Higgs boson for scalar dark matter and for the CMSSM phenomenology, *JHEP* 1205, 061 (DOI: 10.1007/JHEP05(2012)061).
- [116] Gabrielli E. *et al.* (2014), Towards Completing the Standard Model: Vacuum Stability, EWSB and Dark Matter, *Phys. Rev. D* 89, 015017 (DOI: 10.1103/PhysRevD.89.015017).
- [117] Gonderinger M. *et al.* (2010), Vacuum Stability, Perturbativity, and Scalar Singlet Dark Matter, *JHEP* 1001, 053 (DOI: 10.1007/JHEP01(2010)053).
- [118] Clark T. E. *et al.* (2009), The Standard Model Higgs Boson-Inflaton and Dark Matter, *Phys. Rev. D* 80, 075019 (DOI: 10.1103/PhysRevD.80.075019).
- [119] Lerner R. N. and McDonald J. (2009), Gauge singlet scalar as inflaton and thermal relic dark matter, *Phys. Rev. D* 80, 123507 (DOI: 10.1103/PhysRevD.80.123507).
- [120] Cheung C. *et al.* (2012), Higgs and Dark Matter Hints of an Oasis in the Desert, *JHEP* 1207, 105 (DOI: 10.1007/JHEP07(2012)105).

-
- [121] Lebedev O. (2012), On Stability of the Electroweak Vacuum and the Higgs Portal, Eur. Phys. J. C 72, 2058 (DOI: 10.1140/epjc/s10052-012-2058-2).
- [122] Elias-Miro J. *et al.* (2012), Stabilization of the Electroweak Vacuum by a Scalar Threshold Effect, JHEP 1206, 031 (DOI: 10.1007/JHEP06(2012)031).
- [123] Antipin O. *et al.* (2014), Stable $E\chi$ tensions with(out) gravity, Nucl. Phys. B 886, 125-134 (DOI: 10.1016/j.nuclphysb.2014.06.023).
- [124] Khan S. *et al.* (2014), Vacuum Stability constraints on the minimal singlet TeV Seesaw Model, Phys. Rev. D 89, 073021 (DOI: 10.1103/PhysRevD.89.073021).
- [125] Grzadkowski B. and Wudka J. (2002), Bounds on the Higgs-Boson mass in the presence of nonstandard interactions, Phys. Rev. Lett. 88, 041802 (DOI: 10.1103/PhysRevLett.88.041802).
- [126] Branchina V. and Messina E. (2013), Stability, Higgs Boson Mass and New Physics, Phys. Rev. Lett. 111, 241801 (DOI: 10.1103/PhysRevLett.111.241801).
- [127] Lalak Z. *et al.* (2014), Higher-order scalar interactions and SM vacuum stability, JHEP 1405, 119 (DOI: 10.1007/JHEP05(2014)119).
- [128] Branchina V. *et al.* (2014), Top mass determination, Higgs inflation, and vacuum stability, JHEP 1409, 182 (DOI: 10.1007/JHEP09(2014)182).
- [129] Eichhorn A. and Scherer M. M. (2014), The Planck scale, the Higgs mass and scalar dark matter, Phys. Rev. D 90, 025023 (DOI: 10.1103/PhysRevD.90.025023).
- [130] Gonderinger M. *et al.* (2012), Complex Scalar Singlet Dark Matter: Vacuum Stability and Phenomenology, Phys. Rev. D 86, 043511 (DOI: 10.1103/PhysRevD.86.043511).

-
- [131] Belanger G. *et al.* (2013), Global fit to Higgs signal strengths and couplings and implications for extended Higgs sectors, Phys. Rev. D 88, 075008 (DOI: 10.1103/PhysRevD.88.075008).
- [132] Duerr M. *et al.* (2015), Scalar Singlet Dark Matter and Gamma Lines, Phys. Lett. B 751, 119-122 (DOI: 10.1016/j.physletb.2015.10.034).
- [133] Duerr M. *et al.* (2016), Scalar Dark Matter: Direct vs. Indirect Detection, JHEP 1606, 152 (DOI: 10.1007/JHEP06(2016)152).
- [134] Alloul A. *et al.* (2014), FeynRules 2.0 - A complete toolbox for tree-level phenomenology, Comput. Phys. Commun. 185, 2250-2300 (DOI: 10.1016/j.cpc.2014.04.012).
- [135] Belanger G. *et al.* (2011), Indirect search for dark matter with micrOMEGAs2.4, Comput. Phys. Commun. 182, 842-856 (DOI: 10.1016/j.cpc.2010.11.033).
- [136] Belanger G. *et al.* (2014), micrOMEGAs_3: A program for calculating dark matter observables, Comput. Phys. Commun. 185, 960-985 (DOI: 10.1016/j.cpc.2013.10.016).
- [137] Chen C. S. and Tang Y. (2012), Vacuum stability, neutrinos, and dark matter, JHEP, 1204, 019 (DOI: 10.1007/JHEP04(2012)019).
- [138] Spencer-Smith A. (2014), Higgs Vacuum Stability in a Mass-Dependent Renormalisation Scheme, arXiv:1405.1975 [hep-ph].
- [139] Dolle E. M. and Su S. (2009), The Inert Dark Matter, Phys. Rev. D 80, 055012 (DOI: 10.1103/PhysRevD.80.055012).

-
- [140] Gustafsson M. *et al.* (2012), Status of the Inert Doublet Model and the Role of multileptons at the LHC, Phys. Rev. D 86, 075019 (DOI: 10.1103/PhysRevD.86.075019).
- [141] Honorez L. L. and Yaguna C. E. (2010), The inert doublet model of dark matter revisited, JHEP 1009, 046 (DOI: 10.1007/JHEP09(2010)046).
- [142] Goudelis A. *et al.* (2013), Dark matter in the Inert Doublet Model after the discovery of a Higgs-like boson at the LHC, JHEP 1309, 106 (DOI: 10.1007/JHEP09(2013)106).
- [143] Arhrib A. *et al.* (2014), An Updated Analysis of Inert Higgs Doublet Model in light of the Recent Results from LUX, PLANCK, AMS-02 and LHC, JCAP 1406, 030 (DOI: 10.1088/1475-7516/2014/06/030).
- [144] Chakrabarty N. *et al.* (2015), Dark matter, neutrino masses and high scale validity of an inert Higgs doublet model, Phys. Rev. D 92, 015002 (DOI: 10.1103/PhysRevD.92.015002).
- [145] Hambye T. and Tytgat M. H. G. (2008), Electroweak symmetry breaking induced by dark matter, Phys. Lett. B 659, 651-655 (DOI: 10.1016/j.physletb.2007.11.069).
- [146] Coleman S. R. and Weinberg E. J. (1973), Radiative Corrections as the Origin of Spontaneous Symmetry Breaking, Phys. Rev. D 7, 1888-1910 (DOI: 10.1103/PhysRevD.7.1888).
- [147] Chakrabarty N. *et al.* (2014), High-scale validity of a two-Higgs doublet scenario: a study including LHC data, JHEP 1412, 166 (DOI: 10.1007/JHEP12(2014)166).

-
- [148] Barbieri R. *et al.* (2006), Improved naturalness with a heavy Higgs: An Alternative road to LHC physics, Phys. Rev. D 74, 015007 (DOI: 10.1103/PhysRevD.74.015007).
- [149] Pierce A. and Thaler J. (2007), Natural Dark Matter from an Unnatural Higgs Boson and New Colored Particles at the TeV Scale, JHEP 0708, 026 (DOI: 10.1088/1126-6708/2007/08/026).
- [150] Lundstr E. *et al.* (2009), The Inert Doublet Model and LEP II Limits, Phys. Rev. D 79, 035013 (DOI: 10.1103/PhysRevD.79.035013).
- [151] Belanger G. *et al.* (2015), Dilepton constraints in the Inert Doublet Model from Run 1 of the LHC, Phys. Rev. D 91, 115011 (DOI: 10.1103/PhysRevD.91.115011).
- [152] Cao Q. H. *et al.* (2007), Observing the Dark Scalar Doublet and its Impact on the Standard-Model Higgs Boson at Colliders, Phys. Rev. D 76 095011 (DOI: 10.1103/PhysRevD.76.095011).
- [153] Djouadi A. (2008), The Anatomy of electro-weak symmetry breaking. II. The Higgs bosons in the minimal supersymmetric model, Phys. Rept. 459, 1-241 (DOI: 10.1016/j.physrep.2007.10.005).
- [154] Swiezewska B. and Krawczyk M. (2013), Diphoton rate in the inert doublet model with a 125 GeV Higgs boson, Phys. Rev. D 88, 035019 (DOI: 10.1103/PhysRevD.88.035019).
- [155] Krawczyk M. *et al.* (2013), Constraining Inert Dark Matter by $R_{\gamma\gamma}$ and WMAP data, JHEP 1309, 055 (DOI: 10.1007/JHEP09(2013)055).
- [156] Aad G. *et al.* (2014), Measurement of Higgs boson production in the diphoton decay channel in pp collisions at center-of-mass energies of 7 and 8 TeV

- with the ATLAS detector, Phys. Rev. D 90, 112015 (DOI: 10.1103/PhysRevD.90.112015).
- [157] Khachatryan V. *et al.* (2014), Observation of the diphoton decay of the Higgs boson and measurement of its properties, Eur. Phys. J. C 74, 3076 (DOI: 10.1140/epjc/s10052-014-3076-z).
- [158] Honorez L. L. and Yaguna C. E. (2011), A new viable region of the inert doublet model, JCAP 1101, 002 (DOI: 10.1088/1475-7516/2011/01/002).
- [159] Hambye T. *et al.* (2009), Scalar Multiplet Dark Matter, JHEP 0907, 090 (DOI: 10.1007/JHEP05(2010)066).
- [160] Griest K. and Seckel D. (1991), Three exceptions in the calculation of relic abundances, Phys. Rev. D 43, 3191-3203 (DOI: 10.1103/PhysRevD.43.3191).
- [161] Modak K. P. and Majumdar D. (2015), Confronting Galactic and Extragalactic γ -ray observed by Fermi-LAT with Annihilating Dark Matter in Inert Higgs Doublet Model, Astrophys. J. Suppl. 219, 37 (DOI: 10.1088/0067-0049/219/2/37).
- [162] Gustafsson M. (2010), The Inert Doublet Model and Its Phenomenology, PoS CHARGED 2010, 030 (C10-09-27.3).
- [163] Barroso A. *et al.*, Metastability bounds on the two Higgs doublet model, JHEP 1306 (2013) 045 (DOI: 10.1007/JHEP06(2013)045).
- [164] Barroso A. *et al.* (2013), Evading death by vacuum, Eur. Phys. J. C 73, 2537 (DOI: 10.1140/epjc/s10052-013-2537-0).
- [165] Barroso A. *et al.* 2013, Tree-level metastability bounds in two-Higgs doublet models, arXiv:1305.1235 [hep-ph] (C13-02-13.1).

-
- [166] Gil G. *et al.* (2012), Inert Dark Matter and Strong Electroweak Phase Transition, Phys. Lett. B 717, 396-402 (DOI: 10.1016/j.physletb.2012.09.052).
- [167] Elias-Miro J. *et al.* (2012), Higgs mass implications on the stability of the electroweak vacuum, Phys. Lett. B 709, 222-228 (DOI: 10.1016/j.physletb.2012.02.013).
- [168] Veltman M. J. G. (1981), The Infrared - Ultraviolet Connection, Acta Phys. Polon. B 12, 437 (Print-80-0851).
- [169] Hamada Y. *et al.* (2013), Bare Higgs mass at Planck scale, Phys. Rev. D 87, 053009 (DOI: 10.1103/PhysRevD.89.059901).
- [170] Chakraborty I. and Kundu A. (2014), Two-Higgs doublet models confront the naturalness problem, Phys. Rev. D 90, 115017 (DOI: 10.1103/PhysRevD.90.115017).
- [171] Cirelli M. and Strumia A. (2009), Minimal Dark Matter: Model and results, New J. Phys. 11, 105005 (DOI: 10.1088/1367-2630/11/10/105005).
- [172] Cirelli M. *et al.* (2006), Minimal dark matter, Nucl. Phys. B 753, 178-194 (DOI: 10.1016/j.nuclphysb.2006.07.012).
- [173] Mihaila L. N. *et al.* (2012), Gauge Coupling Beta Functions in the Standard Model to Three Loops, Phys. Rev. Lett. 108, 151602 (DOI: 10.1103/PhysRevLett.108.151602).
- [174] Chetyrkin K. G. and Zoller M. F. (2012), Three-loop β -functions for top-Yukawa and the Higgs self-interaction in the Standard Model, JHEP 1206, 033 (DOI: 10.1007/JHEP06(2012)033).

- [175] Zoller M. F. (2014), Vacuum stability in the SM and the three-loop β -function for the Higgs self-interaction, Subnucl. Ser. 50, 557-566 (DOI: 10.1142/9789814603904_0034).
- [176] Chetyrkin K. G. and Zoller M. F. (2014), β -function for the Higgs self-interaction in the Standard Model at three-loop level, Subnucl. Ser. 50, 557-566 (DOI: 10.1142/9789814603904_0034).
- [177] Zoller M. F. (2013), Beta-function for the Higgs self-interaction in the Standard Model at three-loop level, PoS EPS-HEP2013, 322 (C13-07-18).
- [178] Davoudiasl H. *et al.* (2005), The New minimal standard model, Phys. Lett. B 609, 117-123 (DOI: 10.1016/j.physletb.2005.01.026).
- [179] Staub F. (2014), SARAH 4 : A tool for (not only SUSY) model builders, Comput. Phys. Commun.185, 1773-1790 (DOI: 10.1016/j.cpc.2014.02.018).